Detailed Properties of High Redshift Galaxies

Thesis by

Tucker Jones

In Partial Fulfillment of the Requirements

for the Degree of

Doctor of Philosophy

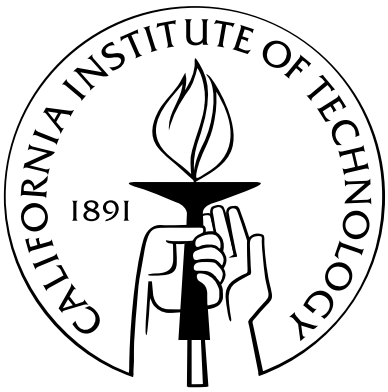

California Institute of Technology

Pasadena, California

2013

(Defended August 16, 2012)

To all the teachers, especially nature.

Acknowledgments

Grad school was a long, strange trip. I'd like to thank my companions for making it a good one.

First of all, a huge thank you to my thesis advisor Richard Ellis for tirelessly supporting this work, encouraging me during the hard parts, and celebrating the successes. Richard's enthusiasm for astronomy and dedication to his work are so inspiring. I count myself fortunate to have such a great mentor. I am also grateful to Johan Richard and Mark Swinbank for all their help in guiding me through my first 2+ years of grad school. Integral field spectroscopy isn't necessarily easy; I was lucky to have a pro like Mark helping me out. Dan Stark, Eric Jullo, Eiichi Egami, Rachael Livermore, and Richard Bower have all been great collaborators as well. I also thank Nick Scoville, Chuck Steidel, Judy Cohen, and Chris Hirata for their service on my thesis committee. It was a pleasure to share my research with them (and with you, dear reader!).

I've been lucky to have great company on observing runs: thanks to Richard, Dan, Mark, Matt Schenker, Sirio Belli, and Drew Newman for all the late night good times. Special props to Matt for looking after me when I was sick and for our epic Mauna Kea snowboarding adventure.

Crucial thanks go out to the Wizards whose black magic makes things happen. Patrick, Anu, and José always satisfied my computational needs. Judy McClain handled way too many logistical headaches. Hard work by the crews at Keck and Palomar was absolutely essential for obtaining the data which made this work possible. And of course, Dipali and Scott conjure up the most wonderful meals and make the Monastery a home for all of us observers.

To my friends and family: what can I say, I love you all. I had the best classmates ever; first year was so much better with all the shenanigans. I had the best office mates ever, with a special secret wink to Mansi and Ann Marie for the rap. I had absolutely the best housemates ever - Nick, Luke, Keenan, Weissman, Wolf, Elisabeth, Hamik, Sid, Matt, Ana and David - the most remarkable thing is that feeling of being in motion. A special recognition is due to my climbing, surfing, backcountry skiing, and general mayhem buddies: Ben, BG, Brian, Dan, Dani, David, Derek, Erik, Hamik, Kedron, Kevin, Joel, Jon, Lauren, Liz, Matt, Mike, Nick, Patrick, PT, Sawyer, Sebastian, Shriharsh, Sid, Stephen, Steve, and many more who literally held my rope. May we have many more excellent adventures! And please, no more helicopter rescues. An extra special shout out to my longtime partner in crime, David Brown. I am grateful to Mariya and her infinite supply of love and good times. And finally, thanks to the fam - Sig, Henry, Ty, and Leif - for everything.

Abstract

Galaxies evolve throughout the history of the universe from the first star-forming sources, through gas-rich asymmetric structures with rapid star formation rates, to the massive symmetrical stellar systems observed at the present day. Determining the physical processes which drive galaxy formation and evolution is one of the most important questions in observational astrophysics. This thesis presents four projects aimed at improving our understanding of galaxy evolution from detailed measurements of star forming galaxies at high redshift.

We use resolved spectroscopy of gravitationally lensed $z \simeq 2-3$ star forming galaxies to measure their kinematic and star formation properties. The combination of lensing with adaptive optics yields physical resolution of $\simeq 100$ pc, sufficient to resolve giant HII regions. We find that $\sim 70\,\%$ of galaxies in our sample display ordered rotation with high local velocity dispersion indicating turbulent thick disks. The rotating galaxies are gravitationally unstable and are expected to fragment into giant clumps. The size and dynamical mass of giant HII regions are in agreement with predictions for such clumps indicating that gravitational instability drives the rapid star formation. The remainder of our sample is comprised of ongoing major mergers. Merging galaxies display similar star formation rate, morphology, and local velocity dispersion as isolated sources, but their velocity fields are more chaotic with no coherent rotation.

We measure resolved metallicity in four lensed galaxies at $z = 2.0-2.4$ from optical emission line diagnostics. Three rotating galaxies display radial gradients with higher metallicity at smaller radii, while the fourth is undergoing a merger and has an inverted gradient with lower metallicity at the center. Strong gradients in the rotating galaxies indicate that they are growing inside-out with star formation fueled by accretion of metal-poor gas at large radii. By comparing measured gradients with an appropriate comparison sample at $z = 0$, we demonstrate that metallicity gradients in isolated galaxies must flatten at later times. The amount of size growth inferred by the gradients is in rough agreement with direct measurements of massive galaxies. We develop a chemical evolution model to interpret these data and conclude that metallicity gradients are established by a gradient in the outflow mass loading factor, combined with radial inflow of metal-enriched gas.

We present the first rest-frame optical spectroscopic survey of a large sample of low-luminosity galaxies at high redshift ($L < L_*$, $1.5 < z < 3.5$). This population dominates the star formation

density of the universe at high redshifts, yet such galaxies are normally too faint to be studied spectroscopically. We take advantage of strong gravitational lensing magnification to compile observations for a sample of 29 galaxies using modest integration times with the Keck and Palomar telescopes. Balmer emission lines confirm that the sample has a median SFR $\sim$ 10 $M_{\odot}yr^{-1}$and extends to lower SFR than has been probed by other surveys at similar redshift. We derive the metallicity, dust extinction, SFR, ionization parameter, and dynamical mass from the spectroscopic data, providing the first accurate characterization of the star-forming environment in low-luminosity galaxies at high redshift. For the first time, we directly test the proposal that the relation between galaxy stellar mass, star formation rate, and gas phase metallicity does not evolve. We find lower gas phase metallicity in the high redshift galaxies than in local sources with equivalent stellar mass and star formation rate, arguing against a time-invariant relation. While our result is preliminary and may be biased by measurement errors, this represents an important first measurement that will be further constrained by ongoing analysis of the full data set and by future observations.

We present a study of composite rest-frame ultraviolet spectra of Lyman break galaxies at $z \simeq 4$ and discuss implications for the distribution of neutral outflowing gas in the circumgalactic medium. In general we find similar spectroscopic trends to those found at $z = 3$ by earlier surveys. In particular, absorption lines which trace neutral gas are weaker in less evolved galaxies with lower stellar masses, smaller radii, lower luminosity, less dust, and stronger Lyα emission. Typical galaxies are thus expected to have stronger Lyα emission and weaker low-ionization absorption at earlier times, and we indeed find somewhat weaker low-ionization absorption at higher redshifts. In conjunction with earlier results, we argue that the reduced low-ionization absorption is likely caused by lower covering fraction and/or velocity range of outflowing neutral gas at earlier epochs. This result has important implications for the hypothesis that early galaxies were responsible for cosmic reionization. We additionally show that fine structure emission lines are sensitive to the spatial extent of neutral gas, and demonstrate that neutral gas is concentrated at smaller galactocentric radii in higher redshift galaxies.

The results of this thesis present a coherent picture of galaxy evolution at high redshifts $2 \lesssim z \lesssim 4$. Roughly 1/3 of massive star forming galaxies at this period are undergoing major mergers, while the rest are growing inside-out with star formation occurring in gravitationally unstable thick disks. Star formation, stellar mass, and metallicity are limited by outflows which create a circumgalactic medium of metal-enriched material. We conclude by describing some remaining open questions and prospects for improving our understanding of galaxy evolution with future observations of gravitationally lensed galaxies.

Contents

Statement of Originality

Parts of this thesis have been previously published as Jones, T. A., Swinbank, A. M., Ellis, R. S., Richard, J., & Stark, D. P. 2010, MNRAS, 404, 1247 (Chapter 2), as Richard, J., Jones, T., Ellis, R., et al. 2011, MNRAS, 413, 643 (Chapter 4), and as Jones, T., Stark, D. P., & Ellis, R. S. 2012, ApJ, 751, 51 (Chapter 5). In addition, the content of Chapter 4 is drawn in part from recent results to be published in a forthcoming paper (Belli et al., in preparation), and the contents of Chapter 3 have been submitted for publication in *The Astrophysical Journal*.

The work presented in this thesis is a collaborative effort with significant contributions by several of my colleagues, described here. Much of the analysis in Chapters 2, 3, and 4 relies on source plane reconstructions determined from the detailed gravitational lens modeling done by Johan Richard and Eric Jullo. Chapter 4 is based on a cumulation of data obtained over several years for different projects with significant contributions by Johan Richard and Sirio Belli. Johan Richard obtained and reduced some of the NIRSPEC data presented in Chapter 4 and performed an initial interpretation in the context of the mass-metallicity relation in collaboration with myself. This original analysis was published as Richard, J., Jones, T., Ellis, R., et al. 2011, MNRAS, 413, 643. In Chapter 4, I have updated this analysis with more recent results from a new survey with Triplespec which I initiated. My role in these projects included planning observations, obtaining and reducing data, and contributing much of the analysis and text presented in Richard et al. (2011). More recently, Sirio Belli has assisted in the Triplespec observations and I have moved to an advisory role on the reduction of the latest data.

Chapter 1

Introduction

The cosmic microwave background, emitted just 380,000 years after the big bang, reveals that the density and temperature of the universe were uniform to within approximately one thousandth of a percent at that time. Slightly over-dense regions subsequently grew through gravitational attraction, eventually becoming dense enough to form stars which produced the first heavy elements. Over time these proto-galaxies continued to accrete matter, form stars, and merge together, forming the massive galaxies which populate the universe today. One of the greatest current challenges in observational astrophysics is to determine how galaxies formed and evolved from the first stellar systems into the massive, symmetric structures seen today. Advances in telescope and detector technology have now enabled astronomers to detect and characterize galaxies as distant as $z \simeq 7$, corresponding to 800 million years after the big bang when the universe was only 5 % of its present age. At this epoch only $\simeq 1$ % of the present-day stellar mass had been formed (Robertson et al., 2010). Large imaging and spectroscopic surveys have detected thousands of galaxies at high redshift, providing a statistical description of their evolution in size, stellar mass, star formation rate, and heavy element content. Although the first stars and galaxies have not yet been detected, a great deal has been learned to date about the formation and evolution of massive galaxies by studying their properties throughout the observable history of the universe.

The goal of this thesis is to provide a better understanding of how galaxies evolve by studying their physical properties at a time when stellar mass assembly was most rapid. This introduction is intended to provide a context for the current work, essentially: what (we think) we know about galaxy formation and how we know it. I begin in §1.1 by describing our current understanding of galaxy formation, including the theories and data which have lead to this understanding, with attention to relevant topics and techniques. The specific goals of this thesis are described briefly in §1.2.

1.1 Galaxy Formation within the ΛCDM Paradigm

Our most commonly accepted understanding of galaxy formation to date is based on the ΛCDM theoretical paradigm. ΛCDM is able to explain essentially all measurements of the contents and history of the universe with relatively few parameters which are now measured to high precision. This theory is extensively applied in extragalactic astronomy to convert measured quantities, such as angular size and flux, into physical properties such as physical size and luminosity. Before describing the relevant details of galaxy formation, it is useful to review the basic tenets and predictions of ΛCDM.

ΛCDM theory, named for the two main components, makes precise predictions for the history of the universe based only on the distribution of energy density. The full details are described in various textbooks (e.g., Longair 2008; Ryden 2003) and I provide a brief synopsis here. Precision measurements suggest that the present day energy density of the universe is composed of $\simeq 70\,\%$ dark energy (Λ), $\simeq 25\,\%$ cold dark matter (CDM), a modest $\simeq 5\,\%$ baryonic matter, and $\lesssim 2\,\%$ radiation, relativistic particles, and spatial curvature (e.g., Spergel et al. 2003). These data imply that the universe originated 13.7 billion years ago in a rapid expansion known as the big bang. Between $\sim 2-20$ minutes after the big bang, the temperature and density were sufficient for nuclear fusion to occur. The resulting big bang nucleosynthesis (BBN) is predicted to produce primarily ^{4}He ($\simeq 25\,\%$ by mass) with trace amounts of deuterium, ^{3}He, lithium, and beryllium. The remaining $\simeq 75\,\%$ of baryonic mass is in the form of unfused hydrogen. The reader is referred to Burles et al. (2001) for an overview of BBN theory and relevant measurements. Importantly, no elements heavier than beryllium are produced in this process. Following the period of BBN, all baryonic matter in the universe was fully ionized and therefore coupled to the electromagnetic radiation field via Thomson scattering. Meanwhile, non-baryonic dark matter is decoupled from the radiation field and non-relativistic. Tiny perturbations in the local density therefore caused dark matter to collapse into "halos" under the force of gravity, while pressure in the photon-baryon fluid prevented baryonic matter from collapsing. Approximately 380,000 years after the big bang, the temperature reached a point at which all electrons combined with nuclei to form neutral atoms, decoupling from the radiation field and releasing what is now observed as CMB radiation from the so-called surface of last scattering. Baryons then began to collapse into gravitational potential wells established by the growing dark matter halos, which ultimately serve as the sites of galaxy formation.

After baryonic matter combined into neutral atoms and the CMB was emitted, the growth of massive baryonic (as well as dark matter) structures in the universe was dominated by gravity. The details of this process have been calculated using N-body computer simulations such as the Millenium Run (Springel et al., 2005) and semi-analytic methods (Press & Schechter, 1974). Impressively, these approaches are able to accurately predict the statistical distribution of massive galaxies and clusters

based on the initial density field derived from CMB measurements. Simulations show that small dark matter halos were the first to collapse (i.e., virialize), and under the influence of perturbations on larger scales, these mini-halos merged together to create larger halos in a "bottom-up" formation process. Merging continues to form increasingly large structures to the present day and is an important aspect of galaxy evolution. Although some predictions are still difficult to reconcile with observations (for example the number of satellite galaxies orbiting the Milky Way), numerical simulations within the context of ΛCDM theory give a self-consistent view of structure formation in the universe.

The remainder of this introduction is devoted to details which are not yet adequately described within the ΛCDM paradigm. In particular, while ΛCDM provides a relatively simple explanation for the spatial distribution and dark matter content of galaxies from gravity alone, additional physical processes are required to explain the variety of observed baryonic properties of galaxies such as morphology, spectral energy distribution, and heavy element content. The baryonic content of a galaxy generally consists of a central supermassive black hole surrounded by a distribution of stars and gas. We can therefore condense the details of galaxy formation and evolution into the simple question, *when and how did the stars, gas, and central black hole assemble?* In principle this question can be addressed by measuring the baryonic content of galaxies throughout the history of the universe. Extensive surveys have made impressive progress toward this goal by characterizing the dominant massive galaxy population throughout the period $0 < z \lesssim 7$, or $\gtrsim 800$ million years after the big bang. A recent review of the techniques used to locate distant galaxies and determine their baryonic content, and the results of these efforts, is given by Shapley (2011). Notable results include determinations of the total stellar mass density, star formation rate density, major merger rate, and heavy element content of massive galaxies throughout most of the observable universe. These studies provide a census which now accounts for the formation of $\gtrsim 95\,\%$ of the star formation and stellar mass in the universe (Figure 1.1; Robertson et al. 2010). Star formation activity peaked during the period $2 \lesssim z \lesssim 4$ (Figure 1.1), and many studies have focused on this epoch when galaxy assembly was most rapid. We therefore know *when* most of the stellar mass was formed, at what rate, and in which galaxies, at least in a statistical sense. The question of how these stars were assembled into the morphologies observed today, and when these structures emerged, is more difficult to address and requires high resolution observations of individual galaxies.

Morphological studies show that significant structural evolution must occur during the process of galaxy assembly. Galaxies are often classified in terms of their morphology according to a scheme developed by Edwin Hubble in 1926 known as the Hubble sequence. Galaxies along the Hubble sequence contain a smooth ellipsoidal bulge of stars, and a disk of stars and gas. Some, known as irregular galaxies, have asymmetric morphologies with no bulge or disk. However the majority of massive local galaxies are axisymmetric with varying contributions of bulge and disk to the total

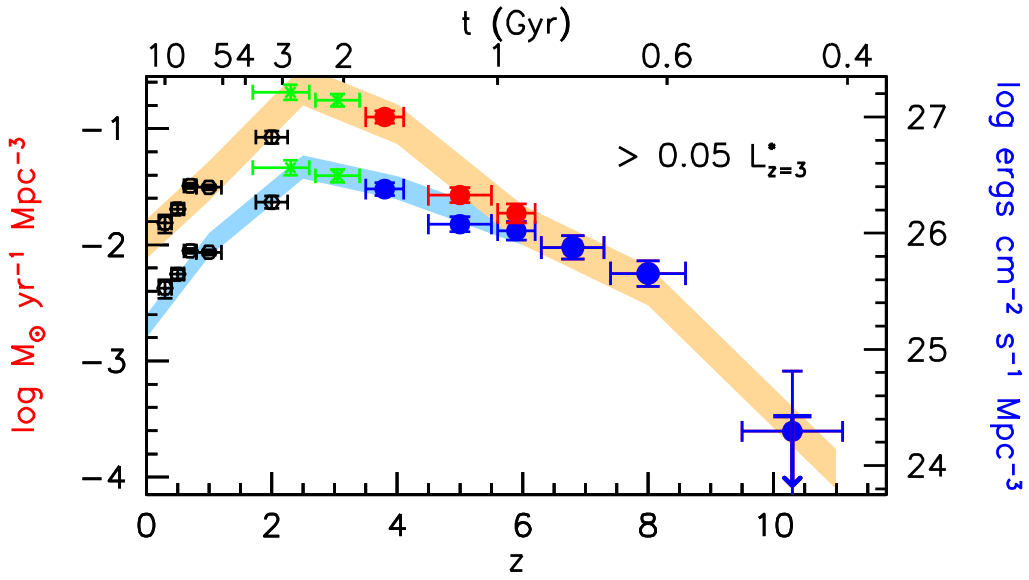

Figure 1.1: Star formation density of the universe since $z \simeq 10$, taken from Bouwens et al. (2011). Star formation density is derived from measurements of the ultraviolet luminosity density, shown on the right axis. The density of star formation peaked during the redshift range $z \simeq 2-4$. Integrated measurements of the star formation density as a function of redshift are in general agreement with the observed stellar mass density (e.g., Robertson et al. 2010).

stellar mass. At high redshifts $z \gtrsim 2$, however, most galaxies are irregular in structure. In fact only one spiral disk galaxy is currently known at $z > 2$ (Law et al., 2012), in stark contrast to their abundance in the local universe. Therefore, massive galaxies must undergo significant structural transformation from the irregular morphologies observed at high redshift into the symmetric Hubble sequence seen today. Four main processes are known to be important in the evolution of a galaxy's stellar content and morphology, briefly summarized here.

- *Accretion and merging* provide the baryonic material needed for growth in stellar mass. Both are important in establishing the angular momentum of a disk, and merging events can significantly alter the overall morphology.

- *Star formation* transforms gas into stellar mass and produces all heavy elements. Major merger events can trigger significant circumnuclear star formation which is thought to contribute to a stellar bulge. In quiescent galaxies, star formation predominantly occurs in an extended gaseous disk and hence contributes to the disk morphology.

- *Outflows* of gas are driven by energy from supernovae, massive stars, and accreting black holes. Essentially all star forming galaxies detected in surveys at $z \gtrsim 1$ drive galaxy-scale outflows, with mass outflow rates often in excess of the star formation rate. This process is important in regulating the gaseous fuel available for star formation.

- *Secular dynamical evolution* is important in redistributing the stellar and gas content of galaxies. Examples of secular evolution processes include Toomre instability, dynamical friction, and gas transport induced by stellar bars.

Different accretion, merging, and star formation histories, combined with dynamical evolution, are thought to give rise to the variety of morphologies observed today. Detailed measurements of the resolved star formation, outflow properties, and the dynamical state of galaxies throughout their period of formation are therefore essential for determining how and when the baryonic structure of galaxies assembled. This is the broad context in which this thesis attempts to further our understanding of the galaxy formation process.

1.1.1 High Resolution with Gravitational Lensing

One of the largest barriers to obtaining detailed information of high redshift galaxies is their small angular size relative to the resolution acheived by modern telescopes. This point is illustrated by Figure 1.2. Seeing-limited telescopes (and most space-based telescopes!) are unable to resolve typical galaxies at $z > 1$. Even with adaptive optics (AO), the resolution of 8−10 meter telescopes corresponds to $\simeq 1$ kpc at $z > 2$, comparable to the half-light radii of typical L_* galaxies. Studies of resolved properties are therefore limited to the largest galaxies at high redshift which are generally not representative of the population as a whole. In fact, one of the primary science goals of planned 30+ meter optical/near-IR telescopes is to resolve the detailed structure of high redshift galaxies via an improved diffraction limit. In rare cases, however, the phenomenon of gravitational lensing can magnify the apparent size and flux of background galaxies by large factors ($\simeq 10 - 30$), providing much better spatial sampling than is otherwise possible. Results presented in Chapters 2 and 3 take advantage of gravitational lensing in combination with AO to measure the physical properties of lensed galaxies with intrinsic physical resolution as fine as 100 parsecs. This represents the highest physical resolution ever achieved in high redshift galaxy studies and has enabled detailed measurements of kinematics, giant HII region properties, and metallicity distributions as described in this thesis. Additionally, results presented in Chapter 4 utilize gravitational lensing to measure the integrated properties of galaxies which are normally too faint for detailed spectroscopic study. In summary, this thesis makes extensive use of gravitational lensing to study faint galaxies and small spatial scales which are otherwise inaccessible with current facilities.

1.1.2 Metallicity as a Probe of Galaxy Evolution

Metallicity is a sensitive probe of galaxy evolution for the simple reason that all metals in the universe are produced as a by-product of galaxies. Before the first generation of stars formed, the universe contained almost no elements heavier than helium and strictly no elements heavier than

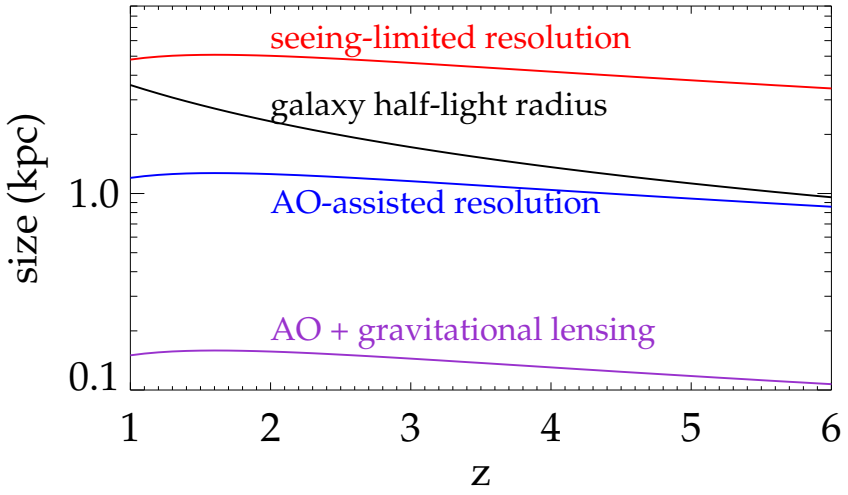

Figure 1.2: Comparison of galaxy size with angular resolution acheived by various observations, as a function of redshift. The typical galaxy half-light radius is measured by Bouwens et al. (2004). Shown for comparison are the physical resolution acheived by seeing-limited data (0.″6 FWHM), adaptive optics (AO) assisted data (0.″15 FWHM), and the combination of AO and gravitational lensing with a linear magnification factor $\mu_1 = 8$. Typical galaxies at $z > 1$ are unresolved in seeing-limited data. At $z > 2$, typical galaxies subtend only a few independent resolution elements in AO-assisted observations. Gravitational lensing, however, can provide well-resolved measurements throughout the observed history of the universe.

beryllium. All subsequent production of metals (defined as elements heavier than helium) is due to stellar nucleosynthesis. Metals generated in stars are released to the gaseous interstellar medium (ISM) via supernovae explosions and stellar winds. The precise distribution of heavy elements in the ISM is therefore sensitive to the amount of previous star formation. This can be expressed quantitatively in terms of the yield y of metals produced per unit stellar mass formed. For a closed system, the gas-phase metal mass fraction Z is given by the simple equation

$$Z = -y \ln (1 - f_*) \tag{1.1}$$

where f_* is the fraction of total baryonic mass which has been converted into stars (Schmidt, 1963). In principle this can provide an independent measurement of the star formation history of the universe, in addition to more direct measures such as Figure 1.1. However, galaxies are not closed systems and require somewhat more complicated chemical evolution models to account for inflow and outflow of gas. Such a model is developed in Chapter 3 of this thesis to interpret metallicity measurements in terms of gas flows.

Gas-phase metallicity measurements in conjunction with chemical evolution models have proven to be a valuable tool for understanding galaxy formation. The metallicity of a galaxy depends on its assembly history, particularly the gas accretion, outflows, and star formation. Direct measurements

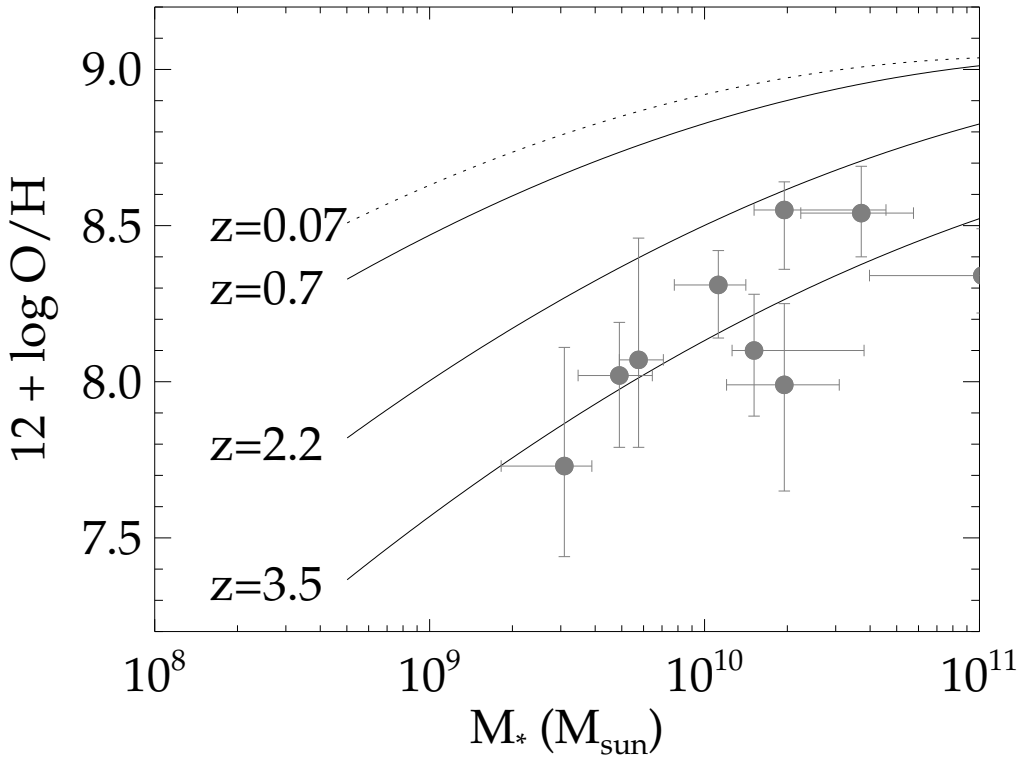

Figure 1.3: Evolution in the mass-metallicity relation with redshift. Solid lines are empirical fits by Maiolino et al. (2008) to data at various redshifts; the dashed line is their fit to local galaxies in the SDSS. Data points show galaxies at $z \simeq 3.5$ reported by Maiolino et al. (2008). Metallicity decreases at higher redshifts for a fixed stellar mass.

of metallicity therefore place direct constraints on these important processes. Many studies have focused on the correlation between galaxy stellar mass and metallicity, first noted by Lequeux et al. (1979). The mass-metallicity relation has since been precisely measured from the vast and uniform data set produced by the Sloan Digitized Sky Survey (SDSS; Tremonti et al. 2004). More massive galaxies are observed to have higher metallicities, usually attributed to the effect of outflows: galaxies with lower mass have lower gravitational potential wells and therefore lose a higher fraction of metal-enriched gas in star formation-driven outflows. Several groups have measured the mass-metallicity relation at high redshifts up to $z \simeq 3.5$, demonstrating clear evolution with galaxies at a fixed stellar mass having lower metallicity at earlier times (Figure 1.3). This evolution is attributed to increasing gas fractions in the high redshift samples.

While Figure 1.3 shows a clear evolution in the mass-metallicity relation with redshift, the samples selected at different redshifts are not necessarily equivalent. In particular, galaxies observed at higher z are inferred to have higher gas fractions at a fixed stellar mass, and have higher measured star formation rates (SFR). In 2009, two groups suggested that apparent evolution in the mass-

metallicity relation is explained by differences in the SFR (Mannucci et al., 2010; Lara-López et al., 2010). These authors showed that lower metallicity is correlated with higher SFR and postulated the existence of a "fundamental metallicity relation" (FMR) between galaxy stellar mass, SFR, and metallicity which does not evolve with time. Indeed, such an FMR is able to accurately reproduce all measurements at $z < 2.5$ suggesting that the processes governing metallicity do not evolve over this time. For example, a time-invariant FMR implies that the mass loading factor (defined as the ratio of mass outflow rate to SFR) and its dependence on stellar mass do not systematically evolve with time (Davé et al., 2011). The mass loading factor is an important ingredient in galaxy formation models and hence this result would have significant consequences for our understanding of galaxy evolution. The FMR has thus been a topic of significant observational and theoretical research. The dependence on SFR is now understood in terms of inflows of metal-poor gas, which reduce the gas-phase metallicity and simultaneously stimulate star formation. However, there is currently no theoretical support for a time-invariant FMR. Furthermore there is no direct evidence that the FMR is truly time-invariant, since samples at different redshifts probe different regions of the mass-SFR plane. This issue is discussed further in Chapter 4 where I present the first direct test of time evolution in the FMR.

In addition to integrated measurements, radial metallicity gradients provide useful constraints on galaxy formation. In the local universe, all disk galaxies are observed to have gradients with decreasing metallicity at larger radii (e.g., Vila-Costas & Edmunds 1992). These gradients are generally explained in terms of inside-out growth scenarios and/or inward radial migration of metal-enriched gas. Numerical simulations and observations both indicate that mergers result in weaker gradients as low-metallicity gas at large radii is driven into the center. This result serves to demonstrate that metallicity gradients are sensitive to the assembly history of a galaxy. Several theoretical models of galaxy formation and chemical enrichment have predicted how gradients should evolve with time (e.g., Pilkington et al. 2012). The precise evolution is sensitive to the history of star formation, mergers, and kinematics of a galaxy, and various models predict different behavior at high redshifts. Direct measurements of metallicity gradients at high redshift will constrain these models and yield new information on the evolution of galaxies. When work on this thesis began, no metallicity gradients had been measured beyond the very local universe. This thesis work produced the first measurement of a gradient at high redshift, and currently more than 30 measurements exist at $z > 1$. Current results of this thesis and other work are discussed in detail in Chapter 3.

1.1.3 Reionization as a Probe of Galaxy Evolution

Cosmic reionization has been a subject of active observational and theoretical research since the 1960s (e.g., Gunn & Peterson 1965), and may ultimately prove to be a powerful probe of the earliest galaxies in the universe. Briefly, reionization is the process by which intergalactic hydrogen - known

to be in the form of neutral HI when the CMB radiation was emitted - is ionized at later times. Observations of the Lyα forest in quasars demonstrate that essentially all intergalactic hydrogen was ionized at $z = 6$, approximately one billion years after the last scattering which produced the CMB. Therefore some process must have reionized the universe during this time period. Lyα forest data combined with the CMB optical depth to Thomson scattering have established that reionization occurs predominantly at $6 \lesssim z \lesssim 20$. Direct observations of this important epoch are elusive despite significant observational efforts. However, recent progress with near-infrared imaging surveys has lead to the detection of numerous galaxies and bright quasars at $z > 7$. Spectroscopic followup of these and other sources has now provided preliminary evidence for a significant neutral fraction ($\sim 10\,\%$) at $z = 7$, suggesting that reionization was not complete until $z \simeq 6 - 7$ (e.g., Schenker et al. 2012; Mortlock et al. 2011).

Several potential sources of reionizing photons have been proposed including primordial black holes, micro-quasars, and exotic particle decay. Perhaps the most promising candidate for the source of reionization is the radiation emitted from hot stars in the earliest galaxies at $z > 6$. If galaxies reionized the universe, then the spatial distribution of neutral hydrogen and its evolution directly trace the ionizing radiation emitted by the first galaxies. Several experiments are already in various stages of construction with the goal of mapping neutral hydrogen in the reionization epoch via the 21 cm line (e.g., LOFAR, MWA, GMRT, PAPER, and SKA). These experiments will potentially constrain when the first galaxies formed and determine the large scale structure of the first luminous sources. However, in order to study formation of the first galaxies using these methods, we must first establish whether galaxies actually reionized the universe.

The open question of whether galaxies reionized the universe depends crucially on the production and propogation of ionizing photons with energy > 13.6 eV. To maintain reionization, a sufficient rate of ionizing photons must be generated by young stars and escape into the intergalactic medium (IGM). Observationally, this requirement is usually framed in terms of three parameters: the SFR, the rate of ionizing photons produced per unit SFR (ζ_Q), and the escape fraction f_{esc} of ionizing photons into the IGM. Measurements of these quantities and associated uncertainties are discussed in a review of the subject by Robertson et al. (2010) to which the interested reader is referred. In brief, deep infrared observations underway with the Hubble Space Telescope will significantly reduce current uncertainties on the SFR and a combination of ζ_Q and f_{esc} at $z = 7-8$. Even with these new data, however, the typical value of f_{esc} will remain a significant uncertainty in determining whether galaxies are able to maintain reionization at $z \simeq 7$. Direct measurements of f_{esc} are not practical at such high redshifts, and data at $z \simeq 3$ show that the escape fraction in individual galaxies is highly variable and not yet understood (e.g., Shapley et al. 2006). In the absence of direct measurements, indirect information relating to f_{esc} at high redshifts (even $z > 3$) is useful and may help guide future observational efforts. One of the most important factors governing the escape fraction is the

areal covering fraction of young stars by neutral gas which absorbs ionizing radiation. Chapter 5 therefore devotes substantial work and discussion aimed at constraining this covering fraction at $z \sim 4$ and its evolution with redshift and galaxy properties. This and future work described in Chapter 6 may help constrain the escape fraction of ionizing radiation in early galaxies.

1.2 Thesis Overview

Having introduced the broad topic of galaxy evolution and specific relevant aspects, I now briefly describe the contents of this thesis. Four separate projects are presented, each providing new information on the details of how galaxies assemble their baryonic content throughout the history of the universe. The motivation and main results of each project are summarized below.

Chapter 2 is based on a survey of gravitationally lensed galaxies with AO-assisted integral field spectroscopy. The main goal of this project was to measure the kinematic properties of typical galaxies at $z \simeq 2-3$ with the highest possible spatial resolution. Larger kinematic surveys at similar redshift had established that approximately one third of luminous $L \gtrsim L_*$ galaxies at this epoch were undergoing major mergers, one third are kinematically dominated by rotation, and the remaining third tend to be compact and dispersion-dominated with little or no rotational structure (e.g., Förster Schreiber et al. 2009; Law et al. 2009). However, limited resolution of these data ($1-5$ kpc FWHM) provides only a few independent measurements in each galaxy, precluding more detailed structural studies. Our observations yielded much better physical resolution of up to 100 pc thanks to lensing magnification. We find significant rotational structure in the compact lensed galaxies which in many cases would not be detected without gravitational lensing. This suggests many of the compact dispersion-dominated galaxies at these redshifts could still exhibit some degree of rotational support, and more recent AO-assisted data show that this is indeed the case (Newman & Genzel, 2012). Additionally our data are of sufficient resolution to measure the size and dynamical mass of giant HII regions in the lensed galaxies. The kinematics and HII region properties indicate that star formation in these galaxies is occuring in turbulent, gravitationally unstable thick disks.

The gain in resolution and sensitivity offered by gravitational lensing led us to extend the resolved study of high redshift galaxies to measurements of the gas-phase metallicity gradient. Variations in heavy element content with radius provide a strong constraint on the recent and subsequent assembly history of galaxies. We reported the first such measurement at high redshift (Jones et al., 2010a) in a typical star forming galaxy, showing that it is growing inside-out with star formation driven by accretion of metal-poor gas at large radii. To examine whether this result is representative, we secured metallicity gradients for three additional lensed galaxies and analyze the combined sample in Chapter 3. By comparing measured gradients with a carefully chosen comparison sample at $z = 0$, we demonstrate that metallicity gradients in isolated galaxies must flatten at later times.

The amount of size growth inferred by the gradients is in rough agreement with direct measurements of massive galaxies. We develop a chemical evolution model to interpret these data and conclude that metallicity gradients are established by spatial variation in the outflow mass loading factor, combined with radial inflow of metal-enriched gas.

Chapter 4 departs from the high spatial resolution regime, focusing instead on integrated measurements of low-luminosity ($L \lesssim L_*$) galaxies at $z = 1.5 - 3.5$. Such galaxies are too faint to be studied spectroscopically and so knowledge of their detailed physical properties has been limited to inferences from broad-band photometry. However this is an important population which dominates the star formation density of the universe at high redshifts. Taking advantage of strong gravitational lensing magnification, we compiled rest-frame optical spectroscopy for the first substantial sample of low-luminosity galaxies at this epoch. Balmer emission lines confirm that the sample has a median SFR $\simeq 10$ $M_\odot yr^{-1}$, significantly lower than probed by other surveys at similar redshift. We derive metallicity, dust extinction, SFR, ionization parameter, and dynamical mass from the spectroscopic data, providing the first accurate characterization of the star-forming environment in low-luminosity galaxies at high redshift.

Chapters 2 through 4 are devoted to the physical conditions associated with rapid star formation in high redshift galaxies. Chapter 5 instead focuses on the properties of galaxy-wide outflows driven by such intense star formation. Neutral gas outflows at high redshift are of particular interest for reionization since their distribution in the circumgalactic medium (CGM) limits the escape fraction of ionizing photons. The outflow properties of Lyman break galaxies (LBGs) at $z = 3$ have been extensively studied via strong far-UV spectral features. The purpose of Chapter 5 is primarily to measure the outflow properties of a similar sample of LBGs at $z \gtrsim 4$ and determine whether there is any evolution, particularly in the neutral gas. We verify that trends in spectral features at $z = 3$ also hold at $z = 4$. Specifically, we show that typical LBGs are expected to display weaker neutral gas absorption features at higher redshifts based on correlations with galaxy properties (e.g., size, luminosity, stellar mass, and UV color). Furthermore we find evidence that the neutral CGM evolves with redshift in two ways. First, galaxies with similar physical properties have weaker neutral gas absorption at higher redshifts. Second, neutral gas in the CGM at $z = 4$ is concentrated at smaller radii than in similar $z = 3$ galaxies. Weaker absorption lines result from a lower covering fraction of neutral gas and/or lower outflow velocities, but we are unable to distinguish these two effects. Nonetheless the possibility of an evolving covering fraction is of considerable interest for determining whether galaxies are responsible for reionization. Therefore we describe additional observations needed to disentangle the outflow kinematics and covering fraction, which are now underway.

Chapter 2

Resolved Spectroscopy of Gravitationally-Lensed Galaxies: Recovering Coherent Velocity Fields in Sub-Luminous z∼2–3 Galaxies

Abstract

We present spatially-resolved dynamics for six strongly lensed star-forming galaxies at $z = 1.7$–3.1, each enlarged by a linear magnification factor $\sim \times 8$. Using the Keck laser guide star AO system and the OSIRIS integral field unit spectrograph we resolve kinematic and morphological detail in our sample with an unprecedented fidelity, in some cases achieving spatial resolutions of $\simeq$100 pc. With one exception our sources have diameters ranging from 1–7 kpc, integrated star formation rates of $2-40$ $M_\odot yr^{-1}$ (uncorrected for extinction) and dynamical masses of $10^{9.7-10.3}$ $M_\odot$. With this exquisite resolution we find that four of the six galaxies display coherent velocity fields consistent with a simple rotating disk model. Our model fits imply ratios for the systemic to random motion, $V_c \sin i/\sigma$, ranging from 0.5–1.3 and Toomre disk parameters $Q < 1$. The large fraction of well-ordered velocity fields in our sample is consistent with data analyzed for larger, more luminous sources at this redshift. We demonstrate that the apparent contradiction with earlier dynamical results published for unlensed compact sources arises from the considerably improved spatial resolution and sampling uniquely provided by the combination of adaptive optics and strong gravitational lensing. Our high resolution data further reveal that all six galaxies contain multiple giant star-forming HII regions whose resolved diameters are in the range 300 pc – 1.0 kpc, consistent with the Jeans length expected in the case of dispersion support. From the kinematic data we calculate that these regions have dynamical masses of $10^{8.8-9.5}$ $M_\odot$, also in agreement with local data. However, the density

of star formation in these regions is $\sim$100$\times$ higher than observed in local spirals; such high values are only seen in the most luminous local starbursts. The global dynamics and demographics of star formation in these HII regions suggest that vigorous star formation is primarily governed by gravitational instability in primitive rotating disks. The physical insight provided by the combination of adaptive optics and gravitational lensing suggests it will be highly valuable to locate many more strongly-lensed distant galaxies with high star formation rates before the era of the next-generation ground-based telescopes when such observations will become routine.

2.1 Introduction

Studies of star-forming galaxies at high redshift ($z > 1.5$) over the past decade have mapped the demographics of the populations as a whole yielding valuable data on their integrated star formation rates, stellar and dynamical masses, metallicities and morphologies (Shapley et al., 2001, 2003; Reddy & Steidel, 2004; Erb et al., 2006; Law et al., 2007a). From these data, a consistent picture of the development of the comoving density of star formation and its contribution to the present day stellar density has emerged (Dickinson et al., 2003; Hopkins & Beacom, 2006). Following a rapid rise in activity at early times, corresponding to the redshift range $2 < z < 6$, the star formation rate has decline markedly over the past 8 Gyr corresponding to the interval $0 < z < 1$. Of particular interest is the relationship between sources observed at the time close to the peak epoch of star formation, $z = 2 - 3$ and the population of massive galaxies observed today.

Recent theoretical work has focused on the mechanisms via which early galaxies assemble their stars and evolve morphologically to the present day Hubble sequence. Minor mergers and cold stream gas accretion have emerged as a possible means of building disks, central bulges and elliptical galaxies from early star forming Lyman break galaxies (Dekel et al., 2009; Brooks et al., 2009). These models of galaxy evolution rely on simple descriptions of complex physical processes such as gas cooling, star formation and feedback mechanisms. It is therefore crucial to undertake relevant observations to constrain these processes. The most direct observational route to making progress is high quality resolved spectro-imaging of early galaxies which can be used to determine both their dynamical state and the distribution of star-formation.

Integral field unit (IFU) spectroscopy of nebular emission lines is now yielding valuable kinematic data for a growing sample of luminous high-redshift star forming galaxies (Genzel et al., 2006, 2008; Förster Schreiber et al., 2006, 2009; Law et al., 2007b, 2009; Wright et al., 2009). Although the galaxies observed so far do not yet in any way constitute a complete well-defined sample, some important results have emerged. The data reveal a mix of dispersion-dominated systems, rotating systems, and major mergers with the common observation that all galaxies studied so far show relatively high velocity dispersions of $\sim 50 - 100$ km s^{-1}. A larger fraction of the more massive

($M_{dyn} \gtrsim 10^{11} M_\odot$) galaxies appear to be rotationally supported, with lower mass galaxies ($M_{dyn} \lesssim 10^{10} M_\odot$) tending to have dispersion-dominated kinematics (Law et al., 2009).

However, these studies are hampered by the poor spatial resolution inherent in studies of distant star-forming galaxies whose typical sizes are $\simeq$ 1–5 kpc. Even with adaptive optics on a 8–10 meter aperture, the physical resolution is limited to FWHM $\gtrsim$ 1 kpc which means only a few independent resolution elements. Consequently it is unclear whether the velocity shear observed in the smaller 2–5 kpc sources arises from rotation or merging. Moreover, although there are suggestions that distant star-forming regions have sizes much larger than those of local HII regions (Elmegreen & Elmegreen, 2005), the claim remains uncertain since the distant regions are not properly resolved. Thus, the diffraction limit of the current generation of optical/infrared telescopes limits progress, even with all the adaptive optics tools of the trade.

Fortunately, sources which undergo strong gravitational lensing are enlarged as seen by the observer and can thus be studied at much higher physical resolution in their source plane (Nesvadba et al., 2006; Swinbank et al., 2007). This improvement in physical resolution enables us to better distinguish various forms of velocity field and to examine the properties of star-forming giant HII regions. A convincing demonstration of the benefits of lensing as applied to this topic was the work of Stark et al. (2008) which analyzed IFU data on a $z = 3.07$ galaxy magnified in area by a factor of 28$\times$ demonstrating resolved dynamics on $\simeq$100 pc scales. This represents an order of magnitude improved sampling compared to the earlier studies cited above.

Here we present IFU observations of a further five strongly lensed galaxies which we add to the source studied by Stark et al. (2008). In addition to studying the well-sampled kinematic structure of a population of sub-L* star-forming galaxies at $z \simeq 2$, our fine resolution allows us to examine the size, dynamical mass, and luminosity of typical star-forming regions, thereby probing the conditions in which most of the star formation takes place. We find that all of our galaxies contain multiple, distinct star forming regions. These results offer a preview of the science which will be possible with 30 meter class optical/near-IR telescopes with a diffraction limit comparable to the resolution of our data; they provide the most detailed view to date of typical high-redshift star forming galaxies.

A plan of the paper follows. In §2 we discuss our selection of targets and Keck observations, including the production and use of gravitational lens modeling essential for achieving a high resolution in the source plane. In §3 we analyze our spectroscopic results, discussing each object in turn and summarizing the kinematic data. In §4 we examine the physical scale of our star forming regions in comparison to those seen locally. We summarize our conclusions in §5. Throughout we use a *WMAP* cosmology (Spergel et al., 2003) with Ω_Λ=0.73, Ω_m=0.27, and H_0=72 km s^{-1} Mpc^{-1}. All quoted magnitudes are in the AB system unless otherwise noted.

2.2 Observations and Data Reduction

2.2.1 Target Selection

Ideally, in considering the selection of high redshift galaxies for more detailed resolved studies, care would be taken to construct a mass-limited sample, perhaps defined additionally according to the integrated or specific star formation rate. In practice, even with 10 meter class telescopes, studies are limited by the surface brightness distribution of gaseous emission lines as discussed by earlier workers (Genzel et al., 2006, 2008; Förster Schreiber et al., 2006, 2009; Law et al., 2007b, 2009). In examining *gravitationally-lensed* systems, which have the unique advantages of probing to less luminous (and presumably more typical) systems, and offering an increased spatial resolution in the source plane, an additional criterion is the reliability of the mass model used to invert the observed data into that of the source plane.

Over the past decade, using the growing archive of *HST* ACS and WFPC-2 images of rich clusters (e.g., Blakeslee et al. 2003; Santos et al. 2004; Sand et al. 2005; Stark et al. 2007) and through specific projects such as the MAssive Cluster Survey (MACS, Ebeling et al. 2001) and Local Cluster Substructure Survey (LoCuSS, Smith et al. 2005), we have studied a large sample of lensing clusters and undertaken a search within these *HST* images for promising magnified galaxies (arcs) at high redshift. The clusters presented herein do not in any way represent a well-defined sample and, inevitably, there are biases to those which act as spectacular gravitational lenses.

The distant sources described here were located and assessed via two sequential programs. Firstly, a comprehensive multi-object spectroscopic campaign involving Keck and the VLT was used to verify the redshift of the candidate arcs as well as to determine the redshifts of other multiply-imaged sources in each cluster in order to construct robust mass models (e.g., Richard et al. 2007). As the follow-up spectroscopy was undertaken at optical wavelengths, for those sources beyond $z \simeq 2$, this provided valuable insight into the strength and distribution of Lyα emission. However, as with previous work (e.g., Shapley et al. 2003) we found that the Lyα line did not necessarily give a good indication of the relative strengths and extended nature of those nebular emission lines ([OII], Hβ, [OIII], Hα) critical for resolved studies with laser guide-star assisted adaptive optics (LGSAO). Accordingly, we used the Keck II spectrograph, NIRSPEC, in seeing limited mode in a second campaign to 'screen' all promising targets in advance of undertaking the more demanding resolved studies with the LGSAO-fed integral field unit spectrograph OSIRIS. Once the redshift of the lensed source was known from optical spectroscopy, we usually followed up the source in more than one near-infrared line, in order to ascertain which would be the most economic tracer of the velocity field.

About 75% of our initial sample of 30 $z > 1.5$ arcs have so far been screened and have suitably close reference stars for tip-tilt correction. In order to achieve an adequate signal to noise with

OSIRIS, we used the NIRSPEC data to limit the sample to those with an emission line surface brightness $\gtrsim 10^{-16}$ erg s^{-1}cm^{-2}arcsec^{-2} in a region uncontaminated by night sky emission. As a guide, this surface brightness criterion corresponds to a SFR density $> 0.3\,M_{\odot}$yr^{-1}kpc^{-2} for Hα at $z = 2$. Our sample of 6 sources is drawn from a list of $\simeq 20$ objects fulfilling these criteria. A full account of the NIRSPEC screening program and a discussion of the distribution of line strengths found in that survey is given by Richard et al. (2009). Key properties for the sample of 6 objects, which includes the source discussed by Stark et al. (2008), are given in Table 2.1. The ACS images of our lensed targets are given in Figure 2.1 and we briefly discuss these below.

Cl 0024+1654 Deep optical and near-infrared imaging of the $z = 0.39$ cluster Cl 0024+1654 with *HST* reveals five distinct images of a background galaxy originally identified by its blue color and clumpy ring-like morphology (Colley et al. 1996, Figure 2.1). Optical spectroscopy established a redshift of $z = 1.675$ from interstellar absorption lines (Broadhurst et al., 2000). Near-infrared spectroscopy shows bright, spatially extended Hα emission at $z = 1.6795$. To map the velocity field, we observed the counter image northwest of the cluster with OSIRIS around the redshifted Hα and [NII]λ6583 emission.

MACS J0451+0006 The *HST* ACS V- and I-band imaging of MACSJ0451+0006 shows a striking, multiply-imaged arc $\simeq$30 arcseconds east of the brightest cluster galaxy (Figure 2.1). Follow-up spectroscopy with the FORS multi-object spectrograph on the VLT confirmed a redshift of $z = 2.008$ via the identification of Lyα and UV ISM absorption lines (SiIIλ1260, OIλ1303, CIVλ1549, and SiIVλ1400) and HeIIλ1640 and CIII]λ1908.7 in emission (PID: 078.A-0420). Follow-up observations targeting the nebular Hα emission with the NIRSPEC longslit spectrograph on Keck II showed strong, spatially extended Hα at a redshift of 2.0139$\pm$0.0001 (Richard et al., 2009).

MACS J0712+5932 *HST* V- and I-band imaging of MACS J0712+5932 reveals a prominent triply-imaged background galaxy. Each image of the galaxy images clearly comprises two prominent clumps with surface brightness $\mu_V > 23$ mags arcsec^{-2} within a diffuse halo (Figures 2.1,2.2). Follow-up near-infrared spectroscopy (Richard et al., 2009) shows strong nebular Hα, Hβ, and [OIII]$\lambda\lambda$5007, 4959 emission at $z = 2.6462$, concentrated in the UV-bright regions.

MACS J0744+3927 *HST* V- and I-band imaging of MACS J0744+3927 reveals a singly-imaged arc approximately 15" west of the cluster center. The optical redshift $z = 2.207$ obtained via identification of strong Lyα absorption and multiple rest-frame UV absorption lines was later confirmed by the detection of strong Hα and [NII] emission at $z = 2.209$ with NIRSPEC.

Cl 0949+5153 The *HST* V-band image of Cl 0949+5153 shows a clumpy, elongated singly-imaged arc resolved into two diffuse components (Figure 2.1). Further spectroscopy around the redshifted nebular emission lines shows extended Hα, Hβ, and [OIII]$\lambda\lambda$5007, 4959 emission at $z = 2.393$.

MACS J2135-0102 For completeness, we also include in our sample discussion of the velocity field of the lensed multiply-imaged Lyman Break Galaxy (LBG) at $z = 3.07$ in MACS J2135-0102 (also

known as the "Cosmic Eye" due to its lensed morphology; Stark et al. 2008). Multi-wavelength studies have shown that the source is a L* Lyman-break galaxy with a stellar age of 80–300 Myr, star formation rate of SFR = 40–60 $M_\odot yr^{-1}$, and stellar mass of $M_\star = 6 \pm 2 \times 10^9$ $M_\odot$ (Coppin et al., 2007; Siana et al., 2009).

2.2.2 OSIRIS Observations and Data Reduction

Detailed 2-D spectroscopic observations of the targets listed in Table 2.1 were made with the near-infrared integral field spectrograph OSIRIS (Larkin et al., 2006) on the 10 meter Keck II telescope using the laser guide star adaptive optics (LGSAO) system (Wizinowich et al., 2006) to correct for atmospheric distortion. A suitably bright star ($R < 17$) within $\sim 50''$ of the target was used for tip-tilt correction. We used the 100 milli-arcsecond pixel scale in all observations which provides a field of view of at least 3.2"×6.4". Narrow band H and K filters (Table 2.1) were selected to target the Hα or [OIII]λ5007 emission line at a spectral resolution $R \simeq 3600$, corresponding to FWHM $\simeq 6$ Å in the K band. MACS J2135-0102 and MACS J0451+0006 were observed on 2007 September 02 and 03 whilst the remaining targets were observed between 2008 November 27 – 30.

All observations were taken in $0.6 - 1.3$" seeing. Before observing each arc, we took short exposures of the tip-tilt reference star to center the IFU pointing. The tip-tilt exposures were also used for flux calibration and to calculate the point spread function. Gaussian fits to the point spread functions of the tip-tilt stars yield 0.13–0.20" FWHM resolution for the 100 milliarcsecond pixel scale. With smaller pixel scales, the resolution delivered by the LGSAO system was 0.11" FWHM. Observations of each target were done in a standard ABBA position sequence to achieve good sky subtraction. In the case of Cl0024+1709 we chopped 8" to sky, whilst in the remaining cases we chopped the galaxy within the IFU. Individual exposures were 600–900 seconds and each observing block was 2.4–3.6 ks which was typically repeated three to six times. The total integration time for each object is given in Table 2.1.

Our data reduction methods closely followed those described in detail by Stark et al. (2008). We used the OSIRIS data reduction pipeline (Larkin et al., 2006) to perform sky subtraction, spectral extraction, wavelength calibration, and form the data cube. To accurately combine the individual data cubes, we created images of the integrated emission line and used the peak intensity to centroid the object. We then spatially aligned and co-added the individual data cubes to create the final mosaic. Flux calibration was performed by equating the flux density of the tip-tilt stars measured from 2MASS photometry with the observed OSIRIS spectra. We estimate that the uncertainty in flux calibration is typically 10%.

Name	α_{J2000} $h\ m\ s$	δ_{J2000} $^\circ\ '\ ''$	z	t_{exp} (ks)	Emission lines; OSIRIS filter	$\mu_1 \times \mu_2$	μ	FWHM (pc)	*HST* ACS photometry and proposal IDs
Cl 0024+1709	00 26 34.43	+17 09 55.4	1.680	16.5	Hα, [NII]; Hn5	0.8 × 1.7	$1.38 \pm .15$	820	B,v,r,i,z,GO-10491
MACS J0451+0006	04 51 57.27	+00 06 20.7	2.014	14.4	Hα, [NII]; Kn1	1.3 × 37.0	49 ± 11	60	V,I,GO-10491,GO-10875
MACS J0712+5932	07 12 17.51	+59 32 16.3	2.648	16.2	Hα, [NII]; Kc5	1.5 × 18.7	28 ± 8	90	V,I,GO-10491,GO-10875
MACS J0744+3927	07 44 47.82	+39 27 25.7	2.209	14.4	Hα, [NII]; Kn2	1.9 × 8.6	16 ± 3	310	v,I,GO-9722
Cl 0949+5153	09 52 49.78	+51 52 43.7	2.394	19.2	[OIII]; Hn4	1.2 × 6.0	7.3 ± 2.0	350	V,GO-9270
MACS J2135-0102	21 35 12.73	-01 01 43.0	3.074	21.6	Hβ, [OIII]; Kn1	3.5 × 8.0	28 ± 3	120	V,I,GO-10491

Table 2.1: Target list. Notes: Gravitational lens modeling is discussed in Section 2.3. The lensing amplification is non-uniform and highly directional, thus we give the typical linear magnifications μ_1, μ_2 along the minor and major lensing axes as well as the overall flux magnification μ. The source plane resolution refers to the typical FWHM of a point source in the direction of highest magnification. The photometric bands B, v. V, r, i, I, z are ACS filters F435W, F555W, F606W, F625W, F775W, F814W, and F850LP, respectively.

2.2.3 Gravitational Lens Modeling

In order to investigate the source plane properties we must first correct for the distortion and magnification by the cluster lens. We summarize here the ingredients necessary to construct the relevant cluster mass models. We will follow the methodology defined by earlier relevant articles (Kneib et al., 1993, 1996; Smith et al., 2005; Jullo et al., 2007) within which further details can be found.

Our basic approach is to use the code `Lenstool`[1] (Kneib et al., 1993; Jullo et al., 2007) to constrain a parameterized model of the dark matter distribution. For each cluster, the model comprises two components: 1 or 2 cluster-scale dark matter halos, parametrized with a dual pseudo-isothermal elliptical mass distribution (dPIE, Elíasdóttir et al. 2007), and ∼50 galaxy-scale dPIE dark matter halos, centered on massive cluster members occupying the strong lensing region in order to account for the presence of substructure. These galaxy-scale halos are assumed to have mass properties that follow a scaling relation based on the luminosity of the underlying galaxy, assuming a constant mass-to-light ratio (e.g., Smith et al. 2005; Natarajan et al. 1998).

Details on the construction of each gravitational lens model are given in Dye et al. (2007) for MACS J2135-0102, Limousin et al. (in preparation) for Cl0024+1709 and MACS J0744+3927 and Richard et al. (2009) for the remaining 3 sources in Table 2.1. Strong lensing constraints originate from the identification of 2-5 multiply-imaged systems per cluster within the various ACS images. We use the astrometric positions and spectroscopic/photometric redshifts of these sources[2] as individual constraints to derive best fit parameters on the mass distribution. `Lenstool` uses a Markov Chain Monte Carlo (MCMC) sampler to derive a family of mass models suitably fitting the strong lensing constraints, and we use these to derive the uncertainty on each parameter of the mass distribution.

For each of the sources presented in this paper, the best model was then used to derive the geometrical transformation necessary for mapping the image plane coordinates into the source plane. This transformation enables us to reconstruct the *HST* morphology and Hα emission line images in the source plane assuming conservation of surface brightness. The spot magnification μ_{xy} and its associated error are computed with `Lenstool` at different positions across the object, using the family of mass models from the MCMC sampler. We can verify this value by computing the total magnification from the ratio of the sizes (or equivalently, the total fluxes) between the image and its source plane reconstruction. As the magnification factor is not isotropic, the angular size of each image is more highly stretched along a specific orientation (Figure 2.1) thus affecting our source plane resolution. The linear factors μ_1 and μ_2 of the magnification (with $\mu = \mu_1 \times \mu_2$) together with their associated errors are listed in Table 2.1. A detailed illustration of the uncertainties of the mass modeling method for MACS J2135-0102 is given in Stark et al. (2008).

[1] `http://www.oamp.fr/cosmology/lenstool`

[2] Spectroscopic redshifts are available for a majority of the systems.

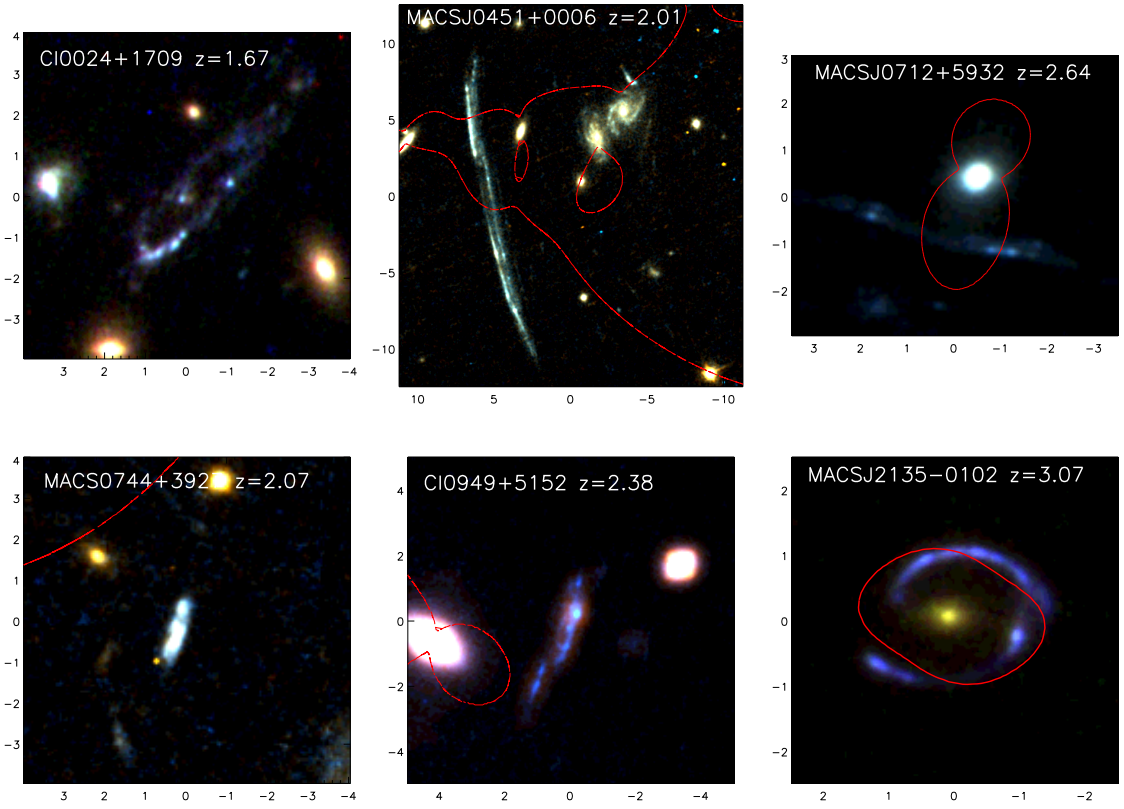

Figure 2.1: True color ACS images of the sample derived from the multi-band data referred to in Table 2.1. The xy scale is in arcseconds. Critical lines for the arc redshifts, derived from lens modeling (§2.3), are shown in red. The critical line for Cl 0024+1709 falls outside the image.

A key parameter in our analysis is the *physical resolution* we achieve in the source plane for each target. To measure this, we use observations of the tip-tilt reference stars. These serve this purpose well as they are point sources observed with conditions and an instrumental configuration identical to those of our distant targets. We "reconstruct" these stars in the source plane as if they were located at the arc position using the same transformation as for the lensed galaxies, and fit a bivariate Gaussian to the point spread function in order to determine the source plane resolution. The typical FWHM of each arc in the direction of highest magnification is listed in Table 2.1 and, with the exception of Cl0024+1709 which is not highly-magnified, varies from 60–350 pc with a mean of 200 pc.

2.3 Analysis

First, we reconstruct the reduced, flux-calibrated data cubes to the source plane using transformations from the gravitational lens models described in §2.3. The resulting data cubes were binned such that each spatial pixel corresponded to 0.5–1 FWHM resolution elements along the direction of highest magnification (Table 2.1). We fit Gaussian profiles to the strongest emission line (Hα or [OIII]) at each spatial pixel using a weighted χ^2 minimization procedure and determine the two-dimensional intensity, velocity, and velocity dispersion maps. To compute the emission line fits we first subtracted the median value at each spatial pixel to remove any source continuum and residual sky background. A blank region of sky within each data cube was used to determine the sky variance spectrum $V(\lambda)$. The spectra to be fit are weighted by $w(\lambda) = V^{-1}$ appropriate for Gaussian noise, so that regions of higher noise (e.g., strong sky emission lines) do not cause spurious fits. We compute the χ^2 statistic for the best-fit Gaussian as well as a for a featureless spectrum ($f(\lambda) = 0$) and require a minimum improvement over the fit with no line of $\Delta\chi^2 = 16$–25 for the various arcs (i.e., 4–5σ emission line detection). If this criterion was not met, we averaged the surrounding 3×3 spatial pixels to achieve higher signal-to-noise. No fit was made if the 3×3 averaging still failed to produce the minimum $\Delta\chi^2$ improvement. We calculated the formal 1σ error bounds by perturbing the Gaussian fit parameters until the χ^2 increases by 1 from the best-fit value. In all following sections, we have deconvolved the line widths with the instrumental resolution ($R \simeq 3600$) by subtracting the instrumental resolution in quadrature from the best-fit Gaussian σ. The resulting source plane intensity, velocity, and dispersion fields for the entire sample are shown in Figure 2.2 and demonstrate detailed kinematic and morphological properties on scales down to 100–200 pc.

From the source plane nebular emission line intensity and dynamics we estimate the size, dispersion, and dynamical mass of each galaxy. The size is calculated as the maximum diameter from pixels with successful emission line fits, roughly equivalent to a major axis diameter with limiting isophote $\sim 10^{-16}\,\mathrm{erg\,s^{-1}\,cm^{-2}\,arcsec^{-2}}$. The uncertainty is dominated by errors in the lensing mag-

nification and is $\leq 20\%$. We estimate the global average velocity dispersion of each galaxy as the flux-weighted mean of the fit pixels, $\sigma_{mean} = \sum \sigma_{pix} I_{pix}$ with typical uncertainty of $\sim 5\%$ estimated from errors in the fit parameters and the spread of σ in individual pixels. This measurement of the dispersion is not affected by resolved velocity gradients. The six galaxies in our sample all have large $\sigma_{mean} = 50 - 100$ km s^{-1}, which is consistent with other resolved observations of non-lensed galaxies at $z \gtrsim 2$ (e.g., Förster Schreiber et al. 2009; Law et al. 2009; Lehnert et al. 2009)

2.3.1 Kinematic Modeling

To test whether the kinematics of each galaxy are consistent with a rotating system, and to estimate the inclination of any disks, we construct and fit simple disk models to the observed velocity fields. The disk model for MACS J2135-0102 is discussed in detail by Stark et al. (2008), and we follow a similar method for the rest of the sample. We use an arctangent function to estimate the circular velocity as a function of radius,

$$V(R) = V_0 + \frac{2}{\pi} V_c \arctan \frac{R}{R_t} \tag{2.1}$$

which Courteau (1997) showed to be an adequate simple fit to galaxy rotation curves in the local universe. The disk models contain seven parameters: inclination i, position angle θ, coordinates (α, δ) of the disk center, scale radius R_t, asymptotic velocity V_c, and systemic velocity V_0.

To test how well these simple models can describe the data, we constructed velocity fields covering a large range of parameter space for each galaxy. From the disk center, inclination, and position angle we compute the disk radius R at each pixel in the source-plane velocity maps via

$$R^2 = (x \cos\theta - y \sin\theta)^2 + \left(\frac{x \sin\theta + y \cos\theta}{\sin i} \right)^2$$

where x and y are the distance from disk center in right ascension and declination, respectively. We then calculate the circular velocity from Equation 2.1, and correct for the azimuthal angle and inclination to obtain the observed velocity field of the model disk. To simulate lensing distortion, the models were then convolved with an elliptical point spread function estimated as the best 2D Gaussian fit to the reconstructed tip-tilt reference star images. To estimate the goodness-of-fit we compute the χ^2 statistic using the 1σ error from emission line fits. The emission line fits routinely yield a reduced χ^2_ν close to unity indicating that these errors are a good estimate of the true uncertainty. To estimate uncertainty in the parameters we perturb the model until the χ^2 increases by one standard deviation from the best fit. Best-fit χ^2_ν values for each galaxy are given in Table 2.2, except for Cl 0949+5152 for which no reasonable fit was found. Velocity contours for the best-fit disk models are shown in Figure 2.2.

For galaxies which can be reasonably well described with disk-like kinematic structure, we extract the rotation velocity, inclination, and disk position angle (major axis) from the model. The latter two values are usually estimated from morphology, but such methods are not necessarily accurate in this case due to the lensing distortion and asymmetric light distribution of these objects. The inclination and position angle estimated from morphology agree reasonably well for Cl 0024+1704, MACS J0744+3927, and MACS J2135-0102 but are inconsistent with best-fit disk models for MACS J0451+0006 and MACS J0712+5932. The morphological major axis in these systems is determined largely by the positions of a few bright clumps which dominate the luminosity. These clumps are likely to be misaligned with the kinematic major axis, which would explain the discrepancies observed. Similarly the clumpy, asymmetric luminosity distribution in these systems causes large uncertainties in estimates of the inclination. While smooth luminosity profiles can give accurate values of the inclination and position angle of disk galaxies, this approach is apparently not reliable for the clumpy systems common at high redshift. We therefore adopt the inclination and position angle from best-fit disk models.

In Figure 2.3 we show the one-dimensional velocity and dispersion profiles extracted from the data along a slit aligned with the disk position angle (or with the morphological major axis for the merger Cl 0949+5153). This allows us to better quantify the kinematic structure and, particularly, to estimate an approximate rotational speed V_{max} for each galaxy. The circular velocity is a parameter in the disk models, however, in some objects the velocity field does not reach an asymptotic value (e.g., MACS J0744+3927). In such cases the best fit value of V_c does not necessarily accurately represent the observed range of velocity. However, 4/5 galaxies in addition to MACS J2135-0102 display a coherent and roughly monotonic velocity curve consistent with the disk model. From these we estimate $V_{max} \sin i$ as half of the range in the one-dimensional model profile in the region detected in Hα emission, which provides a more reliable measure of the observed velocity range than the best-fit $V_c \sin i$. Values of $V_{max} \sin i$ as well as the best-fit inclination from disk models are given in Table 2.2.

To estimate the dynamical mass for each galaxy, we adopt two approaches. First, we use the velocity dispersion and maximum extent of the Hα emission and calculate $M_{dyn}(R) = C\,R\,\sigma^2_{mean}/G$ with $C = 5$ appropriate for a sphere of uniform density and the radius is taken as half the maximum diameter. The geometrical factor C is likely between 3 and 10 for these highly turbulent galaxies (Erb et al., 2006). The dynamical mass is likely uncertain to within a factor 2$\times$ due to the assumed geometry and exclusion of rotationally-supported mass, whereas random uncertainty propagated from R and σ_{mean} is $< 25\%$. We also use the velocity gradient to estimate the dynamical mass via $M_{dyn} \sin^2 i = R\,(V_{max} \sin i)^2/G$ but note that the maximum velocity shear in the sample gives $\Delta V/2\sigma_{mean} \lesssim 1.5$ for all galaxies, so the rotational mass is less than half of the dispersion-supported mass before correcting for inclination. In future sections, we therefore typically adopt the dynamical

mass calculated from velocity dispersion, noting that the total uncertainty is roughly a factor of two dominated by the assumed $C = 5$ with an additional systematic error due to the ignored rotational support. Adopted values of the diameter, dispersion, and dynamical mass are given in Table 2.2.

Before we discuss what can be learned from the sample as a whole, we briefly review the results for each of the six galaxies in turn.

2.3.2 Review of Individual Properties

2.3.2.1 Cl 0024+1709

After accounting for lensing amplification, the extent of Hα emission is $\sim 10 \times 18$ kpc from our lens model, making this the largest object in our sample. The integrated Hα emission line flux implies an intrinsic SFR$= 27 \pm 6$ M$_\odot$yr^{-1} (uncorrected for dust extinction).

The Hα emission line and rest-UV morphologies both show a clumpy ring surrounding a fainter central region (Figure 2.2), similar to that seen in some other massive, extended galaxies at high redshift (e.g., the $z = 2.26$ galaxy Q2643-BX482 in Genzel et al. 2008) as well as local ring galaxies (Romano et al., 2008). The narrow ring, $\sim$10 kpc diameter, and misaligned central feature suggest that the ring of concentrated star formation was triggered by an on-axis collision with another galaxy, as opposed to dynamical resonances within the galaxy. This hypothesis is supported by the numerical simulations of Lynds & Toomre (1976) and identification of interacting companions to ring galaxies by Romano et al. (2008). Unfortunately, the Hα emission in the central region coincides with a detector glitch in most of the IFU exposures and so the central dispersion and star formation density are only poorly constrained, with $\sigma = 50 \pm 21$ km s^{-1}. In the ring, five UV- and Hα-bright knots are resolved with similar isophotal radius, velocity dispersion and luminosity of $R \simeq 0.5$ kpc (for $L_{H\alpha} > 1.5 \times 10^{-16}$ erg s^{-1} cm^{-2} arcsec^{-2}), $\sigma \simeq 45 - 65$ km s^{-1}, and $L_{H\alpha} \sim 2 \times 10^{-17}$ erg s^{-1} cm^{-2}, with uncertainties from the lens model and emission line fits of $\sim 40\%$ in radius, 15% in dispersion and 30% in luminosity. This implies a dynamical mass of the Hα clumps from the velocity dispersion of $M_{dyn} = 2 \pm 1 \times 10^9$ M$_\odot$ assuming uniform density, and a Hα star-formation rate of SFR $= 2.0 \pm 0.7$ M$_\odot$yr^{-1}. The velocity field shows a smooth velocity gradient around the ring with peak-to-peak amplitude $2\,V_c \sin i = 120 \pm 10$ km s^{-1}. Using the axial ratio from the optical imaging, we estimate $\cos i = 0.6 \pm 0.1$ which suggests a rotationally supported mass $M_{dyn} = R\,V_c^2/G = 2.1 \pm 0.8 \times 10^{10}$ M$_\odot$within a radius of 9 kpc. If the galaxy has a uniform spherical mass distribution, then the observed dispersion suggests a larger dynamical mass of 5×10^{10} M$_\odot$. The resolved star forming regions in the ring thus account for about 50% of the integrated Hα flux and 15–25% of the mass interior to the ring.

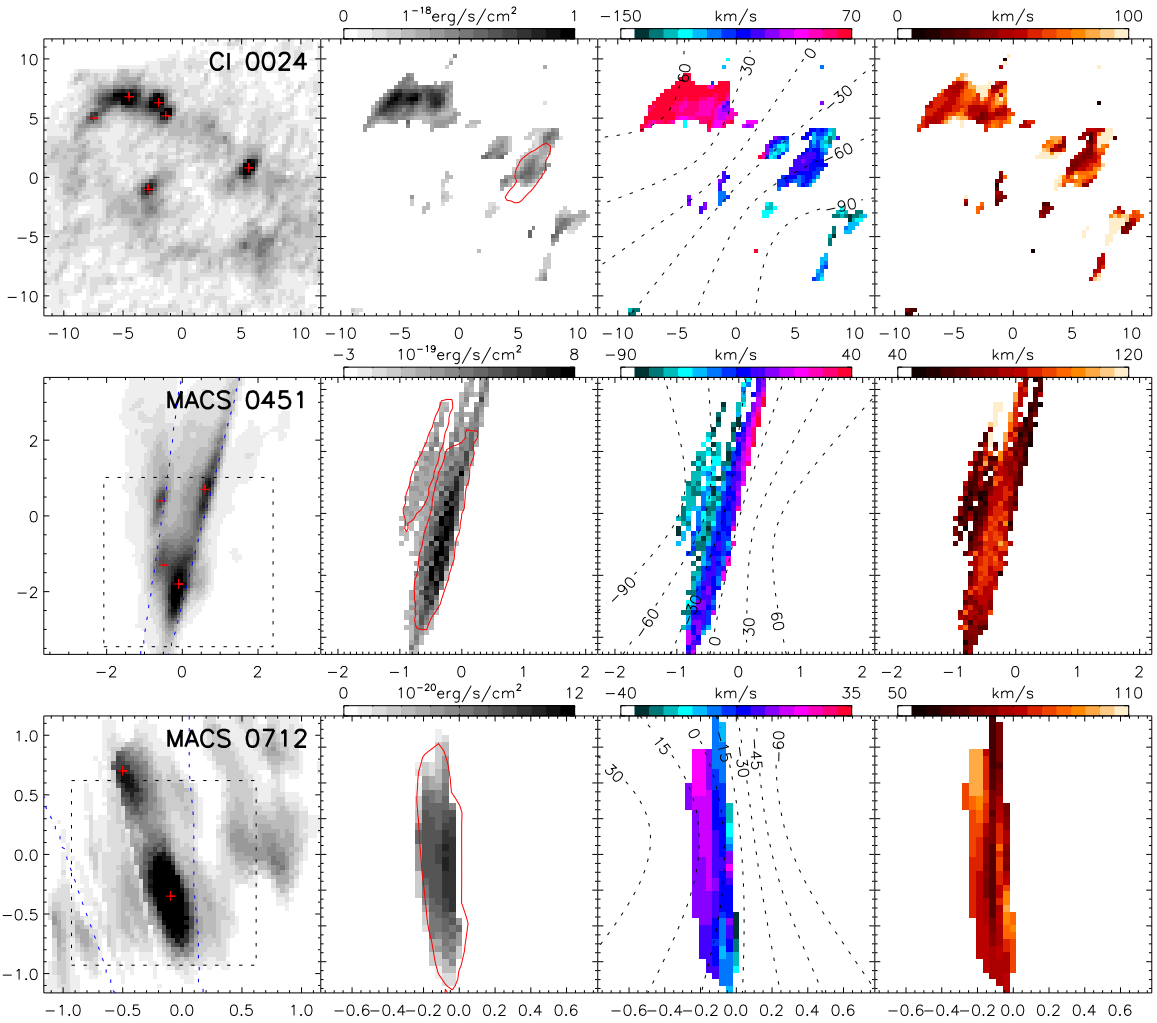

Figure 2.2: Source plane properties of the lensed galaxy sample. From left to right in each row: ACS broad-band emission, line intensity, velocity, and velocity dispersion derived from the OSIRIS nebular emission line data. Axes are in kpc with 1–2 pixels per OSIRIS resolution element. Each galaxy shows morphological and kinematic structure on scales down to $\sim 100 - 200$ parsecs. The nebular line flux distribution is similar to the rest-UV morphology with multiple resolved clumps, shown as red crosses on the ACS images. Red contours on the line intensity maps denote clumps which are spatially extended and unconfused at the $\simeq 3\sigma$ flux isophote in narrow-band emission line images, as described in §4. Best-fit disk model contours are shown on the velocity maps for those galaxies whose dynamics are consistent with rotation (§3.1). Dashed boxes in the ACS images of MACS J0451 and MACS J0712 indicate the smaller regions for which OSIRIS data are displayed. Caustics are shown as dashed blue lines in the ACS images of multiply-imaged arcs.

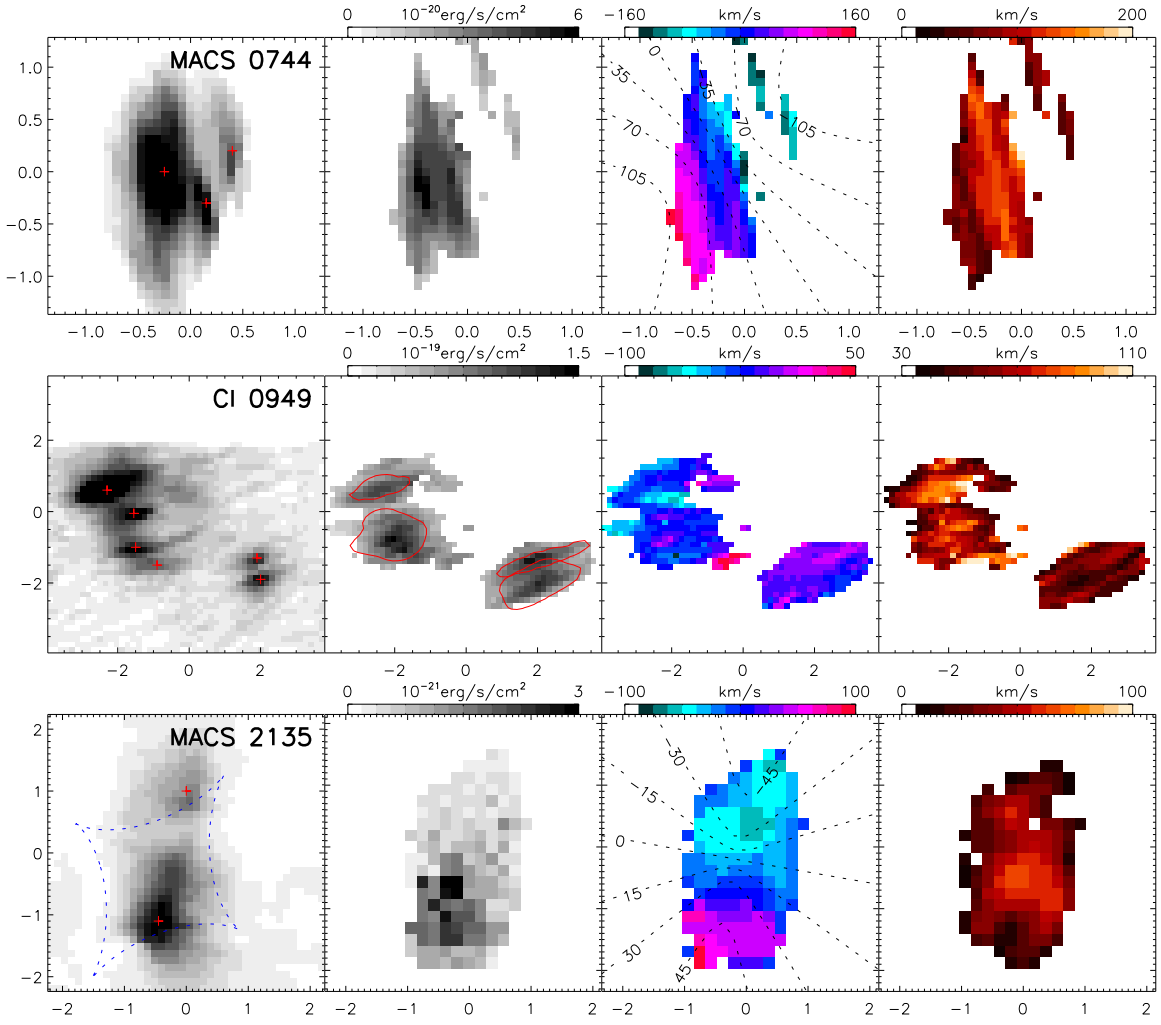

Figure 2.2: (continued)

2.3.2.2 MACS J0451+0006

The integrated Hα emission line flux suggests a star-formation rate of SFR=7 ± 2 $M_{\odot}yr^{-1}$, with the two brightest clumps (Figure 2.2) contributing 0.8 ± 0.2 and 3.6 ± 0.9 $M_{\odot}yr^{-1}$. Some parts of the galaxy were not observed with OSIRIS due to the limited field of view and 20 arcsecond extent of the arc. We expect these regions to contribute an additional 3 ± 1 $M_{\odot}yr^{-1}$based on their rest-frame UV flux. The large magnification of this galaxy ($\mu = 49 \pm 11$) leads to an unprecedented 60 pc typical resolution in the source plane, providing unique insight into the kinematic structure of the star forming regions. The Hα velocity map reveals a coherent velocity field across the galaxy and within the clumps with a peak to peak amplitude of 80 ± 20 $km\,s^{-1}$(Figure 2.3). The bi-symmetric velocity field together with the good disk model fit (χ^2_{ν}=3.6) suggest that the kinematics of this system are likely dominated by rotation rather than merging.

2.3.2.3 MACS J0712+5932

From our IFU observations, only the brightest UV clump is detected in Hα with an intrinsic star-formation rate of SFR $= 5 \pm 1$ $M_{\odot}yr^{-1}$and we place limits on the remaining clumps of SFR $<$ 3 $M_{\odot}yr^{-1}$ (3σ). The Hα flux in the brightest clump is consistent with the total galaxy flux derived from longslit spectroscopy, implying very little star formation in the rest of the system. The two prominent UV-bright regions have FWHM sizes $\lesssim 0.5$ kpc and are separated by 1.5 kpc (Figure 2.2). The Hα emission in the brighter region exhibits a velocity gradient of 38 ± 8 $km\,s^{-1}$along the highly sheared direction. While the disk model provides an excellent fit to the velocity field with $\chi^2_{\nu} = 0.4$, it is unclear whether the dynamical state of MACS J0712+5932 is dominated by rotation, merging, or dispersion since only the strongest Hα-emitting region is detected with OSIRIS. Assuming a uniform density within a radius of 0.2 kpc and $\sigma = 80 \pm 5$ $km\,s^{-1}$we derive a dynamical mass of $M_{dyn} = 1.4 \pm 0.2 \times 10^9$ $M_{\odot}$for the nebular emission region. The N[II]λ6583 emission line is detected at the 2σ level in individual spatial pixels consistent with the flux ratio N[II]λ6583/Hα = 0.2 observed in NIRSPEC longslit spectra, with no measurable gradient in the flux ratio.

2.3.2.4 MACS J0744+3927

Hα emission is detected across 2.0 kpc in the source plane and is resolved into 3 bright clumps in both the rest-frame UV continuum and Hα. The two dimensional velocity map clearly shows a bi-symmetric velocity field and is well described by the disk model with $\chi^2_{\nu} = 3.8$ and peak to peak amplitude of 280 ± 25 $km\,s^{-1}$, the largest observed in any high-redshift galaxy of this size (Figure 2.3). The velocity dispersion varies from $\sim 60 - 130$ $km\,s^{-1}$and peaks near the dynamical center of the galaxy. This suggests a turbulent primitive disk with a total star-formation rate of 2.4 ± 0.5 $M_{\odot}yr^{-1}$. The dynamical mass within a radius of 1 kpc is M_{dyn}=$RV_c^2/G = 5 \pm 1 \times 10^9$

$M_\odot \sin^2 i$ inferred from the velocity gradient, or $M_{dyn} = 11 \pm 2 \times 10^9$ $M_\odot$ from the flux-weighted mean dispersion assuming uniform density.

The large rotation velocity, low SFR, and central dispersion peak conceivably make MACS J0744+3927 the most evolved disk-like galaxy of its size yet observed at high redshift and show that small, low mass ($\sim 10^{10}$ $M_\odot$), turbulent field disk galaxies are already in place only 3 Gyr after the big bang.

2.3.2.5 Cl 0949+5153

The reconstructed image of Cl 0949+5153 at $z = 2.393$ shows two diffuse regions separated by $\simeq 3.9$ kpc, with the southwest component redshifted by 17 ± 6 km s^{-1} from its companion (Figure 2.3). Both components show resolved velocity gradients of order 30 and 100 km s^{-1} but in opposite directions, indicating that these two regions are likely merging (this system can not be described by a disk model). Each component is further resolved into multiple clumps of diameter $0.3 - 0.7$ kpc within an isophote of $L_{[OIII]} = 1.8 \times 10^{-16}$ erg s^{-1} cm^{-2} arcsec^{-2}. Interestingly, while the clumpy [OIII] morphology appears to correlate with the rest-frame UV, the ratio of rest-UV to nebular emission surface brightness varies considerably between clumps. This could be caused by non-uniform extinction or different star formation histories, since the rest-UV traces older star formation episodes than Hα flux ($\lesssim 100$ and $\lesssim 20$ Myr, respectively). Assuming a global Hβ/[OIII] flux ratio from longslit spectra and case B recombination, the Hβ-derived star formation rate of the entire system is $20 \pm 6\, M_\odot$ yr^{-1} with 63% of the nebular emission in the larger northeast region.

Dynamically, it appears that Cl 0949+5153 is the only major merger in our sample, containing two spatially separated components with opposite velocity gradients and enhanced dispersion between components. From the velocity dispersion we crudely estimate that the northeast and southwest components have mass $12\times$ and 4×10^9 $M_\odot$ respectively. Both of these components are fragmented further into multiple large clumps with seemingly coherent velocity fields.

2.3.2.6 MACS J2135-0102

For completeness, we also include in our sample discussion of the velocity field of LBG J2135-0102 (also known as the "Cosmic Eye" due to its lensed morphology). Stark et al. (2008) show that the global dynamics suggest a thick galaxy disk in an early state of assembly with rotation speed (corrected for inclination) of $V_c = 67 \pm 7$ km s^{-1} and $V_c/\sigma_r = 1.2 \pm 0.1$.

The source plane morphology of this galaxy comprises two distinct star-forming regions embedded in a rotating disk. The northern component has a diameter of ~ 0.8 kpc, a star formation rate of 21 ± 3 $M_\odot$yr^{-1} and a peak line width of 50 ± 5 km s^{-1}. Together, these suggest an intensely star forming region with dynamical mass $M_{dyn} = 1.2 \pm 0.5 \times 10^9$ $M_\odot$. The southern component is brighter in the rest-frame UV, but has a lower Hβ-inferred star formation rate of SFR $= 11 \pm 2$ $M_\odot$yr^{-1}. The diameter of 1.3 ± 0.3 kpc and peak line width of 65 km s^{-1} suggest a mass $M = 3 \pm 1 \times 10^9$ $M_\odot$.

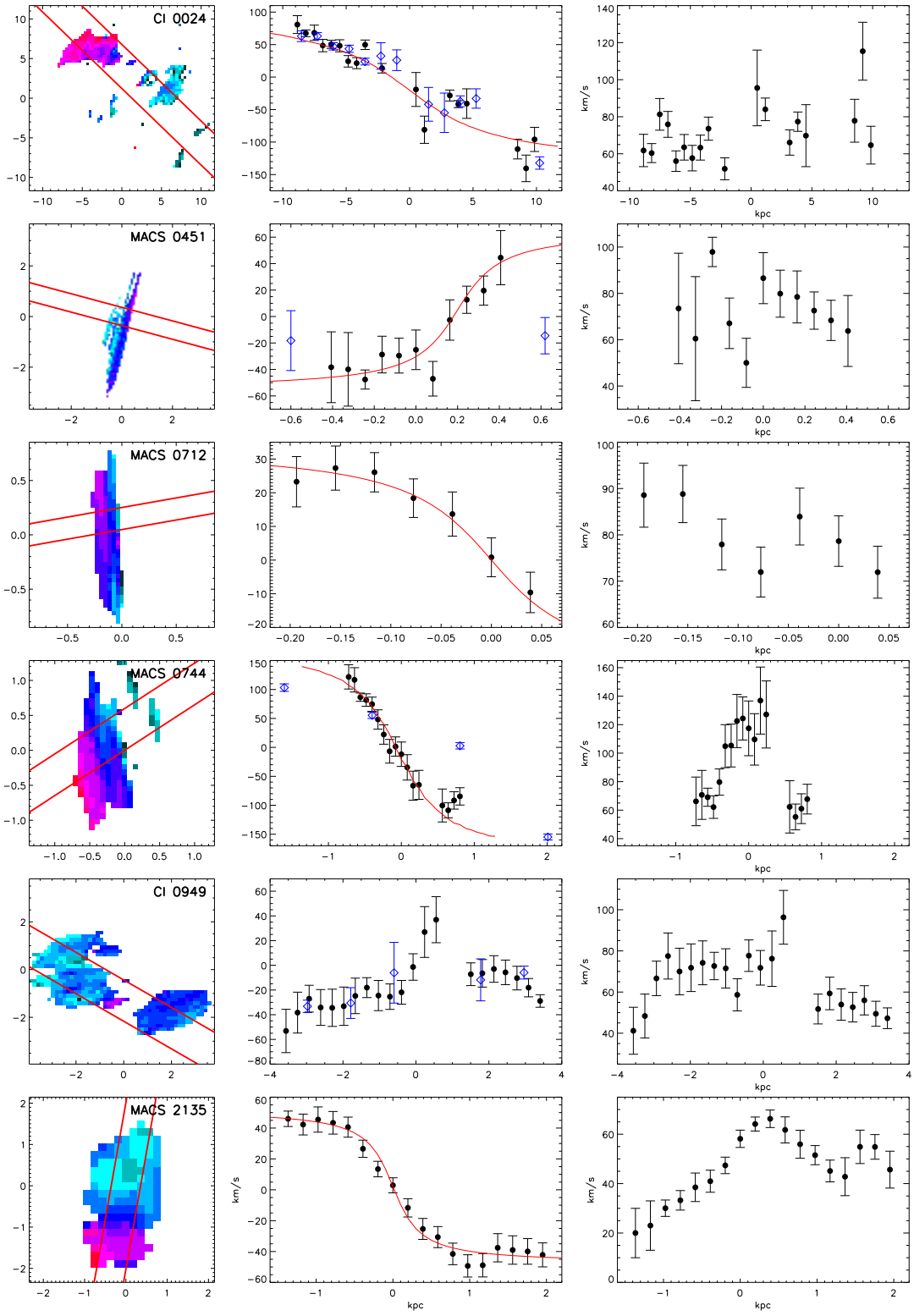

Figure 2.3: Left to right: velocity field, one dimensional extracted velocity profile, and equivalent velocity dispersion profile. Velocity and dispersion curves are extracted from left to right along the slit shown on the left figures. The rotation curve one would obtain in the absence of lensing with 0.15" resolution typical of AO-corrected observations is shown by the blue diamonds. Best-fit profiles of the velocity field are shown in red. No model is shown for Cl 0949+5153 since the velocity field is inconsistent with a rotating disk.

Galaxy (ID)	Diameter (kpc)	L/L^*	SFR ($M_\odot yr^{-1}$)	M_{dyn} (10^9 $M_\odot$)	σ ($km\,s^{-1}$)	$V_{max}\sin i$ ($km\,s^{-1}$)	i (°)	χ^2_ν
Cl 0024+1709 (A)	20 ± 2	0.7	27±6	55±10	69±5	76±12	50^{+10}_{-30}	5.9
MACS J0451+0006 (B)	5 ± 1	0.4	7±2	19±4	80±5	38±10	25^{+20}_{-10}	3.6
MACS J0712+5932 (C)	1.5 ±0.3	0.2	5±1	5.7±1.2	81±2	15±4	40^{+20}_{-25}	0.4
MACS J0744+3927 (D)	2.0 ±0.3	0.1	2.4±0.5	11±2	99±4	129±12	45^{+15}_{-25}	3.8
Cl 0949+5152	7 ± 1	0.5	20±6		66±3			
NE (E1)	4.0 ±0.6		13±5	12±2	71±2			
SW (E2)	2.0 ±0.3		7±3	3.8±0.6	57±2			
MACS J2135-0102 (F)	3.5 ±0.3	1.5	40±5	5.9±1.0	54±4	47±7	55 ± 10	3.7

Table 2.2: Source-plane properties of the lensed galaxies. Values for MACS J2135-0102 are reported in Stark et al. (2008). Diameter is the extent of nebular emission except for MACS J0712+5932 where it represents the extent of detected V-band emission, with uncertainty accounting for spatial resolution and errors in the lens model. The luminosity is compared to L^* for the LBG population at $z = 3$ (see text for methodology). Error in luminosity is 15–30% dominated by the uncertain magnification. Velocity dispersion σ is taken as the flux-weighted mean. $V_{max}\sin i$ is computed as half the maximum peak-to-peak velocity from fits to the velocity field. Inclination i is the value relative to the plane of the sky for the best-fit disk model, with uncertainty given as the range of parameter space within 1σ of the best fit. Cl 0949+5152 is separated into the northeast and southwest merging components; no circular velocity is given since rotating disk models do not provide a good fit. Dynamical mass is calculated as $C\,R\sigma^2/G$ using the diameter and dispersion values given in the table with $C = 5$ and error from R and σ, although the true uncertainty in M_{dyn} is roughly a factor of two due to unknown mass distribution and rotation support. Galaxy IDs (A, B, etc.) correspond to the labeled data points in Figures 2.5 and 2.6.

2.3.3 Properties of the Ensemble

Having discussed the sources individually, we now turn to general conclusions based upon their integrated properties as listed in Table 2.2.

2.3.3.1 Kinematics

All six objects in our sample show well-resolved velocity structure. A visual inspection of Figures 2.2 and 2.3 reveals that four galaxies (Cl 0024+1709, MACS J0451+0006, MACS J0744+3927, and MACS J2135-0102) have smooth velocity gradients suggesting ordered rotation whilst Cl 0949+5153 appears to be a merger with both components showing well-resolved velocity gradients. The dynamical state of MACS J0712+5932 is unclear since only the brightest Hα-emitting region is detected with OSIRIS. The nebular emission shows a smooth velocity gradient in MACS J0712+5932, but subtends only four resolution elements in the most highly magnified of the three images and so it is unclear wither the kinematics of MACS J0712+5932 are dominated by rotation, dispersion, or merging.

For the galaxies studied here, the best fit disk models have χ^2_ν values which range from 0.4 to 5.9 with a mean of 3.5, indicating agreement typically within 2σ for individual pixels. For reference, disk models for 18 galaxies in the SINS survey which show the most prominent rotation yield best-fit χ^2_ν values of 0.2–20 to the models of Cresci et al. (2009), so our simple model provides an equally good fit to the lensed galaxies. All galaxies show small-scale deviations from the model as indicated by

the typical $\chi^2_\nu > 1$; these proper motions could be caused by the effects of gravitational instability, or simply be due to the unrelaxed dynamical state indicated by high velocity dispersions $\sigma > 50$ $\mathrm{km\,s^{-1}}$. We therefore conclude that the model provides an adequate fit to the data and that the velocity fields are consistent with the kinematics of a turbulent rotating disk, except in the case of Cl 0949+5152.

It is illustrative to demonstrate the dramatic improvement in our understanding of the internal dynamics of our sources that arises uniquely through the improved spatial sampling enabled by studying strongly-lensed galaxies. To do this we bin the source-plane data cubes of our targets to a coarser resolution typical of that achievable for *unlensed sources* observed with an AO-corrected resolution of $0.15''$. We then re-fit the emission lines and extract one-dimensional velocity profiles using the same methods as adopted for the original data. Since the lensing magnification results in μ times more flux spread over μ times as many pixels, the binned signal-to-noise ratio is a a factor $\sqrt{\mu}$ higher than equivalent observations of unlensed versions of our galaxies. These simulations therefore represent non-lensed galaxies observed for much longer integrations ($\sim$ 100 hours!). Even so, the resulting velocity profiles (also shown in Figure 2.3) are considerably inferior to those of our lensed data. A credible rotation curve is only retrieved for Cl 0024+1709, our least magnified galaxy, with important kinematic detail lost in all other objects (for example, MACS J0712+5932 is unresolved). Such poor spatial sampling is insufficient to distinguish between rotation and merging. More quantitatively, velocity gradients in all of our objects except Cl 0024+1709 are significantly underestimated (typically $V_{max,non-lens}/V_{max,lens} = 0.6 \pm 0.2$).

2.3.3.2 Physical Characteristics: Size, Luminosity, and Mass

Next, we examine the integrated physical properties of the lensed galaxies. First we briefly compare the luminosity, size and mass to the general Lyman break population at $z \simeq 2$–3. In Figure 2.4 we compare the distribution of apparent R-band magnitudes for our sample to that of the Lyman-break population at $z \sim 3$ (Shapley et al., 2001). The comparison demonstrates that five of our six galaxies are fainter than L^*, ranging from $0.1 - 1.5\,L^*$, with median $0.5\,L^*$ well below that of other spatially resolved IFU studies. The intrinsic Hα flux of the arcs is also lower than in other surveys, with a mean and median inferred SFR of $17\,\mathrm{M_\odot yr^{-1}}$ (Table 2.2) compared to 26–33 $\mathrm{M_\odot yr^{-1}}$ in Law et al. (2009) and Förster Schreiber et al. (2009). Comparing the typical spatial extent of the nebular emission to other surveys, the median radius (extent of detected nebular emission) and dynamical mass of the lensed sample are 2.1 kpc and 1.3×10^{10} $\mathrm{M_\odot}$, somewhat more extended than the compact galaxies studied by Law et al. (2009) which have median radius of 1.3 kpc and $\mathrm{M_{dyn}} = 0.7 \times 10^{10}$ $\mathrm{M_\odot}$. Turning to the dynamics, the flux-weighted mean velocity dispersions σ_{mean} are perfectly consistent with those studied by Law et al. (2009): both samples span a range of 50–100 $\mathrm{km\,s^{-1}}$with mean and median 70–75 $\mathrm{km\,s^{-1}}$, indicating that the two sets of galaxies probe the same range of dynamical

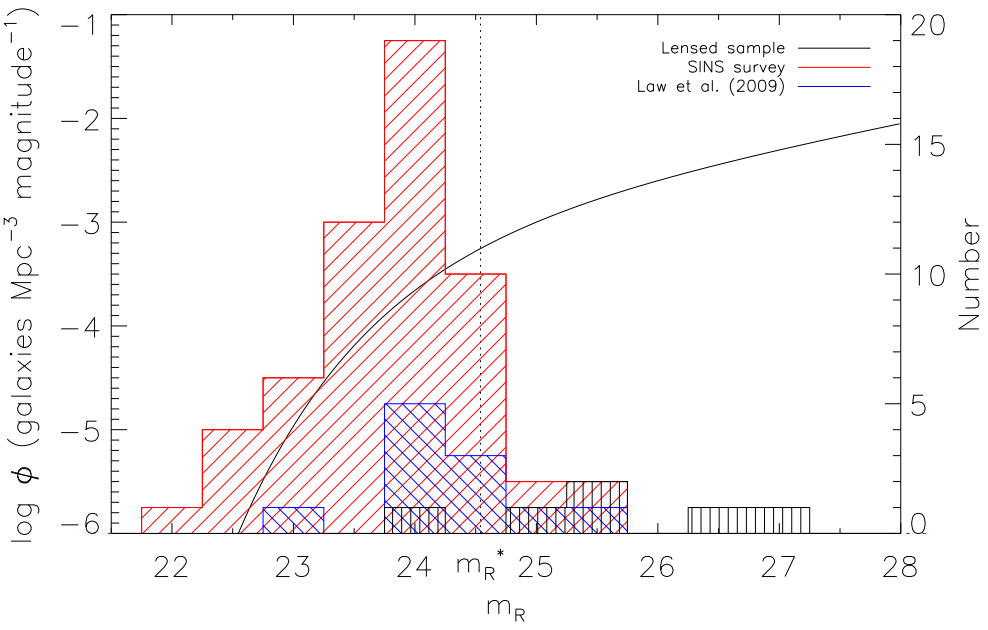

Figure 2.4: Apparent R-band luminosity function of $z \sim 3$ LBGs from Shapley et al. (2001) compared to the distribution of suitably-corrected apparent R magnitudes for our lensed sample as well as the SINS (Forster Schreiber et al. 2009) and Law et al. (2009) samples. We compute the apparent R magnitudes of the IFU samples at $z = 3$ for an effective wavelength $\lambda = 600$–800 nm depending on the available photometry.

mass density. We note that the median Hα FWHM (from longslit spectra; Erb et al. 2006) and stellar mass of $\simeq$6 kpc and 2.9×10^{10} M$_\odot$ are a better representation of the Law et al. (2009) sample as they do not depend on sensitivity of the data. The SINS survey probes somewhat more extended objects, with median Hα FWHM and stellar mass of $\simeq$8 kpc and M$_\star$ $\simeq 3 \times 10^{10}$ M$_\odot$. The mass density and extent of nebular emission of the lensed galaxies are therefore comparable to the more luminous Law et al. (2009) sample and somewhat lower than in the SINS survey. The lensed galaxies are also below the average size and mass for L^* systems at similar redshifts, with the notable exception of Cl 0024+1709.

Our high resolution data enable us to determine reliable dynamical properties and compare with other IFU observations. In particular we can examine the prevalence of dispersion and rotation as a function of size and dynamical mass. Law et al. (2009) report evidence for dispersion-dominated kinematics in compact low-mass galaxies in contrast to the ∼equal mix of rotation, dispersion, and complex/merger kinematics found in the SINS survey (Förster Schreiber et al., 2009), although the dispersion-dominated fraction is higher for more compact SINS galaxies. However, this claim is hampered by the small number of resolution elements ($\simeq$2–4) subtended by each source (although see Epinat et al. 2009). We can address this issue with the superior resolution offered by gravitational lensing. The relevant relations between V/σ and size or dynamical mass is shown in Figure 2.5 for

the five lensed galaxies which are reasonably well fit by disk models compared to the compact LBGs from Law et al. (2009) and the rotation-dominated SINS galaxies described by Cresci et al. (2009), showing that the ratio of velocity shear to dispersion is higher for larger, more massive galaxies. Furthermore, the general agreement between the lensed sample and other comparison samples is also shown in Figure 2.5 and demonstrates that the dynamics of sub-L^* star-forming galaxies do not differ substantially from more luminous objects.

Noting that many galaxies do not reach an asymptotic velocity within the region probed by our IFU observations, it is likely that larger circular velocities exist in faint outer regions of these galaxies. Indeed, the spatial extent and mass inferred from longslit spectra and photometry are higher than from relatively shallow IFU data. We therefore also compare the observed velocity gradient and, where appropriate, inclination-corrected rotational velocity as a function of size and dynamical mass in Figure 2.5. The observed velocity gradients of 3/5 lensed galaxies and the entire comparison sample are within 0.3 dex of the median value $V_{shear}/R = 25\ \mathrm{km\,s^{-1}\,kpc^{-1}}$. The consistent velocity gradients and corresponding V_{shear}/σ obtained with a typical $\sigma = 75\ \mathrm{km\,s^{-1}}$(Figure 2.5) suggest that the extended structure in some of the compact objects may in fact host velocity fields comparable to the larger disk galaxies.

While MACS J0451+0006 and MACS J2135-0102 have velocity gradients consistent with the other samples considered here, the clear outlier MACS J0744+3927 demonstrates that at least some small galaxies at this redshift have significant dynamical support from ordered rotation. This galaxy has an inclination-corrected $V_c/\sigma = 1.8^{+1.2}_{-0.4}$ at radius $R = 1\,\mathrm{kpc}$ and a Hα-derived star-formation rate surface density $\Sigma_{SFR} = 0.8 \pm 0.3$, which is a factor three lower than any galaxy in the dispersion-dominated sample, possibly indicating a later stage of evolution.

Motivated by the relatively large velocity shear and small Σ_{SFR} of MACS J0744+3927, we explore the possibility that the low V/σ observed in many compact galaxies is an effect of selecting galaxies in early stages of evolution with large dispersions and star formation rates. This is expected in models of star formation feedback, which predict that mechanical energy introduced by supernovae leads to higher velocity dispersion and hence lower V/σ as Σ_{SFR} increases. In one such model, Dib et al. (2006) simulate the velocity dispersion within the inter-stellar medium of galaxies induced by supernovae energy injection (assuming a 25% feedback efficiency) and predict a correlation between star-formation surface density and velocity dispersion.

To test whether supernova feedback might be responsible for the high dispersion observed in all $z \gtrsim 2$ star-forming galaxies, we show the velocity dispersion σ as a function of Σ_{SFR} in Figure 2.6. For the range of Σ_{SFR} with modeled supernova feedback, the observed velocity dispersions $\sigma = 30$–$80\ \mathrm{km\,s^{-1}}$are much higher than the predicted $\sigma = 10$–$15\ \mathrm{km\,s^{-1}}$. We note that the density used in these simulations is $\sim 30\times$ lower than inferred for the $z \simeq 2$ galaxies, so the simulated dispersion is likely overestimated by a factor of ~ 5. While the data show a slight trend of σ increasing with

Σ_{SFR}, the observed relation is inconsistent with simulations. We therefore conclude that supernova feedback is insufficient to explain the observed velocity dispersions. Figure 2.6 shows the relation between V/σ–Σ_{SFR}, clearly demonstrating that V/σ decreases with Σ_{SFR}. However, this trend is likely ultimately due to the velocity-size relation: larger galaxies tend to have larger rotation velocities (Figure 2.5) and smaller Σ_{SFR} (Figure 2.6). This is explained by different sensitivities of the data, as deeper spectra (lower Σ_{SFR}) reveal more extended structures at larger radius with larger rotation speed. The velocity-size correlation contributes much more to the observed V/σ–Σ_{SFR} relation than any correlation between Σ_{SFR} and the velocity dispersion. These data thus do not support the hypothesis that V/σ is strongly affected by the density of star formation: σ increases by less than a factor of 2 over two orders of magnitude in Σ_{SFR}.

2.3.4 Star-Formation Scales within Disks

The small $V_{max}/\sigma \leq 1.8$ and clumpy morphology of all galaxies suggest that the rotating disks are highly turbulent and may be dynamically unstable. We therefore explore the scale lengths for gravitational collapse within the high redshift disk galaxies.

Evidence is accumulating that the mode of star formation may be very different in early systems compared to that seen locally (Bournaud et al., 2008; Elmegreen & Elmegreen, 2005). Rather than forming stars within giant molecular clouds which condense out of a stable galaxy, star formation may be triggered by fragmentation of a dynamically unstable system. Briefly, in a rotating disk of gas and stars, perturbations smaller than a critical wavelength L_{max} are stabilized against the inward pull of gravity by velocity dispersion while those larger than some L_{min} are stabilized by centrifugal force. If the dispersion and rotation velocity are too low, $L_{min} > L_{max}$ and perturbations of intermediate wavelength grow exponentially. This interplay is summarized by the Toomre parameter $Q = L_{max}/L_{min}$ which is calculated from the velocity dispersion, rotation curve, and mass distribution (Toomre, 1964). Galaxies with $Q < 1$ are therefore unstable on scales between L_{max} and L_{min} and will fragment into giant dense clumps. This could trigger star formation in clouds of much higher mass and radius than GMCs in local spiral galaxies with $Q > 1$, and can explain the clump-cluster and chain morphologies observed in many high-redshift galaxies. Dynamical friction, viscosity and tidal interactions may cause these clumps to migrate toward the center of the galaxy potential, forming a bulge which stabilizes the system against further fragmentation.

From the galaxies whose velocity fields can be reasonably well described by rotating systems, we calculate the Toomre parameter via:

$$Q = \frac{\sigma_r \kappa}{\pi G \Sigma} \tag{2.2}$$

which describes the stability of a rotating disk of gas. If $Q < 1$ the system is unstable to local gravitational collapse and will fragment into overdense clumps. The value of κ is somewhat uncertain

as it depends on the unknown mass distribution; our observations are consistent with a range $\sqrt{2}\frac{V_c}{R}$–$2\frac{V_c}{R}$ corresponding to constant V_c and $V_c \propto R$ respectively. Adopting $\kappa = \sqrt{3}V_{max}/R$ appropriate for a uniform disk and using dynamical mass to estimate the surface mass density Σ, we find an inclination-corrected $Q \lesssim 0.6$ for all galaxies in our sample. We estimate that the uncertainty in Q is dominated by a factor of $\simeq 2$ error in the dynamical mass. The assumed κ introduces a negligible 15% uncertainty, with an additional random error of $\sim 30\%$ from the input parameters. Disk thickness and stellar abundance also affect the value of Q. Combined, these effects result in roughly a factor of 2 uncertainty. Even so, these galaxies all appear to be dynamically unstable since $Q < 1$. Hence we expect them to fragment into massive clumps on scales of order the Jeans length for dispersion support. In a uniform disk, the largest scale for which velocity dispersion stabilizes against gravitational collapse is

$$L_J = \frac{\pi\sigma^2}{8G\Sigma} \tag{2.3}$$

which is readily estimated from the dispersion and dynamical mass density. As with Q, the uncertainty in L_J is a factor of $\simeq 2$ dominated by the dynamical mass with additional uncertainty from the unknown mass distribution, disk height, stellar content, and directional dependence of σ. The resulting instability scale is 1–3 kpc for Cl 0024+1709 and 0.1–1.5 kpc for all other objects, consistent with the observed clump sizes.

2.4 Star Forming Regions at High Redshift

For each galaxy in our sample, the gain in resolution provided by gravitational lensing reveals multiple resolved giant HII regions which, as a group, dominate the integrated star formation rate. This gain enables us to study, in more detail than hitherto, the properties of individual star forming complexes in typical high redshift galaxies. In the following analysis, we concentrate on those HII regions with extended bright emission which are sufficiently isolated. Ideally we would construct a complete well-defined sample, however, in the exploratory work presented here we wish to limit the sample to objects for which the size and flux can be measured robustly. We therefore specifically exclude HII regions with overlapping emission in the Hα emission line maps (such as those in MACS J0744+3927).

In brief, HII regions were selected with a flux isophote in the image plane where the instrumental response is well known. Thus we can check whether each HII region is sufficiently resolved by comparing with the point-spread function produced by a bright tip-tilt reference star. To measure the area, each HII region was deconvolved with the point spread function using a method which accounts for the distorted shapes produced by gravitational lensing. The intrinsic flux and area were then computed by reconstructing the HII region in the source plane.

HII regions were selected above a flux isophote corresponding to $\simeq 3\sigma$, where σ is the noise level

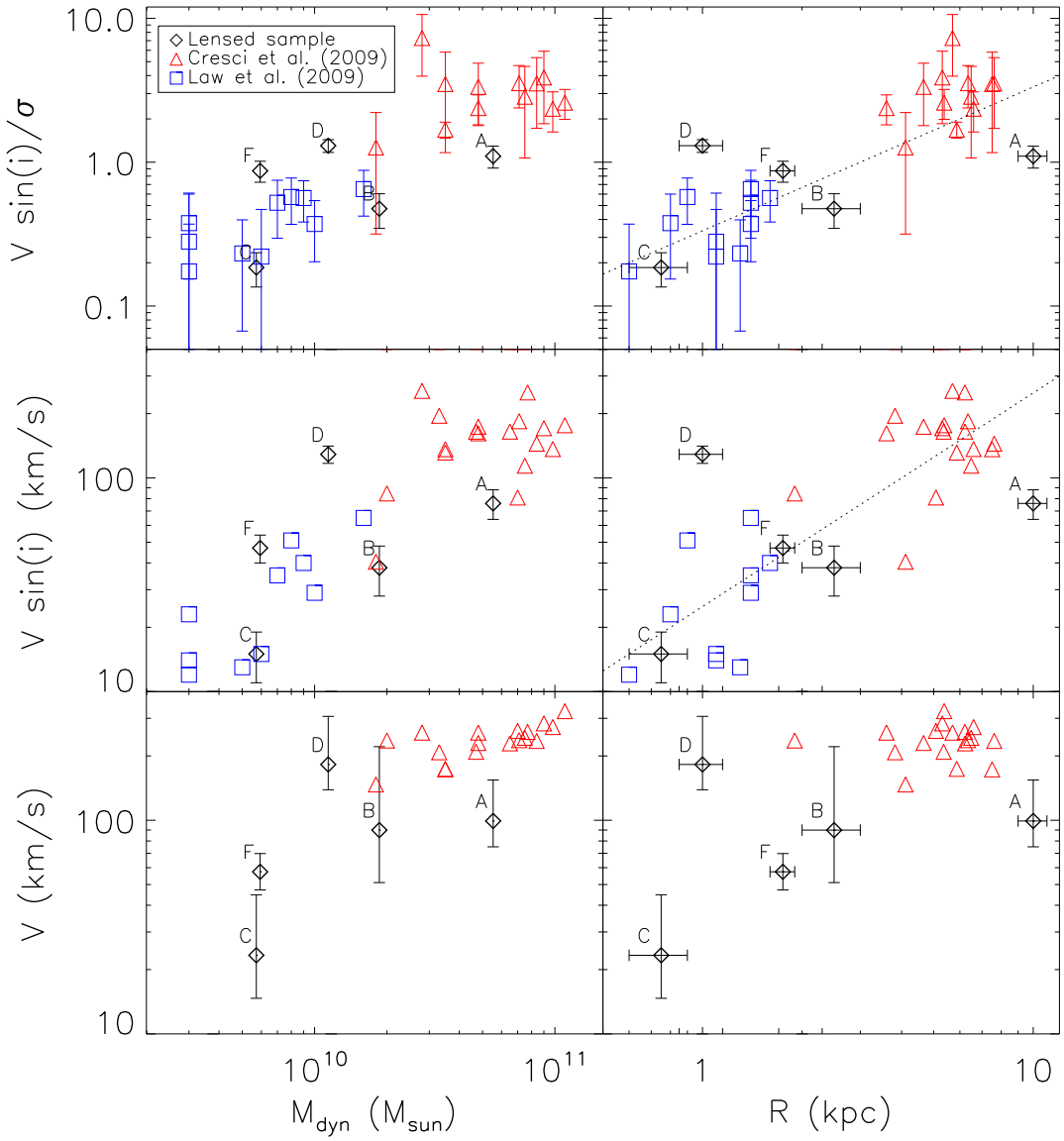

Figure 2.5: Kinematics as a function of dynamical mass and radius. The median $V \sin i/R = 25$ $\mathrm{km\,s^{-1}\,kpc^{-1}}$ is plotted in the middle right panel, and the corresponding V/σ for typical $\sigma = 75$ $\mathrm{km\,s^{-1}}$is shown in the upper right. Data for the lensed sample are given in Table 2.2 and labeled accordingly. Data for the comparison samples are taken from Tables 3 and 4 of Law et al. (2009) and Table 2 of Cresci et al. (2009) and are discussed in §2.3.3.2. We note that the dispersions σ_0 from Cresci et al. (2009) are systematically smaller than σ_{mean} used for the other data sets. σ_0 is better estimated by a simple average of dispersion values, which is typically 5 % smaller than a flux-weighted mean for the lensed galaxies.

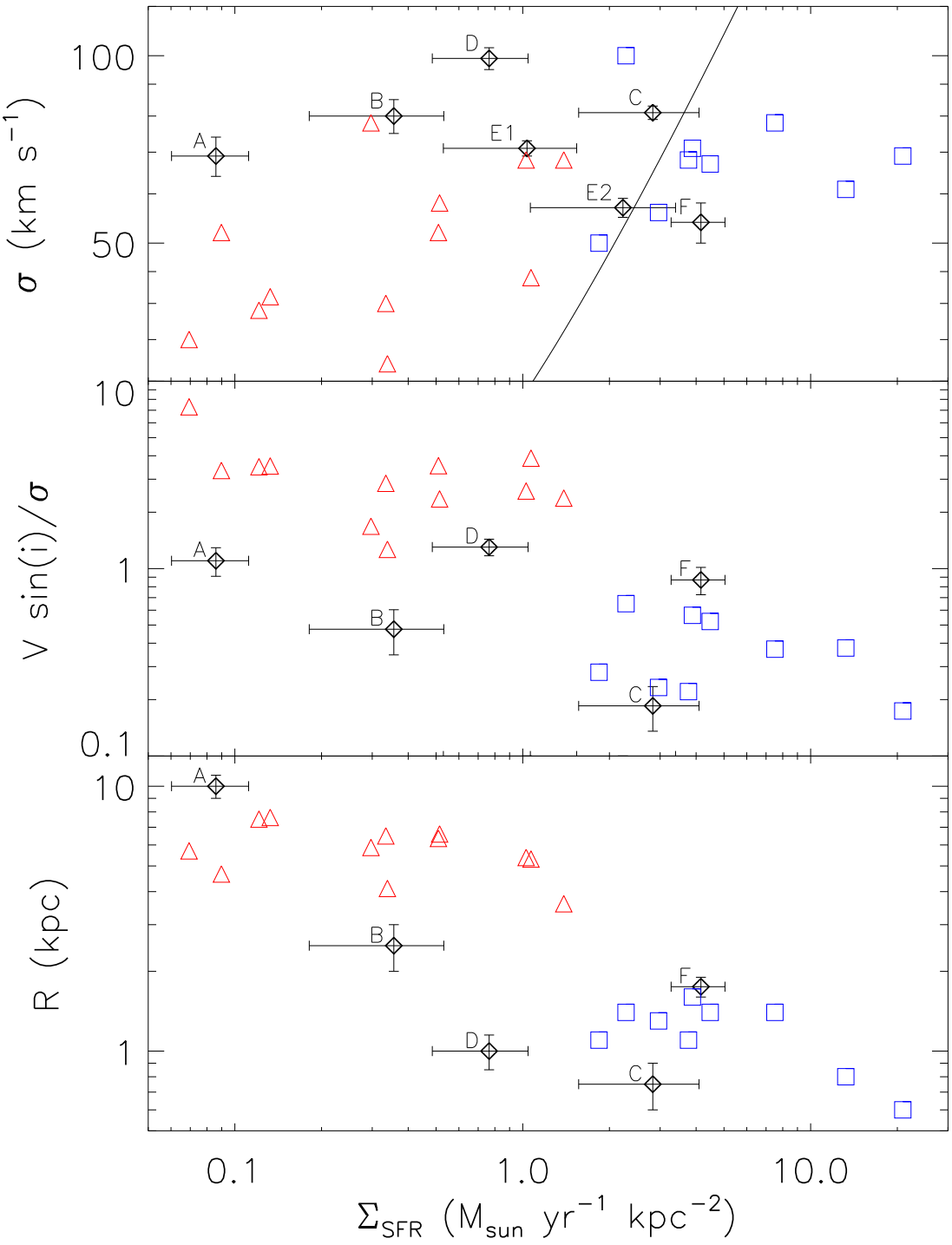

Figure 2.6: Velocity dispersion, V_{shear}/σ, and radius as a function of star formation rate density estimated from Hα flux. Symbols are the same as in Figure 2.5. The solid line in the top panel is a fit to simulations; see text for details. The observed σ is inconsistent with the simulations. Dispersion is at best weakly correlated with Σ_{SFR}. The strong correlation of radius and σ/V_{shear} with Σ_{SFR} is likely due to different sensitivity of the observations.

measured in narrow-band images, constructed by collapsing continuum-subtracted OSIRIS data cubes around the strongest emission feature. Only isolated HII regions (in which there is a single local maximum within the isophote) were selected. Regions not meeting this criterion are excluded from this analysis since attempting to disentangle multiple confused sources would introduce a large uncertainty. The isophote used varies from 1.4–4.6 $\times 10^{-16}$ erg s^{-1} cm^{-2} arcsec^{-2} for different arcs. The isophote for each selected HII region is shown in Figure 2.2. Each HII region subtends 0.5–0.9 arcseconds in the image plane, with the notable exception of the giant clump in MACS J0451+0006 which spans 3.2 arcseconds. The selected HII regions are all well-resolved since the point spread function has FWHM $\leq 0.2''$ in all observations.

For each HII region we calculated the total nebular line flux and intrinsic angular size in the image plane. The luminosity of each HII region was taken as the total flux within the selection isophote, with the uncertainty determined from the noise level in the narrow-band image. The HII region size is more complicated to derive since the effect of the spatial resolution needs to be taken into consideration. We proceed by making two basic assumptions. First, we assume the observed flux distribution is a convolution of the actual distribution with the instrumental point spread function. We can therefore compute the approximate intrinsic spatial variance by subtracting the Gaussian PSF variance from the measured variance within the isophote, $V_{int} = V_{iso} - \sigma^2_{PSF}$. This is equivalent to subtracting $\sigma = \mathrm{FWHM}/2.35$ in quadrature from Gaussian profiles, but the procedure is applicable to non-Gaussian asymmetric distributions. In all cases $V_{iso} > \sigma^2_{PSF}$ confirming that the HII regions are well resolved: $V_{iso}/\sigma^2_{PSF} = 2.3$ for one HII region and ≥ 3.2 for all others. Second, we assume that the isophotal area scales with spatial variance such that intrinsic surface area $A_{int} = A_{iso}\frac{V_{int}}{V_{iso}}$, where A_{iso} is defined as the pixel size multiplied by the number of pixels within the isophote. Uncertainty in the isophotal flux ranges from 12–27% propagated from flux calibration and noise level in the narrow-band image. The uncertainty in A_{iso} is estimated by assuming an error of PSF σ for the isophote diameter. The range of resulting angular diameter ($2\sqrt{A_{iso}/\pi}$) and relative error is 0.12 ± 0.06 to 0.61 ± 0.08 arcseconds.

To determine the source plane properties, each HII region is finally reconstructed using the lens model transformation. The total magnification μ is calculated from the ratio of image- to source-plane flux. The source plane diameter is then defined as $d = 2\sqrt{\frac{A_{iso}}{\mu\pi}}$. This method is robust against the spatially varying magnification of the lensed arcs. Uncertainty in the lens model has little effect on the diameter but significantly contributes to the error in flux. From the Hα flux (converted from [OIII]λ5007 for Cl 0949+5153) we estimate the star formation rate using the Kennicutt (1998) prescription. The values range from 0.8–3.6 M$_\odot$yr^{-1} star formation rate and 0.3–1.0 kpc diameter.

From the source plane diameters and kinematic data, we estimate the dynamical mass of the HII regions. We use the flux-weighted mean velocity dispersion within the clump σ_{mean} and assume a uniform spherical mass distribution ($C = 5$) as discussed in §3.1. The HII regions have large flux-

weighted mean dispersions, with σ_{mean} ranging from 45–80 $\mathrm{km\,s^{-1}}$. The dynamical masses range from 0.7–3 $\times 10^9$ $\mathrm{M_\odot}$, far greater than typical star-forming clusters in the local universe. Statistical uncertainty in the dynamical mass is 20–60%, so the additional factor of ~ 2 systematic uncertainty in C contributes significantly to the dynamical mass estimate. The mass-radius relation of the high-redshift clumps is shown in Figure 2.7 along with a sample of local star clusters and giant HII regions for comparison. This shows that the HII regions studied here are comparable in size and mass to the largest local star-forming complexes and consistent with the mass-radius relation observed locally.

In Figure 2.8 we compare the size–luminosity relation of these star forming regions with equivalent data observed locally (from Gonzalez Delgado & Perez 1997 for normal spirals, and Bastian et al. 2006 for intense starbursts such as the Antennae) and with a lensed arc at $z = 4.92$ (Swinbank et al., 2009). The sizes observed in the high redshift galaxies are comparable to the largest local star forming (HII) regions but with $\sim$100$\times$ higher star formation rates than in local spiral galaxies. However, the implied star formation rate densities are roughly consistent with that observed in the most vigorous local starbursts. This result is not significantly affected by the resolution of different observations, although varying the selection isophote alters the radius-luminosity relation. We note that the flux isophotes used to define HII regions in local spirals are much lower, so to quantify this effect we extract individual HII regions from narrow-band Hα images of local galaxies from the SINGS and 11HUGS surveys (Lee et al., 2007) using various isophotes. The effect on the size–luminosity relation as the isophote is increased is shown in Figure 2.8 as the vector A, which demonstrates that the extracted regions become smaller with higher average surface brightness. The vector B shows the effect of degrading the resolution while the isophote is kept fixed, which causes distinct HII regions to merge together giving the appearance of a larger region with similar surface brightness. Since the surface brightness of the high-redshift HII regions is $\sim 100\times$ higher than in local spirals, we conclude that the offset cannot be explained by different resolution and sensitivity of the various data sets. Metallicity also fails to explain the offset, as demonstrated by MACS J2135-0102 which has an $\mathrm{R_{23}}$ index and CIV P Cygni profile suggesting 0.4–1 $\mathrm{Z_\odot}$ metallicity (Stark et al., 2008; Quider et al., 2009). This implies that the luminosities in the high redshift HII regions are truly much larger than in local spirals. Furthermore the observed diameters are consistent with the Jeans length for support by velocity dispersion, suggesting that they collapsed as a result of disk instabilities. We expect this to occur since the Toomre Q parameter is less than unity for all galaxies in our sample. It therefore seems likely that intense star-formation in high redshift galaxies is driven by the fragmentation of gravitationally unstable systems.

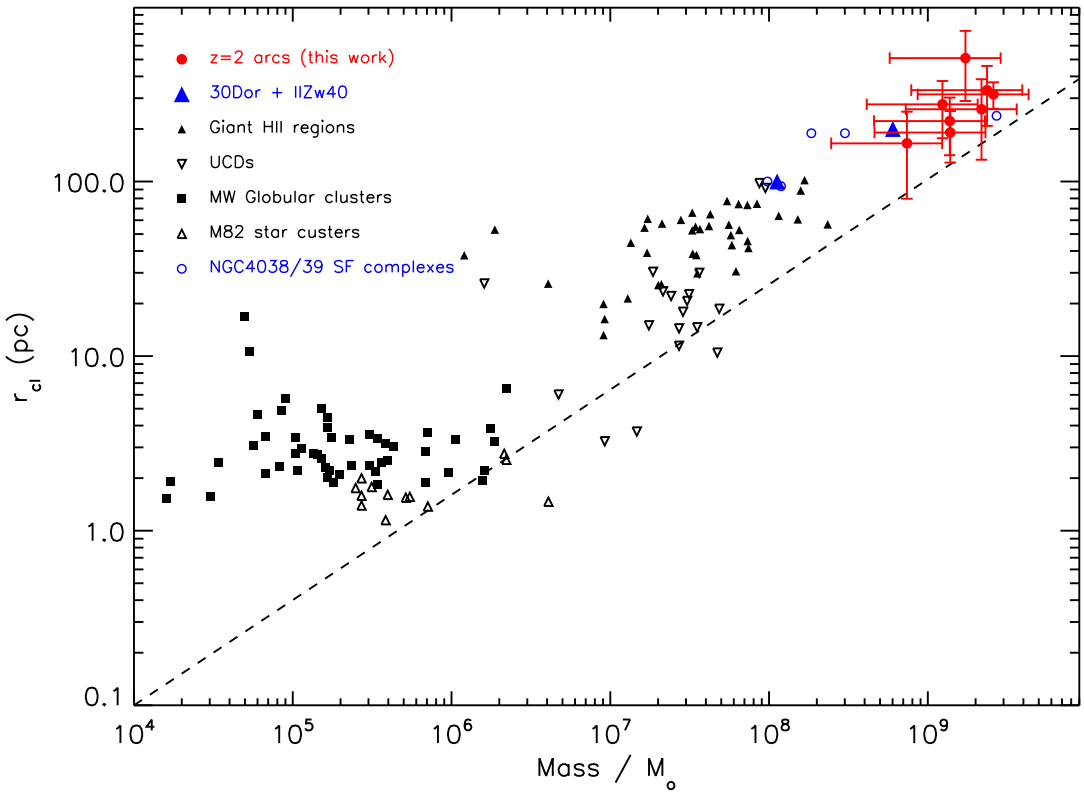

Figure 2.7: Size versus dynamical mass of individual star-forming regions within our high-redshift sample, compared to local star clusters and HII regions. The high-redshift HII regions have size and mass consistent with the largest star-forming complexes in the local universe. Local data are taken from Harris (1996) and Pryor & Meylan (1993) for Galactic globular clusters; Haşegan et al. (2005), Hilker et al. (2007), and Evstigneeva et al. (2007) for ultra-compact dwarf galaxies; McCrady & Graham (2007) for M82 clusters; Fuentes-Masip et al. (2000) for giant HII regions; and Bastian et al. (2006) for star-forming complexes in the Antennae. The dashed line represents a model for regions which are optically thick to far-infrared radiation and have undergone adiabatic expansion (Murray 2008). Dynamical mass for the high-redshift data is calculated as $M_{dyn} = C\frac{R\sigma^2}{G}$ with assumed $C = 5$ appropriate for a uniform-density sphere. The mass error bars account for statistical uncertainty in R and σ.

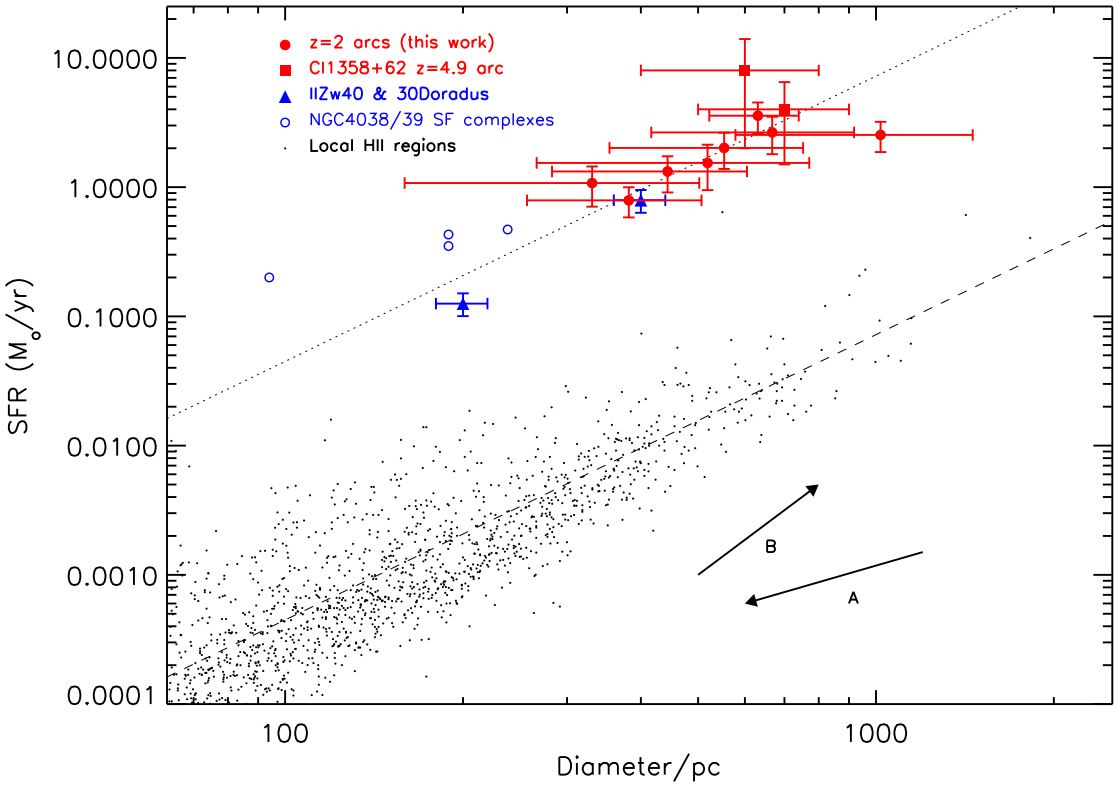

Figure 2.8: Hα-inferred star formation rate as a function of HII region size. Red circles represent individual HII regions from our lensed sample. Cl 0949+5152 was observed in [OIII] with the Hα flux taken to be 1.2 times the [OIII]λ5007 flux as determined from long slit NIRSPEC observations. The value for MACS J2135-0102 was determined from the Hβ flux assuming case B recombination. The star formation rates are all derived from Hα luminosities using the Kennicutt (1998) prescription. Red squares are from the lensed $z = 4.92$ galaxy presented by Swinbank et al. (2009), black points are HII regions in local spiral galaxies from Gonzalez-Delgado and Perez (1996), and blue open circles are star cluster complexes in the interacting galaxies NGC 4038/4039 from Bastian et al. (2006). The vectors A and B are explained in the text. The dashed line shows a fit to the data from local spiral galaxies, and the dotted line is the same but increased by a factor of 100$\times$ in SFR density. The high-redshift star-forming regions have significantly higher density of massive stars than HII regions in nearby spirals, but are comparable to the brightest star cluster complexes found in the local universe.

2.5 Conclusions

We have utilized strong gravitational lensing together with laser-assisted guide star adaptive optics at the Keck observatory to study the internal characteristics of six $z = 1.7 - 3$ star-forming galaxies with a spatial resolution down to $\sim 100 - 200$ parsecs. Extending beyond the diffraction limited capability of current 8–10 meter class telescopes, our study provides an interesting preview of the science that will routinely be possible with future 30 meter class optical/infrared telescopes with adaptive optics systems (Ellis 2009). We demonstrate that enhanced resolution allows us to resolve morphological and kinematic structure which has not been (and cannot be) discerned in AO-based surveys of similar non-lensed sources. In particular we resolve multiple giant star forming regions of size consistent with that expected from Toomre instability in *all* of our targets (including separate merging components). Furthermore we determine the dynamical state of galaxies which would be too poorly sampled to distinguish between rotation, merging, or dispersion-dominated kinematics without gravitational lensing.

The lensed sample allows a unique study of relatively faint and small galaxies at high resolution. The median luminosity of the sample is half of the characteristic L^* for $z = 3$ LBGs and well below that of other high-redshift IFU studies. We find that the kinematics of the sub-L^* population are in general agreement with larger and more luminous galaxies at similar redshifts: four of the six systems are clearly rotating with $V \sin i/\sigma = 0.5$–1.3, one has a velocity gradient consistent with rotation within the small Hα-bright region of the arc detected with OSIRIS, and one is a major merger. All have high velocity dispersion $\sigma = 50$–100 km s^{-1}, consistent with all other resolved observations of $z > 2$ star-forming galaxies and comparable to the value $\sigma \simeq 50$ km s^{-1}for stars which formed in the Galactic disk at $z \simeq 2$ (Sparke & Gallagher, 2000). Galaxies with a larger radius of detected nebular emission tend to have higher velocity shear and V/σ and lower Σ_{SFR}; these trends are consistent with other observations. The case of MACS J0744+3927 with inclination-corrected $V = 180^{+100}_{-40}$ km s^{-1}clearly demonstrates that some small ($R = 1.0 \pm 0.2$ kpc), fast-rotating field disk galaxies are already in place by $z = 2$. Well-sampled velocity fields demonstrate that the ubiquitous giant clumps are often embedded in common rotating systems and are not independent merging components. In contrast, non-lensed clumpy systems with velocity shear have been interpreted as mergers or remained ambiguous. These results demonstrate the need of high-resolution observations to distinguish rotating systems and mergers, as well as to probe the < 1 kpc scale of star formation at high redshift.

The observations presented here represent the best current probe of the scale of star formation at $z \gtrsim 2$ and, as such, can be compared to theoretical predictions. Most of the star formation in our sample occurs within giant HII regions of diameter 0.3–1 kpc comparable to the largest local HII regions, with star formation rate density comparable to the most vigorous local starbursts and

$\sim 100\times$ higher than in typical spiral galaxies. This offset in Σ_{SFR} cannot be explained by the different resolution or sensitivity of low- and high-redshift observations. Only one of our six objects is a clear major merger with both merging components broken into high-SFR clumps, suggesting that star formation episodes in sub-L* high redshift galaxies are triggered by Toomre instability independent of major merger events. We note that the merging system demonstrates no enhancement in star formation (as traced by nebular emission) compared to the non-merging galaxies. The increased high-mass star formation relative to local spirals likely results from some combination of higher gas density, increased star formation efficiency, shorter star formation timescales, and possibly other effects. The clumpy star formation, high Σ_{SFR}, kinematics consistent with rotation, and small $Q < 1$ are in qualitative agreement with the galaxy evolution model of Dekel et al. (2009) in which galaxies accrete their baryonic mass from cold streams. In this model the clumps form due to Toomre instability in turbulent disks and migrate into the galaxy center on timescales of a few hundred Myr, forming a bulge which stabilizes the system and increases the star formation timescale after ~ 2 Gyr. Numerical simulations suggest that cold-stream accretion is a dominant mechanism in galaxy assembly, especially at early times and in galaxies with halo masses less than a few 10^{11} M$_\odot$ (Kereš et al., 2009; Ocvirk et al., 2008; Brooks et al., 2009), although we note that there is no observational evidence for these cold streams. In particular the high-resolution simulations of Brooks et al. (2009) show that accretion of cold gas dominates the buildup of stellar disks and bulges in sub-L^* galaxies and allows disk formation at earlier times than if the accreted gas is shock-heated. The rotating kinematics and distribution of star formation in the lensed sample therefore supports, at least qualitatively, a cold gas accretion scenario for galaxy formation.

Analysis of our sample has shown the benefit of using lensed sources to probe the inner structure of early star-forming galaxies. The advent of many panoramic multi-color imaging surveys will hopefully reveal many further examples of such systems, ensuring further progress with laser-assisted guide star adaptive optics. Ultimately, the next generation of 30-meter optical/near-infrared telescopes will extend the high-resolution studies presented herein to the entire population of high-redshift star forming galaxies.

Chapter 3

The Origin and Evolution of Metallicity Gradients: Probing the Mode of Mass Assembly at $z \simeq 2$

Abstract

We present and discuss measurements of the gas-phase metallicity gradient in gravitationally lensed galaxies at $z = 2.0 - 2.4$ based on adaptive optics-assisted imaging spectroscopy with the Keck II telescope. Through deep exposures we have secured high signal to noise data for four galaxies with well-understood kinematic properties. Three galaxies with well-ordered rotation reveal metallicity gradients in the sense of having lower gas-phase metallicities at larger galactocentric radii. Two of these display gradients much steeper than found locally, while a third has one similar to that seen in local disk galaxies. The fourth galaxy exhibits complex kinematics indicative of an ongoing merger and reveals an "inverted" gradient with lower metallicity in the central regions. By comparing our sample to similar data in the literature for lower redshift galaxies, we determine that, on average, metallicity gradients must flatten by a factor of 2.6 ± 0.9 between $z = 2.2$ and the present epoch. This factor is in rough agreement with the size growth of massive galaxies suggesting that inside-out growth can account for the evolution of metallicity gradients. Since the addition of our new data provides the first indication of a coherent picture of this evolution, we develop a simple model of chemical evolution to explain the collective data. We find that metallicity gradients and their evolution can be explained by the inward radial migration of gas together with a radial variation in the mass loading factor governing the ratio of outflowing gas to the local star formation rate. Average mass loading factors of $\lesssim 2$ are inferred from our model in good agreement with direct measurements of outflowing gas in $z \simeq 2$ galaxies.

3.1 Introduction

Metallicity is one of the most fundamental properties of a galaxy. Gas-phase metallicity (hereafter referred to simply as metallicity) is governed by the cumulative history of baryonic assembly: gas accretion, star formation, and gas outflow. Metallicity is therefore a tracer of the processes responsible for galaxy formation and evolution. The vast database of information made available by the Sloan Digitized Sky Survey (SDSS) has revealed that metallicity is correlated with galaxy stellar mass and anticorrelated with star formation rate (Tremonti et al., 2004; Mannucci et al., 2010; Lara-López et al., 2010). The dependence on stellar mass is explained as the effect of gravity: more massive galaxies lose a smaller fraction of their metal-enriched gas in outflows and are more easily able to re-accrete lost metals due to their stronger gravitational potential (Tremonti et al., 2004). The dependence on star formation rate is primarily an effect of accretion: increased accretion of metal-poor gas drives higher star formation rates and lowers the overall metallicity (e.g., Davé et al. 2011).

The spatial distribution of metallicity and its evolution with time is sensitive to the assembly history of galaxies. Careful measurements in the local universe show that all disk galaxies exhibit negative radial metallicity gradients, with lower metallicity at larger galactocentric radius (e.g., Vila-Costas & Edmunds 1992; van Zee et al. 1998; Considère et al. 2000; Rupke et al. 2010b). In many cases the gradient flattens at large radius indicating efficient radial mixing, possibly induced by interactions or cycling between the disk and halo in a "galactic fountain" process (e.g., Werk et al. 2011; Bresolin et al. 2012). More attention has been given recently to measurements of the time evolution of metal gradients and the implications for galaxy formation. Models of inside-out disk growth predict that gradients should be initially steep and become flatter at later times (e.g., Prantzos & Boissier 2000; Magrini et al. 2007; Fu et al. 2009; Marcon-Uchida et al. 2010). In contrast, numerical simulations show that merger-driven growth will rapidly flatten existing metallicity gradients, which then become steeper with time (Rupke et al., 2010a). This is supported by nearby observations which reveal flatter gradients in interacting galaxies compared to an isolated control sample (Rupke et al., 2010b).

Several groups have now begun to consider the time evolution of radial metallicity gradients through observations. One approach is to examine the situation in detail within the Milky Way. Maciel et al. (2003) have inferred that the metallicity gradient must have been steeper in the past by analyzing the properties of stellar systems with different characteristic ages. However, this method is only feasible in a small number of local galaxies. The alternative approach, adopted here, is to measure the gradient in resolved data for galaxies seen at high redshift and to then compare these measures with those at lower redshift. Although a challenging task, this was first attempted in a previous paper where we showed the metallicity gradient in a gravitationally lensed galaxy at $z = 2$ was significantly steeper than in local disk galaxies (Jones et al., 2010b). Another lensed galaxy at

$z = 1.5$ yielded similar results (Yuan et al., 2011), further suggesting an inside-out mode of galaxy growth. However, some studies at high redshift have suggested that many massive galaxies may have "inverted" (positive) gradients with lower metallicity in the central regions (Cresci et al., 2010; Queyrel et al., 2012). This would imply a radically different mode of growth. One issue with this approach is the technical difficulty of measuring a reliable gradient in seeing-limited data which offers a relatively poor spatial resolution of $\simeq$ 4 kpc FWHM, approximately twice the typical half-light radius of an L_* galaxy at $z = 2 - 3$ (Bouwens et al., 2004). Such measurements cannot provide good spatial sampling except for the very largest sources. Clearly it is advantageous to use adaptive optics as well as the angular magnification afforded by gravitational lensing.

A further issue concerns the fact that some high redshift metal gradients reported in the literature are measured from a limited set of emission lines which may be affected by shocks and/or AGN (e.g., [NII]/Hα, [OIII]/Hβ). Shocks can easily produce a signature indicative of an inverted metallicity gradient in the [NII]/Hα line ratio (e.g., Westmoquette et al. 2012), while AGN can mimic an inverted gradient in [OIII]/Hβ and a strong negative gradient in [NII]/Hα (e.g., Wright et al. 2010). Hence multiple emission line diagnostics are required to distinguish variations in metallicity from the effects of shocks and AGN following methods such as those of Baldwin et al. (1981). While observations of multiple emission lines required for such diagnostics are challenging to obtain, they are necessary for robust metallicity gradient measurements.

This paper is concerned with increasing the number of galaxies at high redshift with reliable high-resolution metallicity measurements. Gravitationally lensed galaxies are ideally suited to this purpose, as the strong magnification provides both an increased flux and higher source plane resolution (e.g., Jones et al. 2010a,b). In this paper we present spatially resolved metallicity measurements of four lensed galaxies at $z = 2 - 2.4$ including one previously studied by Jones et al. (2010b). For the first time this permits us to consider the overall evolution of the metallicity gradient by utilizing lower redshift data. In §2 we describe the source selection, gravitational lens models, observations, and data reduction. In §3 we discuss the kinematic properties of each source which provides valuable insight into variations we see within our sample. In §4 we present resolved metallicity measurements. In §5 we construct and discuss a simple chemical evolution model to describe the origin of metallicity gradients in the context of the growing body of data we assemble for comparison purposes. The details of this model are given in an Appendix. In §6 we discuss the results in the context of our chemical evolution model. Finally, in §7 we summarize the main conclusions and implications of the results.

Throughout this paper we adopt a ΛCDM cosmology with H_0= 70 km s^{-1} Mpc^{-1}, Ω_M=0.30 and Ω_Λ=0.70. At z=2.2, 0.1 arcsec corresponds to 830 pc and the age of the universe was 2.9 Gyr. All magnitudes are in the AB system.

Name	z	Coordinates	Dates	Filter; Lines	T_{int} (s)	FWHM (PSF)	FWHM (source plane)	μ
J0744	2.21	07:44:47.9 +39:27:26	27-11-2008	Kn2; Hα, [NII]	14400	0.″11	0.3×0.8 kpc	16 ± 3
			20-2-2011	Hn2; [OIII], Hβ	10800	0.″08	0.3×0.7 kpc	
J1038	2.20	10:38:41.8 +48:49:19	20-2, 12-3-2011	Kn2; Hα, [NII]	4800	0.″14	0.4×1.6 kpc	8.4 ± 0.7
			20-2-2011	Hn2; [OIII], Hβ	1200	0.″14	0.3×1.7 kpc	
J1148	2.38	11:48:33.3 +19:29:59	20-2-2011	Kc4; Hα, [NII]	7200	0.″11	0.6×0.9 kpc	10.3 ± 5.0
			20-2, 12-3-2011	Hbb; [OIII], Hβ	3600	0.″08	0.6×0.9 kpc	
J1206	2.00	12:06:01.7 +51:42:30	19-5-2010	Kn1; Hα, [NII]	3600	0.″18	0.5×3.0 kpc	13.1 ± 0.7
			19-5-2010	Hn1; [OIII]	1800	0.″33	0.6×3.5 kpc	

Table 3.1: Log of observations.

3.2 Observations and Data Analysis

3.2.1 Source Selection

Our sources were selected as ideal targets for resolved metallicity measurement based on their redshift, nebular emission line intensity, magnification, and the presence of a suitable star for tip/tilt correction. Our lensed sources were selected to lie at $z = 2.0 - 2.4$ such that the diagnostic emission lines Hα, Hβ, [NII], and [OIII] can be observed in the H and K atmospheric windows where the Keck II adaptive optics (AO) system provides the best Strehl ratio. The exception is SDSS J1206 for which Hβ lies in a telluric absorption band and is inaccessible with OSIRIS. Prior to AO-assisted observation, we secured a near infrared spectrum of each source to ensure that the nebular emission lines are sufficiently bright and relatively free of contamination from OH sky lines (Richard et al., 2011). We require that each gravitational lens system has an accurate mass model constrained by the positions of multiply-imaged background sources with known redshift, essential for the source plane reconstruction discussed in §3.2.2. Finally, we require a suitably bright and nearby star to provide tip/tilt correction for the adaptive optics system. The observational details of each galaxy are given in Table 3.1. Below we provide a brief overview of the sources described in this paper.

MACS J0744+3927 (hereafter J0744) is a galaxy cluster lensing system discovered by the MAssive Cluster Survey (Ebeling et al., 2001). The $z = 2.21$ arc was identified in followup optical spectroscopy of the cluster and we secured the near-infrared spectrum as part of our screening program of bright $z \gtrsim 2$ arcs (Richard et al., 2011). We previously observed the Hα emission line with OSIRIS and described the source kinematics in Jones et al. (2010a).

SDSS J1038+4849 (hereafter J1038) is a group-scale lensing system discovered in the CASSOWARY survey for wide-separation gravitational lenses in SDSS imaging (Belokurov et al., 2009). We obtained a near-infrared spectrum of the $z = 2.20$ arc using NIRSPEC on Keck which showed bright nebular emission lines suitable for resolved spectroscopy with OSIRIS. We show in §3.3 that the source is a merger of at least two systems with stellar mass ratio of (6±3):1. Therefore in much of the analysis we consider the two components separately. The components are divided into the region with y-axis > -1 kpc in Figure 3.2 ("North" region) and y-axis < -1 kpc ("South"). The

northern region is brighter in optical WFPC2 imaging and the southern region is brighter in IRAC.

SDSS J1148+1930 (hereafter J1148) is comprised of a background source at $z = 2.38$ lensed into a nearly complete Einstein ring by a massive galaxy at $z = 0.44$. The system was discovered in the SDSS by Belokurov et al. (2007), and near-infrared longslit spectroscopy of the arc is reported in Hainline et al. (2009).

SDSS J1206+5142 (hereafter J1206) is a group-scale lensing system discovered in the SDSS by Lin et al. (2009). We previously obtained resolved metallicity measurements of this source from observations of Hα, [NII], and [OIII] with OSIRIS (Jones et al., 2010b). J1206 has an unusually steep radial metallicity gradient compared to local galaxies, motivating high-resolution studies of additional sources presented in this paper. We include this source in the analysis and discussion of the present paper for completeness.

3.2.2 Gravitational Lens Models

Accurate models of the foreground mass distribution are essential for correcting the gravitational lensing distortion and reproducing the source-plane morphology of background galaxies. Here we briefly describe the adopted procedure. We use the LENSTOOL program (Kneib et al., 1993; Jullo et al., 2007) to parameterize the mass distribution of the lens, using the positions of multiply-imaged background sources as constraints. The mass models used for J0744 and J1206 are described in Limousin et al.(in preparation) and Jones et al. (2010b), respectively. We constructed lensing mass models for the two other systems based on available *HST* imaging and multiple images with spectroscopic redshifts. In the case of J1038, we use the two triple systems at $z = 0.9657$ and $z = 2.198$ (Belokurov et al., 2009) to constrain a double pseudo-isothermal elliptical (dPIE) dark matter profile (including core $r_{\rm core}$ and cut $r_{\rm cut}$ radii, see Jullo & Kneib 2009 for more details). Cut radii are not constrained by strong lensing and so we use a fixed value $r_{\rm cut} = 800$ kpc typical of galaxy groups. For J1148 we use the system of 4 images at $z = 2.38$ forming the "Horseshoe" as constraints for a dPIE mass distribution, following the modeling of Dye et al. (2008). In both lens systems, individual group galaxies detected in the optical bands were added as low-scale dPIE mass components perturbing the model, a procedure similar to the one used for J1206 in Jones et al. (2010b). The best fit parameters of the dPIE potentials for these previously unpublished cases are summarized in Table 3.2.

LENSTOOL also determines the transformation from image plane to source plane position, and we use this mapping to reconstruct all observations onto a uniform grid in the source plane. Intrinsic source-plane morphologies of each galaxy are shown in Figure 3.2. Lensing magnification is calculated as the ratio of Hα flux in the image plane to that in the source plane, or equivalently the ratio of area subtended by Hα emission. In Table 3.1 we give the typical magnification and 1σ lens model uncertainty for the regions observed with OSIRIS. In the case of J1206, multiple images are covered

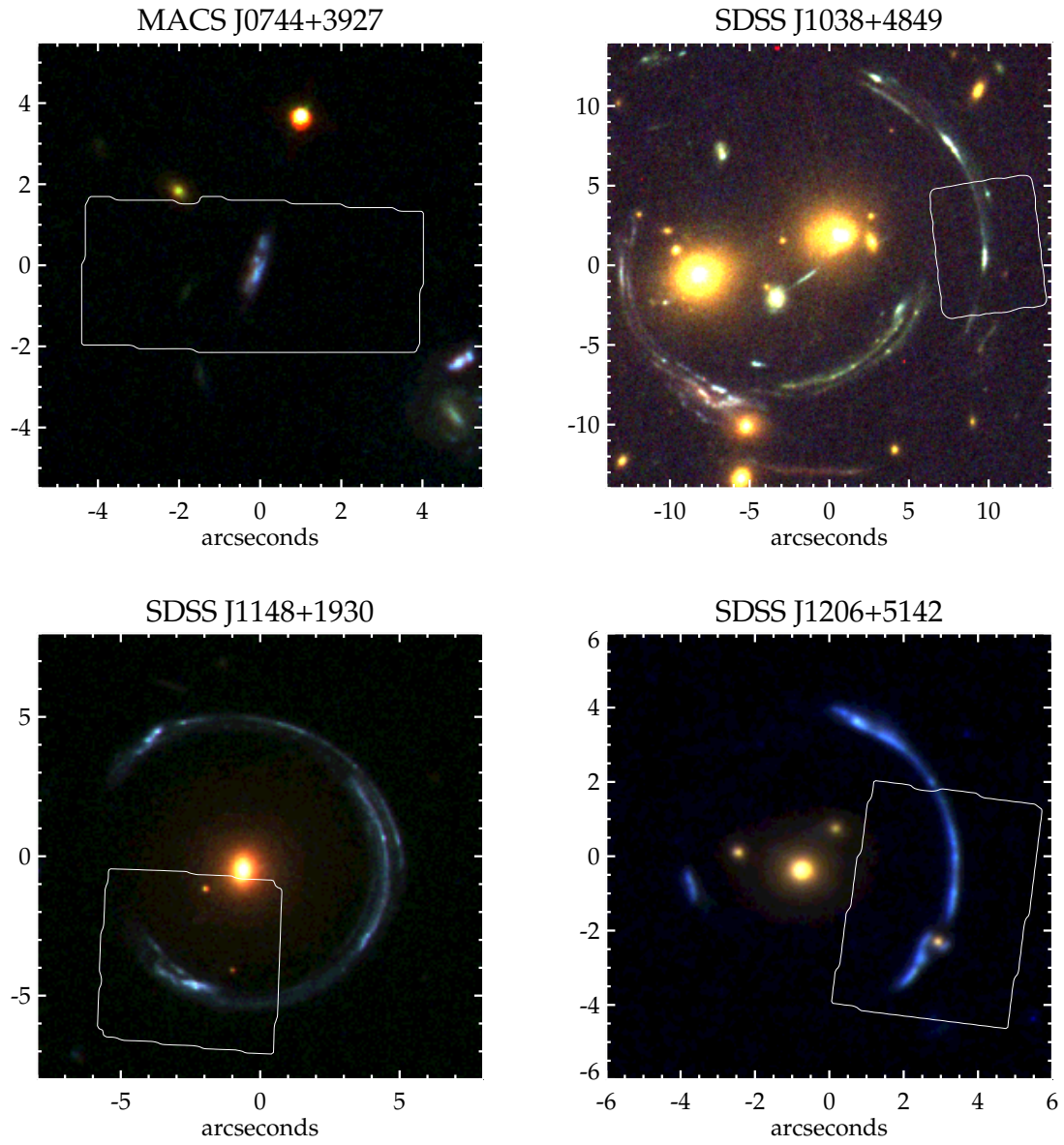

Figure 3.1: Color *HST* images of the sample. The white box in each image shows the OSIRIS field of view used to observe Hα and [NII] emission lines. R/G/B channels of each image are, respectively, ACS F814W/F555W/WFC3 F390W for J0744, WFPC2 F814W/F606W/F450W for J1038 and J1206, and WFC3 F814W/F606W/F475W for J1148.

Parameter	J1038	J1148
X_C [a]	-2.4±0.7	-0.11±0.11
Y_C [a]	-2.6±0.5	0.47±0.13
e [b]	0.76±0.03	0.00±0.02
θ [c]	31±1	134±12
σ [d]	576±12	654±78
r_{core} [e]	34.1±2.9	30.9±10.2
r_{cut} [e]	[800]	[800]

[a] Position from the brightest galaxy of the group (arcseconds).
[b] Ellipticity.
[c] Position angle (degrees).
[d] Velocity dispersion ($\mathrm{km\,s^{-1}}$).
[e] Core and cut radii (kpc).

Table 3.2: Best fit parameters for the previously unpublished lensing potentials (see text).

with OSIRIS such that the total magnification of images within the field of view is $\simeq 20$.

3.2.3 Integral Field Spectroscopy

Spectroscopic observations of the targets in Table 3.1 were taken with the OH-Suppressing Infra-Red Imaging Spectrograph (OSIRIS; Larkin et al. 2006) in conjunction with the laser guide star assisted adaptive optics (AO) system (Wizinowich et al., 2006) on the Keck II telescope. These were carried out during four separate observing runs with seeing ranging from $0\farcs7$ to $1\farcs5$ and clear conditions as summarized in Table 3.1. A suitably bright star ($R < 17$) within 55 arcseconds of each target was used for tip-tilt correction. We used the 100 milliarcsecond pixel scale in all observations which provided a field of view between $1\farcs6\times6\farcs4$ and $4\farcs5\times6\farcs4$ depending on the filter. Observations of each target were done with an AB observing sequence, dithering by $\sim 2-3$ arcseconds to keep the target within the integral field unit. The fields of view for Hα and [NII] are shown for reference in Figure 5.2. Fields of view for [OIII] and Hβ are essentially identical except for J1038, where only the northern region was observed.

Our data reduction methods are essentially identical to those described in Jones et al. (2010b). We used the OSIRIS Data Reduction Pipeline (ODRP; Larkin et al. 2006) to perform dark and bias subtraction, cosmic ray rejection, wavelength calibration, and to assemble the 3D data cubes. Sky subtraction was done with the IDL code described in Davies (2007) using temporally adjacent exposures as sky reference frames. Final data cubes were combined using a σ-clipped mean. Flux calibration for J1206 and the K-band observations of J0744 are described in Jones et al. (2010b) and Jones et al. (2010a) respectively. For the remaining observations, we follow the same method as in Jones et al. (2010a) using observations of the tip/tilt reference stars to calibrate the absolute flux. We additionally check the flux calibration with observations of the UKIRT infrared standard star FS 26 taken at a different time on the same nights. Flux calibrations derived from FS 26 agree

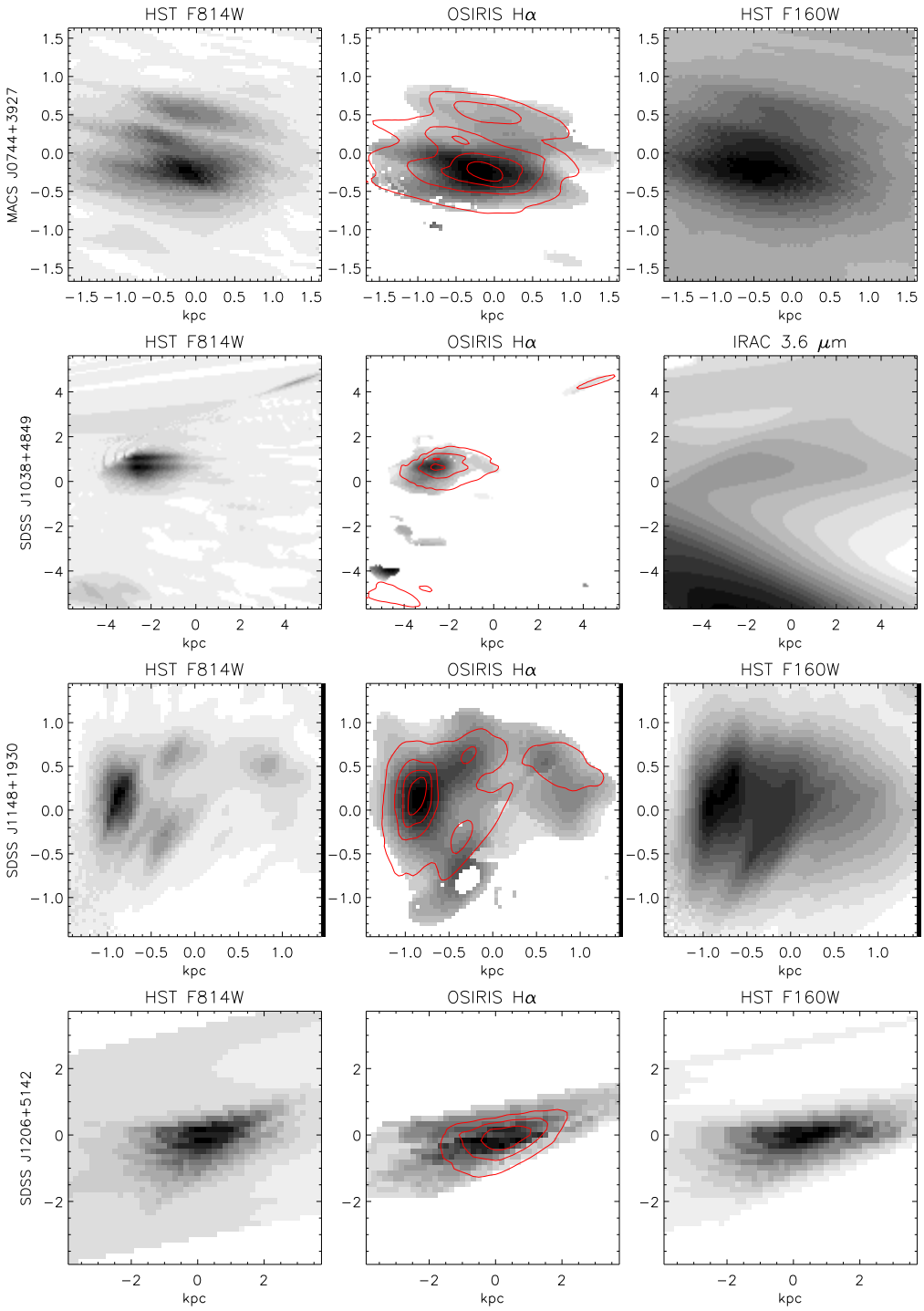

Figure 3.2: Source plane reconstruction of the lensed galaxies. Each row shows the morphology of one galaxy in (from left to right) rest-UV continuum, Hα emission, and rest-optical continuum. No rest-optical continuum image is available for SDSS J1038 so we show the reconstructed IRAC 3.6μm image. In all sources the ionized gas morphology traced by Hα is similar to that of the rest-UV continuum, shown as contours of *HST/ACS* F814W intensity on the Hα maps.

Name	Hα	[NII]	[OIII]$_{5007}$	[OIII]$_{4959}$	Hβ
J0744	20 ± 2	9 ± 2	12 ± 2	6 ± 2	6 ± 2
J1038 (North)	66 ± 5	5 ± 5	100 ± 5	42 ± 8	19 ± 7
J1038 (South)	71 ± 6	0 ± 7			
J1148	67 ± 3	7 ± 3	41 ± 2	8 ± 2	10 ± 3
J1206	236 ± 7	51 ± 7	230 ± 11	108 ± 14	

Table 3.3: Total observed emission line fluxes. All values are in units of 10^{-17} erg s^{-1} cm^{-2}. Uncertainties are 1σ determined from noise in the integrated spectra and do not include systematic errors in absolute flux calibration, which are typically $\lesssim 15\%$. For J1038 we report the northern and southern regions separately; the southern region was not observed in [OIII] and Hβ.

to within 15% suggesting the systematic uncertainty in flux calibration is $\lesssim 15\%$.

3.2.3.1 Extinction and Star Formation Rate

In this subsection we determine the extinction and star formation rate of each galaxy from their integrated spectra. We determine the total flux of nebular emission lines by summing all pixels within 250 km s^{-1} of the systemic redshift and within $\sim 0\farcs5$ of regions where the arc is detected in *HST* imaging. The results are shown in Table 3.3. Balmer line ratios Hα/Hβ are used to determine the dust extinction assuming a Calzetti et al. (2000) reddening curve, such that

$$\mathrm{E(B-V)} = 1.965 \log \frac{\mathrm{H}\alpha/\mathrm{H}\beta}{2.86} \tag{3.1}$$

where Hα/Hβ = 2.86 is the intrinsic line ratio for case B recombination. The extinction in V band and in Hα are then given by

$$\mathrm{A_V} = \mathrm{R_V\,E(B-V)} = 4.05\,\mathrm{E(B-V)} \tag{3.2}$$

$$\mathrm{A_{H\alpha}} = 3.33\,\mathrm{E(B-V)} \tag{3.3}$$

for the Calzetti et al. (2000) reddening curve. Star formation rates are computed from total Hα flux corrected for extinction and lensing magnification (Table 3.1), with the conversion factor from Kennicutt (1998) for a Salpeter IMF. The resulting E(B-V), $\mathrm{A_V}$, SFR, and 1σ uncertainties for each source are listed in Table 3.4. We note that the lower bound on SFR is required to be greater than or equal to the Hα-derived SFR assuming no extinction. Hβ is not observed for the southern region of J1038 and so we give only the extinction-free SFR as a lower limit. For J1206 we use the Balmer line ratios reported by Hainline et al. (2009) to derive E(B-V) = 0.30 ± 0.12 and apply this extinction correction to the Hα flux measured with OSIRIS.

3.2.4 Photometry and Stellar Mass

For an appropriate comparison with lower redshift data, it will be helpful to estimate the masses of our target galaxies. We have determined stellar masses for each galaxy from multi-wavelength photometry and stellar population synthesis modelling. All of our sources have *HST* imaging in multiple optical filters (e.g., Figure 5.2) as well as *Spitzer* IRAC channels 1 and 2. All galaxies except J1038 additionally have high resolution near-infrared imaging from *HST* WFC3/IR. We determine the photometry in matched apertures and then scale to the total flux. All data are first smoothed to match the point spread function of IRAC channel 1, which has the lowest spatial resolution. We then measure the flux in each filter within an aperture selected to encompass the majority of the arc while avoiding contamination from nearby sources. The total flux is determined from high-resolution optical *HST* images and all aperture fluxes are scaled by the same factor to obtain the total flux. Finally, near-infrared fluxes are corrected for nebular emission by subtracting the total line fluxes (Table 3.3). We fit the photometric data with stellar population models using the code FAST (Kriek et al., 2009) with an exponentially declining star formation history, Salpeter initial mass function, and Calzetti et al. (2000) reddening law. Redshifts are fixed to the spectroscopic values and metallicity is allowed to vary within the spectroscopic values for each arc (e.g., Table 3.5). We allow a range of star formation timescales $10^7 - 10^{10}$ yr. Ages are restricted to be > 50 Myr (approximately equal to the dynamical timescale for these sources; see §3.3) and less than the age of the universe ($\simeq 3$ Gyr at $z = 2-2.4$). Dust extinction is allowed to vary within the $\pm 1\sigma$ range of A_V in Table 3.4 and can be as low as half the allowed minimum value, since stellar continuum is often inferred to have a factor of $\simeq 2$ lower A_V than HII regions (e.g., Newman et al. 2012). In all cases we require $A_V \geq 0$, and for the southern region of J1038 we assume $A_V \leq 4$. Finally, we consider only star formation histories which produce a SFR consistent to within 1σ of the Hα-derived values. The best fit stellar mass and 68% confidence levels within these constraints are given in Table 3.4.

Correcting photometric measurements for contamination by nebular emission lines may be important for accurately determining stellar masses of star forming galaxies. Our sources have emission lines with rest-frame equivalent widths $W_0 \simeq 50$ Å for [OIII]$_{5007}$ and Hα. At redshift $z = 2$ this corresponds to roughly 10% of the flux measured in a broad-band filter. Indeed, [OIII] and Hβ contribute $\sim 20\%$ of total H-band flux measured for the lensed sample. To examine the effect on derived stellar mass, we apply the same stellar population synthesis method (and the same constraints) without correcting for nebular emission lines. This results in best-fit stellar masses which are higher by +0.21 dex for J0744, +0.002 dex for J1148, and +0.05 dex for J1206. In general the correction is not large and is consistent in all cases within the uncertainties, however in the case of J0744 the stellar mass is overestimated by 60% if nebular emission is not accounted for. In summary, ignoring the nebular emission contribution would bias the stellar masses to somewhat higher values, but not significantly affect any results in this paper.

	J0744	J1038 North	J1038 South	J1148	J1206
$\log M_*$ ($M_\odot$)	$9.4^{+0.4}_{-0.1}$	$9.1^{+0.2}_{-0.1}$	$9.9^{+0.2}_{-0.3}$	$9.9^{+0.2}_{-0.3}$	$10.1^{+0.2}_{-0.2}$
E(B-V)	0.13 ± 0.27	0.17 ± 0.32		0.73 ± 0.26	0.30 ± 0.12
A_V	0.53 ± 1.20	0.67 ± 1.30		2.94 ± 1.05	1.22 ± 0.47
SFR ($M_\odot yr^{-1}$)	$5.4^{+4.9}_{-1.8}$	38^{+37}_{-15}	> 24	210^{+167}_{-167}	68^{+44}_{-24}
$M_{\rm gas}$ (10^9 $M_\odot$)	$1.8^{+1.1}_{-0.5}$			27^{+14}_{-18}	14^{+3}_{-4}
$f_{\rm gas}$	$0.42^{+0.40}_{-0.08}$			$0.77^{+0.14}_{-0.15}$	$0.52^{+0.25}_{-0.11}$
$\log M_{\rm halo}$ ($M_\odot$)	11.6	11.4	11.8	11.9	12.0
D (kpc)	2.4	13.3		2.7	3.4
ΔV ($km\,s^{-1}$)	252 ± 33	160 ± 10		148 ± 3	159 ± 38
σ ($km\,s^{-1}$)	89 ± 26	82 ± 22		90 ± 33	104 ± 37
M_{dyn} (10^{10} $M_\odot$)	1.1			1.3	2.1
$Q/\sin i$	0.5			0.3	0.3

Table 3.4: Physical properties of the sample. Halo mass corresponds to the redshift of the arcs; see text for details. The diameter, ΔV, and σ listed for J1038 North refer to the entire J1038 system.

3.2.5 Gas Fraction

The gas mass in star forming galaxies at redshift $z \sim 2$ comprises a significant fraction $\sim 50\%$ of their total baryonic mass (Tacconi et al., 2010; Daddi et al., 2010). Ideally we would like to determine the gas mass from direct observations of atomic HI and molecular CO emission. However, in the absence of such data we can estimate total gas mass from the Kennicutt-Schmidt relation. We adopt the best-fit relation of Kennicutt (1998),

$$\Sigma_{\rm gas} = (4.0 \times 10^3\, \Sigma_{\rm SFR})^{0.71}\, M_\odot pc^{-2} \tag{3.4}$$

where $\Sigma_{\rm SFR}$ is in units of $M_\odot yr^{-1} kpc^{-2}$. The baryonic gas fraction is then defined as

$$f_{\rm gas} = \frac{M_{\rm gas}}{M_{\rm gas} + M_*}. \tag{3.5}$$

We calculate the gas mass and gas fraction of all three non-merging galaxies using Hα-derived star formation rates and diameters (Table 3.4) to determine surface densities. The results are given in Table 3.4. The inferred gas fractions of $0.4 - 0.8$ are in good agreement with direct measurements at high redshift (Tacconi et al., 2010; Daddi et al., 2010). Dynamical masses derived in §3.3 also suggest $f_{gas} \approx \frac{M_{dyn} - M_*}{M_{dyn}} = 0.4 - 0.8$ for the arcs, in excellent agreement.

In cases where high resolution *HST* infrared imaging is available, we calculate the spatially resolved gas fraction of the lensed galaxies. For each source-plane pixel we determine Σ_{SFR} from Hα intensity and the extinction factors in Table 3.4, and calculate $\Sigma_{\rm gas}$ from Equation 3.4. The stellar mass density is calculated for the same pixels from the *HST* F160W image, which we reconstruct in the source plane and smooth to match the resolution of the OSIRIS Hα data. We assume a constant stellar mass-to-light ratio in the F160W bandpass to calculate Σ_{M_*}. We extract the average gas and stellar mass densities in radial bins along a psuedo-slit oriented along the kinematic major axis.

(The same slits are later used to measure kinematics and metallicity gradients.) We examined the gas fractions as a function of radius and found it to be nearly constant ($< 15\%$ variation).

3.2.6 Emission Line Fitting

The analysis presented in later sections is based on the resolved properties of emission lines in the galaxy source plane. We determine line flux, velocity, and velocity dispersion from Gaussian fits to the emission lines of interest. The emission line fits for J1206 are described in detail in Jones et al. (2010b). We follow identical methods for the remaining sources presented here, except that emission lines are fit in the source plane rather than the image plane. Here we describe the complete process.

The OSIRIS data for each object is aligned with high resolution *HST* images used to define the lens model transformations from image to source plane (§3.2.2). Each data cube is reconstructed in the source plane and smoothed with a Gaussian kernel to increase signal-to-noise of the fainter emission lines and in regions of low surface brightness. The smoothing kernels have FWHM $\simeq 300$ pc for J0744 and J1038, and 600 pc for J1148. We then fit a Gaussian profile to the Hα line at each spatial pixel using a weighted χ^2 to account for increased noise at the wavelengths of bright sky lines. Weights are determined from the noise measured in a blank sky region of each data cube. Line flux and velocity are derived from the centroid and area of the best fit profile in all cases with signal-to-noise ≥ 5. Intrinsic velocity dispersion is calculated by subtracting the instrumental resolution $\sigma_{inst} \simeq 50$ km s^{-1}(measured from bright OH sky lines) in quadrature from the best-fit line width.

We fit all other emission lines of interest using the velocity and dispersion derived from Hα as constraints. Hα is used because it has the highest signal-to-noise in all cases. The centroid and width of each line is fixed at the best-fit values measured for Hα, and a weighted fit is used to determine the normalization. Each emission line is also fit separately without fixing the centroid and width, and no significant differences are found. We therefore use the emission line fluxes derived with Hα line profiles since these have lower formal uncertainties. Additionally, when considering the ratio of various emission lines, we can be confident that ratios are not biased by different kinematic structure in different lines.

We estimate the physical resolution from observations of tip/tilt reference stars taken at the same time as the emission line data. Tip/tilt stars are reconstructed and smoothed in the same manner and the resulting FWHM is measured along the major and minor axes of reconstructed star images. These values are reported in Table 3.1. Although smoothing degrades the resolution, the FWHM is $\lesssim 1$ kpc for all sources.

3.3 Kinematics

In order to understand the variation in metallicity gradients we see in our sample, it is useful to characterize each source in terms of its kinematic properties. The degree of ordered rotation has been determined from fits to the Hα emission line (§3.2.6). The kinematic properties of J0744 and J1206 are already described in Jones et al. (2010a) and Jones et al. (2010b) respectively. Here we follow a similar analysis for the remaining sources. As in our earlier work, we extract one-dimensional velocity and dispersion profiles in a pseudo-slit oriented along the kinematic major axis (i.e., the direction of highest velocity shear). These profiles are shown in Figure 3.3 along with the two-dimensional velocity maps of each source. Three galaxies (J0744, J1148, and J1206) show ordered rotational motion in both the 2-D maps and 1-D profiles with high local velocity dispersion $\gtrsim 20$ km s^{-1}in all cases. The fourth, J1038, is comprised of multiple spatially and kinematically distinct regions indicating that this source is undergoing a merger. The diameter and peak-to-peak velocity shear ΔV of each source (measured along the pseudo-slit) are given in Table 3.4. For the rotating sources, ΔV is related to the maximum circular velocity V_{max} and inclination angle i as

$$\Delta V = 2V_{max} \sin i. \tag{3.6}$$

Additionally we give the mean local velocity dispersion σ, defined as the unweighted mean of individual pixels with error bars reflecting the 1σ scatter. We note that the adopted definition of σ varies throughout the relevant literature.

We now briefly compare the kinematics with other samples at high redshift reported in the literature. The largest such sample is the SINS survey; observations of 80 SINS galaxies at $z \sim 2$ are described in Förster Schreiber et al. (2009). The median velocity shear of their sample is $\Delta V = 134$ km s^{-1}with an interquartile range of $90 - 220$ km s^{-1}. Approximately one third of the SINS sources are clasified as mergers while the rest have varying degrees of rotation and random motion. Förster Schreiber et al. (2009) tabulate the ratio of velocity shear to velocity dispersion, $\Delta V/(2\sigma)$, which gives an indication of the degree to which each galaxy is dynamically supported by rotation vs. random motions. The SINS sample has a median $\Delta V/(2\sigma) = 0.56$ and interquartile range $0.37 - 0.75$. Other published samples of $z \simeq 2 - 3$ galaxies have median $\Delta V/(2\sigma)$ values of 0.4 (Law et al., 2009) and 0.9 (Jones et al., 2010a). In comparison, velocity shear observed in the lensed galaxies presented here is somewhat higher than in other samples at similar redshift. The values in Table 3.4 give a range $\Delta V/(2\sigma) = 0.76 - 1.4$ for our lensed galaxies, and we note that our values of σ are systematically higher than for the definition used by Förster Schreiber et al. (2009). The lensed galaxies therefore have a higher degree of rotation than typical SINS sources. According to the criteria of Förster Schreiber et al. (2009), all three non-merging sources in our sample are "rotation-dominated" (defined as having $\Delta V/(2\sigma) \geq 0.4$).

A common hypothesis advanced by recent studies is that the evolution of star-forming galaxies at high redshift is driven in large part by global gravitational instability (e.g., Jones et al. 2010a; Genzel et al. 2008; Dekel et al. 2009). Briefly, if the velocity dispersion and rotational velocity are too small, the system is unstable and gravitational perturbations will grow exponentially into giant "clumps". This is quantified by the Toomre parameter Q, where values $Q \lesssim 1$ indicate that a galaxy is unstable and will fragment into giant clumps. We calculate $Q/\sin i$ for the rotating galaxies in our sample using the information in Table 3.4 and following the same method as Jones et al. (2010a). We list the values in Table 3.4 as well as the dynamical mass estimated as $M_{dyn} = 5R\sigma^2/G$. The results indicate that all three galaxies are gravitationally unstable unless the inclinations are very high (> 60 degrees), although the uncertainty is approximately a factor of 2 in Q (see Jones et al. 2010a). This can explain the "clumpy" morphologies apparent in Figure 3.2.

In summary, three galaxies in our lensed sample are rotating and one is undergoing a merger. This merger fraction is consistent with larger samples at similar redshift. The kinematics of galaxies in our sample are more rotation-dominated than others studied at similar redshift, and all rotating galaxies in our sample are likely to be gravitationally unstable. The ratio of shear to velocity dispersion, V/σ, is $\sim 2\times$ higher than for typical galaxies in the extensive SINS survey.

3.4 Gas Phase Metallicity

The multiple emission lines detected by OSIRIS enable us to determine spatially resolved gas-phase metallicities in each galaxy. Robust metallicity measurements rely on knowledge of the temperature and ionization state of a gas. However, this requires accurate measurement of diagnostic emission lines which are usually too faint to be detected at high redshift with current instruments. Instead we use ratios of strong emission lines which can be detected in modest integration times and which correlate with metallicity through locally-calibrated relations. These include ratios such as $\frac{[\mathrm{OIII}]+[\mathrm{OII}]}{\mathrm{H}\beta}$ (the R23 index) and [NII]/Hα (the N2 index) for which calibrations have been determined using direct electron temperature-based measurements or photoionization models (e.g., Pagel et al. 1979; Kewley & Dopita 2002; Pettini & Pagel 2004; Maiolino et al. 2008). As in Jones et al. (2010b) we primarily use the N2 index to determine gas-phase oxygen abundance via

$$12 + \log O/H = 8.90 + 0.57 \times \log [NII]/H\alpha \tag{3.7}$$

(Pettini & Pagel, 2004), with a dispersion of 0.18 dex. The main advantage of N2 is that the two requisite lines are very close in wavelength such that systematic uncertainties from reddening and instrumental effects are negligible.

While the N2 index provides a practical means of estimating metallicity in high-redshift galaxies,

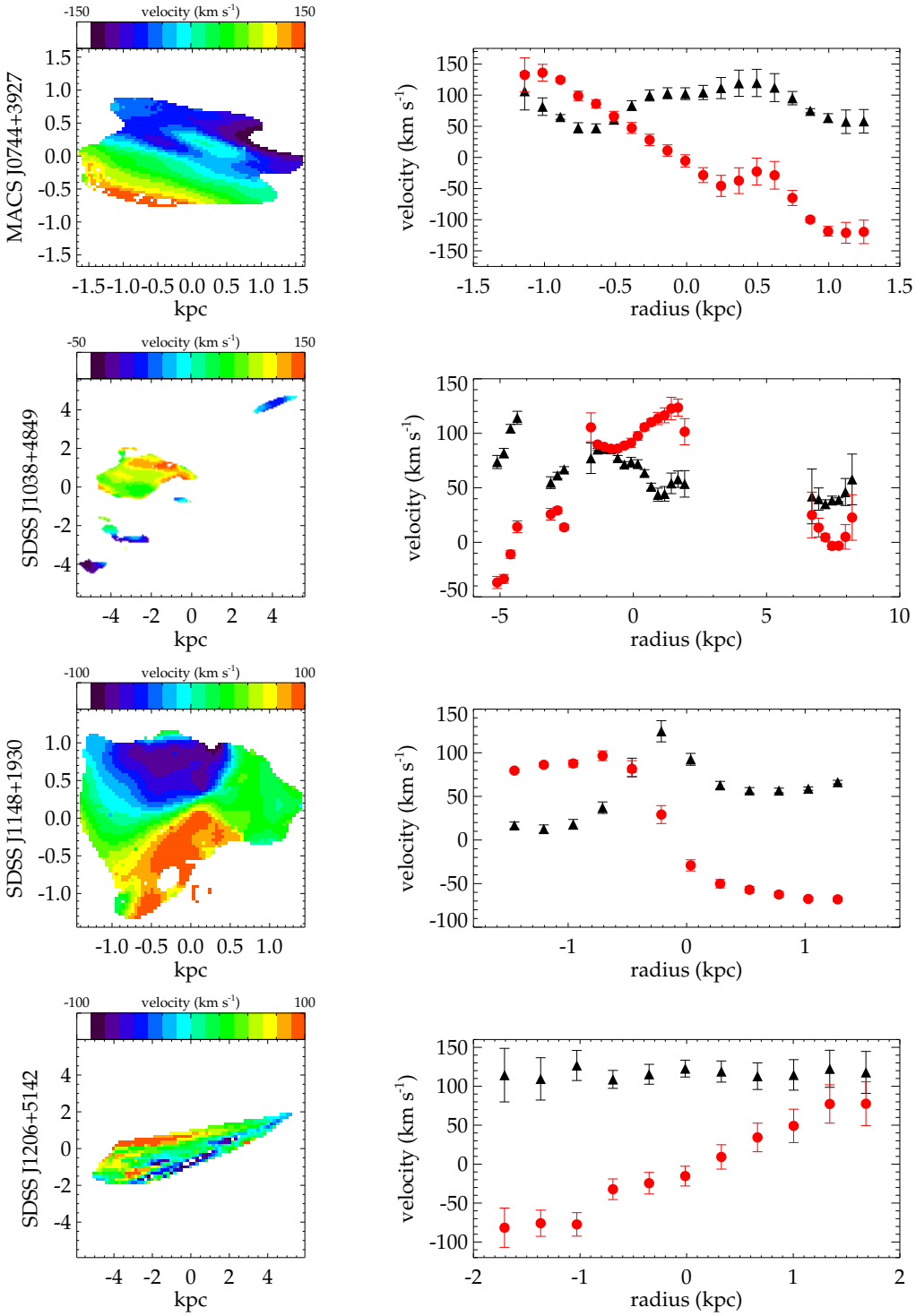

Figure 3.3: Source plane kinematics of the lensed galaxies. Left: two-dimensional velocity field. Right: one-dimensional velocity (red circles) and dispersion (black triangles) of each source, extracted along the kinematic major axis.

it can fail in cases where (*i*) active galactic nuclei (AGN) or shock excitation contribute significantly to the emission line flux, (*ii*) secondary production of nitrogen leads to variations in the N/O ratio, or (*iii*) [NII] cooling saturates (at $12 + \log O/H \gtrsim 9.0$). This last case is not a concern for the galaxies in our sample as they have metallicities significantly below this value. However AGN, shocks, and variations in the N/O ratio are a potential problem and we address this issue with additional observations of [OIII] and Hβ emission lines.

AGN and shocks can be distinguished from star-forming regions on the basis of emission line flux ratios. One of the most widely used diagnosics is the ratio of [NII]/Hα compared to [OIII]/Hβ, as described by Baldwin et al. (1981) (the "BPT diagram"). We show the BPT diagram for individual pixels in each lensed galaxy in Figure 3.4. Only regions where all requisite lines are detected ($> 3\sigma$) are shown on the diagram. We note that some individual pixels are correlated since the point spread function is larger than the pixel size. In the case of J1206 we estimate Hβ flux from the global ratio Hα/Hβ = 4.07 (Hainline et al., 2009); these [OIII]/Hβ values are therefore accurate on average but may deviate significantly within individual pixels. The line ratios of ∼122,000 galaxies from the Sloan Digital Sky Survey (SDSS) are also plotted and clearly show a locus of star forming galaxies with a separate branch of AGN. The lensed galaxies generally follow the locus of local star forming galaxies but are offset to higher [OIII]/Hβ ratios; this has been commonly observed in high redshift galaxies and is generally attributed to high ionization parameters rather than AGN (see discussion in Erb et al. 2010 and Hainline et al. 2009). Some regions of the lensed galaxies have [OIII]/Hβ formally above the theoretical limit from star formation (Kewley et al., 2001), but consistent within the uncertainties. We conclude that emission lines in the lensed galaxies originate predominantly from star forming HII regions with little contribution from AGN or shocks.

To test whether metallicities derived from the N2 index suffer from systematic errors due to variable N/O abundance or any other effect, we calculate metallicities using various other methods. Using the same data as for the BPT diagram (Figure 3.4), we compute 12+log(O/H) using the calibrations of Pettini & Pagel (2004) and Maiolino et al. (2008) and show the results in Figure 3.5. All metallicities are consistent given the intrinsic scatter in each calibration, although [OIII]-based metallicities are typically lower by ~ 0.15 dex than those inferred from [NII] alone. Furthermore the Maiolino et al. (2008) results are systematically higher than for Pettini & Pagel (2004) by ~ 0.2 dex. Overall we conclude that systematic uncertainties in metallicity calculated from the N2 index are limited to $\lesssim 0.2$ dex depending on the calibration used (e.g., N2 vs. O3HB), with an additional ~ 0.2 dex uncertainty in the zero point (e.g., from Pettini & Pagel 2004 vs. Maiolino et al. 2008). In the following section we show how different calibrations affect the derived metallicity gradients.

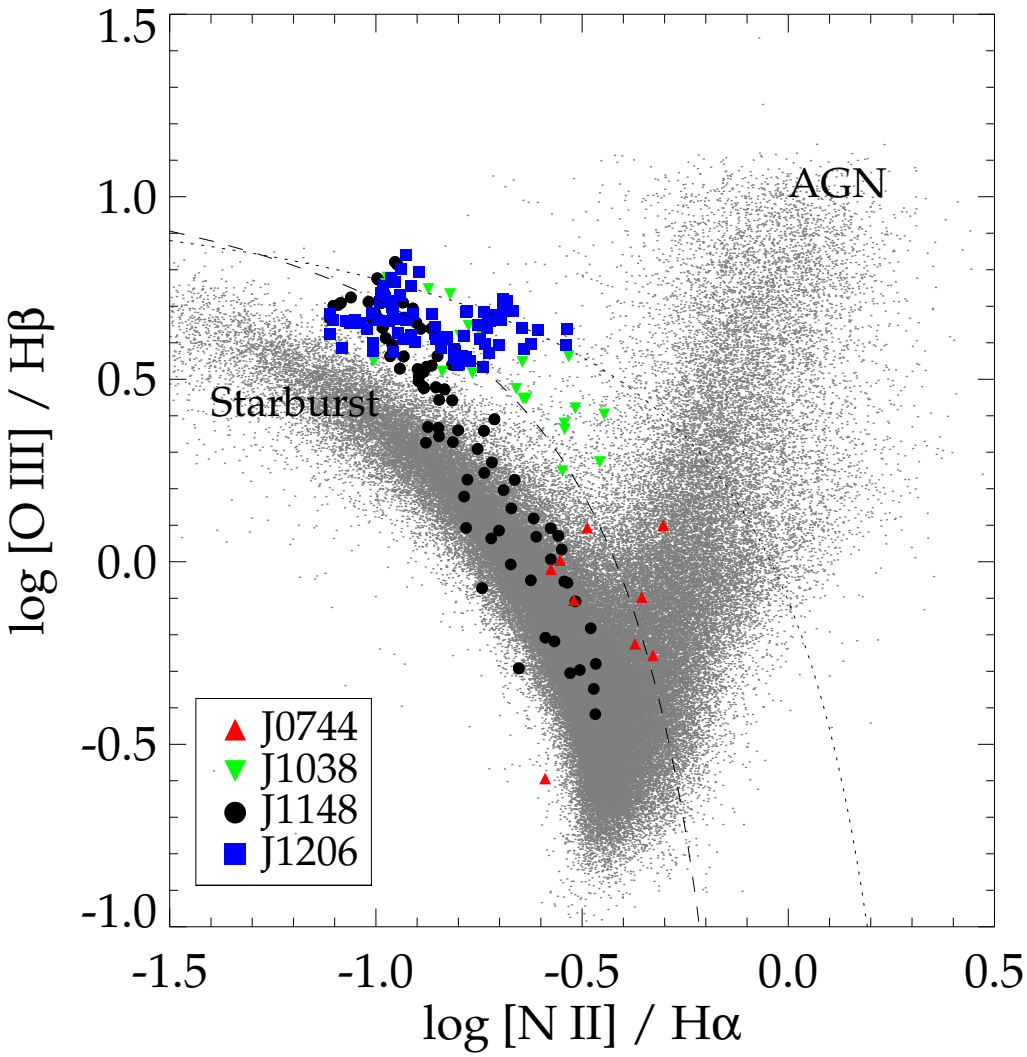

Figure 3.4: Diagnostic diagram of [NII]/Hα and [OIII]/Hβ. Each large point represents a single spatial pixel of OSIRIS, and the small gray points are ∼122,000 galaxies from the Sloan Digital Sky Survey (SDSS) with signal to noise ≥ 5 in all relevant emission lines. SDSS galaxies show a locus of star forming galaxies, and a separate branch of AGN extending to the upper right. The dotted line shows the theoretical maximum [OIII]/Hβ from star forming regions (Kewley et al., 2001), and the dashed line is an empirical division between star-forming galaxies and AGN from Kauffmann et al. (2003). All regions of the lensed galaxies are consistent with pure star formation, although [OIII]/Hβ is typically above the locus of SDSS star forming galaxies at $z \simeq 0$. This is commonly observed at high redshift and is attributed to a high ionization parameter (e.g., Hainline et al. 2009; Erb et al. 2010).

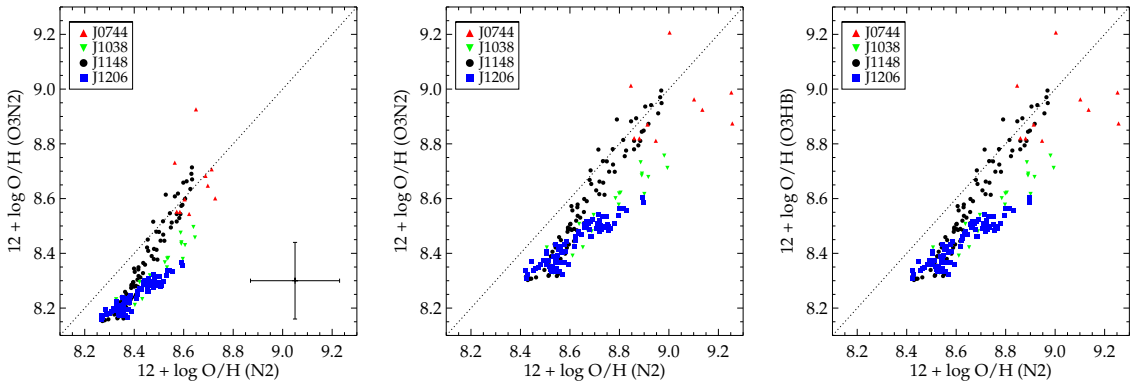

Figure 3.5: Comparison of the different strong-line metallicity diagnostics N2 ([NII]/Hα), O3N2 ([OIII]/[NII]), and O3HB ([OIII]/Hβ). Metallicities are derived from the calibrations of Pettini & Pagel (2004) (left panel) and Maiolino et al. (2008) (center and right panels). Each point represents an individual OSIRIS pixel; data are identical to those in Figure 3.4. The 1σ scatter measured by Pettini & Pagel (2004) is shown in the lower right of the left hand panel. Metallicities derived from different methods are generally in agreement, with [OIII]-based metallicities typically 0.15 dex lower than those derived from N2. Metallicity derived using the Maiolino et al. (2008) calibrations are systematically higher by $\sim$ 0.2 dex compared to Pettini & Pagel (2004).

3.4.1 Metallicity Gradients

We are now in a position to determine gradients in the inferred metallicity along the kinematic major axis of each galaxy. To do so we extract resolved measurements of [NII] and Hα flux along a pseudo-slit in the same manner as for constructing the rotation curves shown in Figure 3.3. While other orientations can also be used, they must be corrected by the uncertain inclination and so we take the major axis to provide the most precise measurement. In the case of J1038 the inclination angle between merging components is unknown, hence the magnitude of gradients for this source should be considered an upper limit. The center of each galaxy is defined kinematically as the position along the pseudo-slit at which the velocity is equal to the systemic velocity (i.e., velocity = 0 in Figure 3.3); for the merging system J1038 we use the systemic velocity of the UV-bright northern region (corresponding to velocity $\simeq$ 100 km s^{-1} in Figure 3.3). We bin individual pixels by their galactocentric radius and compute the total Hα and [NII] flux using all pixels with signal-to-noise $\geq$ 10 in Hα. Metallicity is derived from the resulting [NII]/Hα ratio via Equation 3.7 and shown as a function of radius in Figure 3.6.

Each galaxy shows significant variations in metallicity as a function of radius (Figure 3.6). The three rotating galaxies (J0744, J1148, and J1206) all show significant gradients with decreasing metallicity at larger radii, as observed in all local disk galaxies. The merging system J1038 has significantly lower nuclear metallicity than the rotating galaxies, and exhibits a more complex metallicity distribution. Metallicity is measured for three spatially distinct regions of J1038. The peak of rest-UV and Hα emission (at $R = 0$ in Figure 3.6) has the lowest metallicity at $12 + \log O/H = 8.2$,

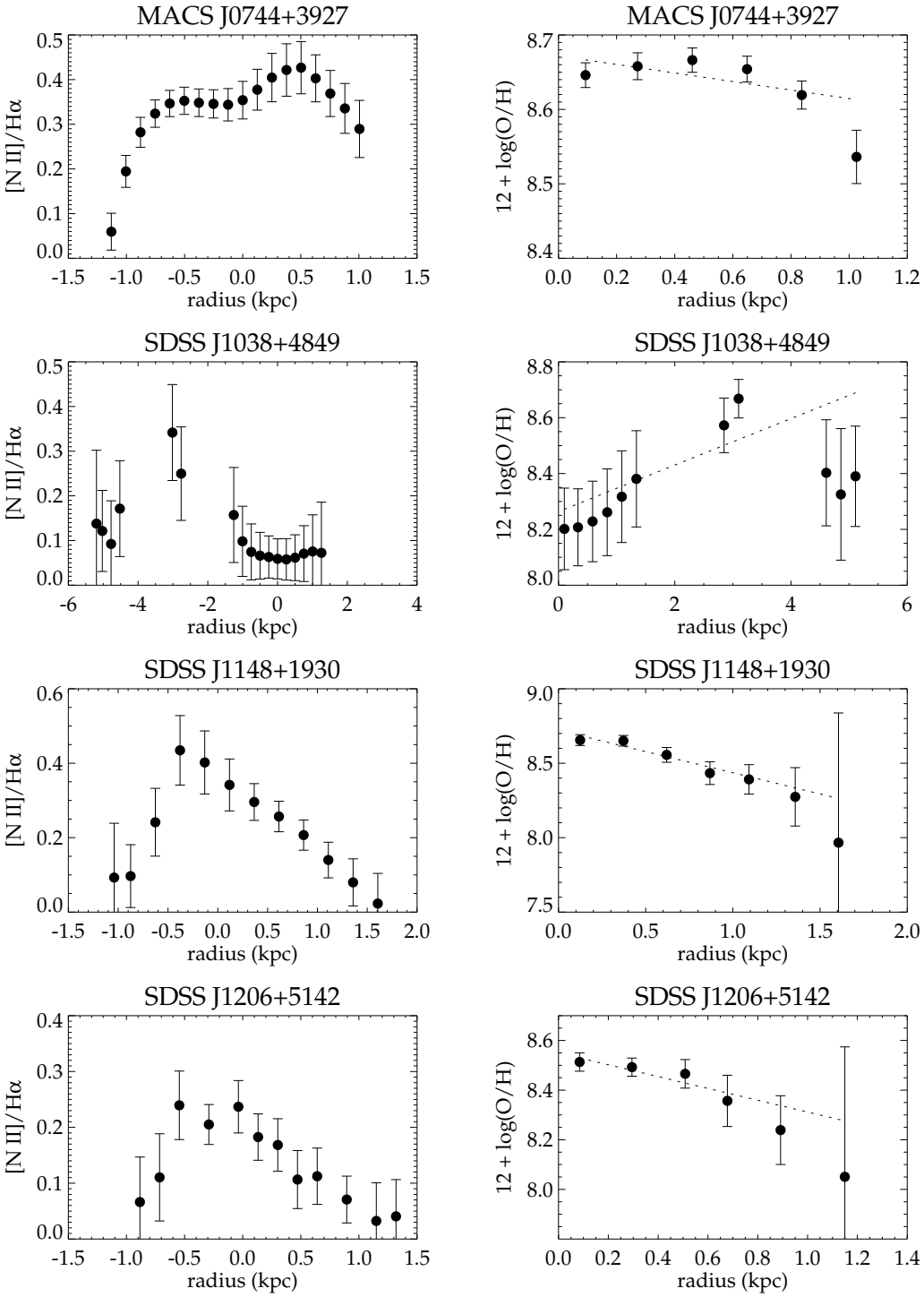

Figure 3.6: Metallicity gradients of the lensed galaxies. Left: [NII]/Hα ratio as a function of radius. Right: Gas-phase metallicity as a function of radius derived from the N2 index calibration of Pettini & Pagel (2004). Dashed lines show the best fit linear metallicity gradient. [NII]/Hα ratios are extracted along the kinematic major axis using the same slit as for the right panels of Figure 3.3.

Name	$12 + \log$ O/H (N2, PP04)	N2 PP04 (dex/kpc)	N2 M+08 (dex/kpc)	O3N2 PP04 (dex/kpc)	O3N2 M+08 (dex/kpc)	O3HB M+08 (dex/kpc)
J0744	8.67 ± 0.18	-0.06 ± 0.04	-0.13 ± 0.05	0.02 ± 0.04	0.02 ± 0.04	0.10 ± 0.07
J1038	8.26 ± 0.19	0.08 ± 0.03	0.15 ± 0.07	0.25 ± 0.07	0.31 ± 0.08	0.37 ± 0.09
J1148	8.72 ± 0.18	-0.28 ± 0.05	-0.51 ± 0.11	-0.33 ± 0.12	-0.37 ± 0.11	-0.37 ± 0.19
J1206	8.55 ± 0.18	-0.25 ± 0.06	-0.45 ± 0.08	-0.40 ± 0.08	-0.46 ± 0.08	-0.40 ± 0.11

Table 3.5: Metallicity gradients derived from different strong-line diagnostics shown in Figure 3.7. Best-fit central metallicity is given in the second column.

while the peak of IRAC 3.6μm flux (at $R = 5$ kpc) has marginally higher $12 + \log O/H = 8.4$. The third component, located between the first two (at $R = 3$ kpc) has the highest measured metallicity.

We now quantify the radial metallicity gradient of each source in order to compare the results with other samples. Gradients in local galaxies are commonly expressed as a linear relation in units of dex/kpc. We compute the best linear fit to $12 + \log O/H$ as a function of radius using a weighted least-squares method. The best fit relations are shown as dashed lines in Figure 3.6 (right panels) and provide a reasonable fit to the data with reduced χ^2 values of $0.3-2.3$, although we note that the linear fits overpredict metallicity at the largest radii in all sources. The best-fit central metallicity and gradient of each source is listed in Table 3.5.

To examine whether these results might be affected by systematic calibration errors, we compute the metallicity gradient in the exact same manner using different strong-line metallicity diagnostics. In Figure 3.7 we show the radial metallicity profiles determined from all available calibrations described by Pettini & Pagel (2004) and Maiolino et al. (2008) as well as their best-fit linear gradients. We note that J1206 is assumed to have a constant Hα/Hβ ratio, that [OIII] and Hβ in J1038 were only observed in the region corresponding to $R < 4$ kpc, and that [OIII] and Hβ are only detected with sufficient signal-to-noise at $R < 1$ kpc in J1148. We further assume a constant Hα/Hβ ratio for J0744 since Hβ is detected in only a few pixels. Systematic offsets between the various calibrations are apparent in Figure 3.7, but in general the different methods agree given their intrinsic scatter. We give the best-fit gradients in Table 3.5. In most cases the resulting gradients are *stronger* than that for our adopted N2 calibration, and in all cases the uncertainty is larger. Importantly, [OIII]-based calibrations (including O3HB which is independent of N2) confirm that line ratio gradients are due to metallicity gradients rather than N/O abundance or other effects. The exception is J0744 for which [OIII] and Hβ ratios suggest a positive metallicity gradient. Overall, the different metallicity derivations are in reasonable agreement, albeit with large uncertainties due to both low signal-to-noise and intrinsic scatter in the calibrations. In the following sections we will consider the N2-based gradients of each galaxy to be the most accurate.

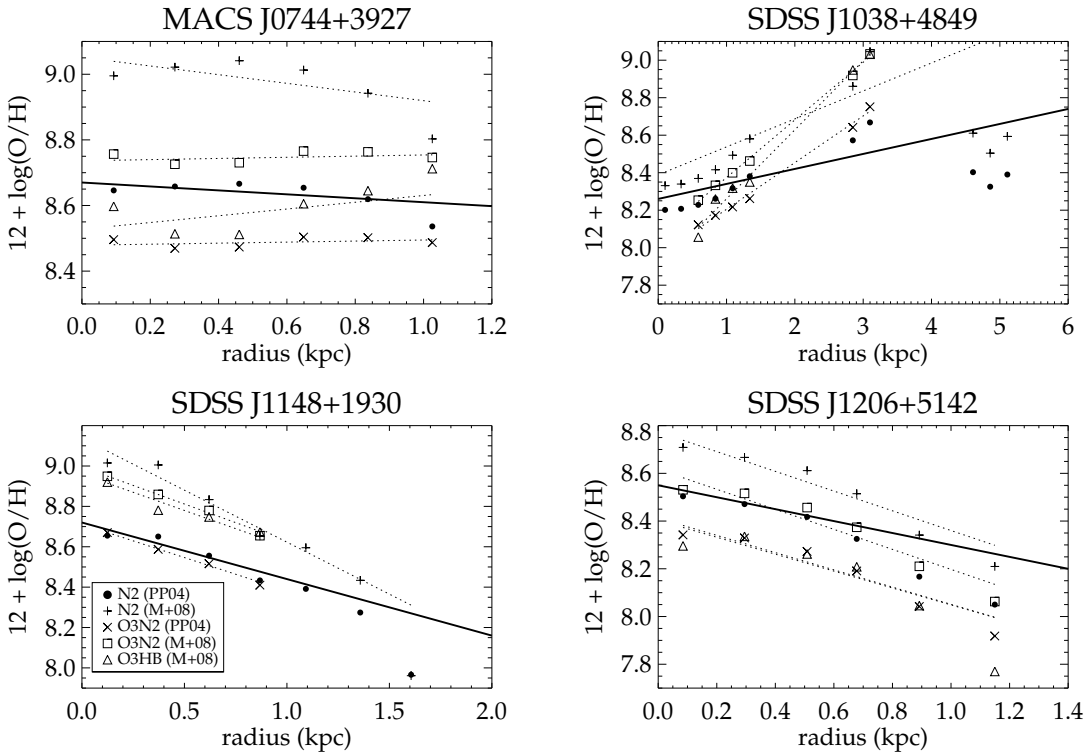

Figure 3.7: Metallicity gradients for each galaxy in our sample based on the use of various strong-line diagnostics. N2, O3N2, and O3HB are as presented in Figure 3.5, and we use the calibrations of Pettini & Pagel (2004) (PP04) and Maiolino et al. (2008) (M+08). Solid lines show the gradient from Figure 3.6 and dotted lines are the best fits to the other diagnostics. For J0744 and J1206, we estimate Hβ from Hα with the global Hα/Hβ ratio. In nearly all cases the gradients are approximately equal to or stronger than the adopted value (N2, PP04). The exceptions are the [OIII]-based results for J0744 which suggest a flat or inverted gradient, although all slopes are within 2σ of the adopted value.

3.4.2 Evolution with Redshift

The metallicity gradients we have determined for our lensed sample can now be compared to those for galaxies at different redshifts. Figure 3.8 shows a comparison with other measurements reported in the literature. It is instructive to separate the sample according to whether the galaxies are isolated or interacting. Figure 3.8 demonstrates that interacting galaxies tend to have flatter gradients and lower central metallicity. Two of the lensed $z \sim 2$ sources, J1148 and J1206, have gradients < -0.2 dex/kpc which are significantly steeper than those found in local massive disk galaxies. The only local galaxies in Figure 3.8 with similar or steeper gradients are barred spiral starbursts from Considère et al. (2000) and dwarf galaxies from Vila-Costas & Edmunds (1992). J0744 has a gradient typical of local disk galaxies. The merging galaxy J1038 has an "inverted" gradient (> 0 dex/kpc) - a phenomenon which has also been observed in local mergers (Rich et al., 2012) and high-redshift sources (Cresci et al., 2010; Queyrel et al., 2012).

Although the overall sample size is still limited, it appears that the metallicity gradients vary systematically with redshift and here we seek to quantify this evolution. However, before doing so, it is important to consider how best to compare galaxies at different redshifts in a consistent manner. One way to proceed is to determine the approximate stellar mass that the lensed galaxies will have at different cosmic epochs based on halo abundance matching techniques. This enables us to select a comparison sample with stellar masses approximately equal to the value inferred for the lensed galaxies at that redshift. The first step in this process is to estimate the halo mass for our lensed galaxies. Several groups have studied the stellar to halo mass ratio and its variation with redshift by combining cosmological simulations with measured stellar mass functions (e.g., Yang et al. 2011; Conroy & Wechsler 2009; Moster et al. 2012). We use the results of Moster et al. (2012) to do this and report the values in Table 3.4. We calculate the corresponding halo mass at different redshifts by integrating the mean halo growth rate determined by Fakhouri et al. (2010), and determine the stellar mass at these redshifts via the Moster et al. (2012) formalism. Next we must determine galaxy stellar masses for the comparison samples. For the MASSIV sample, we use the stellar masses derived by Queyrel et al. (2012). For all other comparison samples at $z \simeq 0$, we extract broadband $B - V$ color and absolute luminosity (M_B and/or M_K) from the NASA Extragalactic Database and calculate the stellar mass using the mass-to-light ratio formulae from Torres-Flores et al. (2011). Finally, we construct two separate comparison samples appropriate for (1) isolated and (2) interacting galaxies. For isolated galaxies we choose a stellar mass range corresponding to $M_* = 10^{9.7\pm0.5}$ at $z = 2.2$; the isolated lensed galaxies are all within 0.3 dex of this value. The stellar mass range for interacting galaxies corresponds to that of J1038. We show the metallicity gradients of each comparison sample as a function of linear cosmic time and equivalent redshift in Figure 3.9.

Figure 3.9 shows a clear trend in metallicity gradients with time (or redshift) for our sample of

galaxies which occupy similar dark matter halos. The scatter at a given redshift presumably reflects the degree of intrinsic variation within the population. To investigate this with more clarity, we show in Figure 3.10 the mean and 1σ scatter of each isolated galaxy comparison sample. Considering only the $z \geq 2$ and $z \sim 0$ data in Figure 3.10, we can see that the average metallicity gradient becomes flatter with time although the intrinsic scatter is similar to the average gradient. However, data at $z \sim 1.2$ from the MASSIV survey do not support this picture; instead they show a mean gradient $\simeq 0$ with relatively low scatter of ~ 0.05 dex. This discrepancy is puzzling and warrants further investigation. Formally the mean metallicity gradient for the samples shown in Figure 3.10 is -0.20 ± 0.07 at $z = 2.2$, 0.005 ± 0.011 at $z = 1.2$, and -0.077 ± 0.005 at $z = 0$. The local data and lensed galaxies suggest that on average, metallicity gradients have declined by a factor of 2.6 ± 0.9 in the past 10 Gyr. Naturally metallicity gradients as steep as -0.2 dex/kpc cannot be common in massive galaxies at $z \simeq 0$ simply because of their size. In the Milky Way, solar metallicity at $R = 8$ kpc would imply $40\times$ solar metallicity in the center with such a gradient.

We now consider the effect of "inside-out" size growth. Supposing that the relative metal enrichment at the center and effective radius R_e of a galaxy remains constant with time, the gradient will scale as $1/R_e$ and will flatten with time as the radius increases. van Dokkum et al. (2010) have measured the size of massive galaxies selected to have a fixed number density at different redshifts (equivalently, approximately the same halos), and find $R_e \propto (1+z)^{-1.27}$. We show the appropriate change in metallicity gradient ($\propto (1+z)^{1.27}$) in Figure 3.10, and find that it is within 1σ of the Milky Way and $z = 0$ data. However, the galaxies used to determine this size growth are significantly more massive (by 0.7 dex at $z = 0$) than the metallicity gradient sample and likely grow at a different rate. Adopting the same functional form $R_e \propto (1+z)^{-\alpha}$, the lensed galaxies must grow in size with $\alpha = 0.8 \pm 0.4$ (cf. $\alpha = 1.27$ from van Dokkum et al. 2010) to match the $z = 0$ comparison sample mean. Metallicity gradients should therefore flatten with time as a natural consequence of inside-out growth, and the amount of size growth required is in rough agreement with direct measurements.

3.5 Chemical Evolution Model

As we have seen a first clear trend of flattening in the metallicity gradients for comparable systems with cosmic time, we seek now to develop a physically-motivated explanation of the trend. Our purpose in this section is to explain the metallicity of a star-forming system (specifically a galaxy or a region within a galaxy) in terms of gas accretion, outflows, and star formation. The simplest such model is the "closed box" in which accretion and outflow rates are both zero. In this case the gas-phase metal mass fraction Z is determined entirely by the yield y and gas fraction $f_{\rm gas}$ as

$$Z = y \ln f_{\rm gas}^{-1} \tag{3.8}$$

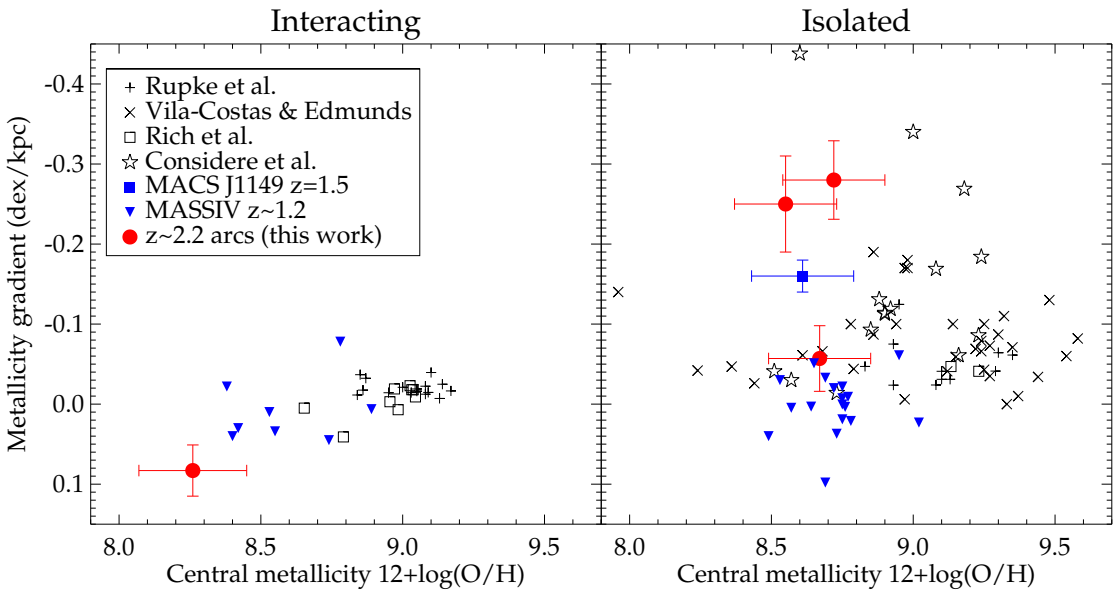

Figure 3.8: Metallicity gradients of the lensed galaxies compared with various other published samples (Rupke et al. 2010b; Vila-Costas & Edmunds 1992; Rich et al. 2012; Considère et al. 2000; MACS J1149: Yuan et al. 2011; MASSIV: Queyrel et al. 2012). The plot is divided into interacting (or merging) systems and isolated galaxies. All data points at high redshift are shown as filled color symbols. Interacting galaxies have generally lower metallicities and relatively flat or inverted gradients ($\lesssim -0.05$ dex kpc^{-1}) compared to isolated galaxies.

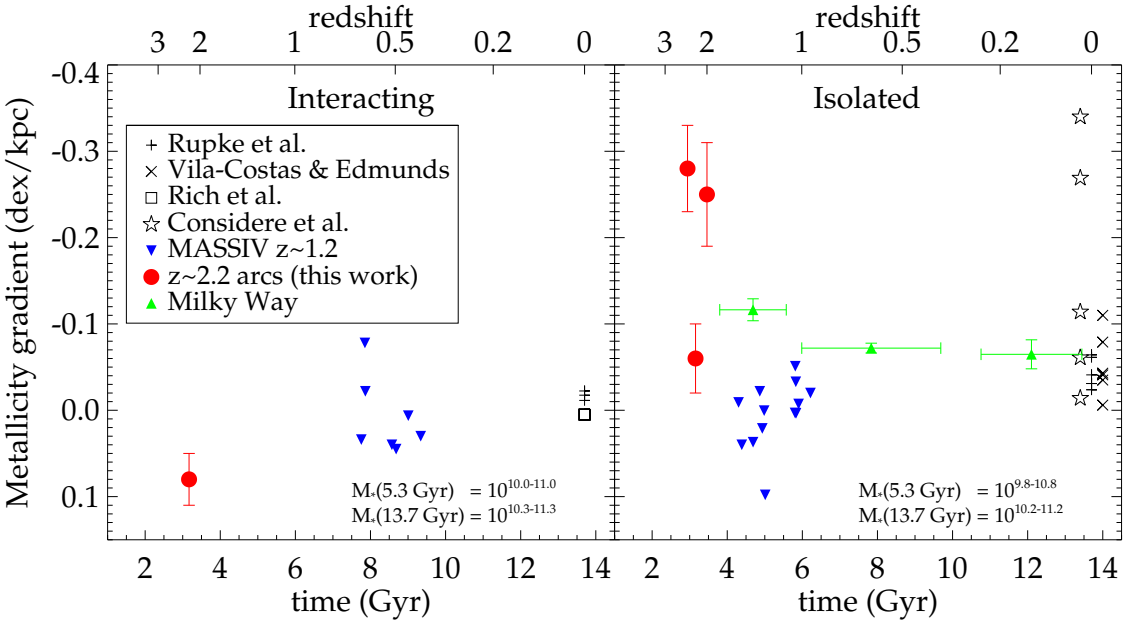

Figure 3.9: Metallicity gradients of the lensed galaxies (red circles) compared to equivalent samples at other redshifts. The x-axis is linear in cosmic time with corresponding redshifts shown on the upper axis. The galaxies shown here are a subset of those in Figure 3.8 and symbols are identical. Comparison samples are selected to occupy the same dark matter halos as the lensed galaxies based on galaxy stellar mass; the corresponding stellar masses at $z = 1.2$ and $z = 0$ are noted at the bottom right of each panel. Samples at $z = 0$ are plotted with slight offsets in redshift for ease of viewing. We also show the time evolution of the Milky Way metallicity gradient measured by Maciel et al. (2003) in the appropriate panel.

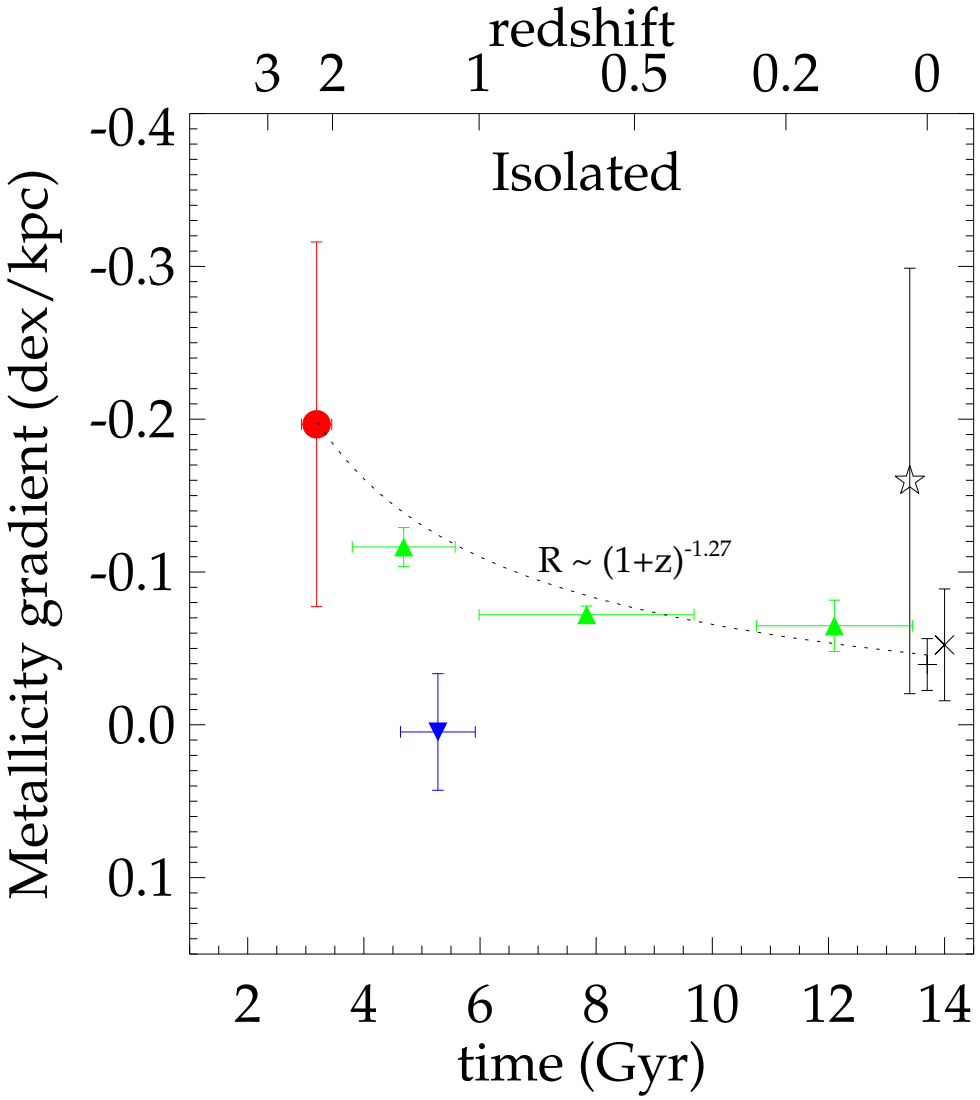

Figure 3.10: Equivalent to the right panel of Figure 3.9, showing the mean values of each sample. Error bars denote the 1σ dispersion within each sample. The dotted line shows how gradients will evolve with time if the range of metallicity remains constant while the characteristic radius grows as $R \propto (1+z)^{-1.27}$ as determined by van Dokkum et al. (2010), scaled to match the lensed galaxies at $z = 2.2$.

(Schmidt, 1963). This can be equivalently expressed in terms of the oxygen number abundance,

$$12 + \log O/H = 12 + \log \frac{y_0}{11.728} + \log \left(\ln f_{\rm gas}^{-1}\right) \tag{3.9}$$

where y_0 is the oxygen yield and the factor 11.728 converts oxygen mass abundance to number abundance (Lee et al., 2006). Throughout this paper we assume a value $y_0 = 0.0087$, appropriate for solar abundance ratios with $y = 0.02$ (Finlator & Davé, 2008).

We now construct a model which includes accretion and outflow of gas. The star-forming system which we model has the following properties: a gas mass M_g, stellar mass M_*, star formation rate SFR$= \dot{M}_*$, total mass of metals in the gas M_Z, and metallicity defined as $Z_g = M_Z/M_g$. We consider four factors which affect the metallicity at a given time:

1. *Inflowing gas.* The gas inflow rate is assumed to be a constant multiple f_i of the star formation rate, $\dot{M}_i = f_i \dot{M}_*$. Inflowing gas is assumed to be metal-free ($Z = 0$) corresponding to pristine gas accreted from the intergalactic medium.

2. *Transported gas.* In addition to inflow $\dot{M}_i$, we assume that some accreted gas is already enriched with a metallicity $Z = Z_g$ and accreted at a constant multiple of the star formation rate, $\dot{M}_{en} = f_{en}\dot{M}_*$. If the system considered is a region within a galaxy, then this term corresponds to the transportation of metal-enriched gas within the galaxy. If the system is a galaxy, this can be thought of as a "galactic fountain" term which describes the re-accretion of gas which has been expunged in outflows.

3. *Outflowing gas.* Outflows are a vital component in any reasonable model of galaxy chemical evolution. Outflows are observed ubiquitously in galaxies with star formation rates $\gtrsim 0.1$ $\mathrm{M_\odot yr^{-1} kpc^{-2}}$ (Heckman, 2002) which is greatly exceeded by the lensed galaxies studied in this paper. The outflowing gas is assumed to have metallicity $Z = Z_g$ and a rate proportional to the SFR, $\dot{M}_o = f_o \dot{M}_*$. The ratio of outflow rate to SFR, f_o, is called the mass loading factor (MLF).

4. *Star formation.* Star formation is ultimately the source of all heavy elements. The amount of metals produced per unit time is defined as the yield multiplied by the star formation rate, $y\dot{M}_*$. Star formation additionally removes metals from the gas reservoir at a rate $Z\dot{M}_*$.

We additionally assume that the gas mass remains constant. With these definitions, the metallicity is expressed as

$$\begin{aligned} 12 + \log O/H =& 12 + \log \frac{y_0}{11.728} - \log\left(1 + f_o'\right) \\ &+ \log\left[1 - \exp\left(-(1 + f_o')\frac{1 - f_{\rm gas}}{f_{\rm gas}}\right)\right] \end{aligned} \tag{3.10}$$

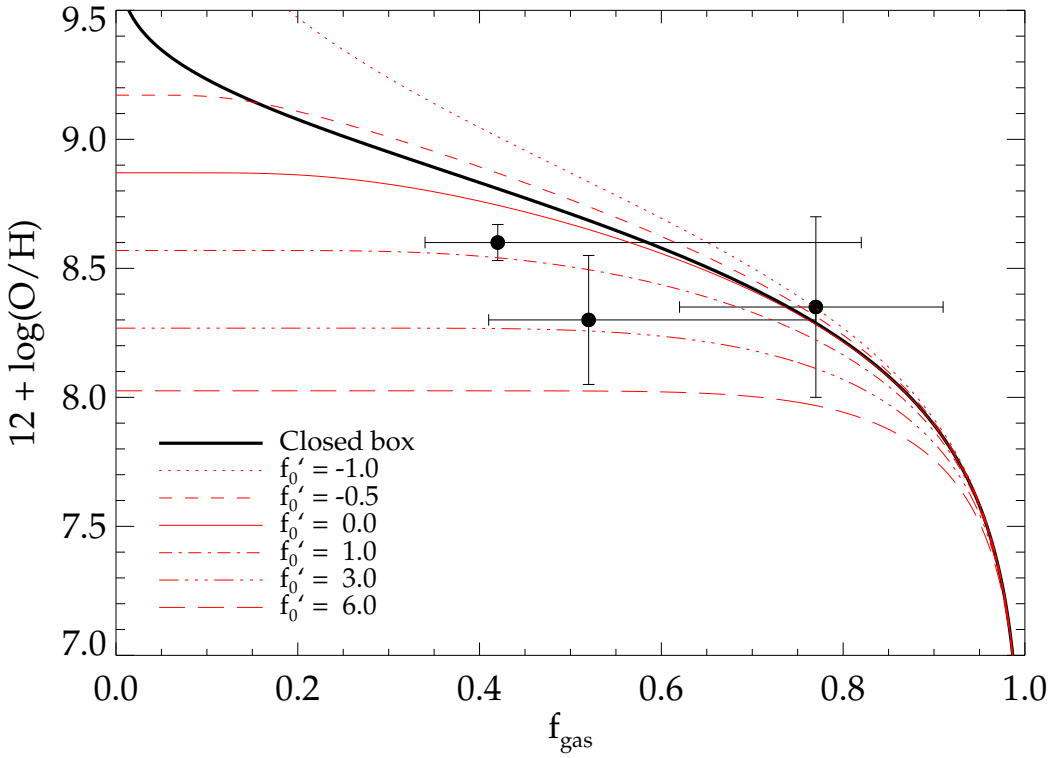

Figure 3.11: Gas phase metallicity as a function of gas fraction. We show predictions from our chemical evolution model as well as the closed box model. Data points correspond to measured values of the galaxies J0744, J1148, and J1206.

where we define the "effective mass loading factor" (EMLF) $f'_o = f_o - f_{en}$. (A complete derivation of Equation 3.10 is provided in Appendix A, along with an assessment of the assumptions made.) Therefore, our model provides the gas phase metallicity as a function of EMLF and gas fraction. Equivalently, f'_o can be determined from measurements of metallicity and gas fraction. We show the results of this model for various values of f'_o in Figure 3.11 along with measurements of the lensed galaxies.

3.5.1 f'_o as the Origin of Metallicity Gradients

The presence of metallicity gradients in local disk galaxies is typically attributed to variations in the mass loading factor with radius and/or inward radial migration of metal-enriched gas. Both of these physical effects can be expressed as a variation of f'_o with radius, where negative metallicity gradients imply that f'_o increases with radius. In Appendix A we derive the relation between gradients in metallicity and f'_o, and here we apply these findings to the lensed galaxies. Equation 3.21 shows that a gradient in f'_o (expressed as $\Delta_R = \frac{df'_o}{dR}$) naturally gives rise to a metallicity gradient $\Delta_Z =$

$\frac{d}{dR}(\log O/H)$. For fiducial lensed galaxy values $f_{\rm gas} \simeq 0.5$ and $f'_o \simeq 2$, the relation is given by

$$\Delta_Z = -0.12\Delta_R$$

dex. A gradient $\Delta_R = 0.5 - 2$ kpc^{-1} can therefore explain the observed metallicity gradients of the isolated galaxies (Table 3.5), and the merger J1038 requires $\Delta_R = -0.7$ kpc^{-1} to explain the inverted gradient.

Let us now consider the evolution of such a gradient with time under the assumption that the gas fraction does not vary significantly with radius. In this case the time derivative $\frac{d\Delta_Z}{dt}$ is given by Equation 3.22. An important qualitative feature of this equation is that $\frac{d\Delta_Z}{dt}$ is *negative* if $\frac{d\Delta_R}{dt} \geq 0$, in which case metallicity gradients will become stronger with time. This is easily understood in terms of Figure 3.11. Physically, we have assumed that the gas fraction is constant throughout a galaxy and declines monotonically with time. As f_{gas} decreases, the difference in metallicity between two regions with different f'_o will become larger and hence gradients will become more pronounced. However, it is unlikely that Δ_R increases with time. For example, taking a typical value $f'_o = 2$ at a radius $R = 1$ kpc, the eventual metallicity is only $12 + \log O/H = 8.4$ or about half the solar value. Descendents of these lensed galaxies typically have super-solar metallicity at such small radii, implying that f'_o must decrease at later times. The required decrease in mass loading factor can be quantified from the observational constraint that $\frac{d\Delta_Z}{dt} \lesssim 0.05$ dex kpc^{-1} Gyr^{-1} (Figure 3.10). Using fiducial values for the lensed galaxies $f_{\rm gas} \simeq 0.5$, $f'_o \simeq 2$, $\dot{M}_* \simeq 100$ M$_\odot$yr^{-1}, $M_{\rm gas} \simeq 2 \times 10^{10}$ M$_\odot$, and $\Delta_R \simeq 2$ kpc^{-1}, Equation 3.22 implies that $\frac{d\Delta_R}{dt} \simeq -4$ kpc^{-1} Gyr^{-1}. Therefore the effective mass loading factor must decrease on a time scale $t_1 = \Delta_R\,(\frac{d\Delta_R}{dt})^{-1} \sim 500$ Myr, comparable to the characteristic age of recent star formation in the lensed galaxies. This result suggests that a phase of strong starburst-driven outflows with high mass loading factors lasts only a few hundred Myr, which matches the duty cycle of strong star formation in LBGs inferred from statistical studies (e.g., Stark et al. 2009).

In summary, we have used the chemical evolution model to show that a radial gradient in the effective mass loading factor Δ_R produces a metallicity gradient. The observed time evolution of metallicity gradients requires that Δ_R must decrease with time, and the characteristic starburst-driven outflow time scale from our model (~ 500 Myr) is in rough agreement with the duty cycle of star formation inferred from statistical measurements of high redshift LBG demographics.

3.6 Discussion

We now discuss what can be learned physically about the mass assembly in $z \simeq 2$ galaxies by applying the model discussed in §3.5 to measurements of the galaxies in our sample.

3.6.1 Mass Loading Factor

The mass loading factor, defined as the ratio f_o of mass outflow rate to star formation rate, is an important ingredient of galaxy formation models. Our simple chemical evolution model can be used to infer f_o from measurements of metallicity and gas fraction via Equation 3.10. We apply this equation to the integrated values of the lensed galaxies (Table 3.4) and list the resulting effective mass loading factors f'_o in Table 3.6. Assuming that accreted gas has an average metallicity significantly lower than that of the galaxies, we set $f_{en} \approx 0$ and equate $f'_o = f_o$ (see discussion in §A.1). Therefore, the model implies a modest mass loading factor $f_o < 2.3$ for all three galaxies studied in detail here.

In the case of J1148, we can estimate the true mass loading factor from direct measurements of the outflow column density. Quider et al. (2009) measure a column density $\log N_{\rm SiII} = 16$ cm^{-2} in the outflowing gas. The SiII/SiIV ratio is $\simeq 12$ suggesting that most of the outflowing mass is in neutral hydrogen gas traced by SiII. Motivated by our chemical evolution model and the results discussed later in this section (cf. Figure 3.12), we assume that most of the outflow occurs at large radius with metallicity $12 + \log O/H \sim 8.1$ (Figure 3.6) or [O/H] ~ -0.6. Since O and Si are both α elements generated by the same nucleosynthetic processes, we assume that [Si/H] ~ -0.6 as well. Indeed, Pettini et al. (2002) show that variation in α element abundances is < 0.2 dex in the ISM of the Lyman break galaxy cB58. Adopting a solar abundance ratio $[{\rm O/H}]_\odot = -4.44$ (Pettini et al., 2002) gives an outflow column density $\log N_H = 21.0$ cm^{-2}. This corresponds to a total mass column density (including Helium) $\Sigma_{M_o} = 1.1 \times 10^7$ M$_\odot$kpc^{-2}. We can crudely estimate the total mass assuming that outflowing gas uniformly fills a sphere of radius R:

$$M_o = \frac{4}{3}\pi R^2 \Sigma_o \sim 3 \times 10^9 \ {\rm M}_\odot$$

for $R = \Delta v M_*/\dot{M}_* \sim 8$ kpc, outflow velocity $\Delta v = 200$ km s^{-1}(Quider et al., 2009), and timescale $M_*/\dot{M}_* = 40$ Myr (Table 3.6). The time-average mass loading factor is then given by $f_o = M_o/M_* \sim 0.4$. Uncertainty in f_o due to the assumed geometry is approximately an order of magnitude, such that we can confidently assert that $f_o \leq 5$ in reasonable agreement with the value derived from our chemical evolution model.

We now turn to spatial variations in the mass loading factor, and radial gradients in particular. Gas fractions in the lensed galaxies have almost no variation with radius, and therefore we can apply the formalism developed in §3.5.1 to estimate Δ_R, $\frac{d\Delta_R}{dt}$, and the characteristic timescale t_1. The results are listed in Table 3.6. We also give the mass assembly timescale $M_*/\dot{M}_*$. We can compare the simple analytic treatment of §3.5.1 with variations in f'_o inferred directly from spatially-resolved measurements via Equation 3.10. We use the measured radial profiles of gas fraction and metallicity to compute f'_o, and show the results in Figure 3.12. As expected, f'_o increases at large radii. The analytic approximation Δ_R is in reasonable agreement with a linear fit to the data, although the

measured radial gradient of f_o' is poorly represented by a straight line. Metallicity gradients observed in the lensed galaxies are therefore likely to originate from radial variations of the effective mass loading factor.

3.6.2 Inflow Rate

Under the equilibrium condition that the gas mass remains constant, the inflow rate is directly related to star formation rate and mass loading factor via Equation 3.13. When considering a galaxy as a whole, f_{en} is negligible and thus $f_i = 1 + f_o$, or $\dot{M}_i = (1 + f_o)\dot{M}_*$. We calculate $\dot{M}_i$ using the relevant values in Tables 3.4 and 3.6 and list the results in Table 3.6. Infall rates range from $1.2 - 2.0\times$ the star formation rate.

3.6.3 Radial Gas Transport

We have suggested that radial metallicity gradients are caused by gradients in the effective mass loading factor. Negative gradients can be caused by increasing mass loading factor with radius ($\frac{df_o}{dR} > 0$), by radial transport of enriched gas ($\frac{df_{en}}{dR} < 0$), or both. The degeneracy between f_o and f_{en} captured by Equation 3.15 essentially means that the chemical evolution model cannot distinguish the contributions of outflow and gas transport. However, in cases where $f_o' < 0$, gas transport is necessarily present. Figure 3.12 shows that the inner regions of J1148 are inferred to have $f_o' < 0$ with $\sim 2\sigma$ significance from uncertainty in the gas fraction, although the significance is marginal when considering a number of other assumptions made (e.g., the Schmidt relation, constant mass-to-light ratio, and the model itself). Nonetheless the high metallicity and high inferred gas fraction suggest that gas in the inner regions of J1148 has likely been enriched by previous star formation episodes at larger radii. This observation, combined with the clumpy structure and low $Q \lesssim 1$ of J1148, are in qualitative agreement with the model of Dekel et al. (2009) in which gravitational instability leads to the formation of giant clumps which migrate into the galactic center in $\lesssim 500$ Myr.

We reiterate that this result depends crucially on the gas fraction, which we have estimated using the Kennicutt-Schmidt law. Future measurements of the gas density, e.g., with ALMA, are needed for direct verification.

3.6.4 Positive Metallicity Gradients

In the local universe, disk galaxies almost invariably show negative metallicity gradients. Only a few positive gradients have been measured, all of which are relatively shallow (< 0.05 dex/kpc) and found exclusively in merging systems (see Figure 3.8). In contrast, *positive* metallicity gradients have been claimed for some high redshift galaxies, including many with no signs of recent interaction

Name	12+log O/H	f'_o	Δ_R (kpc^{-1})	$\frac{d\Delta_R}{dt}$ ($\mathrm{kpc}^{-1}\mathrm{Gyr}^{-1}$)	t_1 (Myr)	$M_*/\dot{M}_*$ (Myr)	model $\dot{M}_i$ ($\mathrm{M}_\odot\mathrm{yr}^{-1}$)
J0744	8.65	$0.4^{+0.2}_{-1.4}$	0.29	-0.38	760	470	8
J1148	8.40	$-1.0^{+2.2}_{-0}$	4.8	-25	110	40	250
J1206	8.35	$2.1^{+0.2}_{-3.1}$	2.2	-4.8	450	190	140

Table 3.6: Properties inferred from the chemical evolution model. Effective mass outflow rates and uncertainties correspond to the formal uncertainties in gas fraction for the tabulated value of $12 + \log O/H$. Δ_R, its derivative, and t_1 are calculated from f'_o except in the case of J1148 where we use $f'_o + \sigma = 1.2$.

or merging (Cresci et al., 2010; Queyrel et al., 2012). In the lensed sample we find that all three isolated galaxies have negative gradients, while the merging system J1038 has a positive gradient. What could explain these claimed positive gradients at high redshifts? Cresci et al. (2010) and Queyrel et al. (2012) have suggested they could be caused by high accretion rates of metal-poor gas which occur only at high redshift or during mergers. Even so it is difficult to form a positive gradient since the fraction of gas converted into stars per unit time must *increase* with radius, while the dynamical time scale generally decreases with radius. The corollary is that a higher fraction of metal-enriched gas must be lost to outflows at small radii, or in terms of our chemical evolution model, f_o must decrease with radius. While gaseous infall is notoriously difficult to detect at high redshift, outflows are relatively easy to detect and in principle f_o can be estimated as a function of radius following the method of §3.6.1. Current planned and ongoing observations will directly address the variation of f_o with radius in high redshift galaxies and determine whether this is a viable mechanism of producing positive metallicity gradients (see §3.6.5).

Alternatively, it is possible that many of the positive (and negative) gradients reported at high redshift are a result of systematic errors rather than actual metallicity gradients. In this paper we have primarily used the ratio of [NII]/Hα as a proxy for metallicity, however this alone is not convincing because of the issues discussed in §4.4.1. For example, Wright et al. (2010) describe a galaxy with strong radial line ratio gradients which mimic a negative metallicity gradient in [NII]/Hα and a positive gradient in [OIII]/Hβ. Using the diagnostic diagram of Figure 3.4, however, Wright et al. (2010) show that these are caused by a central AGN surrounded by an extended star-forming disk rather than a metallicity gradient. In the local universe, Westmoquette et al. (2012) find that [NII]/Hα increases with radius in 7/18 galaxies in their volume-limited sample and show, via measurements of [SII] and [OI] emission, that these are caused by an ionization parameter gradient. The most likely explanation is an increasing contribution of shocks at large radius rather than a positive metallicity gradient. Therefore it is known that the line ratio signatures of both positive and negative metallicity gradients are mimicked by AGN and shocks, and we caution that gradients based on strong line ratios are not reliable unless confirmed with multiple appropriate diagnostics (e.g., Figures 3.4 and 3.7).

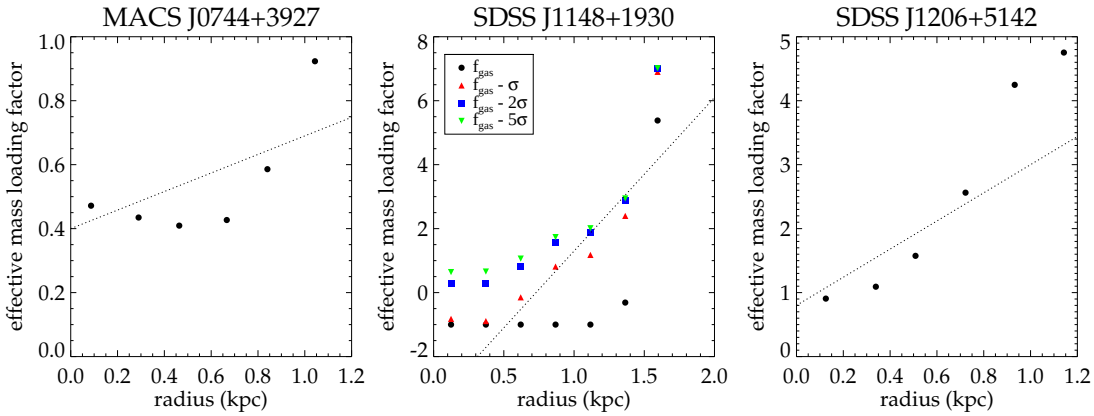

Figure 3.12: Effective mass loading factor f_o' vs. radius. f_o' is calculated from Equation 3.10 and is shown to increase with radius. The measured gas fraction and metallicity of J1148 is unphysical at $R < 1$ kpc in the context of our chemical evolution model, and so we also show the results of perturbing the gas fraction by multiples of the uncertainty $\sigma(f_{\rm gas}) = 0.15$. We note that the overall shape and normalization of $f_o'(R)$ is relatively constant over a range $\Delta f_{\rm gas} = 4\sigma = 0.6$; clearly Equation 3.10 is relatively insensitive to gas fraction in this regime. Dotted lines show the result from the simple analytic approximation described in §3.5.1 (see discussion in the text). For J1148 the analytic prediction applies to the case $f_{\rm gas} - \sigma$.

3.6.5 Future Work

The study of galaxy formation through time evolution of metallicity gradients is still in its infancy. Here we briefly discuss three areas of future work that will improve our understanding: the mass loading factor, sample sizes and redshift range, and gas fractions.

We have shown from simple chemical evolution arguments that metallicity gradients likely originate from radial gradients in the mass loading factor f_o. Figure 3.12 suggests that this quantity is several times higher at large radius ($R \gtrsim 1$ kpc for the lensed galaxies) than at the center. Furthermore, we have shown that a radially decreasing f_o can create the positive metallicity gradients observed at high redshift but for which there are no local analogs. While difficult to measure accurately, f_o can be estimated from rest-UV absorption lines as described in §3.6.1 and spatially resolved measurements can constrain its variation with radius. We are actively pursuing these measurements in lensed galaxies at $z \sim 2$ via an approved program with the Keck II/ESI integral field unit.

The sample of high redshift galaxies with robust metallicity gradient measurements remains very small. Although data exist for more than 30 galaxies at $z > 1$, the majority lack the data needed to distinguish true metallicity gradients from the signatures of shocks and AGN. Furthermore, different samples reported at $z > 1$ (Cresci et al. 2010; Yuan et al. 2011; Queyrel et al. 2012; this work) are discrepant and warrant further investigation. Additionally the range of redshifts $0.1 < z < 1$ has not yet been explored, and our data suggest that gradients should decrease in magnitude by a factor of $\simeq 2$ in this time (e.g., Figure 3.10). It is important to realize that highly multiplexed optical spectrographs can efficiently measure resolved emission line fluxes to large galactocentric radius in

statistically significant samples of galaxies out to $z \lesssim 1.7$ (Miller et al., 2011, 2012). This is an attractive means of procuring a large number of metallicity gradient measurements at intermediate redshifts $z \lesssim 1$, especially in tandem with multi-object near infrared spectrographs to detect Hα and [NII] at $z \gtrsim 0.5$, and we will exploit these capabilities in future work.

Finally, results from chemical evolution modeling are sensitive to the gas fraction which is difficult to measure at high redshift. In the present work we have estimated gas masses by inverting the Kennicutt-Schmidt relation, introducing a considerable degree of uncertainty. Gas mass is difficult to determine even with direct measurements and typically relies on an uncertain factor X_{CO} to convert a CO line luminosity to gas mass. With the advent of ALMA it is now possible to resolve the molecular gas emission in typical star forming galaxies at high redshift, and calibrate gas mass-to-luminosity ratios from independent dynamical measurements (e.g., Daddi et al. 2010; Stark et al. 2008). With such advances, we may be able to confidently determine resolved gas fractions in the near future.

3.7 Summary

This paper presents robust spatially resolved metallicity measurements of four lensed galaxies at $z = 2 - 2.4$ based on the strong emission lines Hα, [NII], [OIII], and Hβ. The combination of gravitational lensing and adaptive optics provides a source plane resolution of up to $300-600$ parsecs in each galaxy. Three targets are isolated rotating galaxies, and one is a merger of at least two systems with mass ratio $(6 \pm 3) : 1$. All three rotating galaxies have negative radial metallicity gradients inferred from the [NII]/Hα emission line ratio and confirmed with [OIII] and Hβ measurements. The merging system has a positive gradient in the UV-bright source, also confirmed with multiple emission line ratios.

Metallicity gradients measured at $z > 2$ are compared with galaxies at lower redshift selected to occupy equivalent dark matter halos. On average, gradients in the rotating galaxies must flatten by a factor of 2.6 ± 0.9 between $z = 2.2$ and $z = 0$. This factor is in rough agreement with size evolution measured for more massive galaxies by van Dokkum et al. (2010), hence radial inside-out growth can account for the variation in metallicity gradients with redshift.

We develop a simple model of chemical evolution to explain the emerging body of data. From a combination of spatially resolved gas fraction and metallicity, the model implies that metallicity gradients are caused by radial variation in the effective mass loading factor. The time-averaged mass loading factor is inferred to be $\lesssim 2$. Finally, inward radial gas transport is required to explain the high metallicity and gas fraction of J1148, and is likely present in the other galaxies although we cannot determine this directly from the model.

The study of metallicity gradients at different redshifts is still relatively new and robust sample

sizes are limited. Future work addressing direct measurements of the molecular gas content, metallicity gradients at intermediate redshifts ($0.2 \lesssim z \lesssim 1$), and direct, spatially resolved measurements of the mass loading factor are planned or ongoing. These new observations will confirm (or refute) the results of this paper and will place additional constraints on the formation of galaxies from the origin and evolution of metallicity gradients.

A Chemical Evolution Model

In this Appendix we provide the mathematical details of the chemical evolution model discussed in the text. All notation and definitions are the same as in §3.5. To begin, the combination of inflowing gas, transported gas, outflowing gas, and star formation as described in §3.5 gives a rate of change of metal mass

$$\frac{dM_z}{dt} = y\dot{M}_* - Z_g\dot{M}_* - Z_g\dot{M}_o + Z_g\dot{M}_{en}. \tag{3.11}$$

The gas mass is assumed to be constant, i.e.,

$$\dot{M}_g = \dot{M}_i + \dot{M}_{en} - \dot{M}_o - \dot{M}_* = 0 \tag{3.12}$$

or equivalently

$$f_i + f_{en} - f_o - 1 = 0. \tag{3.13}$$

Equation 3.11 therefore simplifies to

$$\frac{dM_z}{dt} = y\dot{M}_* - Z_g\dot{M}_* - Z_g f_o'\dot{M}_* \tag{3.14}$$

where we define the "effective mass loading factor" (EMLF) f_o' as

$$f_o' = f_o - f_{en}. \tag{3.15}$$

The rate of change of metallicity is

$$\frac{dZ_g}{dt} = \frac{d}{dt}\frac{M_Z}{M_g} = \frac{1}{M_g}\frac{dM_z}{dt} = \frac{\dot{M}_*}{M_g}(y - Z_g - Z_g f_o') \tag{3.16}$$

from Equation 3.14. Integrating with respect to time gives

$$-\frac{1}{1+f_o'}\ln\left(y - Z_g - Z_g f_o'\right) + \frac{1}{1+f_o'}\ln\left(y\right) = \frac{M_*}{M_g} = \frac{1-f_{\rm gas}}{f_{\rm gas}} \tag{3.17}$$

where we introduce the gas fraction defined in Equation 3.5 and apply the boundary conditions $Z_g = 0$ and $M_* = 0$ at time $t = 0$. With some algebra we obtain the desired expression for metallicity,

$$Z_g = \frac{y}{1+f_o'}\left[1 - \exp\left(-(1+f_o')\frac{1-f_{\rm gas}}{f_{\rm gas}}\right)\right]. \tag{3.18}$$

While Equation 3.18 contains all of the information needed, it is more convenient to express the metallicity in terms of 12+log(O/H). The equation then becomes

$$12 + \log O/H = 12 + \log \frac{y_0}{11.728} - \log\left(1 + f'_o\right) + \log\left[1 - \exp\left(-(1 + f'_o)\frac{1 - f_{\rm gas}}{f_{\rm gas}}\right)\right] \tag{3.19}$$

as given in the text.

We now derive the relation between gradients in metallicity and f'_o and their evolution with time. From Equation 3.19, metallicity varies with f'_o as

$$\frac{d}{df'_o}(\log O/H) = \frac{1 + x - \exp(x)}{\ln(10)(1 + f'_o)[\exp(x) - 1]} \tag{3.20}$$

where $x = (1 + f'_o)(1 - f_{\rm gas})/f_{\rm gas}$. This gives rise to a metallicity gradient of magnitude

$$\Delta_Z = \frac{d}{dR}(\log O/H) = \Delta_R \frac{d}{df'_o}(\log O/H) \tag{3.21}$$

where we define the f'_o gradient $\Delta_R = \frac{df'_o}{dR}$. A radial gradient in f'_o therefore naturally results in a non-zero metallicity gradient. It is instructive to examine the resulting evolution of metallicity gradients with time. Noting that the gas fraction was found to be approximately constant with radius in the lensed galaxies (§3.2.5), we make the simplifying assumption that $\frac{df_{\rm gas}}{dt} = 0$. In this case the rate of change of a metallicity gradient is given by

$$\begin{aligned}
\frac{d\Delta_Z}{dt} &= \frac{d}{dt}\Delta_R \frac{d}{df'_o}(\log O/H) \\
&= \Delta_R \frac{d^2}{dt\, df'_o}(\log O/H) + \frac{d\Delta_R}{dt}\frac{d}{df'_o}(\log O/H) \\
&= \Delta_R \frac{1}{\ln(10)}\frac{\dot{M}_*}{M_{\rm gas}}\frac{(1 - x)\exp(x) - 1}{[\exp(x) - 1]^2} + \frac{d\Delta_R}{dt}\frac{1 + x - \exp(x)}{\ln(10)(1 + f'_o)[\exp(x) - 1]}.
\end{aligned} \tag{3.22}$$

A.1 Validity of the Model

We now discuss important assumptions of the chemical evolution model, their validity, and quantify the implications for interpreting data using this model. There are several assumptions with which we are concerned.

Perhaps the most important assumption is that total gas mass is constant (Equation 3.12). Given that gas accretion and outflows are undoubtedly present, we expect the gas mass to fluctuate with time. However, we also expect the gas reservoir to be in equilibrium between accretion, star formation rate, and outflows. Cosmological simulations which incorporate outflows indeed show that the observed mass-metallicity relation and its dependence on star formation rate can indeed be explained in terms of such an equilibrium (e.g., Davé et al. 2011). In these simulations, departure

from this equilibrium gives rise to scatter about the observed mass-metallicity-SFR relation, which is measured to be only 0.05 dex in metallicity among local star-forming galaxies (Mannucci et al., 2010). Furthermore, if the gas mass remains constant, then the expected growth in stellar mass (see §3.4.2) results in gas fractions $f_{\rm gas} \simeq 0.03 - 0.15$ at $z = 0$ for the lensed galaxies. This is in good agreement with direct measurements of gas fractions in local galaxies with appropriate stellar masses $\log M_* \sim 10.7$ (e.g., Young & Scoville 1991). We therefore expect the assumption that $\dot{M}_g = 0$ to be approximately valid, resulting in an uncertainty of only $\simeq 0.05$ dex in 12+log(O/H).

Another critical assumption is that gas infall and outflow rates (f_i, f_o, f_{en}) are a constant fraction of the SFR. This is clearly not physically true; these rates should therefore be interpreted as a *time-averaged* value over the formation history of the galaxy rather than instantaneous rates. Observationally it is well known that nearly all galaxies observed at high redshift drive outflows of gas, while outflows are much less common in their descendants at $z \simeq 0$. Therefore f_o must decrease with time, while f_i and/or f_{em} must decrease accordingly to maintain equilibrium. Therefore we expect that model-inferred f_i, f_o, and f_{en} correspond to time-averaged values and are generally larger than the instantaneous rates.

We have assumed in the model that accreted gas is divided into two components with metallicity $Z = 0$ and $Z = Z_g$. This is entirely for ease of interpretation in the context of this paper. In reality accreted gas will most likely have an average metallicity within the range $0 < Z < Z_g$; the values of f_i and f_{em} can be adjusted to reach the desired value. However for our analysis it is more convenient to think of the accreted gas as a pristine cosmological component and an enriched component, as formulated. If the enriched component arises from metal transport within a galaxy, then the assumption $Z = Z_g$ is equivalent to the condition that metallicity is a continuous function of position. This is necessarily true. The assumption that infalling gas has $Z = 0$, however, is not true. The infalling gas will have a metallicity Z_i, introducing an additional term $+Z_i\dot{M}_i$ to the right side of Equation 3.14. Functionally this can be though of as a modification to the yield, such that the effective yield is

$$y_{eff} = y + f_i Z_i. \tag{3.23}$$

The IGM oxygen abundance is measured to be [O/H] $= -2.8$ at $z = 2.5$ (Simcoe et al., 2004) corresponding to $Z_i = 0.0015\,Z_\odot = 3 \times 10^{-5}$. For $y_0 = 0.0087$, the effect of IGM metallicity is negligible ($< 10\%$ of y_0) for $f_i < 30$. For an infall rate $f_i = 7$ corresponding to the highest acceptable value for the lensed galaxies (see Figure 3.11), the effective yield differs from y_0 by only 2.5%. For the redshifts and metallicities of interest in this paper, the assumption that accreted gas has $Z = 0$ therefore introduces a negligible systematic error of $\leq 2.5\%$ or ≤ 0.01 dex in metallicity.

In summary, the assumptions used in our chemical evolution model are in reasonable agreement with the best current data and understanding of galaxy formation and of the IGM. The systematic

uncertainties introduced by our assumptions are expected to be negligible (e.g., $\lesssim 0.05$ dex in metallicity). We caution that the inflow and outflow rates must be treated as time-averaged rather than instantaneous values. Values of f_o and f_i inferred from the model are expected to overestimate the current instantaneous rates.

Chapter 4

Rest-Frame Optical Spectroscopy of Gravitationally Lensed $1.5 < z < 3.5$ Galaxies

Abstract

We present and analyze near-infrared spectroscopy for a sample of 29 gravitationally lensed star-forming galaxies in the redshift range $1.5 < z < 3.5$, observed mostly with the Keck II and Palomar 200" telescopes. With typical magnifications of $\simeq$1.5-4 magnitudes, our survey provides a valuable census of star formation rates, gas-phase metallicities and dynamical masses for a representative sample of low luminosity galaxies seen at a formative period in cosmic history. At a fixed stellar mass we find higher metallicities in the lensed galaxies compared to earlier work that focused on more luminous systems at similar redshifts, especially at low stellar mass ($\sim 10^9$ $M_\odot$) where our sample is ~ 0.25 dex more metal-rich. We interpret this offset as a result of the lower star formation rates for a given stellar mass in the lensed galaxies. Taking this effect into account, we conclude that our objects are compatible at the 2σ level with a recently proposed fundamental metallicity relation.

1 Introduction

The period corresponding to the redshift range $2 < z < 4$ is a formative one in the history of star-forming galaxies. During this era, mass assembly proceeds at its fastest rate and the bulk of the metals that establish present-day trends are likely manufactured. Through comprehensive multi-wavelength surveys, much has been learned about the demographics of galaxies during this period (Shapley et al., 2003; van Dokkum et al., 2003; Chapman et al., 2005) as summarized in recent global measures (Hopkins & Beacom, 2006; Shapley, 2011).

Attention is now focusing on the detailed properties of selected star-forming sources in this redshift range. Near-infrared spectroscopy, sampling rest-frame optical nebular emission lines, defines the ongoing star formation rate and the gas-phase metallicity (Erb et al., 2006; Mannucci et al., 2009). Metallicity is a key parameter since it measures the fraction of baryonic material already converted into stars. Quantitative measures can thus be used to test feedback processes proposed to regulate star formation during an important period in cosmic history.

A fundamental relation underpinning such studies is the stellar mass-metallicity relation first noted locally by Lequeux et al. (1979) and recently quantified in the SDSS survey by Tremonti et al. (2004). The oft-quoted explanation for the relation invokes star formation driven outflows, e.g. from energetic supernovae, which have a larger effect in low stellar mass galaxies with weaker gravitational potentials. However, other effects may enter, particularly at high redshifts where star formation timescales and feedback processes and their mass dependence likely differ. With this motivation, much observational effort has been invested to measure *evolution* in the mass-metallicity relation with redshift. The relationship has now been defined using galaxy samples at redshifts up to $z \simeq 3.5$ (Lamareille et al., 2009; Pérez-Montero et al., 2009; Erb et al., 2006; Halliday et al., 2008; Hayashi et al., 2009; Mannucci et al., 2009). These pioneering surveys have demonstrated clear evolution with metallicities that decrease at earlier times for a fixed stellar mass.

Inevitably as one probes to higher redshift, it becomes progressively harder to maintain a useful dynamic range in the stellar mass and galaxy luminosity. In the case of most distant studies (e.g., Mannucci et al. (2009)), only with long integrations can the mass-metallicity relation be extended down to stellar masses of 10^9 $M_\odot$. Samples defined via searches through gravitational lensing clusters are a much more efficient probe of this important low mass regime. LBGs lensed by massive foreground clusters can be magnified by several magnitudes thereby enabling studies of intrinsically less massive systems. Initial results using this technique have been presented for small samples by Lemoine-Busserolle et al. (2003), Hainline et al. (2009) and Bian et al. (2010).

As part of a long-term program to determine the resolved dynamical properties of sub-luminous high redshift galaxies (presented in Chapter 2), we identified a large sample of gravitationally lensed systems with $z > 1.5$ in the HST archive (Sand et al., 2005; Smith et al., 2005; Richard et al., 2010b) and embarked upon a systematic spectroscopic survey with the Keck II Near Infrared Spectrograph (NIRSPEC) to determine their emission line characteristics. The initial motivation was to use the high efficiency of NIRSPEC to screen each target prior to more detailed follow-up with IFU spectrographs sampling the star formation rate and velocity field across each source (Jones et al. 2010a, Livermore et al. in preparation). However, a further product of this extensive spectroscopic survey is detailed information on the star-formation rate, emission line ratios, and line widths for a large sample of lensed $z > 1.5$ galaxies. Recognizing the utility of these data, we initiated a separate spectroscopic survey with the Palomar 200" telescope to observe a larger sample of strongly lensed

galaxies selected to have intrinsically low luminosity and stellar mass. Our ongoing Palomar survey uses Triplespec, a recently commissioned near-IR echelle spectrograph, which is ideal for this study thanks to its high throughput and simultaneous spectral coverage from $1-2.5$ μm. Our eventual sample presented here comprises 29 objects including 5 from the literature mentioned above. The goal of this work is to utilize this sample to extend studies of the mass-metallicity relation and related issues to more representative low luminosity galaxies at early times.

This chapter is structured as follows. Section 2 introduces our sample and discusses the various spectroscopic observations and data reduction as well as associated Spitzer data necessary to derive stellar masses. Section 3 discusses the mass-metallicity relation and the relationship between dynamical mass and stellar mass noting that a subset of our sample has more detailed resolved data (Jones et al. 2010a,b). We discuss the implications of our results in the context of measurements made of more luminous systems in Section 4.

Throughout this chapter, we assume a ΛCDM cosmology with $\Omega_\Lambda = 0.7$, $\Omega_m = 0.3$, and $h = 0.7$. For this cosmology and at the typical redshift $z \sim 2.5$ of our sources, $1''$ on sky corresponds to ~ 8.2 kpc. All magnitudes are given in the AB system.

2 Observations and Data Reduction

2.1 Lensed Sample

We selected a sample of lensed galaxies for spectroscopic observations using criteria similar to those used for for near-infrared spectroscopy of LBGs (e.g., Erb et al. 2006) but extended to lower intrinsic luminosities after correction for the lensing magnification. The relevant criteria are:

- Availability of optical data from the Hubble Space Telescope indicating a prominent rest-frame UV continuum with $V < 24$.
- Spectroscopic redshift $z > 1.5$ derived from the literature or as part of our Keck spectroscopic campaign (Richard et al., 2007, 2009, 2010b).
- An areal magnification factor $\mu \gtrsim 1.5$ mag provided by the foreground lensing cluster for which a well-constrained mass model enables a good understanding of the associated uncertainty (e.g., Richard et al. 2010b).
- Emission lines predicted to lie in an uncontaminated region of the near-infrared night sky spectrum.

The application of these criteria generated a list of ~ 50 arcs for further study with NIRSPEC. Following successful NIRSPEC observations, we began to follow up additional sources known to be

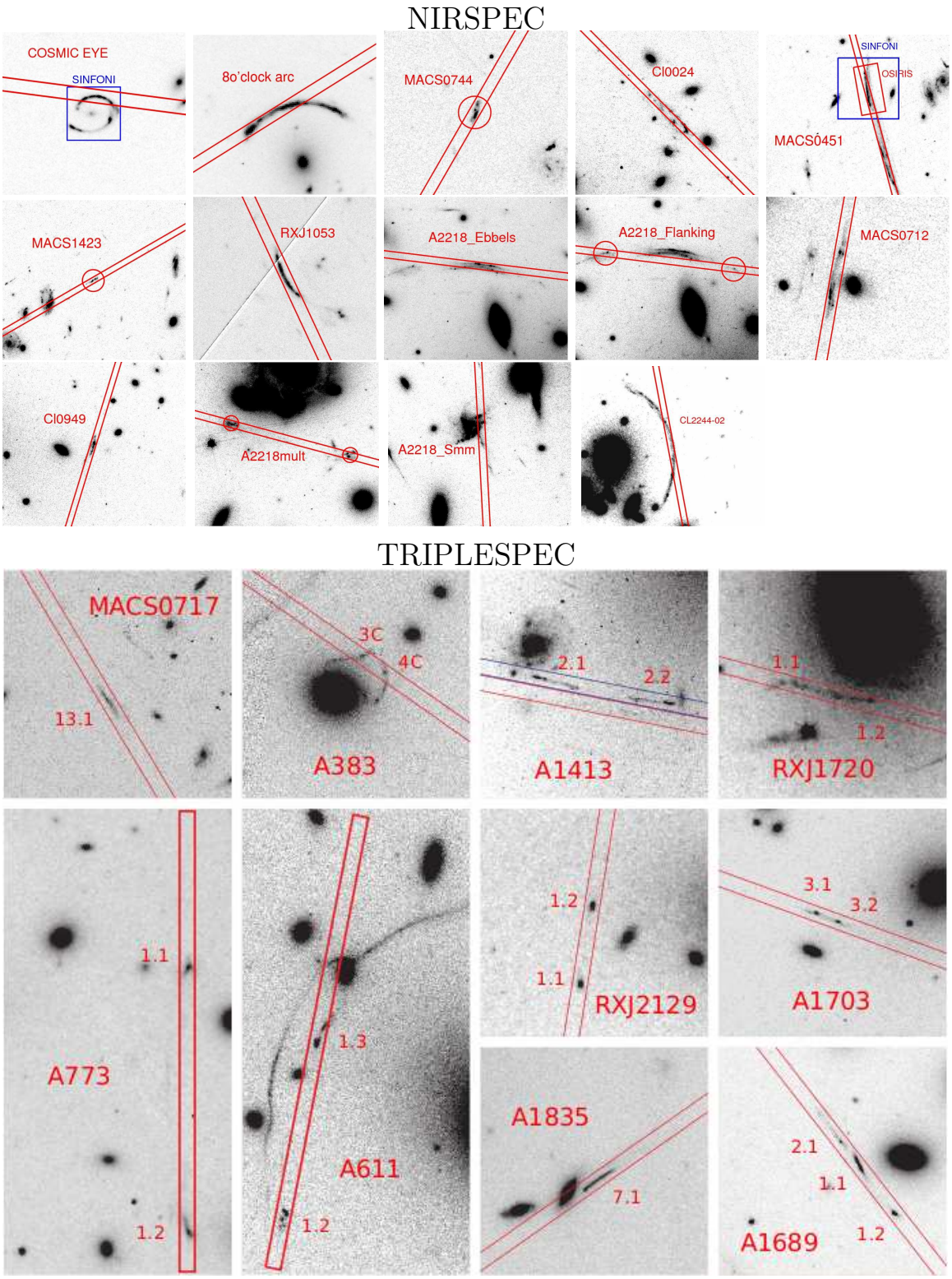

Figure 4.1: Thumbnail *HST* images (V or I band) for each source targeted for near-infrared spectroscopy, showing the orientation of the corresponding NIRSPEC or Triplespec long slit. Targets are marked where there is otherwise ambiguity.

intrinsically faint using Triplespec. Our selection criteria for Triplespec observations includes all of the points above and we further require an intrinsic apparent magnitude $V > 25.5$ (corresponding to a star formation rate $\lesssim 10$ $M_\odot yr^{-1}$) and stellar mass estimated to be $\lesssim 10^9$ $M_\odot$. We summarize in Table 4.1 the sources drawn from this master list for which we were able to measure robust gas-phase metallicity from nebular emission lines. We have augmented this sample with ISAAC archival data and data from the literature for an additional 5 targets (see §2.2.3). In total, the sample comprises 26 lensed sources spanning the redshift range $1.5 < z < 3.3$.

2.2 Near-Infrared Spectroscopy

2.2.1 NIRSPEC Observations and Data Reduction

The bulk of the spectroscopic survey was conducted with the NIRSPEC spectrograph (McLean et al., 1998) on the Keck II telescope in its low resolution mode during 6 observing runs (Table 4.2). A 42×0.76 arcsecond long slit was oriented along the major axis of each object, usually the direction of the highest magnification, in order to maximize the line fluxes (Fig. 4.1). At this resolution, a different wavelength setup was selected for each target using the filters N1 to N7 (corresponding to the z' through K bands) for each group of lines ([OII]; Hβ+[OIII]$_{\lambda\lambda 4959,5007}$; H$\alpha$+[NII]).

A major advantage of targeting lensed sources is the ability to survey a large sample of low luminosity sources in an economic amount of observing time. We typically undertook 2 to 4 dithered exposures of 300−600 seconds each, depending on the magnitude of the source and the sky levels in a given band. We used a three point dithering pattern with offsets larger than the size of the object along the slit. Standard stars were used as flux calibrators. Simultaneously with the NIRSPEC integrations, we took a series of 4−8 short exposures using the slit viewing camera, SCAM, in order to monitor the seeing and slit alignment with the object.

NIRSPEC data were reduced using IDL scripts following the procedure described in more detail in Stark et al. (2007) and Richard et al. (2008). Although the 2D spectrum is distorted on the detector, sky subtraction, wavelength and flux calibration were accomplished in the distorted frame, thereby mitigating any deleterious effect of resampling (see Kelson 2003 for more details). In comparison with the general procedure applied by Stark et al. (2007) for point sources, we took special care to prevent sky over-subtraction for our bright and extended sources.

2.2.2 Triplespec Observations and Data Reduction

In addition to NIRSPEC observations, we have observed several galaxies with Triplespec (Herter et al., 2008) during four observing runs on the Palomar 200" telescope (Table 4.2). These data were taken as part of a survey aiming to characterize the detailed physical properties of low-mass ($M_* \lesssim 10^9$ $M_\odot$), low-luminosity (intrinsic $R_{AB} > 25.5$) galaxies at $z \simeq 2$. The full survey details

and results will be published in a forthcoming paper (Belli et al., in preparation). Triplespec uses a single configuration with a 30×1 arcsecond long slit. The tremendous advantage of Triplespec for this study is simultaneous coverage of the entire near-IR spectrum from $0.8-2.5$ μm, such that all relevant emission lines are observed simultaneously. Despite the smaller telescope aperture, spectra of faint galaxies can be obtained with Triplespec in an integration time comparable to that required with NIRSPEC on Keck. Furthermore, while NIRSPEC data are subject to systematic uncertainties arising from different instrument configurations, Triplespec data do not suffer from these effects. Line ratios measured with Triplespec are therefore generally more accurate than with NIRSPEC, ISAAC, and other instruments with limited spectral coverage.

Each source was observed using $300-450$ second exposures with total integration times of $1.5-5.5$ hours. We used a two point dither pattern configured to ensure that nearby galaxies do not contaminate the target object, and that suitable regions of empty sky are available for sky subtraction. Flux calibration was done using standard A0V stars observed throughout each night. Guide camera exposures were taken simultaneously with object spectra in order to determine slit losses from the seeing and slit position. The data were reduced using a modified version of SPEXTOOL (Cushing et al., 2004; Vacca et al., 2004). Each dithered pair of exposures was reduced separately to produce a spectrum from each exposure. These individual spectra were then combined to produce the final spectrum and determine the uncertainty as a function of wavelength.

2.2.3 Archival, Literature, and IFU Data

A modest amount of additional data on lensed galaxies is available in the literature, in the archive, or through new IFU data. To date, the 21 objects drawn from our Keck and Palomar survey described above represents a major advance in sample size. We include 5 galaxies taken from the literature whose properties match the selection criteria of our surveys: J1038 observed with OSIRIS on Keck (Chapter 3), the Horseshoe and Clone arcs observed with NIRSPEC (Hainline et al., 2009), and two galaxies behind the cluster AC114 observed with ISAAC on the ESO VLT (Lemoine-Busserolle et al., 2003). These additional sources are listed separately in Table 4.1. Finally, we retrieved ISAAC archival data for the giant arc in Cl2244 at $z = 2.24$ (Hammer et al., 1989). These archival J, H and K-band spectra have been reduced with standard IRAF scripts, following the procedure used in Richard et al. (2003).

Together with the IFU data presented in Jones et al. (2010a), three of the targets described above (the Cosmic Eye, A1835 and MACS0451) were observed with the SINFONI integral field spectrograph on the VLT between May 2009 and September 2010 as part of program 083.B-0108. In all three cases we used a $8''\times8''$field of view with $0\farcs25$ pixels and used J, H and K-band gratings with spectral resolution $\lambda/\Delta\lambda = 4000$. We used an ABBA dither sequence while keeping the object inside the IFU at all times. Typical integration times were 7.2 ks (split into 600 second exposures) in $<0\farcs6$

seeing and photometric conditions. Individual exposures were reduced using the SINFONI ESOREX data reduction pipeline and custom IDL routines which perform flat-field correction, wavelength calibration, spectral extraction, and form the data cube. Individual exposures were aligned and combined using a 3σ clip to reject cosmic rays to generate the final data cube. Flux calibration was performed with standard stars observed each night immediately before or after the science exposures. These were reduced in an identical manner to the science observations. Detailed analysis of the spatially resolved properties will be discussed in a forthcoming paper (Livermore et al. in preparation), but here we concentrate on the integrated emission line properties measured from these observations.

2.2.4 Line Fluxes and Line Widths

Typical reduced spectra from NIRSPEC and Triplespec are shown in Figure 4.2. Emission line fluxes were measured by fitting a Gaussian profile to each line, and a double Gaussian to the [OII] doublet with the lines fixed at rest wavelengths of 3726.1, 3728.8 Å. Line widths were measured for the highest signal-to-noise (> 10) emission lines, and corrected for the instrumental resolution measured from bright unblended OH sky lines. The FWHM spectral resolution is $\simeq 115$ km s^{-1} for Triplespec and $160 - 260$ km s^{-1} for NIRSPEC. The error spectrum was used to perform a weighted χ^2 fit and determine uncertainty in line flux and FWHM. Gaussian fits used to determine the line width have residuals $\chi^2_\nu \simeq 1$ suggesting that the error spectrum is a good estimate of the intrinsic noise. After subtracting the instrumental resolution in quadrature, line widths are typically determined to $\sim$10% accuracy. The uncertainty is significantly larger in cases where the line of interest is blended with a sky line, or has a width close to the instrumental resolution. We estimate any systematic uncertainty in the measured instrumental resolution to be < 3 % based on independent measurements of multiple bright sky lines, hence we expect measurement errors to dominate. Line flux and width measurements are given in Table 4.4.

We can test whether the velocity dispersions measured with long slits are reliable by comparing with available 2D kinematic data from integral field spectrographs (Law et al., 2009; Förster Schreiber et al., 2009; Jones et al., 2010a). Here we enlarge the comparison sample by considering all relevant NIRSPEC data, in particular from Erb et al. (2006). As Figure 4.3 shows, the longslit data are in general agreement with the mean IFU velocity dispersion being 1.2 ± 0.3 times that measured with NIRSPEC. This suggests that the longslit data provide a reasonable estimate of the global galaxy dynamics and can be used, for example, with the spatial extent to estimate dynamical masses.

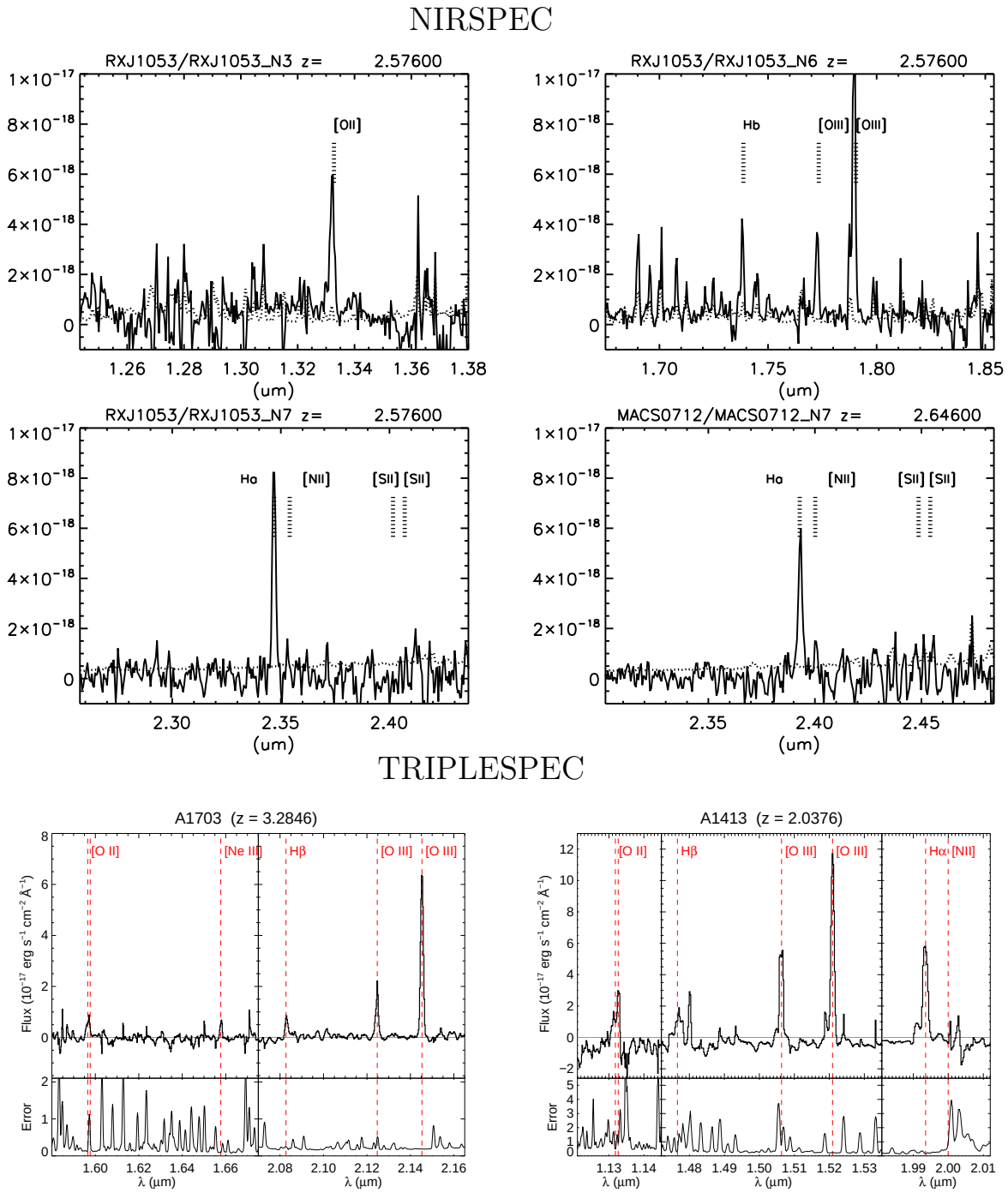

Figure 4.2: Typical extracted spectra of various signal-to-noise ratios with prominent emission lines labeled. NIRSPEC spectra are shown in units of erg s^{-1} cm^{-2} $Å^{-1}$ with dotted lines indicating the 1σ error spectrum. Triplespec captures the entire near-IR spectrum simultaneously, while NIRSPEC requires multiple settings to observe all emission lines of interest. For RXJ1053, the key nebular lines were covered using 3 different spectrograph settings (shown).

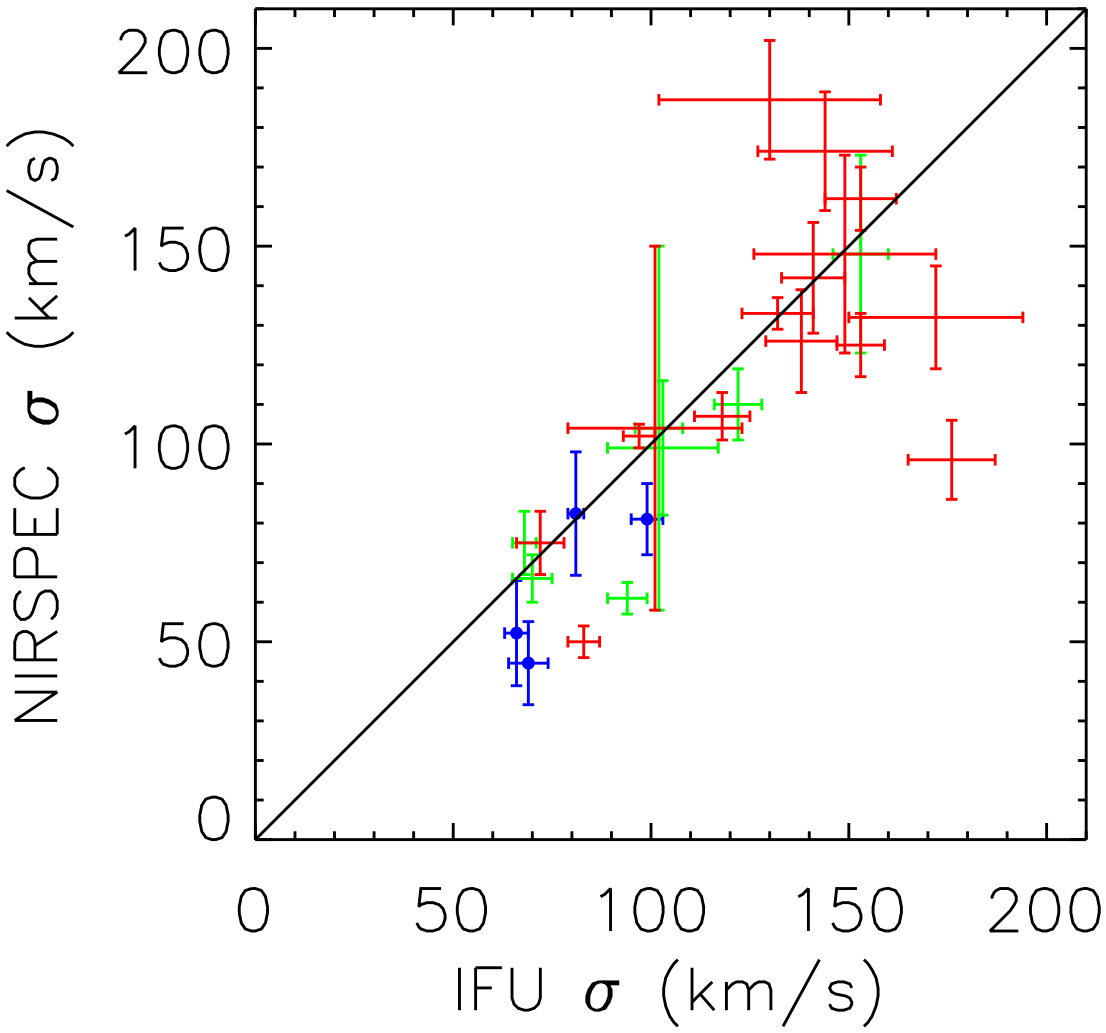

Figure 4.3: Comparison of the velocity dispersion measured from NIRSPEC data with 2D integral field unit data from various sources. Blue points refer to mean dispersions (σ) from OSIRIS IFU observations reported in Jones et al. (2010a). Green crosses show equivalent OSIRIS data from Law et al. (2009) and red crosses are integrated velocity dispersions from SINFONI (Förster Schreiber et al., 2009). NIRSPEC measurements for the latter samples are reported in Erb et al. (2006).

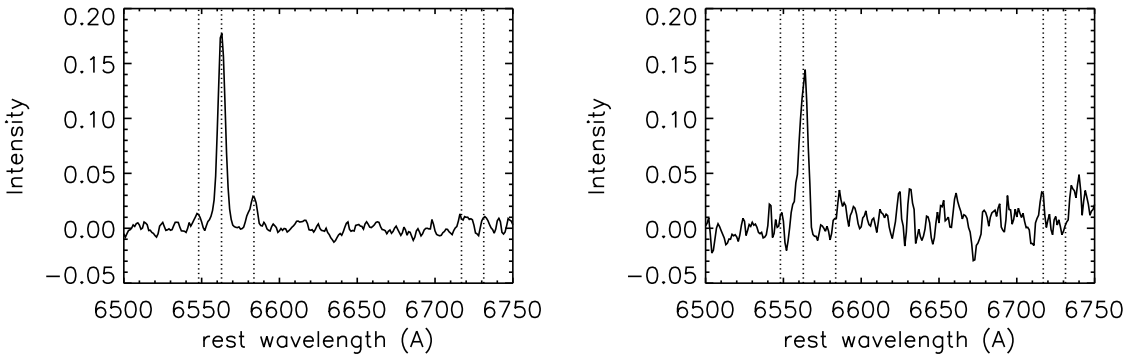

Figure 4.4: Stacked spectra chosen to reveal fainter emission lines. Left: stack of lensed sources with S/N > 10 in the Hα line. Right: stack of lensed sources with stellar mass $< 3 \times 10^9$ M$_\odot$. Dotted lines show the positions of Hα, [NII]$\lambda\lambda$6548, 6584, and [SII]$\lambda\lambda$6717, 6731.

2.2.5 Line Ratios from Stacked Spectra

One of our aims is to measure the mass-metallicity relation in our sample, extending it to low luminosity sources. Given the short exposure times for our survey which has enabled such a large sample to be constructed, inevitably many of the fainter diagnostic lines such as [NII] and [SII] are not always visible in individual spectra. In order to estimate the typical prevalence of such faint emission lines, we construct a stacked spectrum around the Hα line. This has been done for two cases: for all lensed sources where Hα is detected at S/N > 10, and secondly for all cases where the stellar mass (§3.3) is $< 3 \times 10^9$ M$_\odot$. First we resample the Hα spectra into the rest frame with a common dispersion of 1 Å and then scale each spectrum to a common Hα flux. We reject the minimum and maximum values at each wavelength in order to remove outliers (due to sky line residuals, for example), and average the remaining data. The results are consistent with Gaussian noise. The composite spectra are shown in Figure 4.4.

We measure line ratios in the stacked spectra by fitting a Gaussian profile to Hα, then using the position and line width to determine the [NII] and [SII] fluxes and their bootstrap error. The resulting ratios are provided at the bottom of Table 4.3.

2.2.6 Aperture Corrections and Further Checks

One obvious limitation of long-slit spectroscopy is that a significant fraction of the line flux may be missing, especially for the most extended objects or in poor seeing conditions. Our slit widths were 0.″76 for NIRSPEC and 1.″0 for Triplespec and so slit loss is a concern for many objects (see Table 4.2). In order to compare measurements based on long-slit spectroscopy with photometric estimates derived from imaging (see §2.4), we carefully estimated aperture correction factors.

The procedure adopted was the following: we used the SExtractor *segmentation map* to select

those pixels of the HST image associated with an object. We smoothed this new image by our estimate of the seeing conditions (Table 4.2) determined from images taken simultaneously with the spectra, and measured the fraction of the total flux falling inside the region covered by the slit. We found aperture correction factors between 1.2 and 2.9 depending on the object. The error on these corrections was estimated using a $\pm 0\farcs2$ error on the location of the slit, as determined from the images. The correction factors are later used to derive the total star formation rate (SFR) of the object, assuming that measured equivalent widths of the lines are representative of the entire galaxy. Of course, the metallicity and line ratio measurements are unaffected as they rely entirely on the spectroscopic data. We also checked that measurements of the 8 o'clock arc are consistent with the results presented by Finkelstein et al. (2009).

Six sources in our sample have been observed with both NIRSPEC and OSIRIS, allowing us to check the aperture correction factors in cases where the true total line flux is known from integral field spectroscopy. (See Chapter 2 for details of the OSIRIS observations). We found general agreement between the two measurements with an average ratio of NIRSPEC/OSIRIS flux $= 1.03 \pm 0.20$, indicating a typical error of $\simeq 20\,\%$ in total flux values. This uncertainty most likely arises from aperture correction and flux calibration. We adopt this $20\,\%$ uncertainty estimate in total line flux when estimating star formation rates derived later in this paper.

As mentioned earlier, we can use the same six targets to compare the velocity dispersions estimated from the NIRSPEC and OSIRIS data on the same emission lines (§2.2.3). Although the long slit estimates have larger error bars, they are consistent (within 1σ) with the more reliable IFU estimates. Nonetheless we adopt the IFU value whenever availble.

2.3 Magnification and Source Reconstruction

In order to correct all physical properties (star formation rates, masses, physical scales) for the lensing magnification, we correct each source for its corresponding *magnification factor* μ which magnifies the angular size of each object while keeping its surface brightness fixed. As discussed earlier, our targets were specifically chosen to lie in the fields of clusters whose mass models are well-constrained from associated spectroscopy of many lensed sources and multiple-images (see Richard et al. 2010b for further discussion).

The values of μ are obtained through modeling of the cluster mass distribution using the Lenstool software [1] (see references in Table 4.1), or from the literature for the additional targets in Table 4.1. The relative error on μ, when derived from a Lenstool parametric model, follows a Bayesian MCMC sampler (Jullo et al., 2007) which analyses a family of models fitting the constraints on the multiple images. In Table 4.1 we report the final values of μ and their associated errors; these are used to correct μ-dependent physical parameters (star formation rates and masses)

[1] http://www.oamp.fr/cosmology/lenstool/

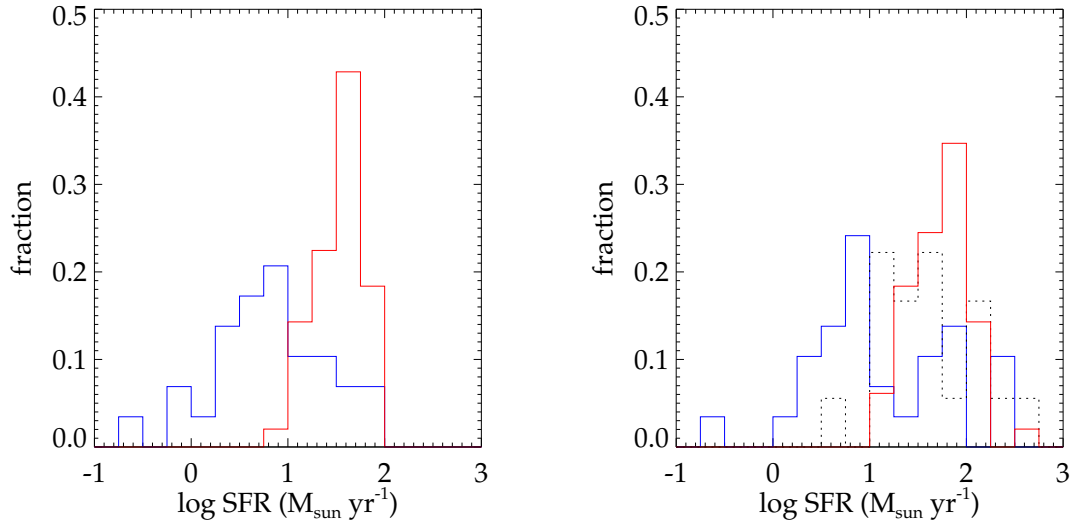

Figure 4.5: Distribution of star formation rates in our sample of lensed objects (blue histogram) compared to the samples of LBGs at $z \sim 2$ (red histogram; Erb et al. 2006) and at $z \sim 3$ (dotted histogram, AMAZE and LSD samples; Maiolino et al. 2008 and Mannucci et al. 2009). The left panel compares the distribution of SFR before correcting for extinction, while the right panel compares the values after applying the extinction correction. All SFRs are calculated for a Salpeter IMF.

throughout the rest of this chapter. Note that the magnification factor does not affect any of the line ratio measurements.

We also construct the demagnified (unlensed) source morphology of each arc modeled with LENSTOOL by ray-tracing the high-resolution HST image back to the source plane, using the best fit lens model. By comparing the sizes of the observed and reconstructed image of a given target, we can verify the agreement of this size ratio with the magnification factor used (cf. discussion in Jones et al. 2010a).

2.4 Photometric Measurements

A large variety of space- and ground-based images are available for each object from archival sources. All HST images (optical and near-infrared) have been reduced using the `multidrizzle` package (Koekemoer et al., 2002), as well as specific IRAF scripts for NICMOS data, as described in Richard et al. (2008). Ground-based near-infrared images were reduced following the full reduction procedure described in Richard et al. (2006), and calibrated using 2MASS stars identified in the field. Archival IRAC data in the first 2 channels (3.6 and 4.5 μm) are available for all sources except MACS1423, but we only consider sources which are not contaminated by nearby bright galaxies when deriving their photometry. We combine the post-BCD (Basic Calibrated Data) frames resampled to a pixel scale of $0\farcs6$.

The HST image providing the highest signal-to-noise was used to measure the integrated bright-

ness with SExtractor (Bertin & Arnouts, 1996), whereas the *double image* mode was used to measure the relative HST colors inside a 1″aperture. A small aperture correction was applied to all HST photometry to deal with the PSF differences between the different ACS, WFPC2 and NICMOS bands. In the case of colors from ground-based or IRAC data, the primary HST image was smoothed by a Gaussian kernel corresponding to the measured point spread function derived from bright unsaturated stars in the image. The full photometry is summarized in Table 4.5.

3 Physical Properties of the Sample

Table 4.4 summarizes the derived quantities which will form the basis of our analysis. We now discuss each physical property in turn.

3.1 Star Formation Rate and AGN Contribution

Intrinsic star formation rates are estimated from the total (aperture-corrected) flux in the Balmer lines (Hα and Hβ) based on the well-constrained calibrations by Kennicutt (1998), including the correction for magnification μ and its associated error. In the absence of Hα we assume a ratio Hα/Hβ=2.86 corresponding to Case B recombination with no reddening. The derived values of SFR span a wide range, between 0.3 and 230 $M_{\odot}$/yr, and are typically a factor of 10 lower than other samples of LBGs with emission line measurements (Figure 4.5). Half of the lensed sources (15 objects) have SFR < 10 $M_{\odot}yr^{-1}$, rates well below those probed in large surveys of non-lensed galaxies (Erb et al., 2006; Maiolino et al., 2008).

An independent estimate of the SFR can be obtained for every object using the ultraviolet continuum luminosity (L_{ν}) estimated at 1500 Å rest-frame. We measure L_{ν} by fitting a power-law $f_{\lambda} \propto \lambda^{-\beta}$ to the broad-band photometry between 1500 and 4000 Å rest-frame. The UV slope (β) is given in the first column of Table 4.5. A value $\beta = 2.0$ (constant AB magnitude) is assumed when only a single photometric datapoint was available. The SFR derived from UV continuum is then calculated from the relation calibrated by Kennicutt (1998).

We can determine from nebular line ratios whether there is a strong contribution from active galaxy nuclei (AGN) in the line emissions. This is done through the diagram of [NII]/Hα versus [OIII]/Hβ flux, known as the BPT diagram (Baldwin et al., 1981). The location of the lensed galaxies on the BPT diagram is shown in Figure 4.6. We also plot $\sim 122,000$ galaxies from the Sloan Digital Sky Survey which show a clear separation of AGN and star forming galaxies. The majority of our sources lie in the region of the BPT diagram where star-forming galaxies are commonly found (Kewley et al., 2001), although MACS0451 lies close to the boundary with the region occupied by AGNs. However, we consider it unlikely that this object is AGN-dominated because of the lack of X-ray emission in Chandra data and CIV lines in the optical spectra. Furthermore, the Spitzer

data shows evidence for the rest-frame 1.6μm stellar bump and no sign of obscured AGN activity, which would produce a rising slope in the redder IRAC channels (e.g., Hainline et al. 2011). Most lensed galaxies are offset from the locus of star forming galaxies in SDSS, suggesting a radiation field characterized by higher ionization parameter similar to that seen in local The location of these objects in the BPT plane simply suggests a higher radiation field, similar to starbursts and the sample of LBGs studied by Erb et al. (2006) at $z \sim 2$ (see also Section 3.5). We thus conclude that the nebular emission we see in our sources arises from intense star formation.

3.2 Extinction

Dust extinction plays an important role when deriving the physical properties of galaxies, as it will affect the observed line fluxes and some of the line ratios. One of the estimators we can use to measure this extinction is the UV spectral slope β, which is related to the extinction affecting the young stars. The Balmer decrement of Hα/Hβ flux is another excellent estimate of extinction in galaxies where both lines are detected with high significance. We can also use the ratio between the two SFR estimates (from the UV continuum and Hα emission) as an independent estimator, as it reflects the differential extinction between the two wavelengths. However we note that even in the case of a perfect reddening correction, the nebular emission and the UV continuum do not probe star-formation on the same timescales (Kennicutt, 1998).

Figure 4.7 compares both SFR estimates for a subsample of the lensed objects, together with the relation predicted by the Calzetti et al. (2000) extinction law. It shows that there is a general agreement with the theoretical predictions, although with quite a large scatter. One of the reasons for the differences is probably a different extinction factor affecting the young and old stellar populations, or a measurement bias towards low extinction regions when measuring β. This is illustrated by the location of the sub-millimetre lensed galaxy A2218-smm (Kneib et al., 2004), which has a high extinction but a measured slope $\beta = 1.6$ (white diamond in Figure 4.7). One way to overcome this issue is to use the full SED (from rest-frame UV to near-infrared) in order to derive the best extinction estimate E(B$-$V) assuming the Calzetti et al. (2000) law, which we calculate in §3.3.1 We also calculate E(B$-$V) from the Balmer decrement in cases where Hα and Hβ emission lines are detected, and find consistent values (typically $0 < \mathrm{E(B-V)} < 0.35$) although with large uncertainties.

We use the best-fit E(B$-$V) values from SED fitting, given in Table 4.4, to correct the SFRs, individual line ratios and metallicities in the next sections. In particular, reddening has a strong effect on individual SFRs and it is very sensitive to unknown factors (differential reddening in a given object, presence of dust in the lightpath through the galaxy cluster, deviation from the Calzetti law as pointed out by Siana et al. 2009). We present both the uncorrected SFR and extinction-corrected SFR$_{corr}$ in Table 4.4 and when comparing with other samples (Figure 4.5).

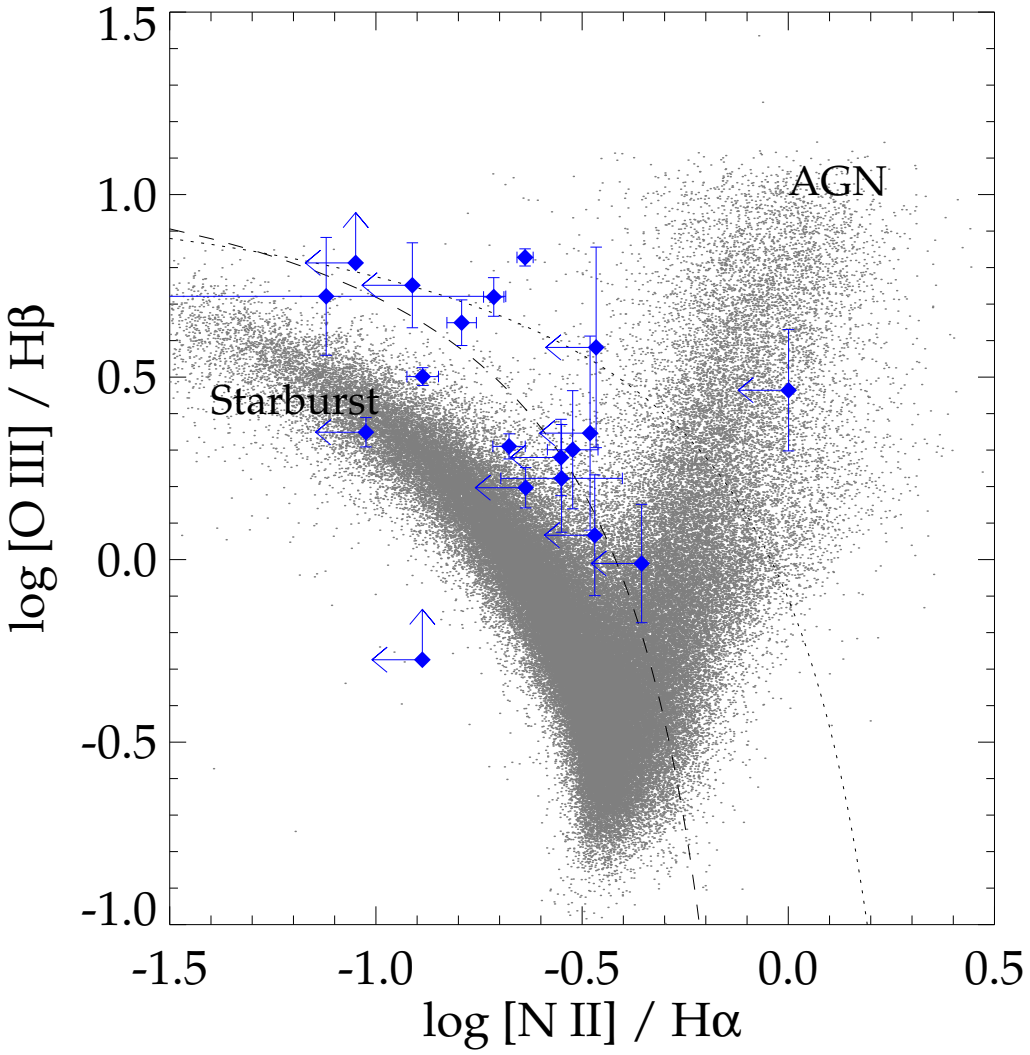

Figure 4.6: Diagnostic diagram of [NII]/Hα and [OIII]/Hβ (the BPT diagram). Galaxies in our sample are shown as blue diamonds with error bars. The small grey points are ∼122,000 galaxies from the Sloan Digital Sky Survey (SDSS) with signal to noise ≥ 5 in all relevant emission lines. SDSS galaxies show a locus of star forming galaxies, and a separate branch of AGN extending to the upper right. The dotted line shows the theoretical maximum [OIII]/Hβ from star forming regions (Kewley et al., 2001) and the dashed line is an empirical division between star-forming galaxies and AGN from Kauffmann et al. (2003).

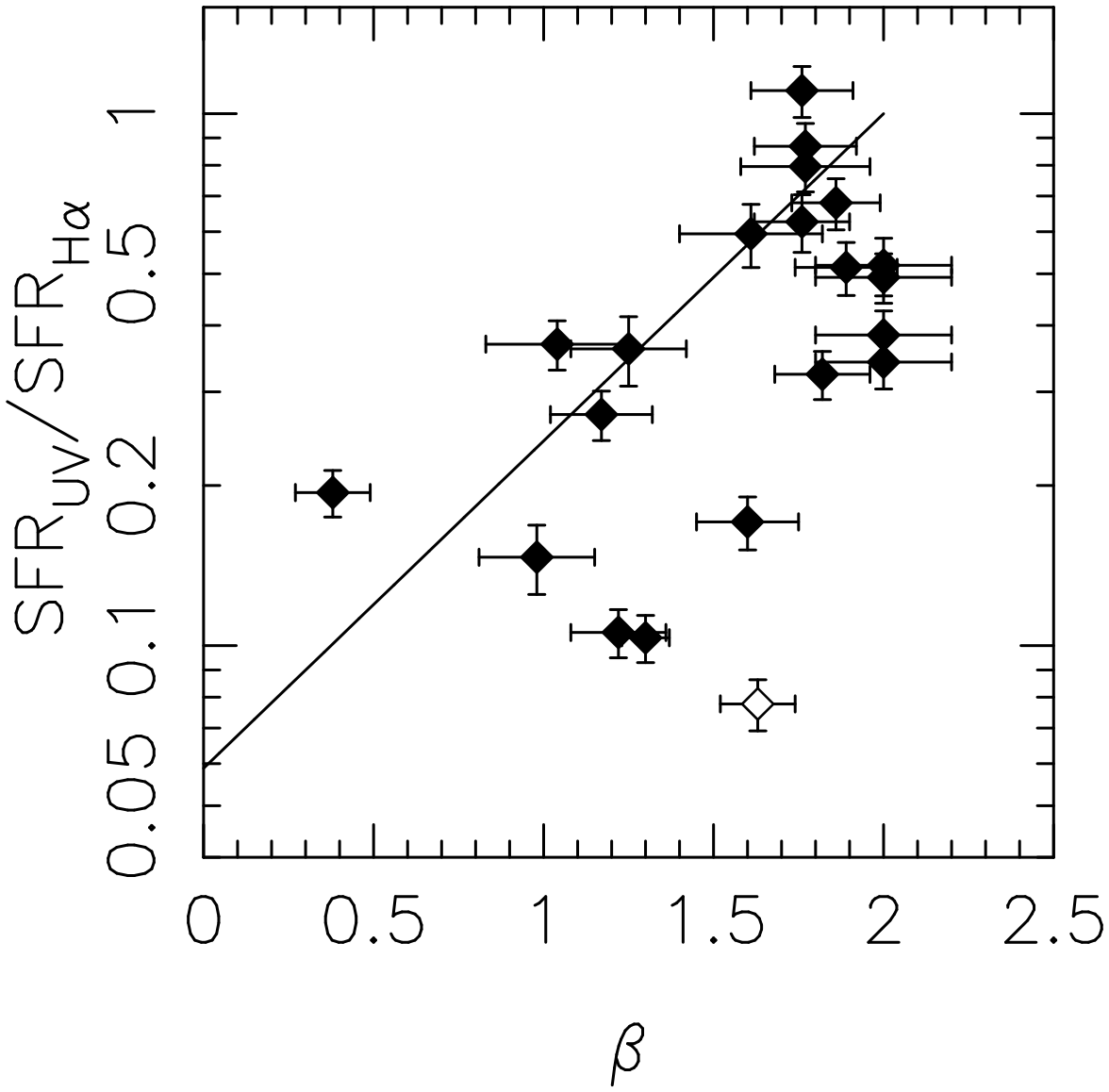

Figure 4.7: Comparison of SFR estimated from the UV continuum and from the Hα emission line, as a function of the UV slope β. The solid curve is the theoretical prediction for the relation between the two values using the Calzetti et al. (2000) extinction law.

3.3 Mass

Two mass estimators can be derived from the available data. Multi-wavelength broad-band photometry gives us access to the stellar mass from SED modeling, while measuring the widths of the most prominent nebular emission lines allow us to infer dynamical masses, which should be closer to the total baryonic mass of these galaxies.

3.3.1 Stellar Mass

Our stellar masses are derived using the precepts discussed in detail by Stark et al. (2009). We derive the stellar masses for our sample by fitting the Charlot & Bruzual (2007, S. Charlot, private communication) stellar population synthesis models to the observed SEDs. We consider exponentially decaying star formation histories with the form SFR(t) $\simeq \exp(-t/\tau)$ with e-folding times of τ = 10, 70, 100, 300, and 500 Myr in addition to models with continuous star formation (CSF). For a given galaxy, we consider models ranging in age from 10 Myr to the age of the universe at the galaxy's redshift. We use a Salpeter (1955) initial mass function (IMF) and the Calzetti et al. (2000) dust extinction law. Finally, we allow the metallicity to vary between solar ($Z_\odot$) and 0.2 $Z_\odot$, the range found for the gas-phase metallicity using nebular line ratios (Sect. 3.4). We account for the intergalactic medium absorption following Meiksin (2006). The best fit values of the stellar mass M_* and extinction E(B−V) are summarized in Table 4.4.

We note that the presence of strong emission lines may affect the broad-band photometry and therefore the mass estimates. We estimate the contribution of the strongest emission lines affecting the H and K band magnitudes in order to assess this effect. In the most extreme cases (largest equivalent widths) the H and K band flux is affected by only $\simeq 10\,\%$, which is not significant given the estimated errors.

3.3.2 Dynamical Mass

We now use the velocity dispersions σ (measured in Sect. 2.2.4) to estimate the dynamical mass. We will express the virial masses M_{dyn} of our objects as a function of σ and their typical size.

Assuming the idealized case of a sphere of uniform density (Pettini et al., 2001) we have $M_{dyn} = Cr_{1/2}\sigma^2/G$ with $C = 5$, or more conveniently

$$M_{dyn} = 1.16 \times 10^{10}\ M_\odot \frac{\sigma^2}{(100\ \mathrm{km\ s^{-1}})^2} \frac{r_{1/2}}{\mathrm{kpc}}. \tag{4.1}$$

Here $r_{1/2}$ is the half-light radius, which we measure on the source plane reconstructions of our targets (see Sect. 2.3) using the `FLUX_RADIUS` parameter from SExtractor. This parameter estimates a circularized size corresponding to half of the total detected flux. Thanks to the high magnification our sources are well resolved in the HST images, but the main source of error in estimating $r_{1/2}$ (which

has a strong impact on M_{dyn}) is the source reconstruction itself. We produced 100 reconstructions of each source sampling the different parameters of the lens model, using the MCMC sampler described in Section 2.3, and use them to derive the mean and dispersion on the measured $r_{1/2}$. We also checked this measurement independently using a half-light radius defined with the Petrosian radius at 20% of the central flux of the object, similar to the work done by Swinbank et al. (2010), and found consistent results.

The values of $r_{1/2}$ and M_{dyn} are reported in Table 4.4. We note that the geometric correction factor C can vary significantly and is likely between 3 and 10 for these highly turbulent galaxies (Erb et al., 2006). Hence the true dynamical mass can differ by up to a factor of 2, while uncertainty in the radius and σ is much smaller. Our choice of $C = 5$ gives slightly higher dynamical masses than in some other studies (e.g., $C = 3.4$, Erb et al. 2006; Bouché et al. 2007).

3.3.3 Comparison

The stellar mass distribution of our lensed galaxies spans a large range ($10^8 - 10^{11}$ $M_\odot$), and the typical stellar mass is $0.4 - 0.7$ dex lower than non-lensed samples surveyed by Erb et al. (2006), Maiolino et al. (2008), and Mannucci et al. (2009) (Figure 4.8, left). Within the subsample with reliable dynamical masses, we can directly compare the two mass estimates. Although we find a large dispersion in the ratio of dynamical to stellar mass (Figure 4.8, right), the average ratio $< \log M_*/M_{dyn} >= -0.21$ dex suggests that stars account for only $\simeq 60\,\%$ of the dynamical mass. This value is similar to the result found by Erb et al. (2006), and confirms the dominance of baryonic mass in the central regions of these galaxies. Additionally this suggests that gas fractions in the lensed galaxies may be as high as $\simeq 40\,\%$ on average, similar to values inferred from direct measurements of molecular gas emission in star forming galaxies at $z = 1 - 2$ (Daddi et al., 2010; Tacconi et al., 2010). We note that a different choice of $C = 3.4$ for the multiplicative factor in Equation 4.1 would give $\sim 30\%$ lower dynamical masses.

The gas mass can be estimated from the SFR and the size of the galaxies if we assume that the Kennicutt (1998) law between star-formation rate and gas densities applies at these redshifts. We use this relation to derive the total gas mass, assuming the star formation is uniform across the projected galaxy surface seen in the UV:

$$M_{\rm gas} = 5.03 \times 10^8 \ {\rm SFR}^{0.71} \ r_{1/2}^{0.58} \ M_\odot \tag{4.2}$$

where $r_{1/2}$ is in kpc and SFR is in $M_\odot {\rm yr}^{-1}$. Defining the gas fraction as $f_{\rm gas} = M_{\rm gas}/(M_{\rm gas} + M_*)$, we find gas fractions ranging from 0.2 to 0.6 after reddening correction, compatible with what is derived from the comparison of stellar and dynamical masses. This is on average $\sim$50% lower that gas fractions inferred by Erb et al. (2006) at $z \sim 2$ and by Mannucci et al. (2009) in the Lyman-break

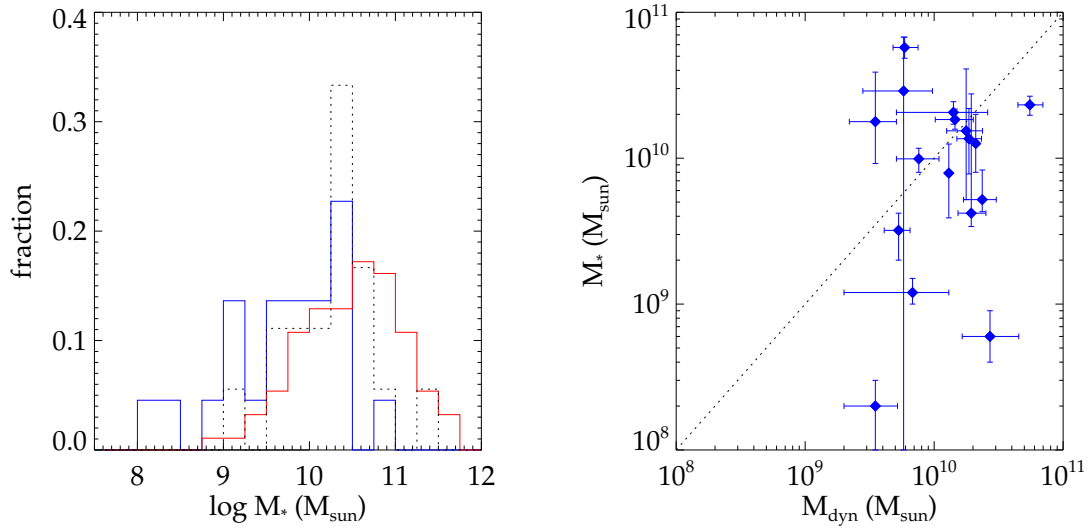

Figure 4.8: (Left) Distribution of stellar masses in our sample of lensed objects (blue histogram) compared to the samples of LBGs at $z \sim 2$ (red histogram; Erb et al. 2006) and at $z \sim 3$ (dotted histogram, from the AMAZE and LSD samples; Maiolino et al. 2008 and Mannucci et al. 2009). (Right) Comparison of stellar and dynamical mass estimates. In general we find a lower stellar mass compared to the dynamical mass with an average ratio of stellar to dynamical mass $\simeq 0.6$.

galaxies Stellar populations and Dynamics (LSD) sample at $z \sim 3$, and reflects the lower SFRs in our objects for a given stellar mass.

3.4 Metallicity

The gas-phase metallicity of a star forming region, defined by the oxygen abundance $12+\log(\mathrm{O/H}) = \log Z$, is highly correlated with the ratios of prominent optical nebular emission lines. The relations between metallicity and various line ratios have been accurately calibrated from local data (e.g., Nagao et al. 2006). Suitable line ratios are available for estimating the metallicity in all of the lensed galaxies presented here, and in many cases we can combine estimates from multiple metallicity diagnostics. In order to usefully compare our results with other surveys, we use the empirical relations recently derived by Maiolino et al. (2008) (used also by Mannucci et al. 2010). For the sake of consistency we use the same line ratios as Maiolino et al. (2008): [OIII]/Hβ, [OIII]/[OII], and [NeIII]/[OII]. The [OIII]/Hβ relation has a "two-branch degeneracy" (e.g., Pettini & Pagel 2004) with a low-metallicity and a high-metallicity value, and we use the other diagnostics to discriminate between these two possible solutions. We additionally use the [NII]/Hα ratio; this useful diagnostic was not available in the data of Maiolino et al. (2008). All four line ratios provide independent estimates of the metallicity.

Metallicities are calculated for each galaxy using the polynomial formulae given in Maiolino et al. (2008), for all of the available line ratios described above. For galaxies with multiple metallicity

measurements, we adopt the mean value and estimate the uncertainty as the standard deviation of all measurements. In cases where only one measurement is possible we assume an uncertainty of 0.2 dex, typical of the scatter about each relation (Pettini & Pagel, 2004). The final adopted metallicities are reported in Table 4.4 for each source. We find metallicity values ranging from $0.06-2.0$ $Z_\odot$ (where $Z_\odot$ corresponds to a value $12 + \log(O/H) = 8.69$; Allende Prieto et al. 2001).

3.5 Ionization Parameter

In the previous section, the parameter O32 = [OIII]/[OII] has been used mainly to measure metallicity. For a given metallicity, the O32 line ratio can also be compared with models of HII regions to measure the ionization parameter U, i.e., the ratio of density of ionizing photons over the density of hydrogen atoms (Kewley & Dopita, 2002). Based on early samples of bright LBGs from Pettini et al. (2001), Brinchmann et al. (2008) measure $\log(U) \sim -2.0$, relatively high compared to local samples. Such a high ionization parameter shifts objects upward toward higher [OIII]/Hβ in the BPT diagram (Figure 4.6), near the boundary between star forming regions and AGN (e.g., Erb et al. 2010).

The O32 parameter can be measured for 15 objects in our sample, and we obtain values in the range $-0.7 < \log \mathrm{O32} < 0.9$ with a mean value 0.2 ± 0.4. Using the metallicity derived for each galaxy, we use the photoionization model results provided by Kewley & Dopita (2002) to derive ionization parameters $-2.9 < \log(U) < -2.2$ whereas typical values for local galaxies are in the range $-4 < \log(U) < -3$ (Lilly et al., 2003). This result of high ionization parameters in our high redshift sample can be illustrated by constructing a diagram of O32 versus the parameter R23 =([OIII]+[OII])/Hβ, a common metallicity diagnostic which has relatively weak dependence on ionization parameter (Kewley & Dopita, 2002). We show the results from our sample of lensed galaxies along with data from Lilly et al. (2003) at $z \lesssim 1$ and the SDSS at $z \simeq 0$ in Figure 4.9. While many of the lensed galaxies are compatible with the trend at lower redshifts, on average our sample is systematically shifted to higher values of O32. This indicates that physical conditions in the relevant HII regions in the lensed galaxies are different from those in the local universe, for example with higher electron density and/or escape fraction of ionizing photons (Brinchmann et al., 2008).

An even more extreme result was found recently in a $z = 2.3$ galaxy by Erb et al. (2010), who derive an ionization parameter $\log U \simeq -1.0$. The very young age found in this object is one of the factors explaining such a high value of U. Indeed, we can see some trend with age in the O32 vs R23 diagram, despite our relatively small sample. Figure 4.9 shows that galaxies in our sample with very young stellar populations (best-fit age < 100 Myr from SED fitting) all lie in the top part of this diagram with high O32 values.

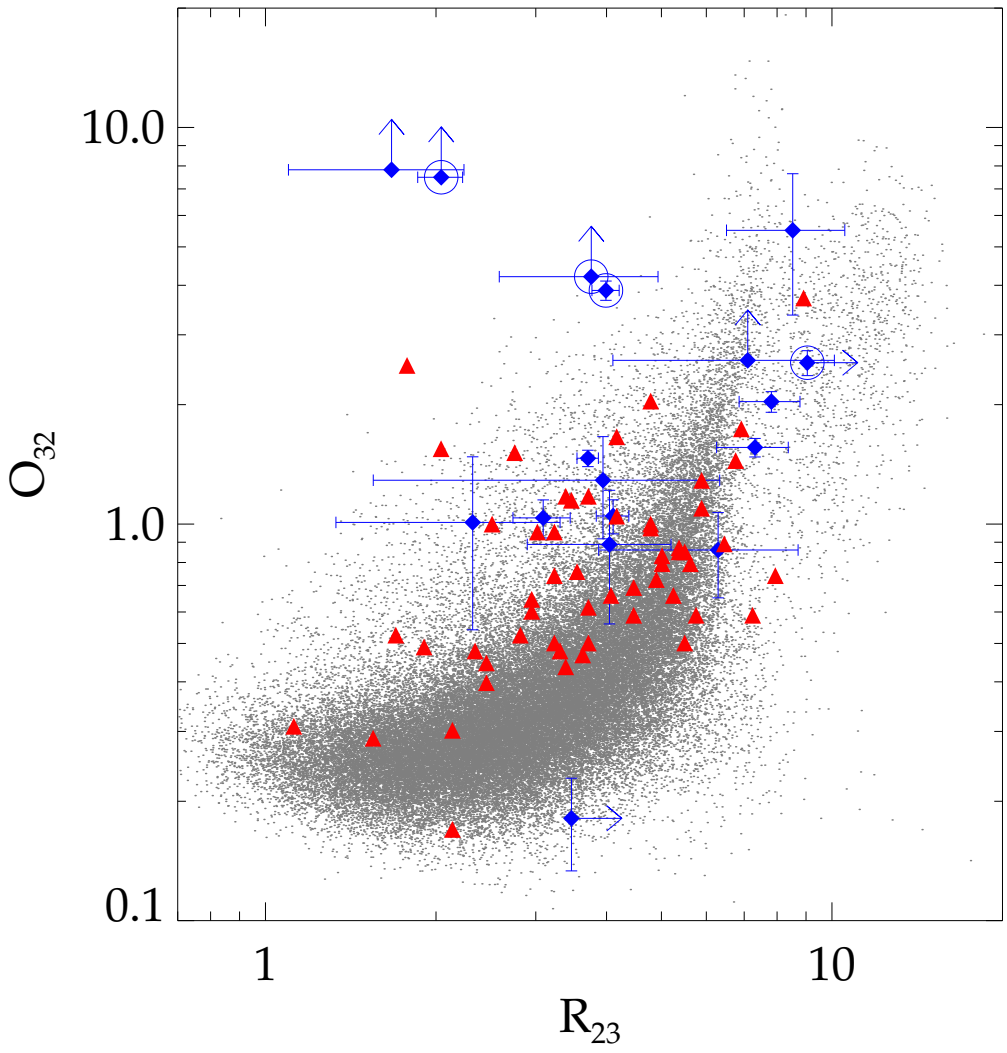

Figure 4.9: O32 vs R23 diagram, showing the effect of the ionization parameter on O32 (adapted from Hainline et al. 2009). The red triangles are the low redshift ($z < 1$) sample of galaxies from Lilly et al. (2003). Our sample of z >1.5 lensed galaxies is shown in blue diamonds. Small gray points show ∼68,000 galaxies from the SDSS with signal to noise ≥ 5 in all relevant emission lines. Sources in our sample with young stellar populations (best-fit age < 100 Myr from SED fitting) are circled and typically lie in the top part of the diagram.

4 The Mass-Metallicity Relation

4.1 Comparison with Earlier Work

We now compare our measurements of lensed galaxies with previous determinations of the mass-metallicity relation at high redshift. Our data extends to lower stellar masses and lower SFR compared to earlier studies by virtue of our gravitational lensing selection (Figures 4.5, 4.8). Figure 4.10 summarizes the mass-metallicity relation of galaxies in our sample compared with other studies. All but one galaxy in our sample lies below the well-defined relation at $z \simeq 0$ (Tremonti et al., 2004), strongly supporting the case for evolution. Figure 4.10 also shows the best-fit mass-metallicity relations determined by Maiolino et al. (2008) based on data at $z \simeq 2.2$ (Erb et al., 2006) and $z \simeq 3.5$ (Maiolino et al., 2008; Mannucci et al., 2009). The lensed galaxies roughly follow these trends with a large scatter (~ 0.25 dex in metallicity), although the evolution implied by our data over $2.2 < z < 3.3$ is much weaker than suggested by Maiolino et al. (2008).

Compared with earlier unlensed surveys, our sample provides an increased number of galaxies with low stellar mass $M_* \sim 10^9$ $M_\odot$ and extends to even lower masses with two galaxies having $M_* \sim 10^8$ $M_\odot$. At these masses, we do not find such a steep decline in metallicity as observed by earlier studies (Figure 4.10). Instead we measure average metallicities in $M_* \sim 10^9$ $M_\odot$ galaxies which are ~ 0.25 dex higher than expected. Although this trend is statistically limited by the small sample size, it is also visible in the composite spectra defined in §2.2.5.

4.2 A Fundamental Metallicity Relation?

By comparing the histograms in Figures 4.5 and 4.8, it is clear that the lensed galaxies presented here typically have much lower SFR than in other spectroscopic surveys at similar redshift, but only slightly smaller masses. This may explain the higher metallicities seen in the lensed galaxies (Figure 4.10), since evolution in the mass-metallicity relation is generally attributed to higher gas fractions (and hence higher SFR) at increasing redshift (e.g., Erb et al. 2006). If this is indeed the case, selecting objects of lower SFR would counteract this effect and explain the deviation of our sample towards slightly higher metallicity.

Recently, Mannucci et al. (2010) have proposed to include the SFR as a third component of the mass-metallicity relation, which would explain its evolution in redshift. They find that a mass-metallicity-SFR relation is able to predict the metallicity of local galaxies in SDSS with a scatter of only $\sigma = 0.05$ dex, somewhat more accurate than the traditional mass-metallicity relation which has $\sigma = 0.08$ dex. Of much greater interest, however, is their discovery that a single mass-metallicity-SFR relation is able to reproduce the observed metallicities of *all galaxies* at *all redshifts* from $0 < z < 2.5$. This "fundamental metallicity relation" (FMR) is most easily expressed in terms of

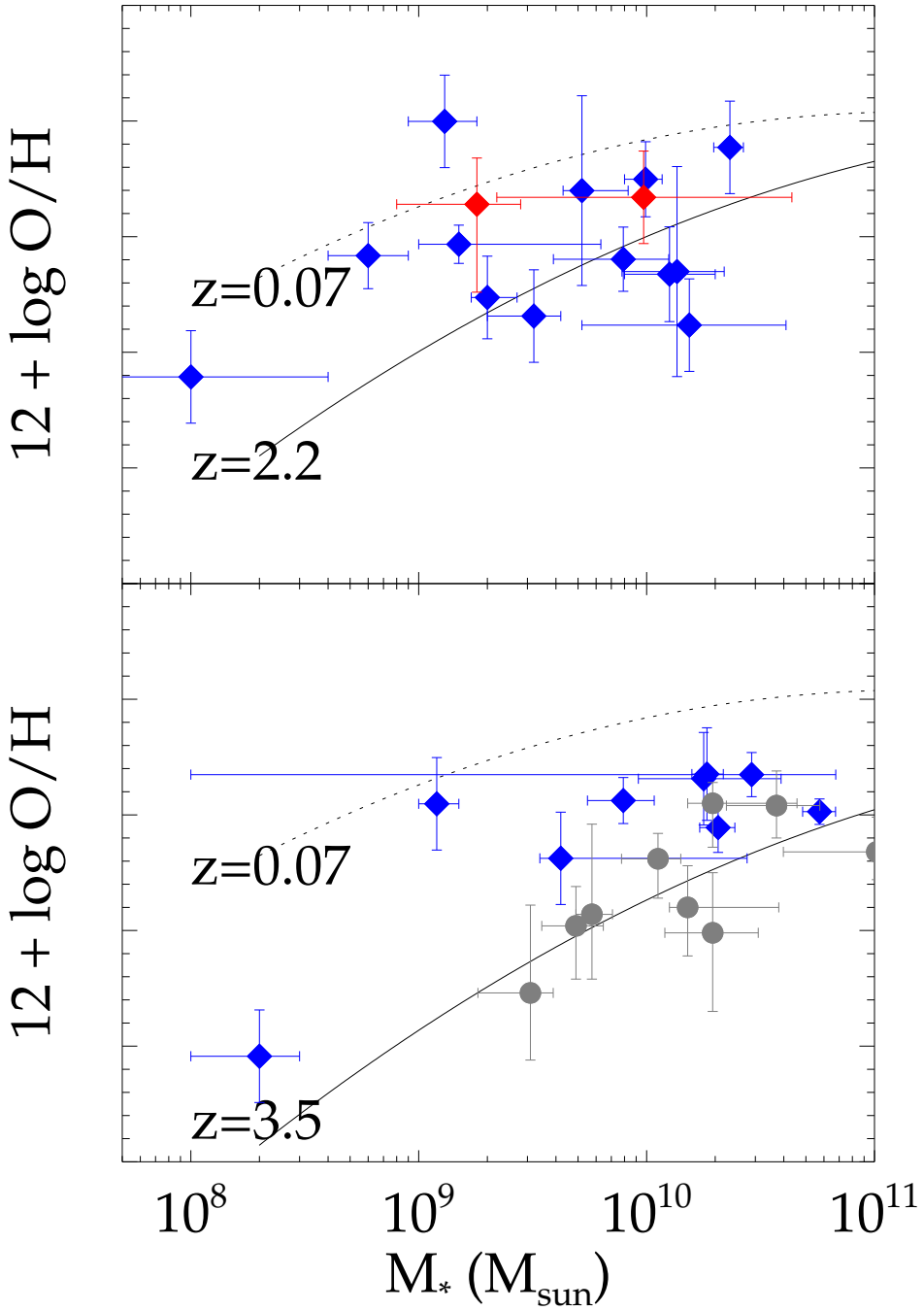

Figure 4.10: The relation between gas-phase metallicity and stellar mass as a function of redshift. This is based on the diagram presented by Maiolino et al. (2008), with their measurements of galaxies at $z \sim 3.5$ shown as grey points. The local mass-metallicity relation is shown as a dotted line for $z = 0.07$, while their best fits at $z \sim 2.2$ and $z \sim 3.5$ are shown as solid lines in the top and bottom panels respectively. The lensed galaxies are shown as blue diamonds and separated into redshift bins of $1.5 < z < 2.5$ (top panel) and $2.5 < z < 3.5$ (bottom panel). Values derived from the two composite spectra (see §2.2.5) are shown as red points in the left panel.

the quantity

$$x = \log M_* - 0.32 \log \mathrm{SFR} - 10 \tag{4.3}$$

where metallicity is given by

$$12 + \log O/H = 8.90 + 0.47x \tag{4.4}$$

for the case $x < 0.2$, which applies to the entire lensed galaxy sample. We computed the expected metallicity for the lensed galaxies using Equation 4.4 and find that on average, measured metallicities are in better agreement with the FMR than with the redshift-dependent mass-metallicity relation. Figure 4.11 shows the difference $\Delta \log \mathrm{O/H}$ between measured metallicity and that predicted by the FMR. Measured metallicities are slightly lower than predicted, with average $\Delta \log \mathrm{O/H} = -0.14$ dex and a standard deviation of 0.30 dex. Considering sample statistics, the mean difference is -0.14 ± 0.06 dex such that our measurements are compatible with the FMR at a 2σ level.

One of the most important caveats of the proposed fundamental metallicity relation is that galaxies observed at different redshifts probe *different regions* of the mass-SFR plane. This is partly due to the trend of specific SFR increasing at higher redshifts, but largely imposed by instrumentation limits. In practice, emission lines needed for metallicity measurements can only be detected in the most actively star forming galaxies at high redshift (e.g., SFR $\gtrsim 10$ $\mathrm{M_\odot yr^{-1}}$at $z \simeq 2$), whereas such high SFR is rare in the local universe. Hence, galaxies used to constrain the fundamental metallicity at $z > 1$ are disjoint from those at $z \simeq 0$ in the sense that the range of SFR in these two samples does not overlap. Therefore, previous surveys do not actually provide any evidence for a fundamental relation which does not evolve with time.

Thanks to the lensing selection which enables us to measure metallicity in a significant sample of galaxies with SFR < 10 $\mathrm{M_\odot yr^{-1}}$, we are uniquely able to constrain whether the proposed FMR is truly time-invariant over $0 < z < 2.5$, a period of 11 Gyr. Four lensed galaxies in our sample (A2218_Ebbels, MACS0451, CL0949, and MACS0712) have stellar mass and SFR within the range of SDSS galaxies from which Mannucci et al. (2010) determine the FMR. Hence, these sources provide a direct measurement of FMR evolution. Figure 4.11 shows that all four have metallicity lower than predicted by the locally-determined FMR. These galaxies have redshifts $2.0 < z < 2.65$ with mean $z = 2.4$. On average, their metallicities are lower than SDSS galaxies at fixed stellar mass and SFR by $\Delta \log \mathrm{O/H} = -0.44 \pm 0.11$ dex. Formally, time invariance of the FMR is therefore ruled out with 4σ significance, however we caution that this is a very small sample and could suffer from systematic errors. In particular, high redshift galaxies selected to have M_* and SFR comparable to samples in the SDSS will have lower specific SFR than typical galaxies at similar redshift. This selection will therefore be biased to include galaxies with measurement errors in the sense that M_* is higher (or SFR is lower) than the true value. Both of these biases will result in a higher predicted metallicity and hence this may explain the observed discrepancy. Of course, it is also likely that the FMR is

not time invariant, as suggested by our data. One possible explanation for the observed increase in gas-phase metallicity at lower redshifts is that gas accreted from the intergalactic and circumgalactic media is more highly enriched at later times, for example by "galactic fountain" processes (e.g., Werk et al. 2011; Davé et al. 2011).

In summary, the lensed galaxies are in better agreement with the FMR proposed by Mannucci et al. (2010) than with the mass-metallicity relation. We have made the first direct measurement of time evolution of the FMR, and find a significant evolution in metallicity at fixed stellar mass and SFR in the sense that metallicity increases at lower redshifts. Although we caution that this result is based on only four galaxies and may suffer from systematic errors, these data suggest that the FMR is *not* a fundamental relation in that it does not adequately describe galaxies at all redshifts.

4.3 Summary and Perspectives

We have presented the results of a near-infrared spectroscopy survey of intrinsically faint gravitationally lensed galaxies at high redshift. Our sample comprises 21 galaxies at $1.5 < z < 3.3$ complemented by an additional 5 sources from the literature. We summarize here our findings:

- After correction for the magnification factor, our sample shows on average $10\times$ smaller star-formation rates and $5\times$ smaller stellar masses than the samples of LBGs at the same redshifts. Half of the galaxies in our sample have intrinsic SFR < 10 $M_{\odot}yr^{-1}$. Such low values of SFR would not be accessible without the strong lensing effect, making our sample complementary to larger surveys of LBGs.

- The comparison of dynamical and stellar mass estimates reveals the presence of significant gas fractions ($\sim 40\%$ in average), which are compatible with a simple estimation from their star formation rate density assuming the Kennicutt (1998) law.

- We estimate the ionization parameter U for 12 galaxies where [OIII]/[OII] line ratios are available, and derive high values of $\log U \sim -2.5$. The highest ionization values are preferentially found in galaxies with the youngest stellar populations (< 100 Myr).

- Gas-phase metallicities are calculated from a combination of independent strong line ratios. We find a weaker evolution in the mass-metallicity relation compared to estimates from bright LBGs observed in blank fields, with an offset in metallicity reaching ~ 0.25 dex in the low stellar mass range ($\sim 10^9$ $M_{\odot}$). This effect is seen both in the majority of individual sources and in composite spectra created from high signal-to-noise data as well as low-mass galaxies.

- Assuming that the evolution in the mass-metallicity relation is due to the increasing SFR at higher redshifts, we compare our results with the fundamental relation of mass, metallicity and SFR as proposed by Mannucci et al. (2010). This relation predicts a metallicity which is on

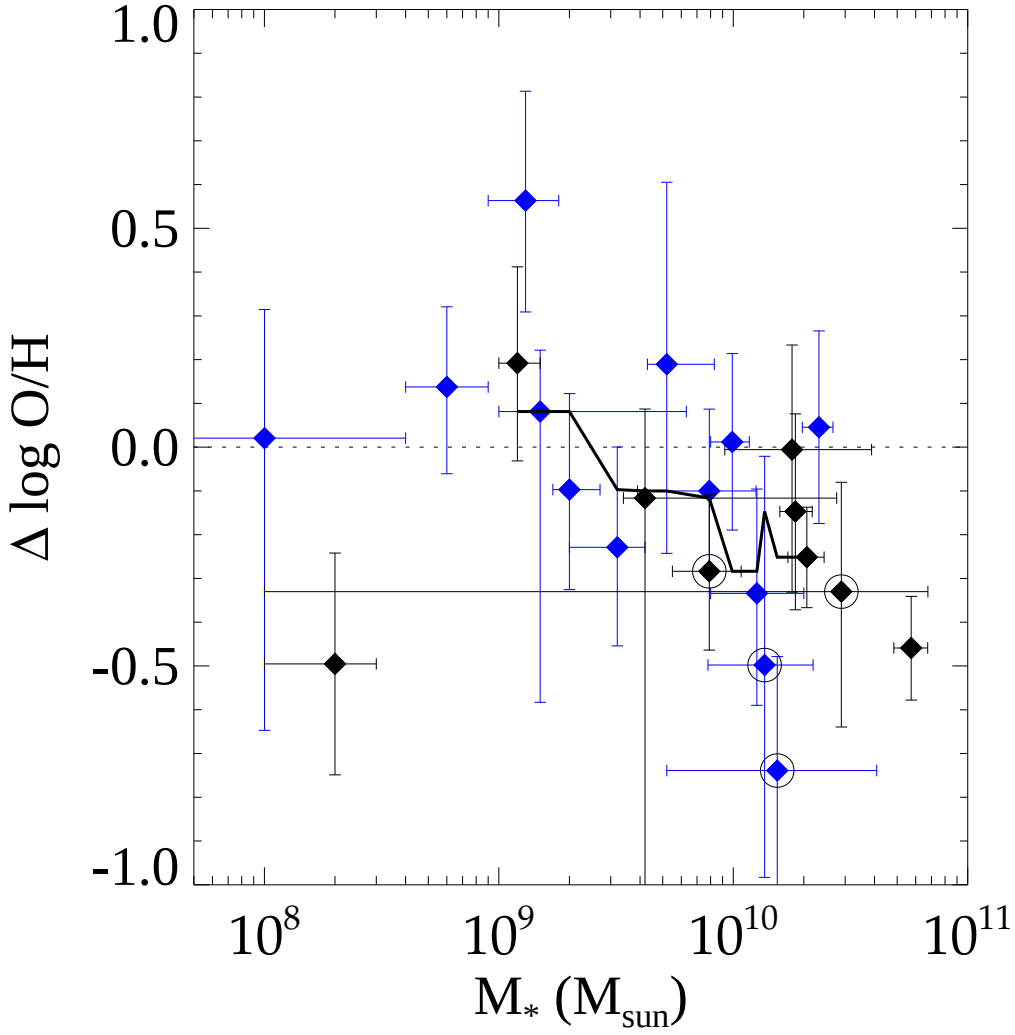

Figure 4.11: Variation between the measured metallicity and the *fundamental metallicity relation* proposed by Mannucci et al. (2010), shown as a function of the stellar mass. Blue and black points are the $1.5 < z < 2.5$ and $2.5 < z < 3.5$ subsamples, respectively, and we show a running median over 7 galaxies as the solid black line. The fundamental relation predicts the average metallicity of our lensed galaxies in both redshift ranges to within 0.14 dex on average. Galaxies with stellar mass and SFR within the range probed by SDSS are circled. Error bars in $\Delta \log \mathrm{O/H}$ include uncertainty in the measured stellar mass, SFR, and metallicity.

average 0.14 dex higher than measured for the lensed galaxies. For the first time we directly test whether this relation varies with time, and find significant evolution with metallicity increasing by 0.44 ± 0.11 dex at fixed mass and SFR between $z = 2.4$ and the present epoch. This result suggests that the mass-metallicity-SFR relation is not fundamental (i.e., not time-invariant), although we caution that it is based on a small sample of only four galaxies and may be affected by systematic errors.

We foresee that ongoing and future HST programs observing lensing clusters will continue to detect large number of strongly magnified high redshift galaxies, which will be ideal targets for deep spectroscopic campaigns similar to the current work. Near-infrared spectrographs such as MOSFIRE, KMOS, and NIRES will soon be able to extend these studies to even fainter luminosities than studied here. Gravitational lensing provides a unique opportunity to extend detailed studies of high redshift galaxies to much lower SFR and stellar mass ($\sim 10^8$ $M_\odot$) and consequently provide more constraints on the mass-metallicity relation for a wide range of stellar mass, SFR, metallicity and redshift.

Target	R.A. (2000.0)	Dec. (2000.0)	z	Ref. z	μ (mags)	Ref. μ
CEYE	21:35:12.712	−01:01:43.91	3.074	(1)	3.69±0.12	(19)
8OCLOCK	00:22:41.009	+14:31:13.81	2.736	(2)	$2.72^{+0.8}_{-0.4}$	(2)
MACS0744	07:44:47.831	+39:27:25.50	2.209	(3)	3.01±0.18	(5)
Cl0024	00:26:34.407	+17:09:54.97	1.679	(6)	1.38±0.15	(20)
MACS0451	04:51:57.186	+00:06:14.87	2.013	(3)	4.22±0.27	(5)
MACS1423	14:23:50.775	+24:04:57.45	2.530	(8)	1.10±0.12	(8)
RXJ1053	10:53:47.707	+57:35:10.75	2.576	(9)	4.03±0.12	(28)
A2218-Ebbels	16:35:49.179	+66:13:06.51	2.518	(11)	3.81±0.30	(12)
A2218-Flanking	16:35:50.475	+66:13:06.38	2.518	(12)	2.76±0.21	(12)
MACS0712	07:12:17.534	+59:32:14.96	2.646	(3)	3.60±0.32	(5)
Cl0949	09:52:49.716	+51:52:43.45	2.394	(13)	2.16±0.24	(13)
A2218-Mult	16:35:48.952	+66:12:13.76	3.104	(12)	3.39±0.18	(12)
A2218-Smm	16:35:55.033	+66:12:37.01	2.517	(14)	3.01±0.16	(12)
CL2244	22:47:11.728	−02:05:40.29	2.240	(15)	4.08±0.30	(15)
J1038	10:38:41.8	+48:49:19	2.20	(27)	2.31±0.09	(27)
HORSESHOE	11:48:33.140	+19:30:03.20	2.379	(17)	3.70±0.18	(17)
CLONE	12:06:02.090	+51:42:29.52	2.001	(18)	3.62±0.12	(24)
AC114-S2	22:58:48.826	−34:47:53.33	1.867	(16)	2.01±0.17	(22)
AC114-A2	22:58:47.787	−34:48:04.33	1.869	(16)	1.70±0.15	(22)
A611	08:00:57.862	+36:03:29.30	1.490	(29)	3.02±0.20	(25)
RXJ2129	21:29:40.843	+00:05:23.00	1.522	(29)	4.45±0.31	(25)
A1413	11:55:18.963	+23:23:58.82	2.038	(25)	3.45±0.28	(25)
A1835	14:01:00.951	+02:52:23.40	2.071	(13)	4.50±0.32	(13)
RXJ1720	17:20:10.251	+26:37:26.91	2.220	(29)	3.38±0.47	(25)
A773	09:17:57.410	+51:43:46.56	2.303	(25)	3.61±0.29	(25)
MACS0717	07:17:32.522	+37:45:02.30	2.552	(25)	2.14±0.45	(25)
A383	02:48:02.283	−03:31:59.52	2.577	(10)	3.66±0.26	(10)
A1689	13:11:26.466	−01:19:56.28	3.042	(4)	4.43±0.33	(13)
A1703	13:15:03.017	+51:49:54.71	3.285	(26)	4.16±0.51	(26)

(1) Smail et al. (2007) (2) Allam et al. (2007) (3) Jones et al. (2010a) (4) Frye et al. (2007) (5) Richard et al. in preparation (6) Broadhurst et al. (2000) (7) Bradač et al. (2008) (8) Limousin et al. (2010) (9) Hasinger et al. (1998) (10) Newman et al. (2011) (11) Ebbels et al. (1996) (12) Elíasdóttir et al. (2007) (13) Richard et al. (2010a) (14) Kneib et al. (2004) (15) Mellier et al. (1991) (16) Lemoine-Busserolle et al. (2003) (17) Belokurov et al. (2007) (18) Lin et al. (2009) (19) Dye et al. (2007) (20) Jauzac et al. in preparation (21) Smith et al. in preparation (22) Campusano et al. (2001) (23) Bian et al. (2010) (24) Jones et al. (2010b) (25) Richard et al. (2010b) (26) Richard et al. (2009) (27) Chapter 3 (28) Richard et al. (2011) (29) Belli et al. in preparation

Table 4.1: The current sample of lensed galaxies. From left to right: astrometry, redshift and reference, magnification and reference. Sources are divided into the NIRSPEC (top), literature (middle), and Triplespec (bottom) samples.

Run	Date	Seeing ($''$)	Conditions
A	2006 July 24	0.8	Clear
B	2007 January 12	1.0	Clear
C	2007 May 3	0.5−0.6	Clear
D	2007 September 1	0.5	Photometric
E	2008 March 23	0.4−0.5	Photometric
F	2008 August 24	0.5−0.9	Clear
G	2010 August 22,25,26	0.9−1.3	Clear/Cirrus
H	2011 April 10−13	0.9−1.3	Cirrus/Cloudy
I	2012 January 12−14	1.0−2.5	Cirrus/Cloudy
J	2012 April 29−May 1	0.9−1.7	Clear/Cirrus

Table 4.2: NIRSPEC (A-F) and Triplespec (G-I) observing runs and conditions.

ID	z	Runs	[OII]	[NeIII]	Hβ	[OIII]λ5007	Hα	[NII]λ6584
CEYE	3.074	A	983 ± 92		490 ± 22	1030 ± 32		
8OCLOCK	2.736	B	2690 ± 66		1582 ± 236		7450 ± 90	1140 ± 37
MACS0744	2.209	B			600 ± 200	1200 ± 200	2000 ± 200	600 ± 60
Cl0024	1.679	D					1140 ± 34	323 ± 19
MACS0451	2.013	D			1174 ± 61	7899 ± 118	3170 ± 59	729 ± 30
MACS1423	2.530	E			123 ± 40	120 ± 22	313 ± 39	< 138
RXJ1053	2.576	E	510 ± 26		624 ± 32	1980 ± 45	1640 ± 42	213 ± 18
A2218_Ebbels	2.518	E	164 ± 13		108 ± 11	170 ± 13	273 ± 18	< 63
A2218_Flanking	2.518	E			180 ± 14	402 ± 20	444 ± 22	< 42
MACS0712	2.646	E	< 96		352 ± 20	719 ± 40	1070 ± 34	225 ± 19
Cl0949	2.394	E	321 ± 20		< 126	819 ± 30	403 ± 20	< 36
A2218_Mult	3.104	F	1310 ± 40		871 ± 31	1920 ± 70		
A2218_Smm	2.517	F			688 ± 29	1030 ± 34		
CL2244	2.239	ISAAC	370 ± 80		< 126	67 ± 10	463 ± 70	< 60
J1038	2.20				1900 ± 700	10000 ± 500	6600 ± 500	500 ± 500
Horseshoe	2.3813		2000 ± 100	< 400	700 ± 100	3120 ± 60	5390 ± 90	870 ± 70
Clone	2.0026		8500 ± 500	< 2800	3300 ± 400	17300 ± 200	20200 ± 500	3900 ± 200
AC114_S2	1.867		370 ± 70			860 ± 40	1560 ± 90	< 120
AC114_A2	1.869		150 ± 40			250 ± 40	770 ± 80	330 ± 40
A611	1.4902	H			1594 ± 422	8995 ± 373	4854 ± 596	< 595
RXJ2129	1.5219	G			667 ± 404	2544 ± 463	1728 ± 317	< 591
A1413	2.0376	H,I,J	< 5421	882 ± 270	1967 ± 790	13970 ± 221	7534 ± 278	< 152
A1835	2.0734	H	4082 ± 1425	806 ± 316	1904 ± 396	3626 ± 440	2911 ± 668	< 818
RXJ1720	2.2200	G	< 618	< 559	2895 ± 878	4833 ± 739	3018 ± 408	851 ± 265
A773	2.303	I	2392 ± 576	< 3265	1389 ± 821	3085 ± 489	2638 ± 660	< 872
MACS0717	2.5515	J	1286 ± 271	< 764	380 ± 138	1106 ± 133	1200 ± 375	< 1202
A383	2.577	I	1064 ± 474	< 3739	921 ± 330	1074 ± 139	1700 ± 442	< 577
A1689	3.042	J	< 1676	1679 ± 651	1875 ± 505	7048 ± 957		
A1703	3.2846	H	1810 ± 702	669 ± 113	1381 ± 314	9963 ± 247		
S/N Composite			[NII]λ6584/Hα=0.16±0.03, [SII]$\lambda\lambda$6717, 6731/Hα=0.11±0.04					
Low M_* Composite			[NII]λ6584/Hα=0.13±0.10					

Table 4.3: Emission line measurements. Fluxes are given in units of 10^{-19} ergs s^{-1} cm^{-2}. 3σ upper limits are given in cases where a line is not detected. Galaxies are separated into three samples: NIRSPEC sources (top), various literature sources (middle), and Triplespec sources (bottom).

ID	z	$r_{1/2}$ (kpc)	σ (km/s)	M_{dyn} (10^{10} $M_\odot$)	M_* (10^{10} $M_\odot$)	SFR ($M_\odot\ yr^{-1}$)	SFR_{corr} ($M_\odot\ yr^{-1}$)	log(Z)	E(B-V)
CEYE	3.074	1.75±0.21	$54\pm4^{(a)}$	$0.59^{+0.16}_{-0.11}$	$5.74^{+1.01}_{-0.90}$	37.6±8.6	77.3±17.6	8.51±0.06	0.17
8OCLOCK	2.736	1.47±0.38	45±5	$0.35^{+0.16}_{-0.13}$	$1.78^{+2.11}_{-0.86}$	98.0±58.	232±137	8.66±0.20	0.22
MACS0744	2.209	1.00±0.22	81^{+9}_{-9}	$0.76^{+0.33}_{-0.25}$	$0.99^{+0.18}_{-0.19}$	6.6±1.7	11.9±3.1	8.75±0.16	0.19
Cl0024	1.679	10.0±1.2	$69\pm5^{(a)}$	$5.52^{+1.45}_{-1.06}$	$2.32^{+0.34}_{-0.35}$	14.6±3.6	34.5±8.4	8.89±0.20	0.28
MACS0451	2.013	2.50±0.33	$80\pm5^{(a)}$	$1.86^{+0.47}_{-0.36}$	$1.36^{+0.83}_{-0.58}$	3.4±1.1	5.9±1.9	8.35±0.45	0.18
MACS1423	2.530					8.5±1.9		8.79±0.20	
RXJ1053	2.576	3.62±0.45	68^{+6}_{-6}	$1.94^{+0.58}_{-0.41}$	$0.42^{+2.34}_{-0.08}$	3.8±0.9	90.5±20.7	8.31±0.19	0.37
A2218-Ebbels	2.518				$0.79^{+0.29}_{-0.24}$	0.7±0.2	1.1±0.3	8.56±0.10	0.16
A2218-Flanking	2.518	2.36±0.55	50^{+17}_{-24}	$0.68^{+0.62}_{-0.48}$	$0.12^{+0.03}_{-0.02}$	2.3±0.6	5.5±1.5	8.55±0.20	0.28
MACS0712	2.646	0.75±0.23	82^{+15}_{-17}	$0.58^{+0.39}_{-0.30}$	$2.89^{+3.87}_{-2.88}$	3.0±1.1	5.6±2.0	8.67±0.10	0.20
Cl0949	2.394	3.50±0.88	$66\pm3^{(a)}$	$1.77^{+0.60}_{-0.52}$	$1.54^{+2.55}_{-1.02}$	3.6±1.1	7.5±2.2	8.12±0.20	0.24
A2218-Mult	3.104	3.75±0.44	57^{+21}_{-30}	$1.41^{+1.19}_{-0.90}$	$2.06^{+0.38}_{-0.35}$	18.6±4.9	216±56	8.44±0.11	0.58
A2218-Smm	2.517	1.86±0.40	82^{+7}_{-7}	$1.45^{+0.56}_{-0.43}$	$1.84^{+0.33}_{-0.26}$	10.1±2.5	21.7±5.4	8.68±0.20	0.18
CL2244	2.2399				$0.13^{+0.05}_{-0.04}$	1.4±0.5	2.1±0.7	9.00±0.20	0.13
Composite 1	2.37 ± 0.34				$0.97^{-0.75}_{+3.37}$			8.67±0.20	
Composite 2	2.52 ± 0.10				$0.18^{-0.10}_{+0.10}$			$8.64^{+0.20}_{-0.38}$	
J1038[(d)]	2.20		82±22		$0.20^{+0.07}_{-0.03}$	23±2	38^{+37}_{-15}	8.24±0.18	0.14
HORSESHOE[(c)]	2.38	1.3	90±33	1.3	$0.79^{+0.46}_{-0.40}$	73±1	210±67	8.40±0.14	0.15
CLONE[(c)]	2.00	1.7	104±37	2.1	$1.26^{+0.74}_{-0.46}$	32±1	68^{+44}_{-24}	8.34±0.21	0.24
AC114-S2[(b)]	1.867			0.53±0.12	$0.32^{+0.10}_{-0.12}$	30±2	75±4	8.16±0.20	0.30
AC114-A2[(b)]	1.869			2.36±0.67	$0.52^{+0.31}_{-0.09}$	15±2	51±5	8.70±0.41	0.40
A611	1.490				$0.01^{+0.03}_{-0.006}$	3.3±0.9	3.8±1.0	7.89±0.20	0.05
RXJ2129	1.522					0.3±0.1	0.3±0.1	7.89±0.43	0
A1413	2.038					7.5±2.4	14.6±4.7	7.90±0.20	0.22
A1835	2.071	1.52±0.07	124^{+39}_{-43}	$2.71^{+1.82}_{-1.06}$	$0.06^{+0.03}_{-0.02}$	0.9±0.3	2.0±0.8	8.42±0.14	0.26
RXJ1720	2.220					4.0±1.8	4.0±1.8	8.71±0.05	0
A773	2.303	0.38±0.05	66^{+21}_{-29}	$0.19^{+0.15}_{-0.11}$	$0.15^{+0.48}_{-0.05}$	3.1±1.1	7.0±2.5	8.47±0.08	0.27
MACS0717	2.552					6.9±3.6	8.7±4.5	8.49±0.04	0.07
A383	2.577					2.5±0.9	2.5±0.9	8.61±0.14	0
A1689	3.042	0.30±0.10	101^{+8}_{-8}	$0.35^{+0.17}_{-0.15}$	$0.02^{+0.01}_{-0.01}$	5.7±2.3	9.9±4.0	7.46±0.20	0.18
A1703	3.285					6.6±3.2	6.6±3.2	7.82±0.04	0

[(a)]Jones et al. (2010a) [(b)]Lemoine-Busserolle et al. (2003) [(c)]Hainline et al. (2009) [(d)]Chapter 3

Table 4.4: Physical properties of the sample. From left to right: ID, redshift, magnification, half-light radius, measured velocity dispersion (corrected from instrumental resolution, see text for details), dynamical mass, stellar mass, SFR, metallicity, stellar extinction from the SED fitting. The SFR and stellar masses are corrected for the lensing magnification factor, and include the aperture corrections. Average redshift and stellar mass are given for the composite spectra described in the text.

ID	β	F450W(B) F475W(B')	F555W(G) F606W(V) F702W(R)	F775W(I') F814W(I)	F850LP	F110W/J	F160W/H	K/Ks	IRAC 3.6μm	IRAC 4.5μm
8OCLOCK	1.60±0.15	B 21.94±0.10	V 21.36±0.10	I 21.10±0.10		J 21.12±0.10	H 20.77±0.10		20.16±0.12	19.84±0.12
COSMICEYE	0.38±0.11		V 20.54±0.02	I 20.01±0.05		J 20.07±0.05	H 19.32±0.05	K 18.82±0.10	18.26±0.15	18.31±0.15
MACS0744	1.30±0.07		G 23.04±0.03	I 22.73±0.03				Ks 21.22±0.24	20.45±0.08	20.42±0.16
A1689-Sextet	1.77±0.19	B' 23.25±0.05	V 22.36±0.05	I' 22.29±0.05	22.34±0.05	J 22.36±0.05	H 21.94±0.05	K 21.89±0.05	21.87±0.05	22.02±0.05
Cl0024	1.04±0.21	B' 21.78±0.06	V 21.53±0.06	I' 21.32±0.06	21.10±0.07	J 20.59±0.08	H 20.27±0.08	K 20.12±0.12	19.56±0.10	19.58±0.10
MACS0451	1.61±0.21		V 19.60±0.07	I 19.47±0.07					17.77±0.16	17.80±0.16
MACS1423	2.43±0.05		V 23.78±0.06	I 23.70±0.06				$Ks > 23.08$		
RXJ1053	[2.0]		V 21.25±0.05				H 20.01±0.10			
A2218-Ebbels	1.89±0.15	B' 21.24±0.11	V 20.75±0.06	I' 20.66±0.06	20.71±0.06	J 20.44±0.08	H 19.78 ±0.08	K 19.79±0.12	19.41±0.16	19.39±0.16
A2218-Flanking	1.86±0.13	B' 23.32±0.05	V 22.70±0.05	I' 22.61±0.05	22.65±0.05	J 22.31±0.08	H 22.08±0.09	K 22.17±0.14		
MACS0712	1.17 ± 0.15		V 21.93±0.05	I 21.65±0.05						
Cl0949	[2.0]		V 22.09±0.05						20.13±0.20	
A1835	1.76 ± 0.15		R 21.35±0.07		21.28±0.05	J 20.84±0.07	H 20.87±0.04	K 20.51±0.08		
A773	[2.0]		R 22.67±0.05						21.26±0.12	21.10±0.14
A2218-Mult	1.22±0.14	B' 24.95±0.16	V 22.23±0.06	I' 21.95±0.05	21.93±0.05			K 19.91±0.13	18.93±0.14	18.74±0.13
A2218-Smm	1.52±0.11	B' 23.52±0.05	V 23.12±0.05	I' 23.13±0.05	22.97±0.04	J 22.65 ±0.07	H 21.88±0.11	K 21.29±0.14	20.45±0.12	20.09±0.13
CL2244	1.76±0.15		G 21.35±0.06	I 21.25±0.06		J 20.74±0.18	H 20.49±0.18		20.53±0.12	20.34±0.12
AC114-A2	0.98±0.17		R 22.16±0.06		21.86±0.05	J 21.19±0.18	H 21.30±0.11	K 20.92±0.13		
AC114-S2	1.25±0.17		R 22.96±0.06		22.74±0.04	J 22.33±0.07	H 22.21±0.06	K 22.04±0.07	21.63±0.12	21.51±0.08

Table 4.5: Multi-walength photometry (AB magnitudes) of the lensed sources in our sample. First column gives the UV β slope (see text for details). We use the notation BB'GVRII'JH as a shortcut for the various HST broad-band filters. Filter names in italics refer to ground-based images.

Chapter 5

The Mean Ultraviolet Spectrum of Lyman Break Galaxies at $z \simeq 4$

Abstract

We present and discuss the mean rest-frame ultraviolet spectrum for a sample of 81 Lyman Break Galaxies (LBGs) selected to be B-band dropouts at $z \simeq 4$. The sample is mostly drawn from our ongoing Keck/DEIMOS survey in the GOODS fields, and augmented with archival VLT data. In general we find similar spectroscopic trends to those found in earlier surveys of LBGs at $z = 3$. Specifically, low-ionization absorption lines which trace neutral outflowing gas are weaker in galaxies with stronger Lyα emission, bluer UV spectral slopes, lower stellar masses, lower UV luminosities, and smaller half-light radii. This is consistent with a physical picture whereby star formation drives outflows of neutral gas which scatters Lyα and produces strong low-ionization absorption lines, while increasing galaxy stellar mass, size, metallicity, and dust content. Typical galaxies are thus expected to have stronger Lyα emission and weaker low-ionization absorption at earlier times, and we indeed find somewhat weaker low-ionization absorption at higher redshifts. In conjunction with earlier results from our survey, we argue that the reduced low-ionization absorption is likely caused by lower covering fraction and/or velocity range of outflowing neutral gas at earlier epochs. Although low-ionization absorption decreases at higher redshift, fine structure emission lines are stronger suggesting a greater concentration of neutral gas at small galactocentric radius ($\lesssim 5$ kpc). Our continuing survey will enable us to extend these diagnostics more reliably to higher redshift and determine the implications for the escape fraction of ionizing photons which governs the role of early galaxies in cosmic reionization.

1 Introduction

Considerable progress has been made over the past decade in charting the demographics of high redshift galaxies. Multi-wavelength surveys have defined the luminosity functions of UV and sub-mm selected star-forming sources (Reddy & Steidel, 2009; Wardlow et al., 2011) as well as the coeval population of quiescent massive red galaxies (Brammer et al., 2011). Spitzer data has revealed the time-dependent *stellar mass density* - a complementary quantity which represents the integral of the past star formation activity (e.g., Stark et al. 2009). Through these surveys a well-defined picture of the history of star formation and mass assembly over $0 < z < 6$ has been empirically determined (Hopkins & Beacom, 2006; Ellis, 2008; Robertson et al., 2010). The redshift range $2 < z < 3$ corresponds to the peak of star formation activity where the Hubble sequence starts to emerge, and the earlier era corresponding to $3.5 < z < 5$ is an even more formative one where mass assembly was particularly rapid.

Intermediate dispersion spectroscopy of carefully-selected Lyman break galaxies (LBGs) has been particularly important in defining population trends that cannot be identified from photometric data alone. A very influential study at $z \simeq 3$ was undertaken by Shapley et al. (2003) who used composite Keck LRIS spectra of various subsets of nearly 1000 LBGs to examine the role of hot stars, HII regions and dust obscuration, as well as to measure the outflow kinematics and absorption line properties of neutral and ionized gas. Composite spectra are particularly useful for measuring weak lines which cannot be studied in detail for individual objects. Through these careful studies, a detailed picture of the mass-dependent evolution of LBGs has emerged (see Shapley 2011 for a recent review).

In earlier papers in this series (Stark et al. 2010, hereafter Paper I; Stark et al. 2011, hereafter Paper II), we introduced an equivalent spectroscopic survey of LBGs selected from a photometric catalog of more distant LBGs with $3 < z < 7$ in the Great Observatories Origins Deep Survey (GOODS) fields (Giavalisco et al., 2004; Stark et al., 2009). Whereas the Shapley et al. (2003) study targeted the study of LBGs close to the peak of activity in the overall cosmic star formation history, this earlier period corresponds to a less well-studied era when the rate of mass assembly is particularly rapid. From photometric data alone, Stark et al. (2009) deduced some significant changes in the characteristics of star formation at $z \simeq 4 - 6$ compared to later times, for example a shorter timescale of activity ($\simeq 300$ Myr). We considered it crucial to understand these changes in LBG properties if these galaxies are to be used as probes of cosmic reionization at higher redshifts.

At the time of writing, our Keck survey is continuing with increasing emphasis at high redshift. Paper I presented the first substantial results from a survey of LBGs at $3.5 < z < 6$ observed with the Keck/DEIMOS spectrograph. Paper II augmented this data with a further sample following more ambitious exposures focusing primarily on $z \simeq 6$ LBGs. Incorporating a sample of ESO VLT spectra, retrospectively selected using similar photometric criteria as those for the Keck sample from

the FORS2 study of Vanzella et al. (2005, 2006, 2008, 2009), the current dataset amounts to a sample of 546 galaxies over the redshift range $3.5 < z < 6.3$.

Our earlier papers in this series concentrated primarily on the rate of occurrence of Lyman α (Lyα) emission in our spectra (the "Lyα fraction"). The overall goal was to understand the significantly different evolutionary trends in the luminosity functions of LBGs and narrow-band selected Lyα emitters (LAEs, Ouchi et al. 2008) prior to the use of the Lyα fraction as a test of when reionization ended (Schenker et al., 2012). Paper I confirmed a result found by Shapley et al. (2003) at lower redshift, namely that Lyα emission is more frequent in lower luminosity LBGs rising to a high proportion $\simeq 50\%$ at $M_{UV} = -19$. More importantly, the Lyα fraction was found to rise modestly with redshift over $3 < z < 6$. By correlating the visibility of Lyα emission with UV continuum slopes derived from the HST photometry, it was argued that these trends in the visibility of line emission most probably arise from different amounts of dust obscuration. Reduced dust extinction in lower luminosity LBGs and those at higher redshift has also been deduced from studies of larger photometric samples (Bouwens et al. 2009, see also Reddy & Steidel 2009).

Paper I also discussed the possibility that the covering fraction of hydrogen may be lower in low-luminosity LBGs. Strong Lyα emission in luminous LBGs is often associated with low equivalent width interstellar absorption lines arising from a non-uniform covering fraction of neutral hydrogen (Quider et al., 2009; Shapley et al., 2003). This trend suggests that the high Lyα fraction in faint LBGs is partially due to a lower covering fraction, which would imply that Lyman continuum photons may more easily escape from intrinsically faint $z \simeq 4-6$ galaxies. Such a result would have great importance in understanding the role of $z > 7$ galaxies in maintaining cosmic reionization (Robertson et al., 2010).

The present paper represents our first analysis of the spectral properties of $z \simeq 4-5$ LBGs derived from composite spectra in the manner pioneered at $z \simeq 3$ by Shapley et al. (2003). The large database now amassed following the campaigns at Keck and the VLT makes a similar study now practical in the redshift range where there is evidence of increased short-term star formation and the mass assembly rate is particularly rapid. Via detailed studies of low-ionization absorption line and emission line profiles, we aim to examine possible changes in the kinematics and covering fraction of neutral gas, which affects the strength of Lyα and the escape fraction of ionizing photons, as we approach the reionization era. As our redshift survey continues, in this paper we focus on a sample of galaxies with $3.5 < z < 4.5$, selected as B-dropout LBGs. Combining our Keck sample with data from the VLT (see Paper I for details), herein we examine the spectral features and trends in composite spectra drawn from a sample of 131 galaxies.

A plan of the paper follows. We briefly review the spectroscopic observations and their data reduction in §2; much of the relevant discussion is contained in Paper I. In §3 we describe the selection of individual spectra that we consider appropriate for forming the composite mean spectrum at $z \simeq 4$

and the associated sources of uncertainty. §4 examines the mean spectrum in detail and introduces the various diagnostic features in the context of a physical model for LBGs of different masses and star-formation rates. In §5 we compare spectroscopic trends grouped by observable properties such as mass and luminosity with those found at $z \simeq 3$ by Shapley et al. (2003). In §6 we discuss those trends which appear to be redshift-dependent, discussing implications for the role of early star-forming galaxies in cosmic reionization. Finally we summarize our results in §7.

Throughout this paper, we adopt a flat ΛCDM cosmology with $\Omega_\Lambda = 0.7$, $\Omega_M = 0.3$, and $H_0 = 70$ h_{70} km s^{-1}Mpc^{-1}. All magnitudes in this paper are quoted in the AB system (Oke, 1974).

2 Observations and Data Reduction

The rationale and procedures used to undertake our spectroscopic survey of LBGs over $3 < z < 7$ were introduced in detail in Paper I and the interested reader is referred to that paper for further detail. Here we recount only the basic details. Our target LBGs were selected as B, V or i'–band "dropouts" based on deep photometry in the two GOODS fields. The photometric catalog used in our analysis will be described in detail in Stark et al. (2011, in preparation). The selection and photometric approach is largely similar to that described in Stark et al. (2009) and Paper I, but we highlight two key updates. First the selection is performed on the v2 GOODS ACS catalogs. Second, we utilize deep ground-based near-IR imaging in GOODS-N obtained from WIRCAM on CFHT (Wang et al., 2010) and deep HST Wide Field Camera 3 / IR imaging of GOODS-S from CANDELS (Grogin et al., 2011; Koekemoer et al., 2011).

2.1 Keck/DEIMOS

The majority of spectra we present are taken from an ongoing survey with the DEep Imaging Multi-Object Spectrograph (DEIMOS; Faber et al. 2003) on the Keck II telescope. In this paper we have used observations taken in 2008 April and 2009 March (masks GN081, GN082, GN083, GN094, and GN095 in Paper I), which targeted a total of 261 B-drop and 88 V-drop galaxies. These data were taken with the 600 lines mm^{-1} grating, covering the wavelength range 4850–10150 Å with a resolution of $\simeq 3.5$ Å. We do not use data at wavelengths $\lambda > 9200$ Å which are affected by strong and variable absorption by atmospheric water vapor. The seeing was typically $0\farcs8$ and ranged between $0\farcs5$ and $1\farcs0$ during the observations.

All data were reduced and calibrated using a modified version of the IDL pipeline SPEC2D, developed specifically for DEIMOS by the DEEP2 survey team (Davis et al., 2003). The data were reduced as described in Paper I, with the addition of two important modifications. First, the continuum traces of all target galaxies and other objects occupying the same slit were carefully masked to exclude object flux from the sky background model. Second, the b-spline fit to the sky

background was modified to include a 2nd-order polynomial fit to the spatial dimension. These modifications significantly improved the sky subtraction, particularly at long wavengths $\lambda > 7000$ Å where bright sky lines can be problematic.

The reduced one- and two-dimensional spectra were visually inspected using the IDL program SpecPro (Masters & Capak, 2011). Spectra which suffered from poor data quality were excluded from further analysis. The exclusions included unacceptable amounts of scattered light within the detector mosaic, defective CCD columns, contamination from bright nearby sources, or poor sky subtraction, for example arising from the location of the slit on the detector. A few low-redshift interlopers were also identified and excluded from further analysis. For the remaining spectra, redshifts were measured from either Lyα emission (where present) or interstellar absorption lines. Galaxies identified as hosting strong AGN based on the presence of CIV or other strong emission lines were excluded. We identified 5 stars, 2 dusty low-redshift galaxies ($z \sim 0.5$), 4 AGN, and 134 star-forming galaxies with secure redshifts $z > 3$. After rejecting poor data, the final sample consists of 94 high-quality spectra with accurate redshifts. Examples of high redshift dropout spectra are shown in Figure 5.1.

2.2 Archival VLT/FORS2 Spectroscopy in GOODS-S

To augment our sample of high redshift spectra, we have also made use of data from the FORS2 program of Vanzella et al. (2005, 2006, 2008, 2009) which targeted dropouts in the GOODS-S field. The characteristics of that survey in terms of resolution and spectral coverage are very similar to that undertaken at Keck with DEIMOS and details can be found in Paper I. Using the coordinates provided in the published FORS2 database we queried the version 2.0 ACS catalogs for GOODS-S and undertook our own photometric measures and dropout selection criteria in an identical fashion to that used for our Keck survey. The magnitude distribution of the FORS2 sample is generally weighted towards sources brighter than those in the overall Keck survey, but for the purposes of constructing the mean spectra discussed in this paper, the bulk of the individual spectra are of comparable brightness.

2.3 Redshift Measurements

Care is needed in deriving accurate systemic redshifts from rest-frame UV spectra since the strongest features trace the kinematics of outflowing gas rather than that of the stars. Stellar absorption lines are usually too faint to be measured precisely given the signal to noise of the spectra. Typically the only features detected in individual spectra are Lyα and strong interstellar absorption lines such as SiIIλ1260, OIλ1302+SiIIλ1304, CIIλ1334, SiIV$\lambda\lambda$1393,1402, SiIIλ1526, and CIV$\lambda\lambda$ 1548,1550 (Figure 5.1). Absorption by outflowing gas results in a blueshift of interstellar absorption lines.

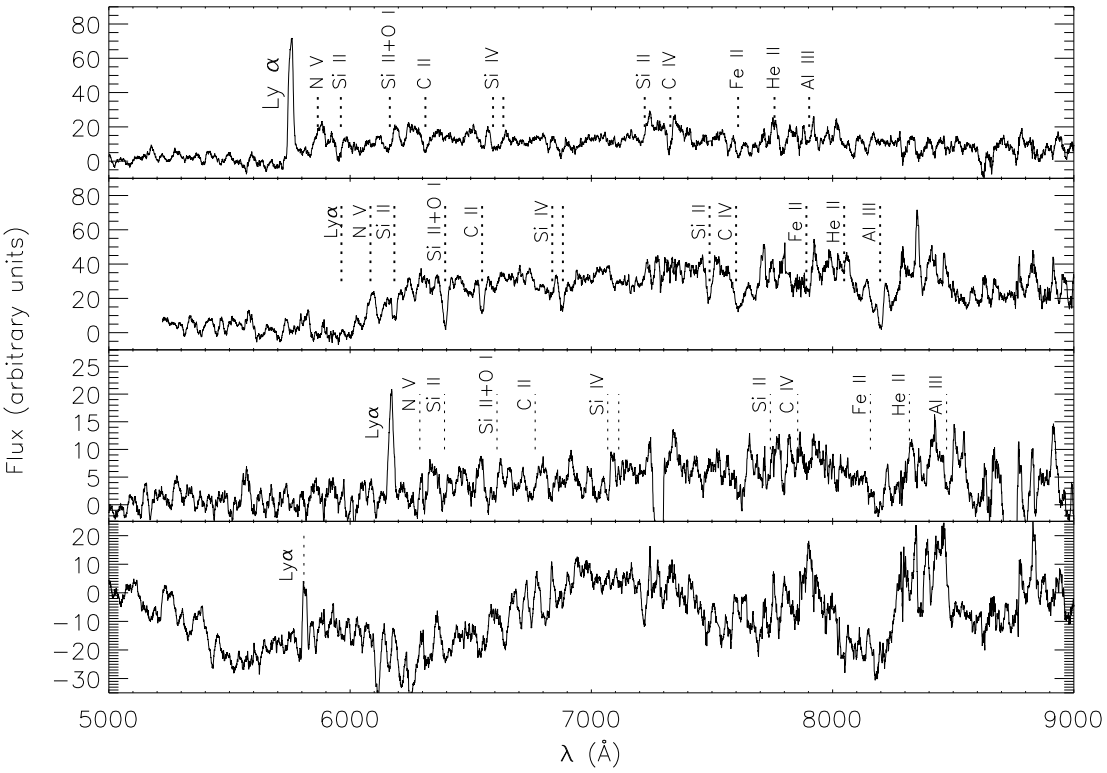

Figure 5.1: Examples of individual DEIMOS spectra for $3.5 < z < 4.5$ LBGs. From top to bottom: a galaxy at $z = 3.73$ with Lyα emission and weak interstellar absorption features; a galaxy at $z = 3.906$ with Lyα and interstellar absorption; a faint galaxy at $z = 4.07$ with Lyα emission and no detectable absorption lines; and galaxy at $z = 3.778$ with Lyα emission whose spectrum is contaminated by scattered light and detector defects. The top three spectra are included in stacking analyses while the bottom spectrum is excluded based on poor data quality. The continuum signal-to-noise in each spectrum degrades noticeably at wavelengths $\lambda > 7000$ Å due to increased OH sky emission.

Outflowing neutral hydrogen along the line of sight leads to a Lyα profile which displays very broad ($\gtrsim 1000$ km s^{-1}) blueshifted absorption and net redshifted emission. The high-ionization SiIV and CIV lines also arise in P-Cygni stellar winds with broad blueshifted absorption. The magnitude of these offsets has been well-quantified for star-forming galaxies at $z \simeq 2.3$, and is typically -200 km s^{-1}for interstellar absorption lines and $+500$ km s^{-1}for Lyα emission (Steidel et al., 2010).

To determine accurate redshifts for making composite spectra, we restrict our sample to those with redshifts measured from either Lyα emission ($z_{Ly\alpha}$) or low-ionization interstellar absorption lines (z_{IS}). Although, as discussed above, these are not at the systemic redshift, we follow well-established techniques to correct for the typical offsets (Steidel et al., 2010). We do not use redshifts based on Lyα absorption or high-ionization lines (SiIV and CIV) because of the complex and variable blueshifts of these features with respect to the systemic redshift. We define $z_{Ly\alpha}$ as the centroid of the emission line and consider only spectra in which the line is detected at $> 5\sigma$ significance. Interstellar absorption line redshifts require careful treatment to avoid spurious identification of sky line residuals. We consider only the low-ionization SiIIλ1260, OIλ1302+SiIIλ1304, and CIIλ1334 features which are typically found in the highest signal-to-noise regions of our spectra. Absorption features at longer wavelengths are less reliable due to the higher density of strong night sky lines, while shorter wavelength transitions are lost in the Lyα forest. To measure absorption line redshifts, we first estimate the redshift from Lyα (either in emission or absorption). We then fit Gaussian profiles to the spectrum near the expected position of the three features above. We require the best fit of all three lines to be consistent to within ± 500 km s^{-1}with a combined significance of $> 5\sigma$. If these conditions are met, we define z_{IS} as the weighted mean redshift of the three interstellar features.

With the criteria above, suitable redshifts are available for a total of 131 high-quality DEIMOS and FORS2 spectra. 91 redshifts are based on measures of $z_{Ly\alpha}$ emission only, 31 have z_{IS} only, and 9 have both $z_{Ly\alpha}$ and z_{IS}. The distribution of redshifts and absolute UV magnitudes for this sample is shown in Figure 5.2. Unless stated otherwise, further analysis in this paper is restricted to the 81 sources with redshift $z < 4.5$ and apparent magnitude $z'_{AB} < 26.0$. We applied this additional magnitude criterion in order to ensure a well-defined continuum signal/noise in each individual spectrum. 53 of these 81 sources are drawn from the Keck survey and 28 from FORS2.

2.4 Sample Bias

While the sample is 90% complete for dropout selected galaxies to an apparent magnitude $z_{AB} = 25$, at fainter magnitudes Lyα emission or strong interstellar absorption features are required for reliable redshifts. This results in a bias towards stronger low-ionization absorption lines for the fraction ($\simeq 35\%$) without Lyα. We can quantify this bias through the detectability of the average low-ionization absorption line strength shown in the composite spectrum in Figure 5.3 (see §3). We find

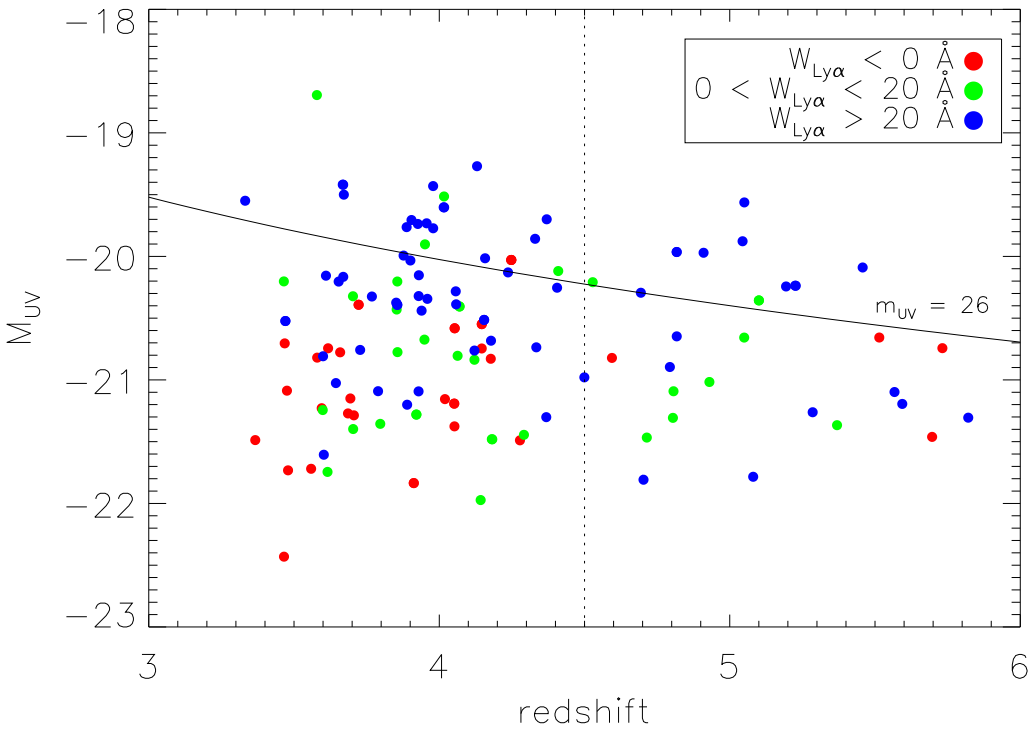

Figure 5.2: Redshifts and UV luminosities for the sample of 131 galaxies with suitably accurate redshifts measured either from Lyα or strong interstellar absorption lines. Points are color-coded according to the equivalent width of Lyα, $W_{Ly\alpha}$. Galaxies brighter than an apparent magnitude $z'_{AB} < 26.0$ (solid line) typically have well-detected continua suitable for forming a composite spectrum. Galaxies with redshift $z < 4.5$ (dashed line) are used for the composite spectra discussed in §3-§5, while §6 includes galaxies at all redshifts shown here.

that we can measure redshifts for this average absorption line strength with 90% completeness at $z_{AB} = 24.7$, declining through 50% at $z_{AB} = 25.2$ to zero at $z_{AB} > 25.5$. Of the galaxies with detected absorption line redshifts, those with $z_{AB} > 25.2$ have line strengths only 10% stronger than for those with $z_{AB} < 25.2$. Clearly this is a small effect.

The bias toward stronger Lyα emission for fainter galaxies is manifest in Figure 5.2 where a paucity of objects with $W_{Ly\alpha} < 20$ Å can be seen at faint magnitudes. This bias was fully quantified in Paper I using Monte Carlo simulations. For galaxies at $3.5 < z < 4.5$, a sample completeness of 95% is reached at $W_{Ly\alpha} \gtrsim 20$ Å for $z'_{AB} = 26$, and $W_{Ly\alpha} \gtrsim 7$ Å for $z'_{AB} = 25$. For the sample presented in this paper, the least biased subset is that with strong Lyα emission, followed by that with bright apparent magnitudes $z'_{AB} < 25$.

A final issue in considering composite spectra is that these are comprised of individual spectra across $3.5 < z < 4.5$ with different rest-frame wavelength ranges. As our spectra generally cover the wavelength range $5000 < \lambda < 9200$ Å, galaxies at $z = 3.5$ contribute to the rest frame $1100 - 2050$ Å, while those at $z = 4.5$ contribute to $900 - 1650$ Å. At longer rest-frame wavelengths the composite spectrum is therefore largely contributed by galaxies at lower redshift. In addition there are wavelength-dependent sources of noise discussed in §3.2. In summary, the data used to construct the composite spectrum in Figure 5.3 correspond to a mean redshift $z = 3.98$ at $\lambda_{rest} = 1100$ Å, $z = 3.95$ at 1200 Å, $z = 3.90$ at 1500 Å, and $z = 3.82$ at 1650 Å. For the wavelength range of interest in this work, the redshift bias $\Delta z < 0.15$ is not particularly troublesome.

3 Composite Spectra

We now turn to the presentation of the composite spectra. We need to account for the difference between the redshifts determined using Lyα on the one hand and the low-ionization interstellar lines on the other hand and the systemic redshift prior to co-addition. We also seek to understand the signal/noise of the composite in terms of the statistical uncertainties and the variance among the individual spectra used to construct the composite.

Composite spectra are constructed by shifting the individual spectra into the rest frame according to a deduced systemic redshift and then averaging the set. In general terms we will first identify a subsample based on their observable properties. Each spectrum in the sample is shifted to the adopted rest frame and interpolated to a common wavelength scale with a dispersion of 0.12 Å. All spectra are normalized to have a median $f_\nu = 1$ in the range 1250–1500 Å. Spectra taken with DEIMOS are smoothed to a resolution of 1.9 Åto match the lower resolution of FORS2 data. The spectra are then averaged at each wavelength using a σ-clipped mean to reject outliers arising from sky subtraction residuals and cosmetic defects. An equal number of positive and negative outliers are rejected at each wavelength, totaling at most 30% of the data. The remaining data are averaged

with an arithmetic mean.

Uncertainty in a composite spectrum will arise from both the finite signal to noise and the variance of the individual galaxies. For example, the variance in Lyα equivalent widths in our sample is much greater than the uncertainty measured in the individual spectra. It is especially important to quantify the sample variance for weak features that are generally not detected in individual spectra. We account for sample variance with a bootstrap technique. For each composite spectrum we create 100 alternate composites using the same number of spectra but drawn at random from the parent sample. Each alternate has an average 63% of the sample represented with 37% duplicates. Every measurement made on the composite spectrum is repeated for each of the 100 alternates. We then take the measurement error to be the standard deviation of the 100 alternate measurements, which reflects both the sample variance and finite signal to noise.

As discussed in §2.3 the most challenging issue is to determine the systemic redshift prior to shifting to the rest-frame. Here we follow the approach used by Shapley et al. (2003). As a first approximation we use the value of $z_{Ly\alpha}$ (where available) to construct a composite spectrum. This enables us to locate the stellar photospheric line CIIIλ1176 in the composite where we detect a velocity difference of -330 km s^{-1} with respect to Lyα. We can thus infer that Lyα emission in our sample is redshifted on average by $\Delta v_{Ly\alpha} = 330$ km s^{-1}. In a similar fashion, stacking spectra using the redshift z_{IS} based on low-ionization interstellar absorption results in a detection of CIIIλ1176 with a velocity offset of $+190$ km s^{-1}. For comparison, at $z \simeq 3$ Steidel et al (2010) find $\langle \Delta v_{Ly\alpha} \rangle = +445$ km s^{-1} and $\langle \Delta v_{IS} \rangle = -164$ km s^{-1}. To construct composite spectra, we use either $z_{Ly\alpha}$ shifted by -330 km s^{-1}or z_{IS} shifted by $+190$ km s^{-1}to approximate the systemic redshift of each galaxy. We use the Lyα-based redshift when available since it is typically determined with greater precision than z_{IS}. Figure 5.3 shows the composite spectrum of 81 galaxies in our sample with $3.5 < z < 4.5$ and apparent magnitude $z'_{AB} < 26.0$ using this method.

3.1 Uncertainties in the Systemic Redshift

A natural concern is the extent to which these applied shifts might vary within the sample used to make the composite. This can be estimated from observations of higher signal to noise from spectra taken at lower redshift. Steidel et al. (2010) quantify the offset between z_{IS}, $z_{Ly\alpha}$, and the systemic redshift $z_{H\alpha}$ in a sample of 89 galaxies at $z \simeq 2.3$. They find velocity offsets $\Delta v_{IS} = -170 \pm 115$ km s^{-1} and $\Delta v_{Ly\alpha} = 485 \pm 185$ km s^{-1}relative to Hα. Assuming this is representative of our data, the uncertainty in our systemic redshift is therefore likely to be $\sigma(v) \sim 150$ km s^{-1}. An upper limit on $\sigma(v)$ can be estimated from the width of spectral lines in the composite spectrum. In particular the rest-wavelength of the stellar line CIIIλ1176 in the composite provides a valuable measurement of the average offset from the systemic velocity and its width provides an upper limit on the effective spectral resolution. We measure a systemic velocity of 21 ± 101 km s^{-1} in the composite spectrum

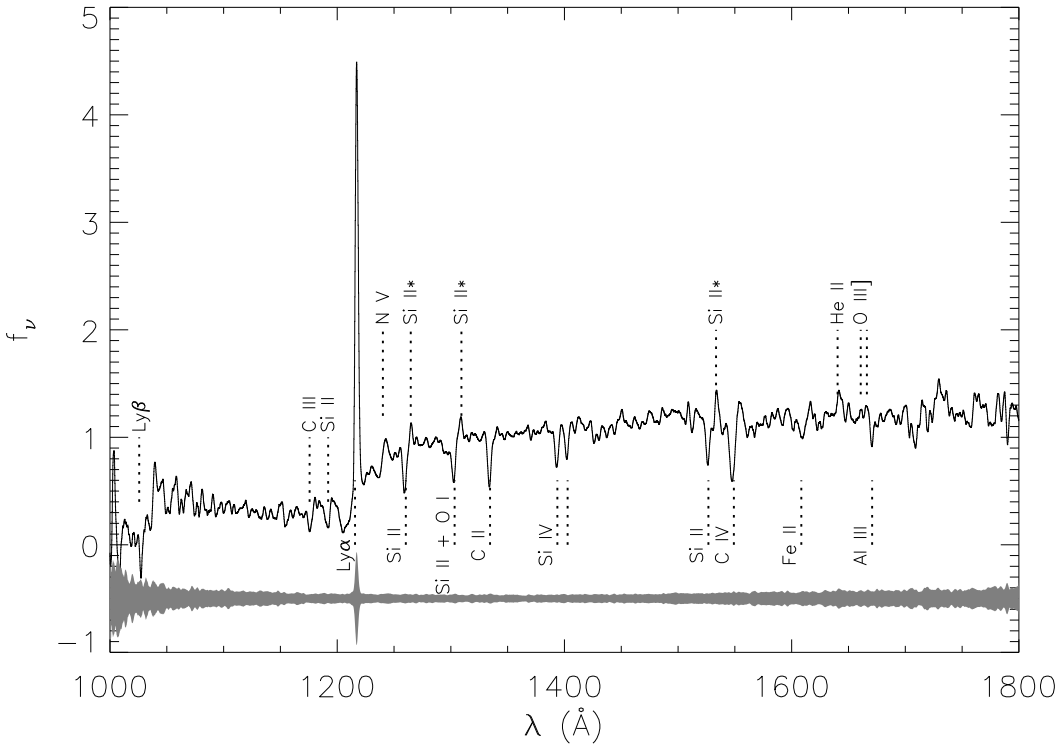

Figure 5.3: The composite spectrum of 81 galaxies in our sample with $3.5 < z < 4.5$ and apparent magnitude $z'_{AB} < 26$. The effective mean redshift for the sample averaged over wavelength is $\overline{z} = 3.9$. The strongest spectral features are labeled. The gray filled region shows the $\pm 1\sigma$ error at each point, determined from the scatter of individual spectra used to create the composite. The error spectrum peak at 1216 Å is due to large scatter in the intrinsic distribution of Lyα equivalent widths. The error is lowest at $\sim 1300-1500$ Å where the continuum signal to noise ratio is $\simeq 30$. The error increases at shorter wavelengths where the instrument throughput is lower, and at longer wavelengths where sky emission is much stronger.

(Figure 5.3) and a FWHM = 520 km s^{-1} (deconvolved from the instrumental resolution $\simeq$ 450 km s^{-1}). The uncertainty in the adopted redshifts about the true systemic stellar value is therefore ≤ 520 km s^{-1} FWHM or equivalently $\sigma(z) \leq 220$ km s^{-1}, comparable in fact to what was achieved for individual spectra at lower redshift by Steidel et al. (2010).

3.2 Error Spectrum

Figure 5.3 shows the composite spectrum of our sample as well as the 1σ error spectrum derived using the bootstrap technique discussed above. The error at each pixel is calculated as the standard deviation of all averaged data points (excluding outliers), divided by the square root of the number of data points. There are several wavelength-dependent factors contributing to the error spectrum in addition to the finite signal-to-noise of individual spectra. One factor is the intrinsic sample variance, seen clearly as a noise spike at the position of Lyα, and also evident for CIIλ1334 and

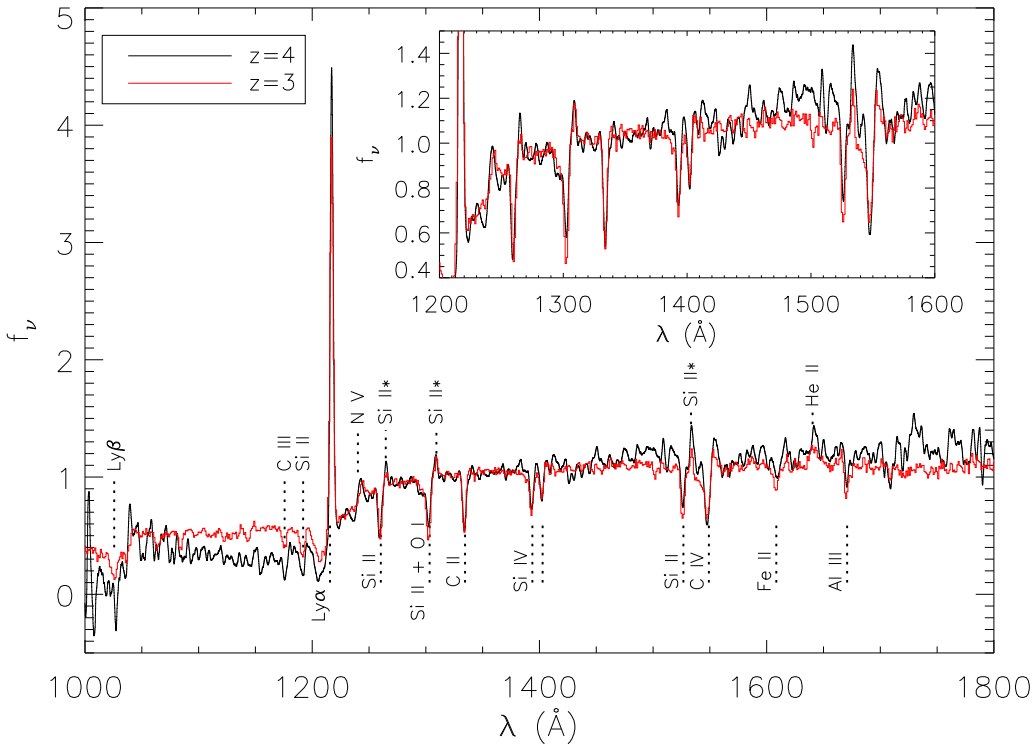

Figure 5.4: Composite spectrum of all 81 galaxies in our sample with $z < 4.5$ and apparent magnitude $z' < 26$, compared to the composite spectrum of 811 LBGs at $z = 3$ presented in Shapley et al. (2003). The higher redshift sample has a much stronger Lyα forest break, slightly redder UV spectral slope, slightly stronger Lyα emission, and weaker absorption lines. The inset shows a zoom-in of the region from 1200−1600 Å, which contains most of the absorption lines of interest in this paper.

other absorption features. Another is the decreased instrument throughput at $\lambda \lesssim 6000$ Å, leading to higher noise at shorter wavelengths. Similarly, stronger sky line emission causes increasing noise at longer wavelengths. Finally, the number of contributing spectra peaks at rest-frame $\lambda \simeq 1150-1350$ Å, with increased noise at higher and lower wavelengths where fewer spectra are included. Our observed wavelength range $5000 < \lambda < 9200$ Å corresponds to a rest-frame $1000 < \lambda < 1800$ Å at the mean redshift $z = 3.9$ of our magnitude-limited sample. Ultimately we acheive a signal to noise ratio in the continuum of ≥ 10 between the Lyα line and rest-frame 1800 Å and $\simeq 5$ in the Lyα forest, with a peak S/N $\simeq 30$ at 1350 Å.

4 Features in the Composite Spectrum

We now discuss the composite spectrum (Figure 5.3) in more detail, focusing on the strong spectral features at 1215–1550 Å where we have the best signal to noise. In this wavelength range we detect Lyα, NV$\lambda\lambda$1239,1243, SiIIλ1260, SiII*λ1265, OIλ1302+SiIIλ1304 (blended), SiII*λ1309, CIIλ1334, SiIV$\lambda\lambda$1394,1403, SiII λ1527, SiII*λ1533, and CIV$\lambda\lambda$1548,1550 at high significance. Our $z = 3.9$ composite spectrum is very similar to the composite of $z = 3$ LBGs presented in Shapley et al. (2003), which we show in Figure 5.4 for comparison. The absolute magnitude distribution of our sample is broadly similar to that at $z = 3$; both cover the range $-22 < M_{UV} < -20$. Our discussion below follows closely that presented originally by Shapley et al. (2003) but we are also interested in whether there are differences seen over the redshift range $3 < z < 4.5$. We will discuss these possible evolutionary trends in §5.

4.1 Lyman Break Galaxies: A Physical Picture

It is helpful to begin by describing a possible physical picture of LBGs based on many analyses of the extensive observations at $z \simeq 3$ (see Shapley 2011 for a recent review). Typical $\mathcal{L}^*$ LBGs at $z = 3$ have ultraviolet half-light radii $\simeq 2.0$ kpc, stellar masses $\sim 3 \times 10^{10}$ M$_\odot$, and star formation rates ~ 50 M$_\odot$yr^{-1}(Bouwens et al., 2004; Ferguson et al., 2004; Shapley et al., 2001). The star formation surface density is sufficient to drive "superwinds" of outflowing gas, similar to those seen in local galaxies where $\Sigma_{SFR} \gtrsim 0.1$ M$_\odot$yr^{-1}kpc^{-2} (Heckman, 2002). Indeed, blueshifted interstellar absorption lines confirm there are outflows with typical velocities of $\simeq 150$ km s^{-1}, and in some cases as high as 800 km s^{-1}(Shapley et al., 2003; Pettini et al., 2002; Quider et al., 2009, 2010). However, the physical origin of these outflows remains unclear (e.g., Murray et al. 2010). It is thought these outflows produce an extended circumgalactic medium (CGM) of ejected material. Outflowing gas is found in both low and high ionization states (e.g., SiII and SiIV). Low-ionization transitions such as SiII and CII are mostly associated with neutral hydrogen whereas high ionization lines occur in the fully ionized component. Based on trends in the strength of the various species, Shapley et al.

(2003) suggest a geometry in which discrete clouds of neutral gas are embedded in a halo of ionized gas. Steidel et al. (2010) show that the neutral and ionized CGM components both extend to radii of at least 125 kpc.

4.2 Lyα

Lyα is the most prominent and diverse feature in our individual spectra. The line originates from hydrogen recombination in H II regions photoionized by massive stars and, as these stars dominate the adjacent continuum, its *intrinsic equivalent width* should be within the range $W_{Ly\alpha} = 100 - 200$ Å for nearly all stellar populations (e.g., Forero-Romero et al. 2011). Our composite spectrum reveals a complex line profile with strong absorption extending blueward to $v = -4000$ km s^{-1}, and redshifted emission to $v = +1000$ km s^{-1}(Figure 5.5) with a peak offset of $v = +330$ km s^{-1}relative to the systemic velocity. The net equivalent width $W_{Ly\alpha} = 21 \pm 3$ Å is only $\lesssim 20\%$ of the expected intrinsic value.

The form of this Lyα profile has been readily understood in terms of the physical picture discussed in §4.1. Lyα emission produced at the systemic velocity can escape only along a line of sight free of neutral hydrogen or if it is shifted in velocity far from resonance. As photons escape they encounter blueshifted clouds of partially neutral gas, which absorb and re-emit isotropically. Photons backscattered from neutral clouds at small radii will appear *redshifted* and have a higher chance of escaping. Additionally, photons scattered from neutral gas at the edge of the CGM can escape into the ionized intergalactic medium and will be observed as blueshifted emission (Steidel et al., 2010). Indeed, Figure 5.5 shows such a weak blueshifted emission peak in the composite spectrum. On the other hand, the reduced equivalent width compared to that expected intrinsically could be due to many effects including dust extinction, scattering at large radii where emission falls outside the spectroscopic slits and a non-zero escape fraction f_{esc} of ionizing radiation. Since these effects cannot easily be disentangled, the absolute strength of the Lyα line must be interpreted with caution (Paper II, Schenker et al. 2012).

We can estimate the spatial extent of the neutral CGM (i.e., the radius at which escaping Lyα is last scattered) based on the strength of the diffuse blueshifted Lyα emission. The spatial profile of extended Lyα emission has been well-quantified at $z \simeq 2.6$ by Steidel et al. (2011) who find that diffuse haloes are a generic property of star-forming galaxies leading to a total Lyα flux $\simeq 5\times$ greater than that measured within the spectroscopic slits.

Average Lyα surface brightness profiles are well-fit at large radii by an exponential form, viz.

$$\Sigma_{Ly\alpha}(b) = \Sigma_0 \exp(-b/b_l) \tag{5.1}$$

where $b_l \simeq 25$ kpc. The blueshifted emission shown in Figure 5.5 has an equivalent width $W =$

1.5 ± 0.3 Å measured within a slit aperture of $\simeq 1\farcs0 \times 1\farcs0$, corresponding to 7.1×7.1 kpc^2 at $z = 4$. Assuming this approximates the peak value, we estimate $\Sigma_0 = 1.5 \pm 0.3$ Å per 50 kpc^2 and integrating Equation 5.1 yields a total equivalent width of $W_{halo} = 2\pi b_l^2 \Sigma_0$. Using the measured value of Σ_0, the scale length is given by

$$b_l = (2.3 \pm 0.2)\sqrt{W_{halo}/\text{Å}}\,\text{kpc}. \tag{5.2}$$

Although the total Lyα flux is not measured, we can estimate its value from theoretical expectations as well as observations at lower redshift. The equivalent width in Figure 5.5 is $W = 21.0$ Å (excluding the blueshifted emission component), thus we can write $W_{halo} = W_{tot} - 21$ Å. As discussed above, the *observed* W_{tot} is diminished by dust and the escape of ionizing radiation. Indeed, Steidel et al. (2011) measure $W_{tot} = 17 - 93$ Å in various subsamples of their data, all lower than the expected intrinsic value, W_{tot}=100-200 Å . Considering the composite DEIMOS spectra shown in Figure 5.5 and assuming an intrinsic $W_{tot} = 135$ Å (Forero-Romero et al., 2011) we derive upper limits of $b_l < 20 \pm 2$ kpc for galaxies with $W_{Ly\alpha} > 0$, and $b_l < 17 \pm 2$ kpc for those with $W_{Ly\alpha} > 20$ Å. This latter constraint is the most stringent, and also likely closest to the true value of b_l. Steidel et al. (2011) find that their sample of Lyα emitters (LAEs, defined as $W_{Ly\alpha} > 20$ Å) has the highest W_{tot} (= 93 Å) and largest scale length ($b_l = 28.4$ kpc) of any sub-sample that they analyze. Our constraint of $b_l < 17$ kpc for the LAEs therefore suggests that the characteristic size of Lyα haloes may be smaller at $z = 4$ than at $z = 2 - 3$.

While the analysis above suggests that Lyα haloes surrounding star forming galaxies may be smaller at higher redshifts, direct measurements of low surface brightness Lyα emission are needed to confirm this possibility. We therefore attempt to measure the characteristic scale length of Lyα haloes in our sample from two-dimensional spectra. To do so we construct a composite DEIMOS spectrum using the same sample of objects as in Figure 5.5 (bottom panel). Each two-dimensional spectrum is normalized by the same f_ν value and interpolated to the same common rest frame wavelength scale as described in §3. Additionally, the continuum centroid position is used to spatially align each spectrum. The composite is then created by averaging spectra at each point in position and wavelength using the σ-clipped mean method described in §3. In the resulting composite, the ultraviolet continuum is detected at impact parameters $b \leq 10$ kpc. To avoid uncertain contamination from the continuum, we fit an exponential profile (Equation 5.1) to the extended Lyα emission at impact parameters $b \geq 10$ kpc. From the best fit we obtain a constraint on the scale length $b_l = 15^{+45}_{-15}$ kpc. While consistent with the values from Steidel et al. (2011), our data clearly lack the precision to directly measure whether the characteristic b_l changes significantly from $z = 2.6$ to $z = 4$. The low sensitivity arises in part from a lack of data at large impact parameters due to small slit lengths. The median usable slit length of $5\farcs4$ corresponds to impact parameters of only $b \leq 20$ kpc, comparable

to b_l. Sensitive data at larger impact parameters are needed to directly determine the spatial extent of Lyα emission at these high redshifts.

4.3 Low-Ionization Metal Transitions

According to the physical picture in §4.1, absorption in low-ionization transitions occurs in both the interstellar medium and outflowing clouds of cool gas. The former is at the systemic velocity while the latter is blueshifted. Such transitions are generally saturated (Shapley et al., 2003; Pettini et al., 2002) so the line depth at a given velocity provides a measure of the areal covering fraction f_c of O and B stars by neutral gas along the line of sight. Specifically, the line profile is given by $f(v) = f_0 \cdot (1 - f_c(v))$ where f_0 is the continuum flux. While typical LBGs are too faint for detailed line profiles, high-resolution spectra of a few bright lensed sources at $z = 2 - 3$ (Pettini et al., 2002; Quider et al., 2009, 2010) have revealed absorption velocities ranging from ~ -1000 to $+500$ km s^{-1} with the highest covering fraction at $v \sim -200$ km s^{-1}. The mean low-ionization absorption line velocity offset in our composite is $v_{LIS} = -190$ km s^{-1}in good agreement with that at $z = 2 - 3$ (Shapley et al., 2003; Steidel et al., 2010).

Of particular diagnostic value are the two relatively unblended transitions of SiII at 1260 and 1527 Å whose equivalent width ratio is a valuable tracer of the optical depth (Shapley et al., 2003). The profiles of both lines and their ratio are shown in Figure 5.6. Gas near the systemic velocity ($|v| < 200$ km s^{-1}) is clearly optically thick, while for $v < -200$ km s^{-1} it is intermediate in optical depth. This difference is also seen in high-resolution spectra of lensed galaxies (Pettini et al., 2002; Quider et al., 2010), and optically thin gas is seen at large galactocentric radii (Steidel et al., 2010) suggesting that smaller, optically thin clouds are more easily accelerated to high velocity and large distances. We note that the column density at which both SiII transitions become optically thick ($\tau > 1$) is $N_{\rm SiII} = 1.9 \times 10^{12}$ cm^{-2}. Assuming $\log({\rm SiII/H}) = -4.86$ as measured for the lensed galaxy cB58 (Pettini et al., 2002), we estimate that optically thin absorption occurs in clouds with hydrogen column densities $N_{\rm HI} \lesssim 10^{17}$ cm^{-2}.

4.3.1 Fine Structure Transitions

A satisfying aspect of our composite spectrum is the successful identification of fine structure emission lines of SiII (see marked features in Figure 5.3). SiII ions in the CGM absorb photons in the resonance transitions and immediately re-emit a photon at approximately the same velocity. A photon absorbed at 1260 Å will be re-emitted at either the same wavelength or to the fine structure transition SiII*λ1265. Likewise a photon absorbed at 1527 Å will be re-emitted as either SiIIλ1527 or SiII*λ1533, and an absorbed SiIIλ1304 photon can be re-emitted as SiII*λ1309. In all three cases the probability of emission in the resonant and fine structure transitions is approximately equal.

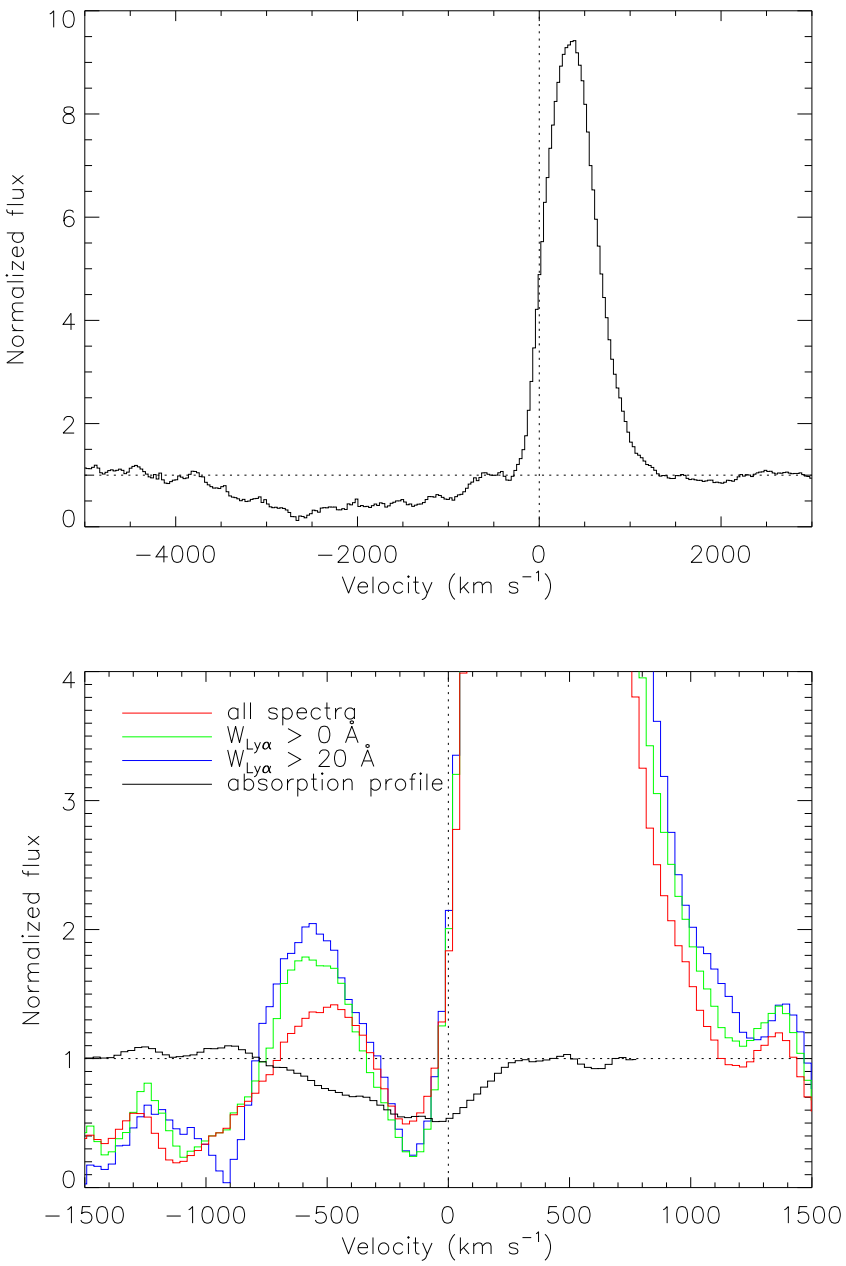

Figure 5.5: **Top:** composite spectrum normalized to continuum flux levels, showing the velocity structure of Lyα. The line profile consists of a broad blueshifted absorption trough at $v \gtrsim -4000$ km s^{-1}and strong redshifted emission extending to $v = +1000$ km s^{-1}. **Bottom:** velocity profile of Lyα showing a blueshifted secondary peak. The composite spectra in this plot are constructed only from DEIMOS data, with spectral resolution $R \simeq 2000$. The composites show a blueshifted Lyα emission peak centered at $v = -600$ km s^{-1}, corresponding to the maximum outflow velocity of neutral gas as seen in the average velocity profile of low-ionization absorption lines (black). Blueshifted Lyα emission arises from photons scattered at the leading edge of outflowing neutral CGM.

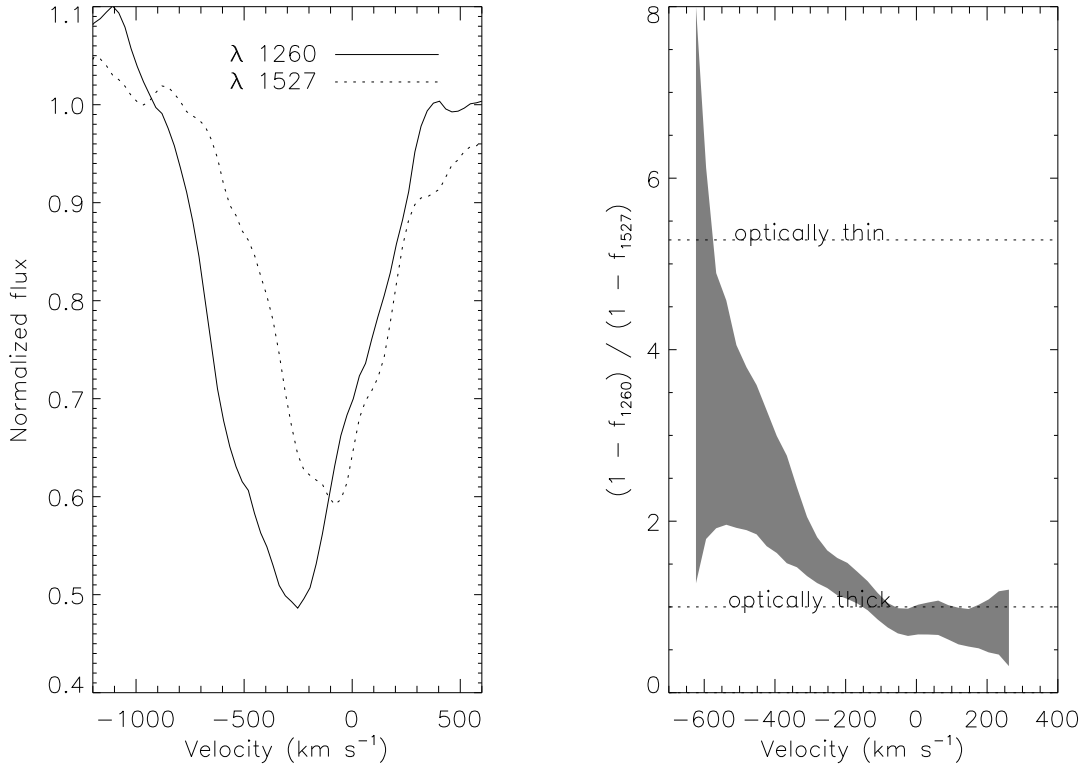

Figure 5.6: (Left:) comparison of the absorption line profiles for SiII transitions at 1260 and 1527 Å in our composite spectrum. (Right:) The profile ratio $(1 - f_{1260})/(1 - f_{1527})$ with the optically thick and thin regimes indicated; the shading refers to the 1σ uncertainty. Although both transitions are optically thick at low velocities $|v| < 200$ km s^{-1}, there is some evidence of optically thin gas at $|v| > 200$ km s^{-1}.

Since no absorption is seen in the fine structure transitions, we infer that atoms in the excited ground state will typically decay to the ground state before absorbing another photon. Since every absorbed photon is re-emitted, the net equivalent width of the resonant and fine structure transitions is $W_{\rm SiII} + W_{\rm SiII^*} = 0$. The precise equivalent widths depend on the initial absorption $W_{\rm SiII,abs}$ and the optical depth. If the gas is optically thin, re-emitted photons will immediately escape giving $W_{\rm SiII,em} = W_{\rm SiII^*,em} = -0.5 W_{\rm SiII,abs}$. In the limit of optically thick gas, resonant photons will be continuously scattered until they emerge as SiII* (after 2 scatterings on average). In this case, $W_{\rm SiII,em} = 0$ and $W_{\rm SiII^*,em} = -W_{\rm SiII,abs}$. Since the majority of absorption occurs in optically thick gas (§4.3), we expect the equivalent width of SiII absorption lines to reflect the kinematics and covering fraction of neutral gas with minimal contamination from SiII re-emission.

4.3.2 The Spatial Extent of Low-Ionization Absorption

From the picture above (§4.3.1), we expect that the equivalent width of the fine structure emission lines should be equal and opposite to the resonant line equivalent width. This is not the case: $W_{1265}/W_{1260} = -0.56 \pm 0.36$ and $W_{1533}/W_{1527} = -0.52 \pm 0.20$. ($W_{1309}/W_{1304}$ is more difficult to quantify since SiIIλ1304 is blended with OIλ1302). There are two possible explanations. One is that scattered photons have larger path lengths and are subject to greater dust attenuation. Since the UV continuum slopes imply little differential extinction (mean E(B-V) = 0.10) and we expect only 2 scatterings for the average SiII* photon, this seems unlikely. More reasonably, the emitting region could be larger than that sampled by our slits. Although the $1\farcs0 \times 1\farcs0$ slit aperture samples most of the continuum light and its line of sight absorption, the CGM which absorbs and isotropically re-emits scattered photons extends to much larger radii (Steidel et al., 2010, 2011). The strength of fine structure emission provides a direct measurement of the amount of absorption at small radii contained within the slit. The fine structure to resonant absorption line ratio suggests that a fraction 0.53 ± 0.17 (combining both λ1265 and λ1527 measures) of the total fine structure emission is contained within the extraction aperture of 1 arcsec^2. The half-light radius of SiII* emission, and hence SiII absorption, thus corresponds to $\sim 0\farcs5 = 3.5$ kpc at $z = 4$. This scale is only slightly larger than the median half-light radius $r_h = 0\farcs31$ of galaxies in our sample, and would be reached in only 20 Myr at the typical outflow velocity (190 km s^{-1}).

It is instructive to reconsider the $z = 3$ composite spectrum from Shapley et al. (2003) where the fine structure lines are clearly seen (but were not interpreted fully along the discussion above at the time). The SiII* lines are noticeably stronger in our $z \simeq 4$ composite, with an average $W_{\rm SiII^*} = 0.7 \pm 0.2$ at $z \simeq 4$ c.f. 0.30 ± 0.05 Å at $z = 3$. Furthermore, the SiII absorption lines are *weaker* in the $z = 4$ composite, suggesting the absorption takes place at larger radii at $z = 3$. This difference cannot be explained through instrumental differences between the two surveys. Smoothing our $z = 4$ composite to match the 3.25 Å resolution of Shapley et al. (2003) reduces the equivalent

widths by $< 5\%$. Likewise the wider slits used for the $z = 3$ data ($1\farcs4$, 11 kpc) c.f. the $z = 4$ data ($1\farcs0$; 7 kpc) is not the cause. If the CGM properties are similar, we expect the fine structure strength to constitute a *larger* fraction of the resonant absorption line strength in the $z = 3$ data, contrary to observations. Defining $R_{FS} = -(W_{1265} + W_{1533})/(W_{1260} + W_{1527})$, we find $R_{FS} = 0.53 \pm 0.17$ for the $z = 4$ composite spectrum and $R_{FS} = 0.16 \pm 0.04$ for $z = 3$, indicating a smaller characteristic radius of fine structure emission at $z = 4$.

Inescapably, therefore, we conclude the circumgalactic gas around LBGs at $z = 4$ differs in two important ways from that at $z = 3$: there is *greater low-ionization absorption* at small radii at $z = 4$ and *less total low-ionization absorption*. In addressing the origin of this effect, Figure 5.10 shows that the difference in equivalent width is at least partially linked to the kinematic offset from the Lyα emission. Thus it seems a higher covering fraction at small radii is required to produce the stronger fine structure emission. Higher resolution observations of individual bright, or perhaps gravitationally-lensed, galaxies at $z \simeq 4$ will ultimately be required to separate the relative contributions of covering fraction and kinematics in explaining this result.

4.4 High-Ionization Lines

The high-ionization lines SiIV and CIV arise both in interstellar gas and in stellar P-Cygni winds. The velocity centroid of SiIV, $v = 140\ \mathrm{km\,s^{-1}}$, is consistent with the low-ionization interstellar absorption lines suggesting that most absorption is interstellar in origin. This is supported by the absence of a significant redshifted emission component expected for a P-Cygni profile. In contrast, CIV is broader with a larger absorption velocity offset $v = -370\ \mathrm{km\,s^{-1}}$and redshifted P-Cygni emission indicating a large contribution from stellar winds. We also detect the NV$\lambda\lambda$1239,1243 P-Cygni feature, although the proximity to Lyα makes this feature difficult to study in detail.

We can determine the optical depth of highly ionized outflowing gas from the ratio of SiIV absorption lines. The ratio $W_{\mathrm{SiIV}\lambda1394}/W_{\mathrm{SiIV}\lambda1403} = 2.0$ for optically thin absorption, and 1.0 in the optically thick case. Shapley et al. (2003) find optically thin absorption in composite spectra of LBGs at $z = 3$, whereas we measure a ratio 1.4 ± 0.4 in the composite spectrum shown in Figure 5.3 indicating a significant contribution of optically thick absorption at $z \sim 4$. The total equivalent width of the SiIV doublet is weaker by a factor 0.72 ± 0.12 in Figure 5.3 compared to the $z = 3$ composite of Shapley et al. (2003). The combination of higher optical depth and lower equivalent width suggests that the velocity range and/or covering fraction of the ionized gas traced by SiIV is lower at higher redshift.

4.4.1 Metallicity

The P-Cygni profile of CIV is sensitive to metallicity, and the combination of CIV and HeII equivalent widths constrains both the age and metallicity. Here we compare the equivalent widths measured

in the composite spectrum (Figure 5.3) with theoretical models in order to estimate the typical metallicity of galaxies in our sample. We note that the equivalent width of CIV contains significant interstellar absorption, so the value reported in Table 5.1 should be treated as an upper limit on the P-Cygni component. Assuming the interstellar absorption component of CIV is similar to that of SiIV ($W \simeq 1.0$ Å), we take the P-Cygni absorption component to have equivalent width -1.6 ± 1.0 Å with a conservative uncertainty. We compare this estimate and the measured equivalent width of HeII (reported in Table 5.1) with predictions from the stellar population synthesis code BPASS presented in Eldridge & Stanway (2009). We consider BPASS models which include binary evolution with continuous star formation rate, and determine the difference ΔW between observed and predicted equivalent width as a function of metallicity and relative carbon abundance. We restrict the stellar population age to be within the 1σ scatter of the median value for galaxies in our sample, determined to be $10^{8.5 \pm 0.6}$ years from spectral energy density fits assuming constant star formation with a Kroupa (2002) initial mass function. Figure 5.7 shows the resulting relative error between BPASS models and measured equivalent width, which we define as

$$\text{Relative error} = 0.5 \left[\left(\frac{\Delta W_{\text{CIV}}}{\sigma_{\text{CIV}}} \right)^2 + \left(\frac{\Delta W_{\text{HeII}}}{\sigma_{\text{HeII}}} \right)^2 \right]. \tag{5.3}$$

Relative error values $\lesssim 1$ are thus consistent with the data.

Models with $Z \leq 0.004$ and somewhat depleted carbon abundance are in good agreement with the data. We note that observations of both local and high-redshift galaxies indicate typical relative carbon abundances (C/O) $\simeq 2 - 5\times$ lower than the solar value (equivalent to $X_C = 0.2 - 0.5$ in Figure 5.7) for metallicities $Z \lesssim 0.004$ (Kobulnicky & Skillman, 1998; Shapley et al., 2003; Erb et al., 2010; Eldridge & Stanway, 2011). Solar metallicity models ($Z = 0.020$) do not fit the data. We conclude that the typical metallicity of galaxies in our sample is $Z \lesssim 0.004$ or $\lesssim 0.2\times$ solar metallicity. Bright galaxies at $z < 3.8$ in the FORS2 sample have gas-phase metallicity $12 + \log(O/H) = 7.7 - 8.5$ or about $0.1 - 0.6\times$ the solar value, in reasonable agreement (Maiolino et al., 2008). These values are consistent with the allowed metallicity range $0.1 < Z/Z_\odot < 0.6$ inferred for the Shapley et al. (2003) composite using the same BPASS models (Eldridge & Stanway, 2011). Given that the equivalent widths of CIV and HeII in Shapley et al. (2003) agree well with those in Table 5.1, we expect the typical metallicity of galaxies to be similar in both samples.

5 Spectroscopic Trends

We now turn to an analysis of how the various spectroscopic features discussed in §4 are related to observable properties of LBGs as a prelude to considering how they might evolve with redshift. We will begin with the dependence of low-ionization absorption line strength with Lyα equivalent

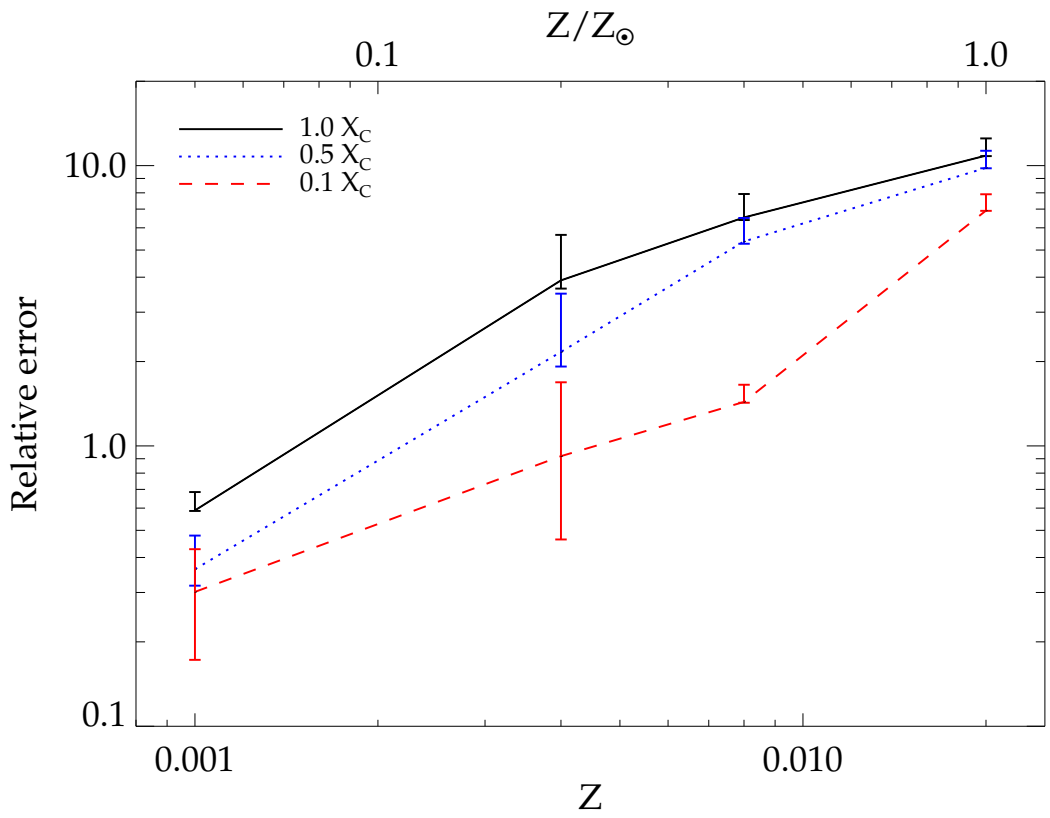

Figure 5.7: Relative error in the equivalent widths of CIV and HeII predicted by the stellar population synthesis code BPASS and values measured for the composite spectrum shown in Figure 5.3 (see text for details). Relative error values $\lesssim 1$ indicate good agreement. Model results for a range of metallicity Z and carbon depletion factor X_C as a function of age are described in Eldridge & Stanway (2011). The values $X_C = 0.5$ (0.1) correspond to a carbon abundance reduced by a factor of 2 (10) relative to solar abundance ratios. Lines are plotted for the median age of our sample ($10^{8.5\pm0.6}$ years) determined from spectral energy density models with the same initial mass function and star formation history used in BPASS, and error bars indicate the allowed range for ages within 1σ of the median. Measurements of C/O abundance at both low and high redshift indicate carbon depletion factors $X_C \simeq 0.2-0.5$ in galaxies with $Z < 0.2\,Z_\odot$ (e.g., Erb et al. 2010). For this range of X_C, models with $Z \lesssim 0.004$ (equivalent to $Z = 0.2\,Z_\odot$) are in good agreement with the data. Solar metallicity models are unable to reproduce the observed equivalent widths.

width. This is motivated by the common physical dependence of these features – both are governed by the kinematics and covering fraction of neutral circumgalactic gas – and also because this has been examined in detail for LBGs at $z = 3$ (Shapley et al., 2003).

We construct composite spectra of three sub-samples of galaxies divided according to their Lyα equivalent width. Defining W_{LIS} as the average equivalent width of λ1260, λ1303, λ1334, and λ1527 Å features, Figure 5.8 shows weaker W_{LIS} for galaxies with stronger Lyα. This was also noted for $z = 4$ LBGs by Vanzella et al. (2009). Both the z=3 and z=4 samples show this trend, although W_{LIS} is weaker at $z = 4$ for galaxies with strong Lyα emission. This difference can be attributed to the luminosity-dependent trend of stronger $W_{Ly\alpha}$ and weaker W_{LIS} in fainter galaxies (Paper I; Shapley et al. 2003; Vanzella et al. 2009). If we consider a subset of galaxies in our sample with similar absolute magnitudes to those observed at $z = 3$ ($-21.5 < M_{UV} < -21.0$), we recover the same normalization (Figure 5.8). Our sample is 90% complete at the corresponding apparent magnitudes, so we expect a negligible bias.

Having established the correlation of W_{LIS} with $W_{Ly\alpha}$, we now examine the dependence with other demographic properties. We divide the full sample into two bins of equal size according to each property of interest. The results are shown in Figure 5.9. We briefly review the trend of each property with W_{LIS} and $W_{Ly\alpha}$ and discuss the physical origin. Many of these trends were seen in Shapley et al. (2003) and Vanzella et al. (2009) and are clearly inter-related due to correlations between the demographic properties.

Less luminous galaxies have stronger $W_{Ly\alpha}$ and weaker W_{LIS} illustrating that higher star formation rates drive larger amounts of neutral gas into the CGM with higher velocity and/or covering fraction. Defining the ultraviolet spectral slope as $\beta = 5.30 \cdot (i_{AB} - z_{AB}) - 2.04$ for B-drops (Bouwens et al., 2009), we also find that bluer galaxies with lower β have stronger $W_{Ly\alpha}$ and weaker W_{LIS}. This trend was also noted in Paper I, which showed that LBGs with strong Lyα emission have systematically bluer β. Since neutral gas also presumably contains dust, the same gas which gives rise to W_{LIS} also reddens the continuum. Stellar masses M_* are measured for 60% of our sample for which there is unconfused *Spitzer*/IRAC photometry. As expected from the trends with luminosity, lower mass galaxies have stronger $W_{Ly\alpha}$ and weaker W_{LIS}. Finally, measuring half-light radii r_h from the GOODS ACS data with SExtractor, we find smaller galaxies have stronger $W_{Ly\alpha}$ and weaker W_{LIS}.

Could these trends could be due to selection effects or sample bias? The trend of stronger Lyα for less luminous LBGs is of particular concern, since fainter galaxies will require a larger $W_{Ly\alpha}$ for detection. To address this, we consider only the 32 galaxies with apparent magnitudes $z'_{AB} < 25$ for which the spectroscopic sample is 90% complete. This sub-sample is divided into two equal bins and the results confirm that trends seen in the larger sample also hold in brighter galaxies unaffected by sample bias.

The trends shown in Figure 5.9 are generally consistent with the overall trend of W_{LIS} with $W_{Ly\alpha}$ (Figure 5.8). The $W_{Ly\alpha}$ variations mostly arise from the distribution of neutral gas (traced by W_{LIS}), with relatively little effect from other demographic properties examined (M_{UV}, β, M_*, r_h). However, demographic properties do have some effect. The strongest deviation seen in Figure 5.9 is that with β, which shows stronger W_{LIS} than would be expected at a given $W_{Ly\alpha}$ for galaxies with red UV slopes. Noted also by Shapley et al. (2003), this suggests that outflowing neutral gas contains dust which reddens the continuum. Also, more luminous galaxies (i.e., those with higher star formation rates) have stronger W_{LIS} at a given $W_{Ly\alpha}$ (Figure 5.8). This is likely due to increased absorption at large velocities in galaxies with higher SFR, as observed at $z \simeq 1.4$ (Weiner et al., 2009). For all other demographics, the composite spectra have values of W_{LIS} within 1σ of that expected purely based on $W_{Ly\alpha}$.

In summary, the trends seen in Figure 5.9 arise almost entirely because of variations in the neutral gas covering fraction and/or kinematics, which are themselves correlated with the demographic properties.

5.1 Kinematics

We have now established that outflowing neutral gas is the dominant factor in determining both $W_{Ly\alpha}$ and W_{LIS}. However, variations from the trend of W_{LIS} with $W_{Ly\alpha}$ are apparent, particularly with β and M_{UV} as discussed above. The most obvious mechanism for this behavior is a systematic difference in the covering fraction f_c and kinematics of neutral gas. Assuming $W_{LIS} \propto \int f_c(v)dv$ (where v is the outflow velocity), a higher f_c and lower velocity range can conspire to give a constant W_{LIS}. However, changing f_c and v will also affect the transmission of Lyα photons resulting in a different $W_{Ly\alpha}$. It is therefore of interest to consider how to distinguish between the covering fraction and kinematics of neutral gas.

The kinematics of neutral gas can be roughly parameterized by the velocity dispersion and centroid of low-ionization interstellar absorption lines. We have measure the velocity Δv of low-ionization absorption lines with respect to Lyα as a proxy for outflow velocity. Δv is strongly correlated with $W_{Ly\alpha}$ and W_{LIS} in LBGs at $z = 3$ (Shapley et al., 2003) in the sense that larger velocities are associated with stronger interstellar absorption and weaker Lyα emission. Figure 5.10 shows Δv measured from the same composite spectra used to determine demographic trends (e.g., Figure 5.9), as well as the results from Shapley et al. (2003). All $z \simeq 4$ composites are consistent (within 1σ) with the relation measured at $z = 3$ as well as the mean Δv measured for B-dropout galaxies by Vanzella et al. (2009). We measure a velocity dispersion for each composite, and find that each is within 1.2σ of the effective spectral resolution $\sigma = 290$ km s^{-1}(measured for the stellar [CIII] feature in Figure 5.3). We are therefore unable to detect trends in outflow kinematics with demographic properties in composite spectra. Higher signal-to-noise data, higher spectral resolution,

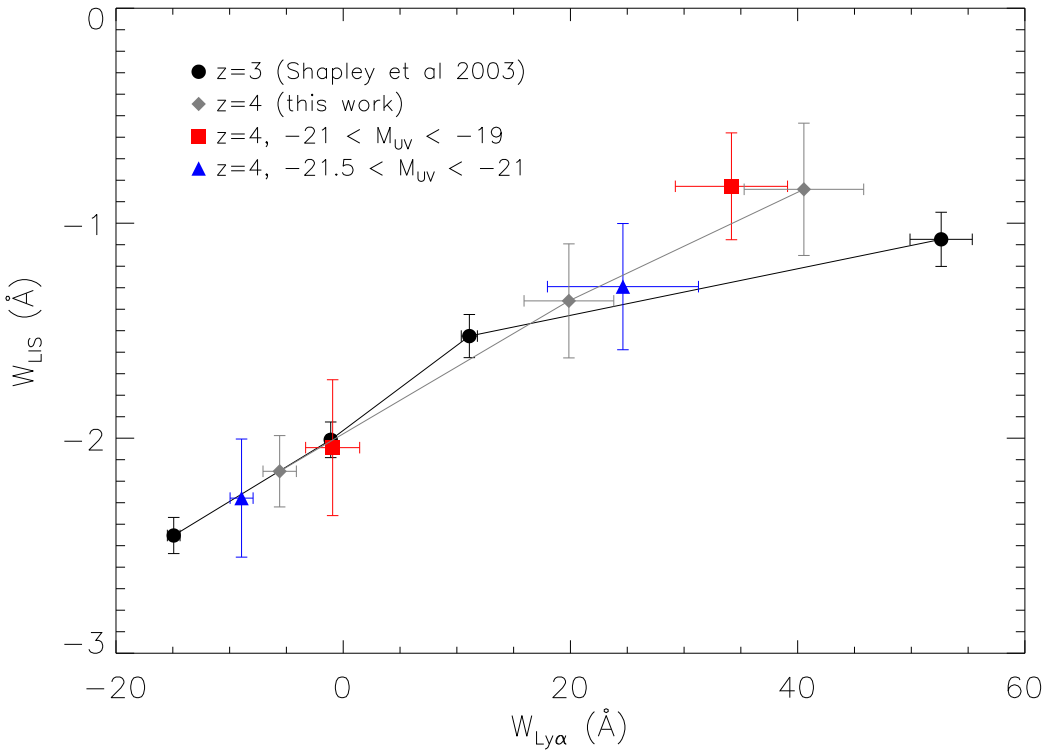

Figure 5.8: Equivalent width of low-ionization absorption lines compared to that of Lyα. Gray diamonds are from our sample at $z \simeq 4$ divided into bins of $W_{Ly\alpha} < 0$, $W_{Ly\alpha} = 0 - 40$ Å, and $W_{Ly\alpha} > 40$ Å. Black circles show the sample of Shapley et al (2003) at mean $z = 3$, divided into quartiles of $W_{Ly\alpha}$. Galaxies in the $z = 3$ sample have typical luminosities $-21.5 < M_{UV} < -21.0$ corresponding to the blue triangles. Galaxies of the same luminosity lie on the same correlation between $W_{Ly\alpha}$ and W_{LIS} at both $z = 3.9$ and $z = 3$. Fainter galaxies have weaker low-ionization absorption lines at fixed $W_{Ly\alpha}$.

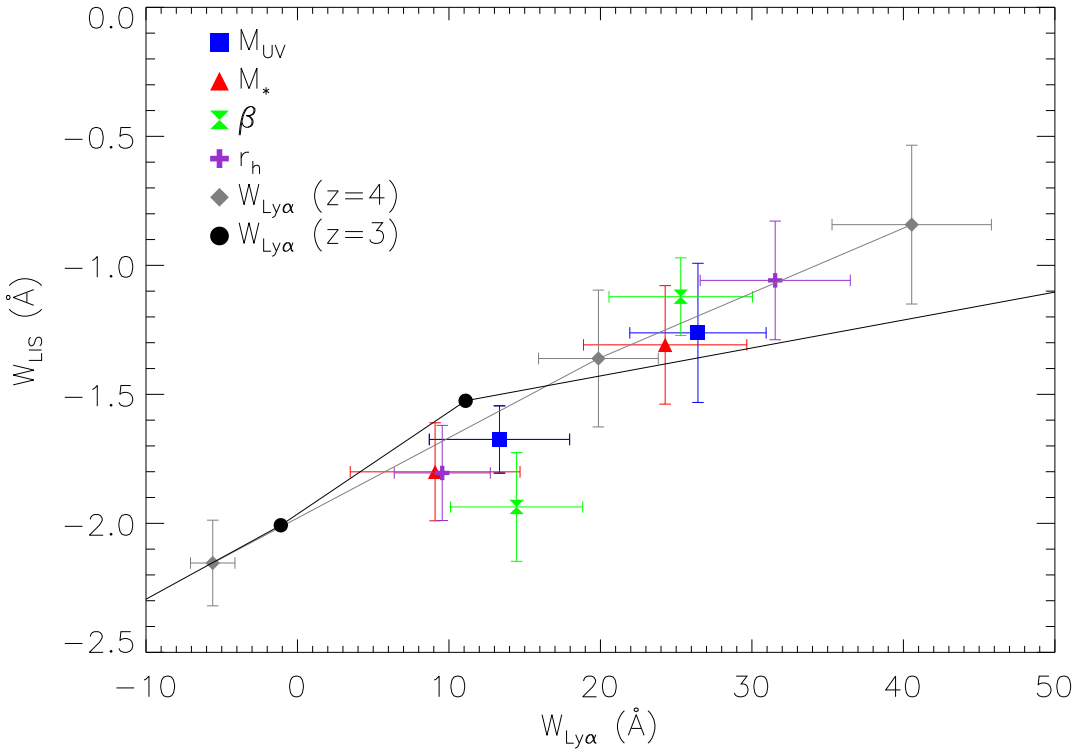

Figure 5.9: Equivalent width of low-ionization absorption lines compared to that of Lyα, divided according to observable demographic properties as described in the text. Points binned by $W_{Ly\alpha}$ at $z = 3$ and $z = 4$ are the same as in Figure 5.8. The sample was divided into two bins for each demographic property (M_{UV}, M_*, β, and r_h), with $W_{Ly\alpha}$ and W_{LIS} measured from composite spectra of the galaxies in each bin.

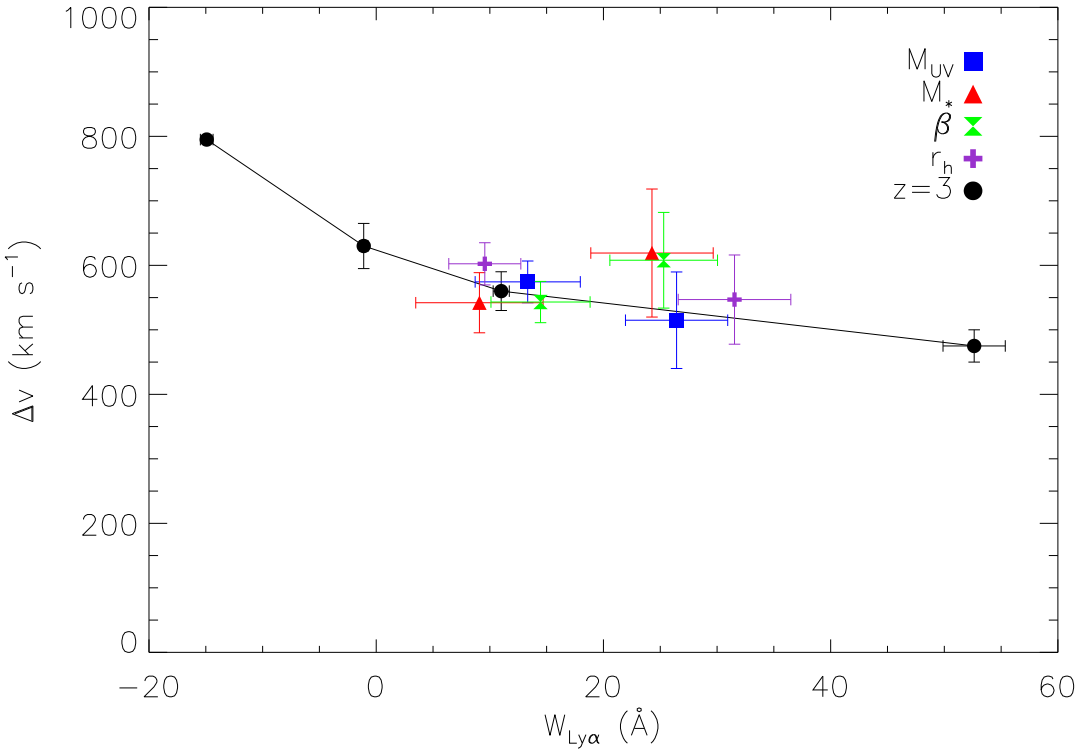

Figure 5.10: Kinematic offset Δv between Lyα emission and low-ionization absorption lines, as a function of $W_{Ly\alpha}$. The composites used to measure Δv and $W_{Ly\alpha}$ are the same as in Figure 5.9. Data at $z = 3$ are from Shapley et al. (2003).

or detailed studies of individual galaxies are required to address trends in kinematics and covering fraction of neutral gas at $z = 4$.

6 The Evolving CGM

We now turn to a discussion of the redshift evolution of the neutral CGM surrounding typical LBGs. The most useful probes are Lyα and low-ionization absorption lines which trace the kinematics and covering fraction of neutral gas, and fine structure emission lines which provide a constraint on the spatial extent of the absorbing gas (§4.3.2).

The common dependence of Lyα and low-ionization absorption lines on the neutral CGM results in a strong correlation between W_{LIS} and $W_{Ly\alpha}$. Various physical properties of LBGs are correlated with both W_{LIS} and $W_{Ly\alpha}$, but in such a way that the relation between W_{LIS} and $W_{Ly\alpha}$ remains nearly constant (Figure 5.9). Furthermore, the W_{LIS}–$W_{Ly\alpha}$ relation at fixed M_{UV} does not change significantly with redshift between $z = 3$ and $z = 4$ (Figure 5.8).

To further examine evolutionary trends with redshift, we now divide our spectroscopic sample

into two bins of redshift at fixed M_{UV}, now including galaxies at all redshifts (no longer restricted to $z < 4.5$ as in previous sections). We consider galaxies with absolute magnitude $-21.5 < M_{UV} < -20.5$, chosen to be representative of the sample in Shapley et al. (2003). There are 64 galaxies in our sample within this M_{UV} range (see Figure 5.2). We construct composite spectra of galaxies with redshift above and below the median $z = 4.1$ and measure the equivalent width of $Ly\alpha$ and low-ionization lines (both resonant absorption and fine structure emission) in each composite. The results are given in Table 5.2 along with the demographic properties of galaxies in each sub-sample. The quantities M_{UV}, M_*, and r_h are measured from photometry while β is determined from a direct fit to the ultraviolet continuum in the composite spectrum. We define $f_\lambda \propto \lambda^\beta$ and fit the rest frame $1300 - 1700$ Å to determine β, with uncertainty quantified using the bootstrap method described in §3. Aside from redshift, the demographics of each sub-sample are quite similar. The higher redshift galaxies have slightly higher average M_*, smaller r_h, and smaller (bluer) β. $W_{Ly\alpha}$ is consistent for both to within the sample variance, and is also consistent with the value $W_{Ly\alpha} = 14.3$ Å measured for the composite spectrum of $z = 3$ LBGs in Shapley et al (2003). The most striking difference is in the strength of the low-ionization absorption lines, which are significantly weaker at higher redshifts (Figure 5.11). The variation in W_{LIS} is *not* explained by systematic differences in $W_{Ly\alpha}$ or demographic properties, hence we seek an alternate explanation.

We first examine whether the evolution in W_{LIS} could arise as a result of different equivalent width distributions for Lyα. Although the mean $W_{Ly\alpha}$ across our two redshift subsamples is similar, the lower redshift subsample has a broader distribution and contains more galaxies with Lyα in absorption ($W_{Ly\alpha} < 0$). This is reflected in the larger sample variance in $W_{Ly\alpha}$ at lower redshift (Table 5.2). We evaluate the effect of this potential bias on W_{LIS} by constructing a composite spectrum from a subset of the $z < 4.1$ galaxies with intermediate $W_{Ly\alpha} = 0 - 30$ Å, resulting in a consistent mean $W_{Ly\alpha}$ with sample variance reduced by a factor of 2.5. This composite has $W_{LIS} = -1.5$ Å, 0.2 Å higher than when the full range of $W_{Ly\alpha}$ is used, but still considerably lower than the value $W_{LIS} = -1.0$ Å measured for the higher redshift galaxies. We therefore conclude that differences in the $W_{Ly\alpha}$ distribution are insufficient to explain the observed variation in absorption line strength with redshift.

There are several possible physical explanations for the evolution of W_{LIS} with redshift shown in Figure 5.11. One possibility is that the kinematics and/or covering fraction of neutral gas are systematically different. For example, an outflowing wind with fixed input energy and momentum will reach higher velocity at lower redshifts due to lower density of the intergalactic medium (IGM). However, this effect should be stronger between $z = 3.0 - 3.8$ than from $z = 3.8 - 4.7$, whereas the decrement in W_{LIS} is much stronger from $z = 3.8 - 4.7$ (Figure 5.11). Furthermore, we measure a higher offset between the velocity centroid of Lyα emission and low-ionization absorption for $z > 4.1$ galaxies ($\Delta v = 660 \pm 80$) than for $z < 4.1$ ($\Delta v = 550 \pm 40$). Both measurements are consistent with

the trend shown in Figure 5.10. Based on the trend of W_{LIS} with Δv seen at $z = 3$ (Shapley et al., 2003), we would then expect *stronger* W_{LIS} at higher redshift. Kinematics are thus unable to explain the difference in W_{LIS}, at least with the information currently available. Data with higher spectral resolution and signal-to-noise are needed to fully address differences in the covering fraction and kinematics of neutral gas.

Another obvious potential cause of weaker W_{LIS}, or equivalently decreased $W_{Ly\alpha}$ at a fixed W_{LIS}, is the presence of neutral hydrogen with very low column density of heavy elements such as the IGM. Indeed, Laursen et al. (2011) examine the transmission of Lyα through the IGM and conclude that the Lyα line is increasingly attenuated between rest-frame $1215 < \lambda < 1216$ Å at higher redshifts ($2.5 < z < 6.5$). We can examine whether this affects the apparent evolution shown in Figure 5.11 by artificially attenuating the Lyα flux in the lower-redshift composite. If the entire flux at $1215 < \lambda < 1216$ Å is set to zero, the equivalent width of Lyα decreases from $W_{Ly\alpha} = 15.4$ Å (as in Table 5.2) to 12.9 Å. Recognizing that the assumed systemic redshifts are imprecise, we set a firm limit on the maximum effect of IGM attenuation by setting the peak position of Lyα emission to zero over a range $\Delta\lambda = 1$ Å. This results in $W_{Ly\alpha} = 10.2$ Å which we take as a lower limit of the flux that would be observed at higher redshifts. This limit is still consistent with the value $W_{Ly\alpha} = 12.2 \pm 3.7$ measured in the high redshift composite, hence we conclude that IGM transmission does not significantly affect the observed evolution of W_{LIS}. If the weaker W_{LIS} is due to another source of neutral hydrogen with low column densities of heavy elements, we would expect optically thin absorption line profiles. This could be directly tested as shown in §4.3.1, but the signal-to-noise of SiIIλ1527 in the high redshift composite is too low to constrain the optical depth. We do see some evidence that the column density of neutral gas is lower at higher redshifts based on Lyα line profiles in the composite spectra, shown in Figure 5.12. The Lyα absorption trough at $\sim 1200 - 1215$ Å is significantly weaker in the higher redshift composite. This absorption arises at least in part from damping wings of high column density gas with $N_{\rm HI} \gtrsim 10^{20}$ cm^{-2} associated with the low-ionization metal absorption lines (e.g., Pettini et al. 2000, 2002). The higher redshift galaxies are therefore characterized by lower typical $N_{\rm HI}$ or/and a lower covering factor of high column density gas. Higher signal-to-noise data at $z \simeq 5$ is required to determine whether this affects the optical depth of low-ionization metal transitions.

Weaker low-ionization lines could also be caused by a systematically higher ionization state at higher redshifts resulting in lower column densities of low-ionization gas. This would also explain the weaker damped Lyα absorption trough seen at higher redshifts (Figure 5.12). This scenario can be tested by measuring the equivalent widths of higher-ionization silicon transitions, in particular SiIIIλ1206 and SiIV$\lambda\lambda$1393,1402. We find that the SiIV lines are weaker at higher redshift by a factor of 0.68 ± 0.25 in $W_{\rm SiIV\lambda\lambda 1393,1402}$, consistent with the decrement in $W_{\rm SiII}$. We do not detect the SiIIIλ1206 line in the high redshift composite, with a 1σ upper limit of $W_{\rm SiIII} < 0.8$ times that of

the lower redshift composite. SiIIIλ1206 is marked in Figure 5.12 and is clearly stronger at lower redshift. We therefore find no evidence of a significant change in the ionization state of outflowing gas at higher redshifts.

A final possibility for lower column density of heavy elements is that Lyα is scattered by "cold streams" of nearly metal-free neutral gas, predicted by simulations to accrete onto galaxies at small radii and with increasing rates at higher redshift (e.g., Dekel et al. 2009; Faucher-Giguère et al. 2011). If they exist, such streams could be identified as HI absorption systems with no corresponding absorption from heavy elements. Steidel et al. (2010) find little evidence for the presence of such streams around LBGs at $z = 2 - 3$. A similar study at higher redshift would be very interesting but also extremely challenging with current observational facilities.

Could the difference in W_{LIS} with redshift be caused in part by a different physical extent of circumgalactic gas? In §4.3.2 we showed that fine structure emission lines can be used to measure the amount of absorption taking place within the size of the spectroscopic aperture. This quantity does appear to change with redshift, in the sense that absorption takes place at smaller characteristic radius in LBGs at higher redshift. The composite spectra of LBGs at $z = 4$ has weaker absorption lines and stronger fine structure emission than the $z = 3$ composite of Shapley et al. (2003) (Figure 5.4), in qualitative agreement with trends seen at $z = 3$ (Shapley et al. 2003; see their Figure 9). We have only a weak constraint on the redshift evolution at $z > 4$ due to limited signal-to-noise in the high redshift composite. The ratio of total SiII fine structure emission W_{SiII^*} in the high- and low-redshift composites is 1.1 ± 0.5 (taken as

$$\frac{W_{1265} + W_{1309} + W_{1533}}{W_{1260} + W_{1303} + W_{1527}}$$

with values given in Table 5.2), while the corresponding ratio of absorption line strength W_{LIS} is 0.6 ± 0.2. The inferred fraction of low-ionization absorption within the slit aperture is thus a factor 1.8 ± 1.0 larger in the higher redshift sample, consistent with no evolution. Higher signal-to-noise is required to accurately constrain the spatial extent of low-ionization absorption at $z > 4$.

To summarize, we find weaker low-ionization absorption lines in LBGs at higher redshift with fixed M_{UV}. The difference in W_{LIS} is not consistent with the trends observed for Lyα and various demographic properties examined in §5. We have discussed several possible causes for this discrepancy including variation in the kinematics, covering fraction, optical depth, ionization state, and spatial extent of absorbing gas. The data show that the ionization state has no significant effect, but we are unable to conclusively address other possible causes. Spectra of galaxies at $z > 4$ with higher signal-to-noise are required to more accurately constrain the optical depth and spatial extent. Additionally, spectra of individual galaxies taken with higher spectral resolution will be required to independently determine the covering fraction and kinematic structure of absorbing gas.

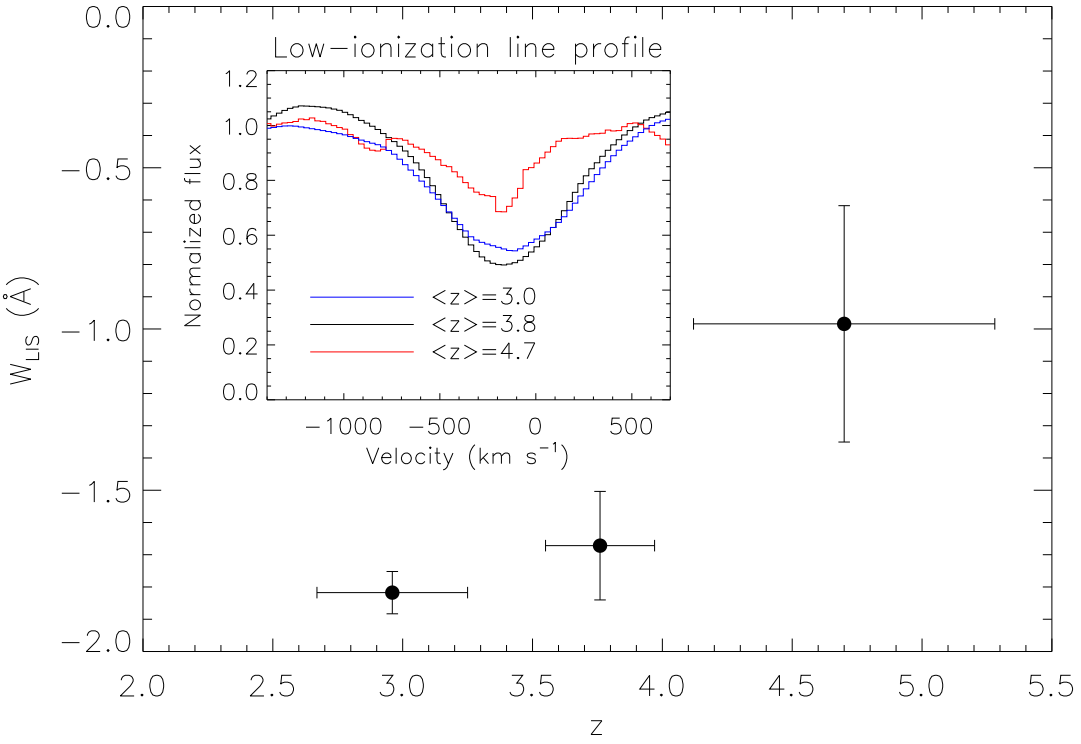

Figure 5.11: Equivalent width of low-ionization absorption lines measured from composite spectra of LBGs at different redshifts. The DEIMOS and FORS2 data presented in this paper are separated into two sub-samples of equal size as described in the text. We also show the equivalent result at $z = 3$ from the composite spectrum of Shapley et al. (2003), with redshift distribution described in Steidel et al. (2003). The average low-ionization line profile of each composite is shown in the inset. Low-ionization absorption lines are significantly weaker for galaxies in the highest redshift composite. All three samples have consistent mean luminosity and $W_{Ly\alpha}$.

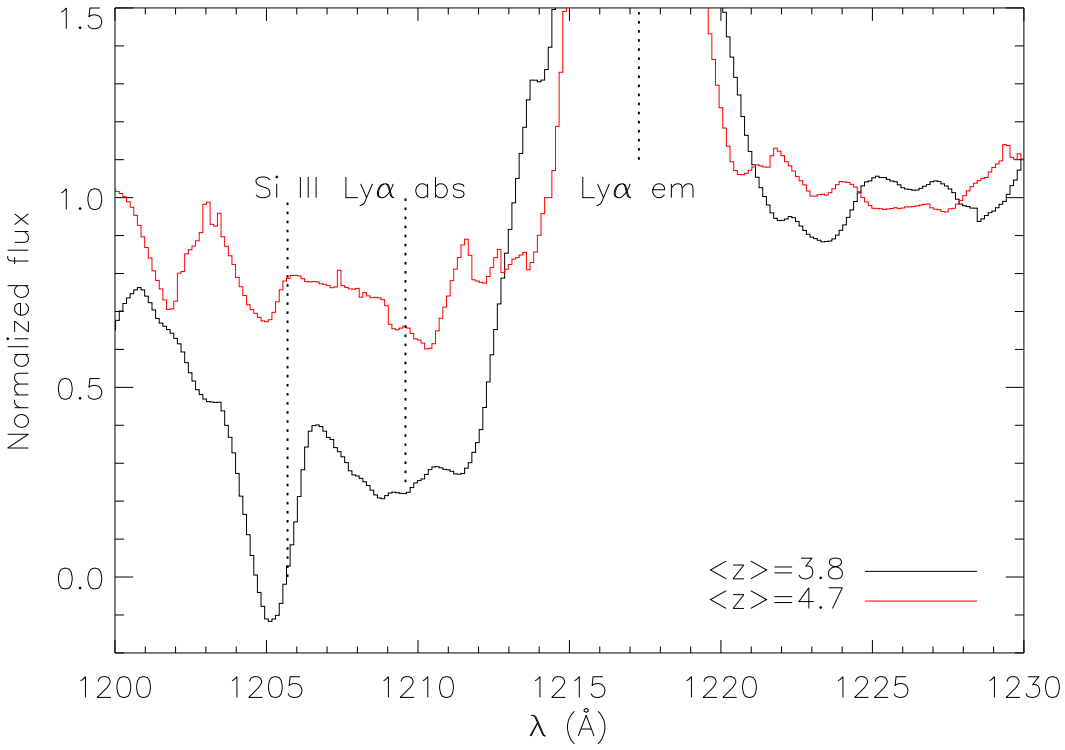

Figure 5.12: Composite spectra of LBGs showing the region around Lyα for the two redshift ranges described in §6. We show the position of SiIIIλ1206 blueshifted by 200 km s^{-1}, Lyα emission redshifted by 400 km s^{-1}, and Lyα absorption blueshifted by 1500 km s^{-1} where it is seen most prominently. The Lyα absorption trough is weaker in the higher redshift composite indicating a lower incidence of neutral gas with high column density. SiIII absorption is also weaker in the higher redshift composite.

6.1 Galaxy Evolution

We argue in §5 that Lyα equivalent width is determined primarily by the neutral CGM, which is correlated with various demographic galaxy properties (Figure 5.9). It is well established that these demographic properties vary with redshift and we expect $W_{Ly\alpha}$ to vary accordingly. Large photometric surveys have shown that Lyman break galaxies at increasingly higher redshifts $z > 3$ have lower luminosities (Bouwens et al., 2007, 2011), bluer UV spectral slopes (Bouwens et al., 2009, 2012), smaller stellar masses (Stark et al., 2009; González et al., 2011), and smaller sizes (Bouwens et al., 2004; Ferguson et al., 2004). This is in accordance with inside-out galaxy growth: galaxies increase in size and stellar mass as they evolve with time, while increasing metallicity and dust content reddens the ultraviolet continuum. Simultaneously, star formation drives large-scale outflows of gas which reach larger distances and are accelerated to larger velocities at later times (e.g., Murray et al. 2010). Galaxies which are more evolved (i.e., larger, more massive, redder) should therefore have a CGM characterized by larger spatial extent, larger velocity range, and higher covering fraction of neutral gas. Observationally this results in weaker $W_{Ly\alpha}$, stronger W_{LIS}, and relatively weaker fine structure emission. These are precisely the trends observed at both $z = 3$ (Shapley et al., 2003) and $z = 4$ (this work).

6.2 Lyα in the Epoch of Reionization

We reiterate that Lyman break galaxies at increasingly higher redshifts $z > 3$ have lower luminosities, bluer UV spectral slopes, smaller stellar masses, and smaller sizes. Notably, *all trends in the demographics of galaxies at higher redshift are correlated with stronger* $W_{Ly\alpha}$ *and weaker* W_{LIS} (Figure 5.9). We therefore expect typical galaxies at higher redshifts to have, on average, stronger Lyα emission. Earlier results from this survey confirm that strong Lyα emission is more frequent in galaxies at higher redshift (Paper I; Paper II). We find no evidence of this trend reversing. In fact, galaxies with extremely small size, low mass, and blue β tend to be the strongest Lyα emitters (e.g., Erb et al. 2010). We do, however, expect the average Lyα emission strength to decrease significantly at increasing redshifts in the epoch of reionization due to neutral hydrogen in the IGM (e.g., Haiman & Spaans 1999).

We have devoted considerable discussion to the properties of Lyα in part because Lyα is of great interest as a tracer of cosmic reionization. Several authors have now presented evidence that reionization was incomplete at $z \simeq 7$ based on a rapidly decreasing fraction of galaxies with strong Lyα emission at $z \gtrsim 6.5$ (Schenker et al., 2012; Ono et al., 2011; Pentericci et al., 2011). Although trends at $z = 3 - 4$ suggest that the galaxies observed by these authors should have a higher fraction of strong Lyα emission, we have presented evidence that the relation between $W_{Ly\alpha}$ and W_{LIS} is systematically different at $z > 4$ (Figure 5.11). This implies a systematic difference in the spatial,

kinematic, or optical depth structure of neutral circumgalactic gas compared to galaxies at lower redshift. The physical origin of this evolution and its effect on $W_{Ly\alpha}$ at $z > 4$ will need to be understood in order to fully interpret the results of Lyα surveys at higher redshifts in the context of reionization.

7 Summary

The rest-frame ultraviolet spectra of star-forming galaxies contains a wealth of information about the properties of the circumgalactic medium. In this paper we have presented an analysis of several features which trace the CGM with a focus on the properties of neutral gas. We find that the trends observed at lower redshift ($z = 3$; Shapley et al. 2003) also hold at $z = 4$ with approximately the same normalization (Figure 5.8). However, we find evidence for rapid evolution at $z > 4$ with lower W_{LIS} at fixed $W_{Ly\alpha}$ and M_{UV}, suggesting a systematic difference in the spatial distribution, kinematics, ionization state, or optical depth of circumgalactic gas at higher redshifts. We determine that the ionization state is not responsible for the observed evolution but are unable to distinguish between kinematics, covering fraction, optical depth, or the spatial extent of neutral gas as the likely cause. We are collecting additional spectra of LBGs at $z > 4$ with our ongoing survey, including high spectral resolution observations of bright lensed galaxies from which we can disentangle the kinematic profile and covering fraction of neutral gas. These data will allow us to address the precise magnitude and physical origin of evolution in circumgalactic gas properties.

As a final note, we emphasize that the neutral CGM is of great interest in the context of reionization of the universe. Neutral gas in the circumgalactic medium absorbs ionizing radiation, thereby inhibiting the ability of galaxies to reionize the universe. The escape fraction of ionizing photons is one of the most important and uncertain factors in determining the contribution of star-forming galaxies to reionization (Robertson et al., 2010). We have shown that typical galaxies at higher redshift have weaker low-ionization absorption lines based on their demographic trends, and presented new evidence that absorption lines are systematically weaker at $z > 4$ even for fixed demographic properties. This is likely caused by a lower covering fraction and/or velocity range of neutral gas, and we will address the physical origin of this evolution with future data from our ongoing survey. Determining the redshift evolution of neutral gas covering fraction in LBGs will be of great interest for interpreting surveys of Lyα emission in the context of reionization and addressing the role of star-forming galaxies in reionizing the universe.

Ion	$\lambda_{\rm rest}$ (Å)	W (Å)	$v_{\rm cen}$ ($\rm km\,s^{-1}$)
CIII	1175.71	-2.4 ± 0.8	21 ± 101
HI	1215.67	20.9 ± 2.9	376 ± 13
SiII	1260.42	-1.4 ± 0.3	-281 ± 38
SiII*	1264.74	0.9 ± 0.3	89 ± 61
OI + SiII	1303.27	-1.6 ± 0.3	-258 ± 62
SiII*	1309.28	0.7 ± 0.2	-118 ± 80
CII	1334.53	-1.6 ± 0.2	-136 ± 39
SiIV	1393.76	-1.1 ± 0.2	-122 ± 50
SiIV	1402.77	-0.8 ± 0.2	-160 ± 45
SiII	1526.71	-1.3 ± 0.3	-99 ± 54
SiII*	1533.43	0.8 ± 0.3	114 ± 64
CIV	1549.48	-2.6 ± 0.4	-374 ± 57
HeII	1640.40	1.3 ± 0.7	141 ± 282

Table 5.1: Equivalent width and velocity of absorption and emission lines in the composite spectrum (Figure 5.3).

Property	$z < 4.1$	$z > 4.1$
z	3.76 ± 0.21	4.70 ± 0.58
M_{UV}	-21.0 ± 0.3	-21.0 ± 0.3
$\log M_*/\mathrm{M}_\odot$	9.6 ± 0.6	9.8 ± 0.6
r_h (kpc)	2.42 ± 0.97	1.94 ± 0.74
β	-2.02 ± 0.08	-2.12 ± 0.19
$W_{Ly\alpha}$ (Å)	15.4 ± 5.9	12.2 ± 3.7
W_{1260} (Å)	-1.7 ± 0.4	-0.7 ± 0.4
W_{1265} (Å)	0.8 ± 0.3	1.0 ± 1.0
W_{1303} (Å)	-2.1 ± 0.4	-0.9 ± 0.4
W_{1309} (Å)	1.0 ± 0.3	0.9 ± 0.4
W_{1334} (Å)	-1.7 ± 0.3	-1.7 ± 0.9
W_{1527} (Å)	-1.2 ± 0.3	-0.6 ± 1.0
W_{1533} (Å)	0.7 ± 0.3	0.9 ± 0.5

Table 5.2: Mean demographic and spectroscopic properties of LBGs at different redshifts. Error bars correspond to the standard deviation of values for individual galaxies in each sub-sample. β and equivalent widths of Lyα and low-ionization metal transitions are measured directly from composite spectra, with error bars determined from a bootstrap method (see text for details).

Chapter 6

Synthesis and Future Prospects

The work described in this thesis represents a step forward in our understanding of high redshift galaxy evolution on several fronts. In this final chapter I summarize the main results of this thesis in the context of our growing body of knowledge. Throughout this section I revisit some open questions raised by this work and discuss ongoing and future observations that will address these issues.

1 Resolved Properties of High Redshift Galaxies

Near-infrared integral field spectrographs coupled with adaptive optics on large telescopes have recently enabled studies of the internal structure of high redshift galaxies. Chapters 2 and 3 describe how we utilized this technology to obtain detailed measurements of the morphology, kinematics, and chemical enrichment of gravitationally lensed $z \simeq 2-3$ star forming galaxies with the highest spatial resolution yet achieved at these redshifts. The majority of these galaxies ($\sim 70\,\%$) exhibit rotation with high local velocity dispersions indicating a turbulent thick disk, and steep radial metallicity gradients. Together these results yield a coherent physical picture in which isolated galaxies are growing inside-out via accretion of gas at large radii. Star formation is driven by gravitational instability which causes the gas-rich disks to fragment into massive clumps. Vigorous star formation is concentrated in these clumps with SFR densities $\sim 100\times$ higher than in local spiral galaxies. In subsequent work not reported in this thesis, my collaborators and I found that such large SFR densities are explained naturally by the high gas surface densities and observed kinematics in these galaxies (Livermore et al. 2012, submitted).

Two systems studied in Chapters 2 and 3 are undergoing mergers and thus we also probe this important mode of growth with high resolution data. We find similar star formation and morphological properties in the merging and isolated galaxies. Mergers display similar local velocity dispersion as isolated galaxies, but their velocity fields are more chaotic with no coherent rotation. In the one case where we have resolved metallicity information, we find an inverted gradient suggesting that mass loading may be concentrated near the galaxy center, in contrast to isolated galaxies. Thus

merger-driven and *in situ* star formation result in distinct kinematic and chemical structure despite similar star formation rates.

The results in Chapters 2 and 3 represent a coherent picture of the internal kinematic, morphological, and chemical properties of typical star forming galaxies at $z \simeq 2-3$ based on a modest sample. This work is complemented by extensive surveys of the largest massive galaxies at similar redshifts (e.g. Förster Schreiber et al. 2009; Epinat et al. 2012; Gnerucci et al. 2011). These surveys benefit from the statistical power of large samples but are hampered by poor spatial resolution (typically $\simeq 4$ kpc FWHM). Large samples confirm that $\sim 1/3$ of massive star forming galaxies at this epoch are undergoing mergers while the remaining $\sim 2/3$ are isolated with high velocity dispersion and varying degrees of rotational support. Deep observations with adaptive optics have confirmed the prevalence of clumpy, gravitationally unstable disks with increasingly large samples (e.g. Genzel et al. 2011). However, measurements of metallicity gradients at high redshift give discrepant results that are not yet understood. Reports of inverted metallicity gradients in isolated rotating galaxies at high redshift (Queyrel et al., 2012) are especially puzzling. Most high redshift measurements rely solely on the [NII]/Hα ratio which, as discussed in Chapter 3, is not necessarily a good tracer of the true metallicity, and so it remains to be determined whether the reported prevalence of inverted gradients is real or due to systematic errors. Additional measurements of multiple line ratios such as [OIII]/Hβ in addition to [NII]/Hα will resolve this issue.

Our analysis in Chapter 3 represents an important first step in the statistical study of metallicity gradients and their evolution at high redshift. This subject has gained attention only recently and the next few years will likely see significant progress in both theoretical and observational studies. Wide-field integral field unit and multi-slit spectrographs such as KMOS, MUSE, DEIMOS, and MOSFIRE will provide resolved line ratio measurements in large samples of galaxies at high redshift, providing good statistics over a wide range in redshift. Meanwhile theoretical models of galaxy evolution are beginning to utilize constraints provided by these data (e.g. Pilkington et al. 2012). Metallicity gradients and their evolution with time provide valuable constraints on the physical processes relevant to galaxy evolution (often implemented as unresolved "sub-grid" prescriptions in numerical simulations). The combination of large, statistically well-defined samples of measured metallicity gradients with suitable theoretical models offers the potential for significant new insights into the formation and evolution of galaxies which are just beginning to be realized.

2 Low-Luminosity Galaxies at High Redshift

Faint galaxies with luminosities lower than the characteristic L_* dominate the total star formation rate at high redshifts and are thought to contribute most of the photons responsible for reionizing the universe at $z > 6$. Despite their significance, they are too faint for practical spectroscopic study

and so our knowledge of these galaxies has been limited to information based on broadband photometric measurements. Chapter 4 represents the first detailed spectroscopic study of this important population at $z = 1.5 - 3.5$, taking advantage of gravitational lensing to amplify their flux by up to 4 magnitudes. We use optical emission line measurements to determine the metallicity, SFR, ionization parameter, dust extinction, and dynamical mass for a significant sample of 29 galaxies with star formation rates extending to limits $\sim 10\times$ lower than in surveys of non-lensed galaxies at this epoch. Among other results, we show that metallicities are higher than expected from previous determinations of the mass-metallicity relation, and attribute this to lower specific SFR in the lensed galaxies. For the first time, we directly test the proposed fundamental metallicity relation (FMR) of Mannucci et al. (2010) by comparing our data to local galaxies with identical stellar mass and SFR. We find lower gas-phase metallicity in the high redshift galaxies than in local sources drawn from the SDSS, arguing against a time-invariant FMR. While our result is preliminary and may be biased by measurement errors, this represents an important first measurement that will be further constrained by ongoing analysis of the full data set.

Chapter 4 represents the first characterization of detailed physical properties in a large sample of low-luminosity galaxies at high redshifts. Moreover, much of the data were obtained with modest integration times on the Palomar 200" telescope thanks to a powerful combination of gravitational lensing and the high bandwidth of Triplespec. The NIRES instrument, under construction for Keck, will make these studies even more economical. Meanwhile, sensitive multi-object near-IR spectrographs such as MOSFIRE and KMOS are now enabling studies of larger, well-defined samples of the sub-L_* population. Large surveys in the next few years should produce similar measurements spanning a wide range of luminosity and redshift with good statistics, thanks to the efficiency of multi-object observations.

3 The Circumgalactic Medium at High Redshift

Intense star formation in high redshift galaxies drives large scale outflows of gas and dust which are detected ubiquitously via kinematic signatures in rest-UV spectral lines. Outflows form a circumgalactic medium (CGM) of metal-enriched material extending to large distances, now known to extend > 100 kpc from typical Lyman break galaxies (Steidel et al., 2010). The CGM contains neutral gas traced by HI and low-ionization metal lines, warm ionized gas traced by SiIV and CIV, and a hot phase revealed by OVI absorption. Theoretical and chemical evolution arguments suggest that the mass outflow rate is comparable to the SFR in LBGs and the few available direct measurements also support this conclusion (e.g. Pettini et al. 2002; Quider et al. 2009; Erb et al. 2006; and see Chapter 3). Outflows are thus extremely important in limiting the star formation, stellar mass, and metal enrichment of high redshift galaxies. Outflowing material likely interacts with pristine

gas falling into dark matter halos under the influence of gravity and may inhibit the accretion of this material onto galaxies, an important process which is not yet understood (Steidel et al., 2010). These reasons alone provide strong motivation to study the detailed properties of outflows and the CGM. Properties of the CGM such as outflow velocity, spatial extent, heavy element content, and their relation to galaxy demographic properties have now been charted in star forming populations at $0 < z < 3$ (e.g. Shapley et al. 2003; Steidel et al. 2010; Kornei et al. 2012; Tumlinson et al. 2011). The CGM at higher redshifts is of even greater interest for studies of reionization and Lyα emission (Stark et al., 2011; Schenker et al., 2012).

Neutral gas in the CGM absorbs ionizing photons and thus limits the ability of star forming galaxies to reionize the universe. The relevant quantity for reionization is the escape fraction f_{esc} of ionizing photons into the CGM. Currently f_{esc} is highly uncertain even at $z = 3$ and extremely difficult to measure directly at higher redshifts (Robertson et al., 2010). However, measurements of the covering fraction of neutral gas directly constrain the escape fraction since the two are related by $f_{cov} = 1 - f_{esc}$. Covering fractions can be measured from the absorption profiles of resonant transitions arising in neutral HI gas, but in practice this is complicated by the velocity structure of the CGM and lack of spatial information. We can obtain a rudimentary indication from the equivalent widths of absorption lines which probe a combination of outflow kinematics and covering fraction. We examine these equivalent widths in Chapter 5 with attention to trends with galaxy properties and with redshift. The trends observed by Shapley et al. (2003) at $z = 3$ also hold at $z = 4$, with less evolved galaxies (i.e. those with smaller size, lower mass, less dust extinction, and lower luminosity) showing weaker absorption equivalent widths. We additionally find evidence for weaker absorption at higher redshift in galaxies with similar physical properties. Typical galaxies at increasing redshift are therefore inferred to have weaker absorption as expected for a reduced covering fraction of HI gas, although we are unable to distinguish whether this evolution actually reflects a change in the covering fraction. We are limited in this interpretation by relatively coarse spectral resolution, particularly in stacked spectra. Recently we have obtained deep observations of three bright lensed galaxies at $z \simeq 4$ with higher resolution (70 $\mathrm{km\,s^{-1}}$FWHM) in order to address this issue. Although the sample is small, these data will provide an important indication of whether the observed evolution implies a reduced covering fraction at higher redshifts.

In addition to probing the kinematics and covering fraction, resonant UV transitions are sensitive to the spatial distribution of neutral gas in the CGM. In Chapter 5, we show that fine structure emission arises from the outflowing gas. We then demonstrated that the combination of resonant absorption and associated fine structure emission lines give a direct constraint on the spatial extent of absorbing CGM - even in integrated spectra. Applying this result shows that neutral gas is concentrated at smaller galactocentric radii at $z = 4$ compared to $z = 3$. This well-defined evolution in the distribution of neutral gas may partially explain the evolution we find in absorption line

strength. Furthermore fine structure emission may prove to be a valuable diagnostic of the spatial distribution of outflows at lower redshifts, complementary to absorption studies. While spatially extended SiII* emission lines are too faint to detect at $z = 4$, the technique we develop could be useful at lower redshifts ($z \sim 0.5 - 2$) where strong FeII* transitions are redshifted to optical wavelengths.

3.1 Implications for Reionization

The results of Chapter 5 have important implications for experiments which attempt to constrain the epoch of reionization by measuring Lyα emission line strengths. Several groups have recently reported a rapid decline in the fraction of star-forming galaxies with strong Lyα emission over the redshift range $z = 6 - 7$, claiming that this is due to attenuation by a non-negligible IGM neutral fraction $\gtrsim 10\,\%$ at $z = 7$ (Schenker et al., 2012; Ono et al., 2011; Pentericci et al., 2011). If so, the long-sought end of reionization has finally been found. The ramifications of this result are widespread: it provides a critical constraint on reionization models which in turn inform the design of 21cm reionization experiments, provide interpretation of their results, and make inferences about the formation and evolution of the first stars and galaxies in the universe (e.g. Trac & Gnedin 2011; Tozzi et al. 2000) However, Chapter 5 clearly shows that Lyα is affected by many other factors in addition to neutral IGM, and so it is imperative to test whether other effects could explain the reduced Lyα emission. Similar to the results of Stark et al. (2010), we find that the average Lyα equivalent width varies slowly with redshift at $z = 3 - 5$ when comparing galaxies of similar physical properties and CGM absorption characteristics, in contrast to the rapid change detected in the short interval of < 200 Myr between $z = 6 - 7$. Our results therefore support the interpretation that the decrease in Lyα at $z > 6$ is due to a rising neutral IGM fraction.

4 Future Work: Resolved Outflow Diagnostics of Individual Galaxies

Great progress has been made in understanding the formation and evolution of galaxies via detailed astrophysical studies of high redshift sources. Thousands of galaxies have now been spectroscopically confirmed at $2 < z < 7$ (e.g. Steidel et al. 2003; Stark et al. 2010; Schenker et al. 2012). HST imaging surveys have measured the star formation rate, stellar mass, age, and dust content of individual high redshift galaxies (e.g. Law et al. 2012) while metallicities have been derived from near-infrared spectroscopy (e.g. Chapter 4 and references therein). Kinematic data for well over 100 galaxies at $2 < z < 5$ show that approximately two thirds are rotating systems with high velocity dispersion while the remainder are undergoing major mergers (e.g. Chapter 2 and references therein).

Metallicity gradients indicate that isolated high redshift galaxies are growing inside-out via accretion of gas and high mass loading factors at large radius, although existing data sets yield discrepant results (Chapter 3; Queyrel et al. 2012; Yuan et al. 2011; Cresci et al. 2010). Together, these studies give a clear picture of the properties of individual high redshift galaxies and their likely evolution onto the Hubble morphological sequence observed in the local universe.

Despite excellent progress, many puzzles remain in our limited understanding of galaxy evolution. Among the most important are the detailed properties of circumgalactic gas around individual galaxies. The statistical properties of outflows and the resulting CGM have been well studied for large samples at high redshift, however these results generally rely on stacking a large number of spectra in order to measure weak spectral features (e.g. Chapter 5; Shapley et al. 2003). As demonstrated throughout this thesis, gravitational lensing is a powerful tool which in this case provides a practical means to study individual galaxies in comparable detail as composite spectra. This was demonstrated by Pettini et al. (2002) who obtained a high quality Keck/ESI spectrum of MS1512-cB58, a highly magnified LBG. This spectrum provided the first reliable estimate of the mass outflow rate from an LBG, accurate abundances of 8 different elements, and the velocity profile and covering fraction of outflowing gas with 50 $\mathrm{km\,s^{-1}}$resolution. The inferred outflow rate is larger than the SFR confirming the importance of outflows, with a maximum outflow speed 750 $\mathrm{km\,s^{-1}}$in excess of the escape velocity. Chemical abundances show a clear α-element enhancement confirming a young age $\lesssim 300$ Myr for this galaxy. Most notably, few such measurements have been made to date *even for composite spectra* of hundreds of galaxies.

While lensed LBGs clearly offer a wealth of information, suitably bright sources are rare and until recently very few were known. However, systematic searches in lensing clusters and the SDSS have uncovered a number of promising new candidates in recent years (e.g. Belokurov et al. 2009) and many have already been the subject of detailed studies, for example in Chapter 3. We have secured spectroscopic redshifts for a large number of bright lensed galaxies throughout the course of this thesis work and are now poised to obtain high quality optical spectra for a considerable sample. We have begun this work with an approved allocation with Keck/ESI to obtain spectra of this sample with similar quality to that of MS1512-cB58. Additionally we will take advantage of the ESI integral field unit to obtain spatially resolved diagnostic information of the brighter sources. In total we have 15 suitable lensed galaxies to date with $z \simeq 2-3$ and apparent magnitudes $R = 20-21$. With these observations we will address a number of open questions related to galaxy evolution including several that arose during the course of this thesis work, briefly described here. Measurements of column densities and kinematics will yield mass outflow rates and hence mass loading factors. Spatially resolved data will directly test the conclusion from Chapter 3 that metallicity gradients originate from radial gradients in the mass loading factor. Relative abundances of α-elements, Fe-peak elements, and N will provide information on the age and star formation history. Various

stellar features will further constrain the age, stellar metallicity, and high-mass slope of the stellar IMF via comparison with stellar evolution models such as BPASS (Eldridge & Stanway, 2009) and empirical diagnostics (e.g. Sommariva et al. 2012). We will compare measurements of stellar and ISM metallicity with gas-phase oxygen abundance determined from nebular emission lines following the methods of Chapter 4, and determine the accuracy of empirical metallicity diagnostics in high redshift galaxies. Spectrally resolved absorption line profiles will yield the covering fraction of neutral gas as a function of velocity, and we will also examine spatial variations. Constraints on the covering fraction will be of interest in the context of escaping ionizing radiation. Ultimately these data will provide valuable information on the detailed physical characteristics of individual sources as well as the degree of intrinsic scatter within the population, which is not known from studies of composite spectra.

Tremendous progress has already been made in measuring the properties of high redshift galaxies and understanding their evolution. Our survey of spectrally and spatially resolved outflow properties will address many remaining key questions, provide detailed measurements which are often not possible even for composite spectra, and will likely unearth new puzzles. Finally, studies of gravitationally lensed galaxies provide a glimpse of the increased resolution and sensitivity that the next generation of $20-40$ meter diameter optical/IR telescopes will routinely provide. Future observations of lensed galaxies with these telescopes will be impressive indeed.

Bibliography

Allam, S. S., Tucker, D. L., Lin, H., et al. 2007, ApJL, 662, L51

Allende Prieto, C., Lambert, D. L., & Asplund, M. 2001, ApJL, 556, L63

Baldwin, J. A., Phillips, M. M., & Terlevich, R. 1981, PASP, 93, 5

Balestra, I., Mainieri, V., Popesso, P., et al. 2010, A&AP, 512, A12

Bastian, N., Emsellem, E., Kissler-Patig, M., & Maraston, C. 2006, A&AP, 445, 471

Belokurov, V., Evans, N. W., Moiseev, A., et al. 2007, ApJL, 671, L9

Belokurov, V., Evans, N. W., Hewett, P. C., et al. 2009, MNRAS, 392, 104

Bertin, E., & Arnouts, S. 1996, AAPS, 117, 393

Bian, F., Fan, X., Bechtold, J., et al. 2010, ApJ, 725, 1877

Blakeslee, J. P., et al. 2003, ApJL, 596, L143

Bouché, N., Cresci, G., Davies, R., et al. 2007, ApJ, 671, 303

Bournaud, F., et al. 2008, A&AP, 486, 741

Bouwens, R. J., Illingworth, G. D., Blakeslee, J. P., Broadhurst, T. J., & Franx, M. 2004, ApJL, 611, L1

Bouwens, R. J., Illingworth, G. D., Franx, M., & Ford, H. 2007, ApJ, 670, 928

Bouwens, R. J., Illingworth, G. D., Franx, M., et al. 2009, ApJ, 705, 936

Bouwens, R. J., Illingworth, G. D., Oesch, P. A., et al. 2011, ApJ, 737, 90

Bouwens, R. J., Illingworth, G. D., Oesch, P. A., et al. 2012, ApJ, 754, 83

Bradač, M., Allen, S. W., Treu, T., et al. 2008, ApJ, 687, 959

Brammer, G. B., Whitaker, K. E., van Dokkum, P. G., et al. 2011, ApJ, 739, 24

Bresolin, F., Kennicutt, R. C., & Ryan-Weber, E. 2012, ApJ, 750, 122

Brinchmann, J., Pettini, M., & Charlot, S. 2008, MNRAS, 385, 769

Broadhurst, T., Huang, X., Frye, B., & Ellis, R. 2000, ApJL, 534, L15

Brooks, A. M., Governato, F., Quinn, T., Brook, C. B., & Wadsley, J. 2009, ApJ, 694, 396

Burles, S., Nollett, K. M., & Turner, M. S. 2001, PRD, 63, 063512

Calzetti, D., Armus, L., Bohlin, R. C., et al. 2000, ApJ, 533, 682

Campusano, L. E., Pelló, R., Kneib, J.-P., et al. 2001, A&AP, 378, 394

Chapman, S. C., Blain, A. W., Smail, I., & Ivison, R. J. 2005, ApJ, 622, 772

Colley, W. N., Tyson, J. A., & Turner, E. L. 1996, ApJL, 461, L83

Conroy, C., & Wechsler, R. H. 2009, ApJ, 696, 620

Considère, S., Coziol, R., Contini, T., & Davoust, E. 2000, A&AP, 356, 89

Coppin, K. E. K., et al. 2007, ApJ, 665, 936

Courteau, S. 1997, AJ, 114, 2402

Cresci, G., et al. 2009, ApJ, 697, 115

Cresci, G., Mannucci, F., Maiolino, R., et al. 2010, Nature, 467, 811

Cushing, M. C., Vacca, W. D., & Rayner, J. T. 2004, PASP, 116, 362

Daddi, E., Bournaud, F., Walter, F., et al. 2010, ApJ, 713, 686

Davé, R., Finlator, K., & Oppenheimer, B. D. 2011, MNRAS, 416, 1354

Davies, R. I. 2007, MNRAS, 375, 1099

Davis, M., Faber, S. M., Newman, J., et al. 2003, Proc. SPIE, 4834, 161

Dekel, A., Birnboim, Y., Engel, G., et al. 2009, Nature, 457, 451

Dib, S., Bell, E., & Burkert, A. 2006, ApJ, 638, 797

Dickinson, M., Papovich, C., Ferguson, H. C., & Budavári, T. 2003, ApJ, 587, 25

Dye, S., Smail, I., Swinbank, A. M., Ebeling, H., & Edge, A. C. 2007, MNRAS, 379, 308

Dye, S., Evans, N. W., Belokurov, V., Warren, S. J., & Hewett, P. 2008, MNRAS, 388, 384

Ebbels, T. M. D., Le Borgne, J.-F., Pello, R., et al. 1996, MNRAS, 281, L75

Ebeling, H., Edge, A. C., & Henry, J. P. 2001, ApJ, 553, 668

Eldridge, J. J., & Stanway, E. R. 2009, MNRAS, 400, 1019

Eldridge, J. J., & Stanway, E. R. 2011, MNRAS, 1595

Elíasdóttir, Á., Limousin, M., Richard, J., et al. 2007, ApJ submitted, arXiv:0710.5636

Ellis, R. S. 2008, Saas-Fee Advanced Course 36: First Light in the Universe, 259

Elmegreen, B. G., & Elmegreen, D. M. 2005, ApJ, 627, 632

Elmegreen, B. G., Elmegreen, D. M., Fernandez, M. X., & Lemonias, J. J. 2009, ApJ, 692, 12

Epinat, B., Amram, P., Balkowski, C., & Marcelin, M. 2009, MNRAS, 1917

Epinat, B., Tasca, L., Amram, P., et al. 2012, A&AP, 539, A92

Erb, D. K., Shapley, A. E., Pettini, M., et al. 2006, ApJ, 644, 813

Erb, D. K., Steidel, C. C., Shapley, A. E., et al. 2006, ApJ, 646, 107

Erb, D. K., Steidel, C. C., Shapley, A. E., et al. 2006, ApJ, 647, 128

Erb, D. K., Pettini, M., Shapley, A. E., et al. 2010, ApJ, 719, 1168

Evstigneeva, E. A., Gregg, M. D., Drinkwater, M. J., & Hilker, M. 2007, AJ, 133, 1722

Faber, S. M., Phillips, A. C., Kibrick, R. I., et al. 2003, Proc. SPIE, 4841, 1657

Fakhouri, J., Ma, C.-P., & Boylan-Kolchin, M. 2010, MNRAS, 406, 2267

Faucher-Giguère, C.-A., Kereš, D., & Ma, C.-P. 2011, MNRAS, 417, 2982

Ferguson, H. C., Dickinson, M., Giavalisco, M., et al. 2004, ApJL, 600, L107

Finkelstein, S. L., Papovich, C., Rudnick, G., et al. 2009, ApJ, 700, 376

Finlator, K., & Davé, R. 2008, MNRAS, 385, 2181

Forero-Romero, J. E., Yepes, G., Gottloeber, S., & Prada, F. 2011, arXiv:1109.0228

Förster Schreiber, N. M., Genzel, R., Lehnert, M. D., et al. 2006, ApJ, 645, 1062

Förster Schreiber, N. M., et al. 2009, ApJ, 706, 1364

Frye, B. L., Coe, D., Bowen, D. V., et al. 2007, ApJ, 665, 921

Fu, J., Hou, J. L., Yin, J., & Chang, R. X. 2009, ApJ, 696, 668

Fuentes-Masip, O., Muñoz-Tuñón, C., Castañeda, H. O., & Tenorio-Tagle, G. 2000, AJ, 120, 752

Genzel, R., Tacconi, L. J., Eisenhauer, F., et al. 2006, Nature, 442, 786

Genzel, R., et al. 2008, ApJ, 687, 59

Genzel, R., Newman, S., Jones, T., et al. 2011, ApJ, 733, 101

Giavalisco, M., Ferguson, H. C., Koekemoer, A. M., et al. 2004, ApJL, 600, L93

Gnerucci, A., Marconi, A., Cresci, G., et al. 2011, A&AP, 528, A88

González, V., Labbé, I., Bouwens, R. J., et al. 2011, ApJL, 735, L34

Gonzalez Delgado, R. M., & Perez, E. 1997, APJS, 108, 199

Grogin, N. A., Kocevski, D. D., Faber, S. M., et al. 2011, arXiv:1105.3753

Gunn, J. E., & Peterson, B. A. 1965, ApJ, 142, 1633

Haiman, Z., & Spaans, M. 1999, ApJ, 518, 138

Hainline, K. N., Shapley, A. E., Kornei, K. A., et al. 2009, ApJ, 701, 52

Hainline, L. J., Blain, A. W., Smail, I., et al. 2011, ApJ, 740, 96

Halliday, C., Daddi, E., Cimatti, A., et al. 2008, A&AP, 479, 417

Hammer, F., Rigaut, F., Le Fevre, O., Jones, J., & Soucail, G. 1989, A&AP, 208, L7

Harris, W. E. 1996, VizieR Online Data Catalog, 7195, 0

Haşegan, M., et al. 2005, ApJ, 627, 203

Hasinger, G., Giacconi, R., Gunn, J. E., et al. 1998, A&AP, 340, L27

Hayashi, M., Motohara, K., Shimasaku, K., et al. 2009, ApJ, 691, 140

Heckman, T. M. 2002, Extragalactic Gas at Low Redshift, 254, 292

Herter, T. L., Henderson, C. P., Wilson, J. C., et al. 2008, Proc. SPIE, 7014,

Hilker, M., Baumgardt, H., Infante, L., Drinkwater, M., Evstigneeva, E., & Gregg, M. 2007, A&AP, 463, 119

Hopkins, A. M., & Beacom, J. F. 2006, ApJ, 651, 142

Jones, T. A., Swinbank, A. M., Ellis, R. S., Richard, J., & Stark, D. P. 2010, MNRAS, 404, 1247

Jones, T., Ellis, R., Jullo, E., & Richard, J. 2010, ApJL, 725, L176

Jullo, E., Kneib, J.-P., Limousin, M., Elíasdóttir, Á., Marshall, P. J., & Verdugo, T. 2007, New Journal of Physics, 9, 447

Jullo, E., & Kneib, J.-P. 2009, MNRAS, 395, 1319

Kauffmann, G., Heckman, T. M., Tremonti, C., et al. 2003, MNRAS, 346, 1055

Kelson, D. D. 2003, PASP, 115, 688

Kennicutt, R. C., Jr. 1998, ApJ, 498, 541

Kereš, D., Katz, N., Fardal, M., Davé, R., & Weinberg, D. H. 2009, MNRAS, 395, 160

Kewley, L. J., Dopita, M. A., Sutherland, R. S., Heisler, C. A., & Trevena, J. 2001, ApJ, 556, 121

Kewley, L. J., & Dopita, M. A. 2002, APJS, 142, 35

Kewley, L. J., Rupke, D., Zahid, H. J., Geller, M. J., & Barton, E. J. 2010, ApJL, 721, L48

Kneib, J. P., Mellier, Y., Fort, B., & Mathez, G. 1993, A&AP, 273, 367

Kneib, J.-P., Ellis, R. S., Smail, I., Couch, W. J., & Sharples, R. M. 1996, ApJ, 471, 643

Kneib, J.-P., van der Werf, P. P., Kraiberg Knudsen, K., et al. 2004, MNRAS, 349, 1211

Kobulnicky, H. A., & Skillman, E. D. 1998, ApJ, 497, 601

Koekemoer, A. M., Fruchter, A. S., Hook, R. N., Hack, W. 2002, HST Calibration Workshop (eds. S. Arribas, A. Koekemoer, B. Whitmore; STScI: Baltimore), 337

Koekemoer, A. M., Faber, S. M., Ferguson, H. C., et al. 2011, arXiv:1105.3754

Kornei, K. A., Shapley, A. E., Martin, C. L., et al. 2012, arXiv:1205.0812

Kriek, M., van Dokkum, P. G., Labbé, I., et al. 2009, ApJ, 700, 221

Kroupa, P. 2002, Science, 295, 82

Lamareille, F., Brinchmann, J., Contini, T., et al. 2009, A&AP, 495, 53

Lara-López, M. A., Cepa, J., Bongiovanni, A., et al. 2010, A&AP, 521, L53

Larkin, J., et al. 2006, New Astronomy Review, 50, 362

Laursen, P., Sommer-Larsen, J., & Razoumov, A. O. 2011, ApJ, 728, 52

Law, D. R., Steidel, C. C., Erb, D. K., Pettini, M., Reddy, N. A., Shapley, A. E., Adelberger, K. L., & Simenc, D. J. 2007, ApJ, 656, 1

Law, D. R., Steidel, C. C., Erb, D. K., Larkin, J. E., Pettini, M., Shapley, A. E., & Wright, S. A. 2007, ApJ, 669, 929

Law, D. R., Steidel, C. C., Erb, D. K., Larkin, J. E., Pettini, M., Shapley, A. E., & Wright, S. A. 2009, ApJ, 697, 2057

Law, D. R., Shapley, A. E., Steidel, C. C., et al. 2012, Nature, 487, 338

Lee, H., Skillman, E. D., Cannon, J. M., et al. 2006, ApJ, 647, 970

Lee, J. C., Kennicutt, R. C., Funes, S. J., José G., Sakai, S., & Akiyama, S. 2007, ApJL, 671, L113

Lehnert, M. D., Nesvadba, N. P. H., Tiran, L. L., Matteo, P. D., van Driel, W., Douglas, L. S., Chemin, L., & Bournaud, F. 2009, ApJ, 699, 1660

Lemoine-Busserolle, M., Contini, T., Pelló, R., et al. 2003, A&AP, 397, 839

Lequeux, J., Peimbert, M., Rayo, J. F., Serrano, A., & Torres-Peimbert, S. 1979, A&AP, 80, 155

Lilly, S. J., Carollo, C. M., & Stockton, A. N. 2003, ApJ, 597, 730

Limousin, M., Ebeling, H., Ma, C.-J., et al. 2010, MNRAS, 405, 777

Lin, H., et al. 2009, ApJ, 699, 1242

Longair, M. S. 2008, Galaxy Formation. Berlin: Springer, 2008. ISBN 978-3-540-73477-2

Lynds, R., & Toomre, A. 1976, ApJ, 209, 382

Maciel, W. J., Costa, R. D. D., & Uchida, M. M. M. 2003, A&AP, 397, 667

Magrini, L., Corbelli, E., & Galli, D. 2007, A&AP, 470, 843

Maiolino, R., Nagao, T., Grazian, A., et al. 2008, A&AP, 488, 463

Mannucci, F., Cresci, G., Maiolino, R., et al. 2009, MNRAS, 398, 1915

Mannucci, F., Cresci, G., Maiolino, R., Marconi, A., & Gnerucci, A. 2010, MNRAS, 408, 2115

Marcon-Uchida, M. M., Matteucci, F., & Costa, R. D. D. 2010, A&AP, 520, A35

Masters, D., & Capak, P. 2011, PASP, 123, 638

McCrady, N., & Graham, J. R. 2007, ApJ, 663, 844

McLean, I. S., Becklin, E. E., Bendiksen, O., et al. 1998, Proc. SPIE, 3354, 566

Meiksin, A. 2006, MNRAS, 365, 807

Mellier, Y., Fort, B., Soucail, G., Mathez, G., & Cailloux, M. 1991, ApJ, 380, 334

Miller, S. H., Bundy, K., Sullivan, M., Ellis, R. S., & Treu, T. 2011, ApJ, 741, 115

Miller, S. H., Ellis, R. S., Sullivan, M., et al. 2012, arXiv:1201.4386

Mortlock, D. J., Warren, S. J., Venemans, B. P., et al. 2011, Nature, 474, 616

Moster, B. P., Naab, T., & White, S. D. M. 2012, arXiv:1205.5807

Murray, N. 2009, ApJ, 691, 946

Murray, N., Quataert, E., & Thompson, T. A. 2010, ApJ, 709, 191

Nagao, T., Maiolino, R., & Marconi, A. 2006, A&AP, 459, 85

Natarajan, P., Kneib, J.-P., Smail, I., & Ellis, R. S. 1998, ApJ, 499, 600

Neistein, E., van den Bosch, F. C., & Dekel, A. 2006, MNRAS, 372, 933

Nesvadba, N. P. H., et al. 2006, ApJ, 650, 661

Newman, A. B., Treu, T., Ellis, R. S., & Sand, D. J. 2011, ApJL, 728, L39

Newman, S., & Genzel, R. 2012, American Astronomical Society Meeting Abstracts, 219, #441.19

Newman, S. F., Shapiro Griffin, K., Genzel, R., et al. 2012, ApJ, 752, 111

Ocvirk, P., Pichon, C., & Teyssier, R. 2008, MNRAS, 390, 1326

Oke, J. B. 1974, APJS, 27, 21

Ono, Y., Ouchi, M., Mobasher, B., et al. 2011, arXiv:1107.3159

Ouchi, M., Shimasaku, K., Akiyama, M., et al. 2008, APJS, 176, 301

Pagel, B. E. J., Edmunds, M. G., Blackwell, D. E., Chun, M. S., & Smith, G. 1979, MNRAS, 189, 95

Pentericci, L., Fontana, A., Vanzella, E., et al. 2011, arXiv:1107.1376

Pérez-Montero, E., Contini, T., Lamareille, F., et al. 2009, A&AP, 495, 73

Pettini, M., Steidel, C. C., Adelberger, K. L., Dickinson, M., & Giavalisco, M. 2000, ApJ, 528, 96

Pettini, M., Shapley, A. E., Steidel, C. C., et al. 2001, ApJ, 554, 981

Pettini, M., Rix, S. A., Steidel, C. C., et al. 2002, ApJ, 569, 742

Pettini, M., & Pagel, B. E. J. 2004, MNRAS, 348, L59

Pilkington, K., Few, C. G., Gibson, B. K., et al. 2012, A&AP, 540, A56

Prantzos, N., & Boissier, S. 2000, MNRAS, 313, 338

Press, W. H., & Schechter, P. 1974, ApJ, 187, 425

Pryor, C., & Meylan, G. 1993, Structure and Dynamics of Globular Clusters, 50, 357

Queyrel, J., Contini, T., Kissler-Patig, M., et al. 2012, A&AP, 539, A93

Quider, A. M., Pettini, M., Shapley, A. E., & Steidel, C. C. 2009, MNRAS, 398, 1263

Quider, A. M., Shapley, A. E., Pettini, M., Steidel, C. C., & Stark, D. P. 2010, MNRAS, 402, 1467

Reddy, N. A., & Steidel, C. C. 2004, ApJL, 603, L13

Reddy, N. A., & Steidel, C. C. 2009, ApJ, 692, 778

Rich, J. A., Torrey, P., Kewley, L. J., Dopita, M. A., & Rupke, D. S. N. 2012, arXiv:1204.5520

Richard, J., Schaerer, D., Pelló, R., Le Borgne, J.-F., & Kneib, J.-P. 2003, A&AP, 412, L57

Richard, J., Pelló, R., Schaerer, D., Le Borgne, J.-F., & Kneib, J.-P. 2006, A&AP, 456, 861

Richard, J., Kneib, J.-P., Jullo, E., et al. 2007, ApJ, 662, 781

Richard, J., Stark, D. P., Ellis, R. S., et al. 2008, ApJ, 685, 705

Richard, J., Pei, L., Limousin, M., Jullo, E., & Kneib, J. P. 2009, A&AP, 498, 37

Richard, J., Kneib, J.-P., Limousin, M., Edge, A., & Jullo, E. 2010, MNRAS, 402, L44

Richard, J., Smith, G. P., Kneib, J.-P., et al. 2010, MNRAS, 404, 325

Richard, J., Jones, T., Ellis, R., et al. 2011, MNRAS, 413, 643

Robertson, B. E., Ellis, R. S., Dunlop, J. S., McLure, R. J., & Stark, D. P. 2010, Nature, 468, 49

Romano, R., Mayya, Y. D., & Vorobyov, E. I. 2008, AJ, 136, 1259

Rupke, D. S. N., Kewley, L. J., & Barnes, J. E. 2010, ApJL, 710, L156

Rupke, D. S. N., Kewley, L. J., & Chien, L.-H. 2010, ApJ, 723, 1255

Ryden, B. 2003, Introduction to cosmology. San Francisco, CA, USA: Addison Wesley, ISBN 0-8053-8912-1

Salpeter, E. E., 1955, ApJ, 121, 161

Sand, D. J., Treu, T., Ellis, R. S., & Smith, G. P. 2005, ApJ, 627, 32

Santos, M. R., Ellis, R. S., Kneib, J.-P., Richard, J., & Kuijken, K. 2004, ApJ, 606, 683

Schenker, M. A., Stark, D. P., Ellis, R. S., et al. 2012, ApJ, 744, 179

Schmidt, M. 1963, ApJ, 137, 758

Shapley, A. E., Steidel, C. C., Adelberger, K. L., et al. 2001, ApJ, 562, 95

Shapley, A. E., Steidel, C. C., Pettini, M., & Adelberger, K. L. 2003, ApJ, 588, 65

Shapley, A. E., Steidel, C. C., Pettini, M., Adelberger, K. L., & Erb, D. K. 2006, ApJ, 651, 688

Shapley, A. E. 2011, ARAA, 49, 525

Siana, B., Smail, I., Swinbank, A. M., et al. 2009, ApJ, 698, 1273

Simcoe, R. A., Sargent, W. L. W., & Rauch, M. 2004, ApJ, 606, 92

Smail, I., Swinbank, A. M., Richard, J., et al. 2007, ApJL, 654, L33

Smith, G. P., Kneib, J.-P., Smail, I., Mazzotta, P., Ebeling, H., & Czoske, O. 2005, MNRAS, 359, 417

Sommariva, V., Mannucci, F., Cresci, G., et al. 2012, A&AP, 539, A136

Sparke, L. S., & Gallagher, J. S., III 2000, Galaxies in the Universe. Cambridge, UK: Cambridge University Press

Spergel, D. N., et al. 2003, APJS, 148, 175

Springel, V., White, S. D. M., Jenkins, A., et al. 2005, Nature, 435, 629

Stark, D. P., Ellis, R. S., Richard, J., Kneib, J.-P., Smith, G. P., & Santos, M. R. 2007, ApJ, 663, 10

Stark, D. P., Swinbank, A. M., Ellis, R. S., Dye, S., Smail, I. R., & Richard, J. 2008, Nature, 455, 775

Stark, D. P., Ellis, R. S., Bunker, A., et al. 2009, ApJ, 697, 1493

Stark, D. P., Ellis, R. S., Chiu, K., Ouchi, M., & Bunker, A. 2010, MNRAS, 408, 1628

Stark, D. P., Ellis, R. S., & Ouchi, M. 2011, ApJL, 728, L2

Steidel, C. C., Adelberger, K. L., Shapley, A. E., et al. 2003, ApJ, 592, 728

Steidel, C. C., Erb, D. K., Shapley, A. E., et al. 2010, ApJ, 717, 289

Steidel, C. C., Bogosavljević, M., Shapley, A. E., et al. 2011, ApJ, 736, 160

Swinbank, A. M., Bower, R. G., Smith, G. P., Wilman, R. J., Smail, I., Ellis, R. S., Morris, S. L., & Kneib, J.-P. 2007, MNRAS, 376, 479

Swinbank, A. M., et al. 2009, MNRAS, 400, 1121

Swinbank, A. M., Smail, I., Chapman, S. C., et al. 2010, MNRAS, 405, 234

Tacconi, L. J., et al. 2008, ApJ, 680, 246

Tacconi, L. J., Genzel, R., Neri, R., et al. 2010, Nature, 463, 781

Toomre, A. 1964, ApJ, 139, 1217

Torres-Flores, S., Epinat, B., Amram, P., Plana, H., & Mendes de Oliveira, C. 2011, MNRAS, 416, 1936

Tozzi, P., Madau, P., Meiksin, A., & Rees, M. J. 2000, ApJ, 528, 597

Trac, H. Y., & Gnedin, N. Y. 2011, Advanced Science Letters, 4, 228

Tremonti, C. A., et al. 2004, ApJ, 613, 898

Tumlinson, J., Thom, C., Werk, J. K., et al. 2011, Science, 334, 948

Vacca, W. D., Cushing, M. C., & Rayner, J. T. 2004, PASP, 116, 352

van Dokkum, P. G., Förster Schreiber, N. M., Franx, M., et al. 2003, ApJL, 587, L83

van Dokkum, P. G., Whitaker, K. E., Brammer, G., et al. 2010, ApJ, 709, 1018

van Zee, L., Salzer, J. J., Haynes, M. P., O'Donoghue, A. A., & Balonek, T. J. 1998, AJ, 116, 2805

Vanzella, E., Cristiani, S., Dickinson, M., et al. 2005, A&AP, 434, 53

Vanzella, E., Cristiani, S., Dickinson, M., et al. 2006, A&AP, 454, 423

Vanzella, E., Cristiani, S., Dickinson, M., et al. 2008, A&AP, 478, 83

Vanzella, E., Giavalisco, M., Dickinson, M., et al. 2009, ApJ, 695, 1163

Veilleux, S., & Osterbrock, D. E. 1987, APJS, 63, 295

Vila-Costas, M. B., & Edmunds, M. G. 1992, MNRAS, 259, 121

Wang, W.-H., Cowie, L. L., Barger, A. J., Keenan, R. C., & Ting, H.-C. 2010, APJS, 187, 251

Wardlow, J. L., Smail, I., Coppin, K. E. K., et al. 2011, MNRAS, 415, 1479

Weiner, B. J., Coil, A. L., Prochaska, J. X., et al. 2009, ApJ, 692, 187

Werk, J. K., Putman, M. E., Meurer, G. R., & Santiago-Figueroa, N. 2011, ApJ, 735, 71

Westmoquette, M., Clements, D., Bendo, G., & Khan, S. 2012, arXiv:1205.0203

Wizinowich, P. L., et al. 2006, PASP, 118, 297

Wright, S. A., Larkin, J. E., Law, D. R., Steidel, C. C., Shapley, A. E., & Erb, D. K. 2009, ApJ, 699, 421

Wright, S. A., Larkin, J. E., Graham, J. R., & Ma, C.-P. 2010, ApJ, 711, 1291

Yang, X., Mo, H. J., van den Bosch, F. C., Zhang, Y., & Han, J. 2011, arXiv:1110.1420

Yuan, T.-T., Kewley, L. J., Swinbank, A. M., Richard, J., & Livermore, R. C. 2011, ApJL, 732, L14

Young, J. S., & Scoville, N. Z. 1991, ARAA, 29, 581